

THE UNIVERSITY OF CHICAGO

GENERALIZATION OF BCS THEORY TO SHORT COHERENCE LENGTH
SUPERCONDUCTORS: A BCS–BOSE-EINSTEIN CROSSOVER SCENARIO

A DISSERTATION SUBMITTED TO
THE FACULTY OF THE DIVISION OF THE PHYSICAL SCIENCES
IN CANDIDACY FOR THE DEGREE OF
DOCTOR OF PHILOSOPHY

DEPARTMENT OF PHYSICS

BY
QIJIN CHEN

CHICAGO, ILLINOIS
AUGUST 2000

To my parents

Copyright © 2000 by Qijin Chen.
All rights reserved.

ABSTRACT

The microscopic theory of superconductivity by Bardeen, Cooper and Schrieffer (BCS) is considered one of the most successful theories in condensed matter physics. In ordinary metal superconductors the coherence length ξ is large, and a simple mean field approach, such as BCS, is thereby justified. This theory has two important features: the order parameter and excitation gap are identical, and the formation of pairs and their Bose condensation take place at the same temperature T_c . It is now known that BCS theory fails to explain the superconductivity in the underdoped copper oxide superconductors: the excitation gap Δ is finite at T_c and thus distinct from the order parameter Δ_{sc} . Since these superconductors belong to a large class of inter-related, generally small ξ materials, this failure has the potential for widespread impact.

In this thesis, we have extended BCS theory in a natural way to short coherence length superconductors, based on a BCS–Bose-Einstein condensation (BEC) crossover scenario. We arrive at a simple physical picture in which incoherent, finite momentum pairs become progressively more important as the pairing interaction becomes stronger. The ensuing distinction between Δ and Δ_{sc} can be associated with these pairs. These finite momentum pairs are treated at a mean field level which addresses the pairs and the single particles on an equal footing. Within our picture, the superconducting transition from the fermionic perspective and Bose-Einstein condensation from the bosonic perspective are just two sides of the same coin.

In contrast to many other theoretical approaches, our theory is capable of making quantitative predictions, which can be tested. This theory was applied to the cuprates to obtain a phase diagram. In addition, because this fitted (with one free parameter) phase diagram represented experiment quite well, it was possible to quantitatively address derived quantities, such as the hole concentration and temperature dependences of the in-plane penetration depth and specific heat. The mutually compensating contributions from fermionic quasi-particles and bosonic pair excitations have provided a natural explanation for the quasi-universal behavior of the normalized in-plane superfluid density as a function of reduced

temperature. Our bosonic pair excitations also provide an intrinsic mechanism for the long mysterious linear T terms in the specific heat. We found new qualitative effects as well, associated with predicted low T power laws, which arise from our incoherent pair contributions. These power laws seem to be consistent with existing experiments, although more systematic experimental studies are needed. Finally, we demonstrated that the onset of superconducting long range order leads to sharp features in the specific heat at T_c , (although the excitation gap is smooth across T_c), which are consistent with experiment.

ACKNOWLEDGEMENTS

I would like to thank my thesis advisor, Professor Kathryn Levin, for her support throughout my graduate research. This thesis work was completed under her careful guidance. Her support has made it possible for me to present our work at various conferences, and to communicate with the community of high T_c superconductivity. Both her insights in physics and her expertise in communicating science have greatly enhanced these presentations and communications. Her constant enthusiasm for physics has been an excitement and an encouragement that help me make rapid progress during the research. Her careful reading and revision have significantly enhanced this manuscript.

I am very grateful to have Ioan Kosztin as a collaborator and a friend during my graduate career at the University of Chicago. His support has greatly facilitated this research, and his insights in physics have been critical in extending the BCS-BEC crossover theory below T_c . The countless memorable late nights we spent together in the Research Institute building have been very fruitful. I am also grateful to Boldizsár Jankó for his generous help, useful advice, and, especially, for collaborations during the early stages of this project. In addition, I wish to thank Ying-Jer Kao for collaborations on the collective mode issues and for other useful discussions during my graduate study at the University.

I wish to thank G. Deutscher, A. J. Leggett, G. F. Mazenko, M. R. Norman, B. R. Patton, N. E. Phillips, M. Randeria, A. A. Varlamov, and P. B. Wiegmann for helpful discussions, D. A. Bonn, A. Carrington, R. W. Giannetta, W. N. Hardy, S. Kamal, N. Miyakawa, C. Panagopoulos, T. Xiang, J. F. Zasadzinski, and X. J. Zhou for useful discussions and for sharing their experimental data with us, J. R. Cooper, S. Heim, A. Junod, I. O. Kulik, J. W. Loram, and K. A. Moler for useful communications.

Finally, my gratitude goes to my thesis committee members, Gene Mazenko, Jeffery Harvey, and Thomas Rosenbaum, for their careful reading of this manuscript and for their precious time spent on the committee meetings and the thesis defense. I also wish to thank Woowon Kang for his time on my first committee meeting.

TABLE OF CONTENTS

ABSTRACT	v
ACKNOWLEDGEMENTS	vii
LIST OF FIGURES	xiii
1 INTRODUCTION AND OVERVIEW	1
1.1 Background: High T_c <i>problem</i>	1
1.1.1 Overview of BCS theory	1
1.1.2 Failure of BCS theory in high T_c superconductors	5
1.1.3 A successful theory for high T_c superconductors is yet to come	7
1.2 Crossover from BCS to Bose-Einstein condensation	9
1.2.1 Relevance of Bose-Einstein condensation	9
1.2.2 Overview of BCS-BEC crossover	12
1.3 Current work — Generalizing BCS theory to arbitrary coupling strength	14
2 THEORETICAL FORMALISM	18
2.1 Physical picture at arbitrary coupling strength	18
2.2 General formalism – Derivation of the Dyson’s Equations	21
2.2.1 Truncation of equations of motion	22
2.2.2 Dyson’s equations	25
2.3 Solution to Dyson’s equations	28
2.3.1 Superconducting instability condition	28
2.3.2 T matrix formalism of BCS theory: Relationship to the Nambu Gor’kov Green’s function scheme	29
2.3.3 Beyond BCS: Effects of a pseudogap at finite $T \leq T_c$	32
3 T_c AND THE SUPERCONDUCTING INSTABILITY OF THE NORMAL STATE	37
3.1 Specifications for various models	38
3.2 Overview: T_c and effective mass of the pairs	39
3.3 Effects of dimensionality	43
3.4 Effects of a periodic lattice	45
3.5 Effects of d -wave symmetry	46
3.6 Phase diagrams	48

4	SUPERCONDUCTING PHASE	50
4.1	Excitation gap, pseudogap, and superconducting gap	51
4.2	Superfluid density	54
4.3	Low temperature specific heat	60
5	GAUGE INVARIANCE AND THE COLLECTIVE MODES	65
5.1	Introduction	65
5.2	Electromagnetic response and collective modes of a superconductor: Beyond BCS theory	66
5.2.1	Gauge invariant electromagnetic response kernel	67
5.2.2	The Goldstone boson or AB mode	70
5.2.3	General collective modes	71
5.3	Effect of pair fluctuations on the electromagnetic response: Some examples	72
5.3.1	$T = 0$ behavior of the AB mode and pair susceptibility	73
5.3.2	AB mode at finite temperatures	75
5.4	Numerical results: Zero and finite temperatures	79
5.5	Some additional remarks	82
5.5.1	Pair excitations vs phase fluctuations	82
5.5.2	Strong coupling limit: Composite vs true bosons	82
6	APPLICATION TO THE CUPRATES	85
6.1	Cuprate phase diagram	85
6.2	In-plane penetration depth and c -axis Josephson critical current	89
6.2.1	Quasi-universal behavior of normalized superfluid density vs T/T_c .	89
6.2.2	Quasi-universal behavior of c -axis Josephson critical current	92
6.2.3	Search for bosonic pair excitation contributions in penetration depth	94
6.2.4	Slope of in-plane inverse squared penetration depth: Quantitative analysis	95
6.3	Specific heat at low T	98
7	THERMODYNAMIC SIGNATURES OF THE SUPERCONDUCTING TRANSITION	100
7.1	Spectral functions and the density of states	102
7.2	Specific heat	105
7.3	Application to the cuprates	109
7.3.1	Tunneling spectra	109
7.3.2	Specific heat	111
7.4	Low T extrapolation of the pseudogapped normal state	114
8	CONCLUDING REMARKS	117
8.1	Summary	118
8.2	Remarks	119
8.3	Speculations	120

8.4	Future directions	121
A	EXPRESSION FOR PAIR DISPERSION, Ω_q	122
A.1	3D s -wave jellium	126
A.2	Quasi-2D s -wave jellium	127
A.3	Quasi-2D lattice: s - and d -wave	129
A.3.1	Quasi-2D lattice: s -wave	129
A.3.2	Quasi-2D lattice: d -wave	130
A.4	Weak coupling limit	131
A.5	Effects of the Ω^2 term of the inverse T matrix	132
B	BCS–BEC CROSSOVER FOR A QUASI-2D D -WAVE SUPERCONDUCTOR AT ARBITRARY DENSITY	135
B.1	Bosonic d -wave superconductors: Extreme low density limit	135
B.2	n - g phase diagram	137
B.3	Comparison with s -wave superconductors	139
B.4	Effective pair mass	140
B.5	Pair size or correlation length	141
C	EXTRAPOLATION FOR THE COUPLED EQUATIONS ABOVE T_c	144
D	DERIVATION FOR THE PAIRON CONTRIBUTION TO THE SPECIFIC HEAT	145
E	EVALUATION OF THE VERTEX CORRECTIONS	148
F	FULL EXPRESSIONS FOR THE CORRELATION FUNCTIONS \overleftrightarrow{P} , P_0 , AND P_{00}	152
	BIBLIOGRAPHY	153

LIST OF FIGURES

1.1	Comparison between BCS prediction and experimental measurements for the excitation gap for ordinary metal superconductors.	4
1.2	In BCS theory Cooper pairs highly overlap with each other.	5
1.3	Schematic phase diagram for the cuprates and evidence from ARPES measurements for pseudogap in underdoped samples from ARPES.	6
1.4	Comparison between the weak coupling BCS and strong coupling BEC limits.	10
1.5	Uemura plot, showing a scaling between T_c and the Fermi energy or the superfluid density for short coherence length superconductors.	11
1.6	Typical evolution of the temperature dependence of the excitation gap, the order parameter, and the pseudogap with the coupling strength.	16
1.7	Evolution of the excitations of the system below T_c as the coupling strength increases.	16
2.1	Schematic picture for BCS–BEC crossover: Evolution of the excitations in the system with coupling g above T_c	19
2.2	Diagrammatic representation of Eqs. (2.12) and (2.13) for the two particle scattering matrix L^{+-}	25
2.3	Diagrams for the self-energy and the T matrix.	27
2.4	Feynman diagrams for BCS self-energy and its T matrix representation.	31
2.5	Approximation scheme for the pseudogap self-energy, $\Sigma_{pg}(K)$	34
3.1	T_c , the inverse pair mass, and the pair density as a function of coupling constant at low and high densities in 3D jellium.	43
3.2	Effects of low dimensionality on the crossover behavior of T_c , μ and Δ	44
3.3	Lattice effects on the crossover behavior of T_c and the inverse pair mass with respect to the coupling strength.	46
3.4	Effects of the pairing symmetry on the crossover behavior of T_c , μ and Δ_{pg} on a quasi-2D lattice.	47
3.5	Phase diagrams on a temperature – coupling constant plot for a 3D and quasi-2D jellium, and a quasi-2D lattice with d -wave symmetry.	48
4.1	Temperature dependence of the pseudogap, order parameter and the excitation gap, as well as the chemical potential and relevant T matrix expansion coefficients, below T_c for various coupling strength g in 3D jellium.	52
4.2	Temperature dependence of the normalized superfluid density for different coupling strength from weak to moderately strong in 3D jellium.	57

4.3	Temperature dependence of the normalized superfluid density in s - and d -wave, BCS and pseudogap cases on a quasi-2D lattice.	59
4.4	Diagrammatic representation of the pair excitation contribution to the thermodynamic potential.	62
4.5	Temperature dependence (normalized at T_c) of the specific coefficient γ for s - and d -wave pairing with and without pseudogap.	63
5.1	Diagrammatic representation of the polarization bubble, and the vertex function used to compute the electrodynamic response functions.	76
5.2	AB mode velocity as a function of the coupling strength for various densities in 3D jellium, as well as the strong coupling asymptote as a function of density.	79
5.3	Normalized AB mode velocity on a 3D lattice with an s -wave pairing interaction for various densities as a function of g , and the large g limit for the velocity as a function of density for fixed g	80
5.4	Temperature dependence of the real and imaginary parts of the AB mode velocity for moderate coupling and weak coupling BCS in 3D jellium.	81
6.1	Cuprate phase diagram, and comparison with experiment.	87
6.2	Temperature dependence of various gaps for different doping concentrations.	88
6.3	Quasi-universal behavior of the normalized in-plane superfluid density as a function of reduced temperature with respect to the doping concentration.	90
6.4	Quasi-universal behavior of normalized c -axis Josephson critical current as a function of reduced temperature T/T_c with respect to doping concentration.	93
6.5	Comparison of a -axis penetration depth data in pure YBCO _{6.95} single crystal, with different theoretical fits corresponding to BCS d -wave and to BCS-BEC predictions.	94
6.6	Quantitative analysis of the doping dependence of the zero temperature penetration depth, λ_0 , and the temperature derivative of the inverse squared penetration depth, $ d\lambda^{-2}/dT $ for various cuprates.	97
6.7	Quantitative analysis of the quadratic (associated with quasiparticles) and the linear (associated with pair excitations) T contributions to the specific heat in various cuprates.	98
7.1	Effects of the superconducting long range order on the behavior of the spectral function at the Fermi level $\epsilon_{\mathbf{k}} = 0$ as a function of temperature in a pseudogapped superconductor.	104
7.2	Effects of superconducting long range order on the behavior of the density of states as a function of temperature in a pseudogapped s -wave superconductor.	106
7.3	Comparison of the temperature dependence of the specific heat in the weak coupling BCS case and moderate coupling pseudogap case.	108

7.4	Temperature and doping dependence of tunneling spectra across an SIN junction.	110
7.5	Temperature dependence of the specific heat for various doping concentrations.	112
7.6	Temperature dependence of the excitation gaps for various doping concentrations used for calculations in Fig. 7.5.	113
7.7	Comparison of the extrapolated normal state below T_c in BCS and pseudogap superconductors.	115
7.8	Density of states and SIN tunneling dI/dV characteristics of an extrapolated pseudogap “normal state” below T_c	116
A.1	Effects of the $a_1\Omega^2$ term in the inverse T matrix expansion on the solutions for various gaps as well as T_c as a function of g and T	134
B.1	Crossover behavior of T_c with respect to g for different electron densities on a quasi-2D lattice with d -wave pairing.	136
B.2	Crossover behavior of T_c , $\Delta_{pg}(T_c)$, and $\mu(T_c)$ unphysically low density $n = 0.05$ on a quasi-2D lattice with d -wave pairing symmetry.	136
B.3	Phase diagram of a quasi-2D d -wave superconductor on a density–coupling plot.	137
B.4	Contour plot of T_c on the $n - g$ phase diagram of a quasi-2D d -wave superconductor.	138
B.5	$n - g$ phase diagram of an s -wave superconductor on a quasi-2D lattice, as well as in an isotropic 3D jellium.	140
B.6	Evolution of the effective in-plane pair mass with respect to the coupling constant in quasi-2D with s - and d -wave pairing.	141
B.7	Different behavior of the pair size as a function of g between s - and d -wave pairing on a quasi-2D lattice.	143
D.1	Typical behavior of the pair dispersion and of the scattering phase shift in the T matrix with s -wave pairing.	146

CHAPTER 1

INTRODUCTION AND OVERVIEW

1.1 BACKGROUND: HIGH T_c PROBLEM

Since its discovery in 1986, high critical temperature (T_c) superconductivity in the cuprates has been a great challenge for scientists. While people celebrate the miracle that for the first time mankind can achieve superconductivity at liquid nitrogen temperatures (77K) and thus make superconductors industrially applicable, they find themselves left with a puzzle: Why is the superconducting transition temperature so high? How do we describe superconductivity in these materials? And what is the underlying physics? Although the beautiful microscopic theory by Bardeen, Cooper, and Schrieffer (BCS) [1] has been extremely successful in explaining superconductivity in ordinary metals, scientists have yet to find an answer to these questions, after more than a decade of research.

Many theories have been put forward to attack the high T_c puzzle, yet none has been very successful. Due to the lack of a better theory, for experimentalists, BCS theory is still by far the most widely applied theory to interpret experimental data, and to extract physical quantities. In this work, we will show that BCS theory is a special case of a more general mean field approach and that this generalization can accommodate quantitatively various aspects of experimental observations.

1.1.1 Overview of BCS theory

As in all superconductors, electrons are paired in the superconducting phase. This pairing arises from an (attractive) pairing interaction. In BCS theory, pairing takes place only between electrons with opposite momenta ($\pm k$), and is negligible otherwise. This can be described by the following Hamiltonian:

$$H^{BCS} = \sum_{\mathbf{k}\sigma} \epsilon_{\mathbf{k}} c_{\mathbf{k}\sigma}^{\dagger} c_{\mathbf{k}\sigma} + \sum_{\mathbf{k}\mathbf{k}'} V_{\mathbf{k},\mathbf{k}'} c_{\mathbf{k}\uparrow}^{\dagger} c_{-\mathbf{k}\downarrow}^{\dagger} c_{-\mathbf{k}'\downarrow} c_{\mathbf{k}'\uparrow}, \quad (1.1)$$

where $c_{\mathbf{k}\sigma}^\dagger$ creates a particle in the momentum state \mathbf{k} with spin σ , and $\epsilon_{\mathbf{k}}$ is the energy dispersion measured from the chemical potential μ (we take $\hbar = k_B = 1$). As usual, we assume a separable potential, $V_{\mathbf{k},\mathbf{k}'} = g\varphi_{\mathbf{k}}\varphi_{\mathbf{k}'}$, where $g = -|g|$ is the coupling strength; the momentum dependent function $\varphi_{\mathbf{k}}$ will determine the symmetry of the order parameter. For ordinary metal superconductors, the pairing interaction originates from the electron-phonon interaction, and $\varphi_{\mathbf{k}} = 1$ for \mathbf{k} within a narrow shell of the Fermi sphere, and zero otherwise. The thickness of the shell is determined by the Debye frequency of the materials. Note in Eq. (1.1) we have assumed singlet pairing, which is relevant for both (*s*-wave) normal metal superconductors and the (*d*-wave) cuprate superconductors.

In the normal state, the quantum expectation value of the pair operator $c_{-\mathbf{k}}c_{\mathbf{k}}$ (and its complex conjugate) vanishes (we have suppressed the spin index, following the usual practice). In the superconducting state, where the electrons are paired into Cooper pairs, this expectation value does not vanish: this defines the superconducting order parameter,

$$\Delta_{\mathbf{k}} \equiv - \sum_{\mathbf{k}'} V_{\mathbf{k},\mathbf{k}'} \langle c_{-\mathbf{k}'} c_{\mathbf{k}'} \rangle = \Delta \varphi_{\mathbf{k}}, \quad \Delta \equiv |g| \sum_{\mathbf{k}} \varphi_{\mathbf{k}} \langle c_{-\mathbf{k}} c_{\mathbf{k}} \rangle. \quad (1.2)$$

One key assumption of BCS theory is that the difference between the quantum operator $c_{-\mathbf{k}}c_{\mathbf{k}}$ and its mean field value, $\langle c_{-\mathbf{k}}c_{\mathbf{k}} \rangle$ is small, so that the quadratic term $(c_{-\mathbf{k}}c_{\mathbf{k}} - \langle c_{-\mathbf{k}}c_{\mathbf{k}} \rangle)^2$ is negligible. As a consequence of such a mean field treatment, the Hamiltonian is linearized,

$$H^{BCS} = \sum_{\mathbf{k}\sigma} \epsilon_{\mathbf{k}} c_{\mathbf{k}\sigma}^\dagger c_{\mathbf{k}\sigma} - \sum_{\mathbf{k}} \left(\Delta \varphi_{\mathbf{k}} c_{\mathbf{k}}^\dagger c_{-\mathbf{k}}^\dagger + \Delta^* \varphi_{\mathbf{k}} c_{-\mathbf{k}} c_{\mathbf{k}} \right) - \frac{\Delta^2}{g}. \quad (1.3)$$

This Hamiltonian is not diagonal, and the particles and holes will thus be mixed via the equations of motion for $c_{\mathbf{k}}$ and $c_{-\mathbf{k}}^\dagger$. Eq. (1.3) can, however, be diagonalized via a Bogoliubov transformation

$$\alpha_{\mathbf{k}} = u_{\mathbf{k}} c_{\mathbf{k}} + v_{-\mathbf{k}} c_{-\mathbf{k}}^\dagger, \quad \alpha_{\mathbf{k}}^\dagger = u_{\mathbf{k}} c_{\mathbf{k}}^\dagger + v_{-\mathbf{k}} c_{-\mathbf{k}}, \quad (1.4)$$

provided

$$u_{\mathbf{k}}^2 = \frac{1}{2} \left(1 + \frac{\epsilon_{\mathbf{k}}}{E_{\mathbf{k}}} \right), \quad v_{\mathbf{k}}^2 = \frac{1}{2} \left(1 - \frac{\epsilon_{\mathbf{k}}}{E_{\mathbf{k}}} \right), \quad (1.5)$$

where $E_{\mathbf{k}} = \sqrt{\epsilon_{\mathbf{k}}^2 + \Delta^2 \varphi_{\mathbf{k}}^2}$ is the excitation energy of quasiparticles created by $\alpha_{\mathbf{k}}^\dagger$. Note here and throughout this thesis, we choose $\Delta = \Delta^*$ to be real, which is always possible in the absence of a supercurrent.

At zero temperature, the ground state wavefunction can be expressed as

$$\Psi_0 = \prod_{\mathbf{k}} (u_{\mathbf{k}} + v_{\mathbf{k}} c_{\mathbf{k}}^\dagger c_{-\mathbf{k}}^\dagger) |0\rangle. \quad (1.6)$$

At $T \leq T_c$, the diagonalized Hamiltonian takes the form

$$H^{BCS} = E_0 + \sum_{\mathbf{k}} E_{\mathbf{k}} (\alpha_{\mathbf{k}}^\dagger \alpha_{\mathbf{k}} + \alpha_{-\mathbf{k}}^\dagger \alpha_{-\mathbf{k}}), \quad (1.7)$$

where

$$E_0 = \sum_{\mathbf{k}} (\epsilon_{\mathbf{k}} - E_{\mathbf{k}}) - \frac{\Delta^2}{g} \quad (1.8)$$

is T -dependent. The system energy (per unit volume), measured from the bottom of the band, is thus given by

$$E = \mu n + E_0 + 2 \sum_{\mathbf{k}} E_{\mathbf{k}} f(E_{\mathbf{k}}), \quad (1.9)$$

where $f(x)$ is the Fermi distribution function, and n is the electron density. Note here I consider the general case where the chemical potential μ is not pinned at E_F . This becomes important as the attractive interaction g increases.

Now to create a quasiparticle excitation of the ground state Ψ_0 , it takes at least an energy 2Δ to break a Cooper pair. Thus the excitation spectrum is gapped, unlike that in a Fermi liquid. The value of the excitation gap can be determined via Eq. (1.2). Substituting Eq. (1.4) into Eq. (1.2), one obtains

$$\Delta = -g \sum_{\mathbf{k}} \varphi_{\mathbf{k}} u_{\mathbf{k}} v_{\mathbf{k}} [1 - 2f(E_{\mathbf{k}})] = -g \sum_{\mathbf{k}} \frac{\Delta}{2E_{\mathbf{k}}} [1 - 2f(E_{\mathbf{k}})] \varphi_{\mathbf{k}}^2, \quad (1.10)$$

or

$$1 + g \sum_{\mathbf{k}} \frac{1 - 2f(E_{\mathbf{k}})}{2E_{\mathbf{k}}} \varphi_{\mathbf{k}}^2 = 0. \quad (1.11)$$

BCS theory predicts that the normalized excitation gap $\Delta(T)/\Delta(0)$ as a function of

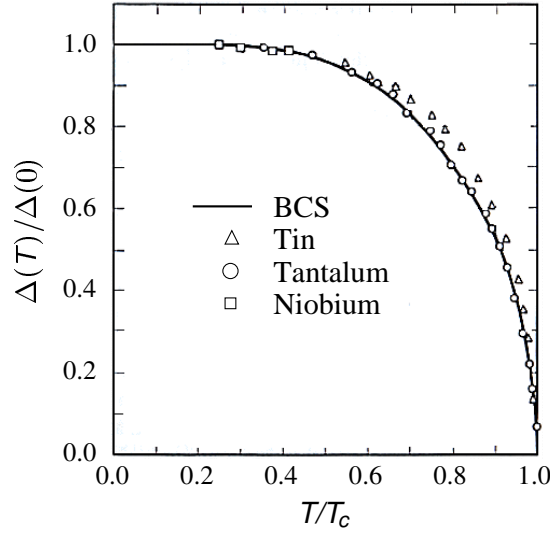


Figure 1.1: Comparison between BCS prediction and experimental measurements for the excitation gap for ordinary metal superconductors.

reduced temperature T/T_c follows a universal curve. Moreover, the ratio $2\Delta(0)/T_c = 3.52$ is also universal.

Figure 1.1 shows the BCS prediction and experimental measurements for the excitation gap for a variety of metals. It is clear that the agreement between theory and experiment is remarkable.

This figure also shows that the excitation gap closes at T_c . In fact, *one important feature of BCS theory is that the excitation gap and the (magnitude of the) order parameter are identical*. This is a consequence of the linearization procedure in the mean field treatment of the Hamiltonian. This procedure may not be valid when the difference $c_{-\mathbf{k}}c_{\mathbf{k}} - \langle c_{-\mathbf{k}}c_{\mathbf{k}} \rangle$ is not small. Indeed, what makes BCS theory work so well for normal metal superconductors is that the coherence length ξ (or, equivalently, the Cooper pair size) for these materials is extremely large. A typical value is of the order of $10^3 - 10^4 \text{ \AA}$, which is about 100-1000 times the size of the lattice constant a . In this way the pairs highly overlap with each other, as schematically shown in Fig. 1.2. In this case, indeed, $c_{-\mathbf{k}}c_{\mathbf{k}} - \langle c_{-\mathbf{k}}c_{\mathbf{k}} \rangle$ is very small, and thus mean field theory is a very good approximation.

Physically, a large pair size usually means a weak pairing interaction. In such a case, Cooper pairs form only at and below T_c , and, therefore, the gap vanishes at T_c .

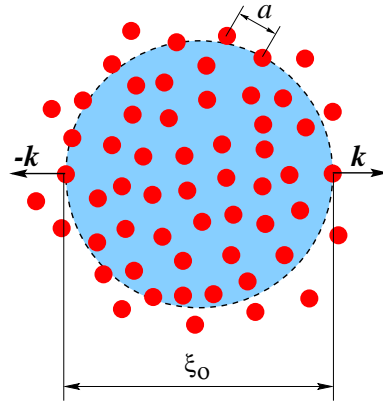


Figure 1.2: In BCS theory Cooper pairs highly overlap with each other.

1.1.2 Failure of BCS theory in high T_c superconductors

Unlike in ordinary metal superconductors, where the symmetry factor associated with the order parameter, $\varphi_{\mathbf{k}}$, is isotropic, in the cuprate superconductors, $\varphi_{\mathbf{k}}$ has been experimentally established to have a $d_{x^2-y^2}$ symmetry; it changes sign across the diagonals of the two dimensional (2D) Brillouin zone, and, consequently, the gap has four nodes on the Fermi surface, and four maxima at the $(\pi, 0)$ points.

An important property of the cuprates, is that, although it works very well for normal metal superconductors, BCS theory manifestly breaks down when applied to high T_c superconductors. We can explore this breakdown by exploring the schematic phase diagram for the cuprates, shown in Fig. 1.3(a). In contrast to ordinary metal superconductors, the parent compounds of these materials, with precisely one electron per unit cell, are Mott insulators as well as antiferromagnets at half filling. The electronic motion is highly confined within the copper-oxide planes, with very weak inter-plane coupling. Therefore, they are a highly anisotropic three dimensional (3D) or quasi-2D electronic system with tetragonal or near-tetragonal symmetry. As the system is doped with holes, the insulator is converted into a metal as well as superconductor (at low T). As indicated by Fig. 1.3(a), there exists an optimal doping concentration, around 0.15 hole per unit cell, which gives the highest T_c value. In the underdoped regime a new and important feature has been observed; this is the unexpected excitation gap (called pseudogap) above T_c . This gap persists up to a much higher crossover temperature, $T^* > T_c$.

Shown in Fig. 1.3(b) are the angle resolved photoemission spectroscopy (ARPES) mea-

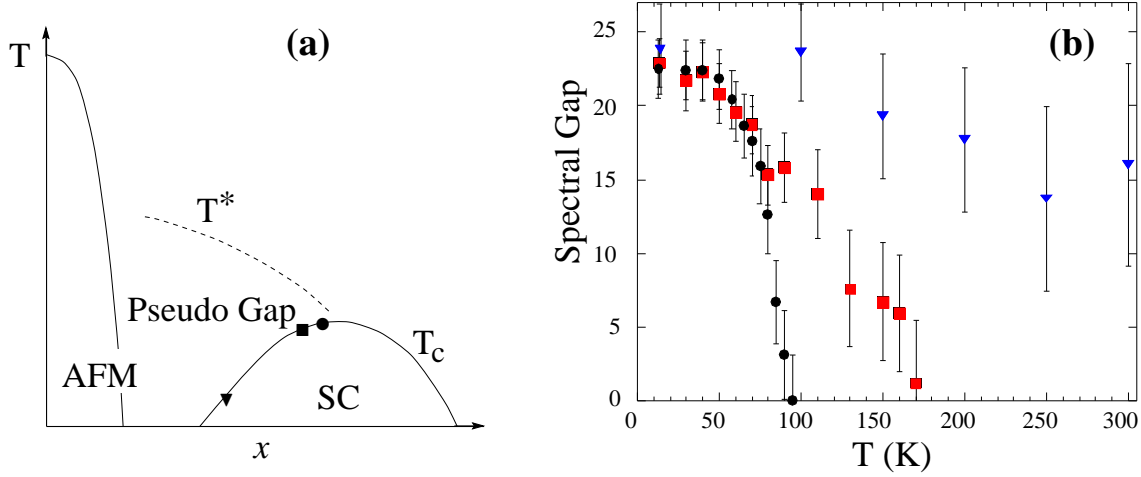


Figure 1.3: (a) Schematic phase diagram for the cuprate superconductors (The horizontal axis is the doping concentration), and (b) ARPES measurement of the temperature dependence of the excitation gap at $(\pi, 0)$ in a near-optimal $T_c = 87$ K sample (\bullet), underdoped 83 K (\blacksquare) and 10 K (\blacktriangledown) samples. The units for the gap are meV. (b) is taken from Ref. [2].

measurements of the excitation gap as a function of temperature for $\text{Bi}_2\text{Sr}_2\text{CaCu}_2\text{O}_{8+\delta}$ (Bi2212 or BSCCO) with a variety of doping concentrations.¹ Although the gap roughly closes at T_c for the near-optimal sample, it persists well above T_c for the 83 K underdoped sample. The more underdoped sample has a much lower $T_c = 10$ K and a higher zero temperature gap $\Delta(0)$, but the gap now persists to a much higher temperature. The gap evolves continuously across T_c . Moreover, it has been confirmed that the pseudogap above T_c follows the same symmetry (i.e., $|d_{x^2-y^2}|$) as the gap does below T_c . Figure 1.3(b) should be contrasted with Fig. 1.1 for the BCS case.

Note that the superconducting order parameter (which we will refer to as Δ_{sc} from now on) has to vanish above T_c . Thus, without referring to other experimental quantities, one arrives at the conclusion that BCS theory breaks down for the cuprates. This breakdown can be characterized as follows:

- The excitation gap and the order parameter are distinct, $\Delta \neq \Delta_{sc}$;
- The ratio $2\Delta(0)/T_c$ increases with decreasing doping concentration x , no longer a universal value.

¹The measured gap values were not very accurate due to the limitation of the energy resolution (22-27 meV) of ARPES in 1996, as reflected by the large error bars in Fig. 1.3(b). But this does not change the qualitative behavior of the excitation gap as a function of temperature and of doping concentration.

What causes BCS theory to fail? Some of the most obvious reasons proposed are that the cuprates all have

- very short coherence lengths, $10 \sim 15 \text{ \AA}$, only a few times larger than the lattice constant; and
- quasi-two dimensionality.

In the case of a short coherence length, the fluctuation $c_{-\mathbf{k}}c_{\mathbf{k}} - \langle c_{-\mathbf{k}}c_{\mathbf{k}} \rangle$ is no longer small, and, thus, a mean field theory such as BCS theory should not work. The low dimensionality further enhances these fluctuations, as is consistent with the Mermin-Wagner theorem.

1.1.3 A successful theory for high T_c superconductors is yet to come

Since the discovery of the cuprate superconductors, many theories have been put forward. Shortly after their discovery, Anderson proposed [3] a resonating valence bond (RVB) theory. Here the combination of proximity to a Mott insulating phase and low dimensionality would cause the doped material to exhibit new behavior, including superconductivity, not explicable in terms of conventional metal physics. Anderson further proposed that as the system is doped with holes, the antiferromagnetic order would be destroyed by quantum fluctuations, and the resulting “spin liquid” would contain resonating valence bonds which are electron pairs whose spins are locked in a singlet configuration. Anderson argued that the valence bonds resemble the Cooper pairs in BCS theory, and thus could lead to superconductivity. Although this theory was able to explain qualitatively the doping dependence of T_c in the underdoped regime [4], it is still considered controversial.

Within a closely related RVB framework, the pseudogap phenomena and the antiferromagnetism of the parent compounds have led other people [5] to postulate a picture based on the spin-charge separation idea from one dimensional Luttinger liquid physics. In this picture, the strong antiferromagnetic correlation forces the spins (spinons) to form singlets, and thus causes a gap in the electron excitation spectrum above T_c . In this way, the pseudogap is a spin gap. On the other hand, the charge carriers are holes (holons). These holons form Cooper pairs below T_c . Thus the gaps below and above T_c have different origins. This picture has successfully addressed the doping dependence of T_c in the underdoped regime [6], but it still may be problematical in the overdoped regime. In addition, it does not seem

to explain why the gap evolves continuously across T_c , or why the superconducting gap in the very underdoped regime is so large, where the charge carrier concentration is very low. So far, there has been no microscopic theory which establishes the validity of spin-charge separation in a 2D system.

In a slightly different vein, Zhang [7] proposed an SO(5) model, in an attempt to unify the two-component superconducting and the three component antiferromagnetic order parameters. However, this theory has not yet addressed the phase diagram of Fig. 1.3. Emery and Kivelson proposed a model of a very different flavour [8]. They argued that Cooper pairs form at temperature T^* , and this leads to an excitation gap. However, due to the small size of the phase stiffness, superconductivity will not set in until phase coherence is established at a lower temperature T_c . In this scenario, the superconductivity is destroyed purely by phase fluctuations of the order parameter. Some concerns about this approach are that it is associated with a very large critical regime in underdoped materials, which does not seem to be consistent with experiment. Moreover, there is concern that the phase mode will be pushed up to the plasma frequency by the Coulomb interaction, and therefore become less important. Finally, this scenario so far has not been able to make detailed predictions.

The above theories are distinct from BCS theory. While BCS theory fails in the underdoped regime, it seems to work reasonably well in the overdoped regime. This leads naturally to the idea that one should generalize BCS theory to accommodate the short coherence lengths of the cuprates rather than abandon it all together.

The school of thought which we have pursued is the BCS – Bose-Einstein (BEC) crossover scenario. This is a natural mean field extension of BCS which is based on the distinction between the excitation gap and the order parameter. In this scenario, pairs form above T_c , leading to the pseudogap (Δ), and then these pairs Bose condense at T_c , leading to superconductivity with order parameter Δ_{sc} . This general physical picture did not originate with us. But we have made the important contribution of taking this approach and extending it below T_c and, thereby, establishing how the weak coupling BCS superconducting state is altered as one crosses over towards the BEC limit, where the coupling or attractive interaction is strong.

1.2 CROSSOVER FROM BCS TO BOSE-EINSTEIN CONDENSATION

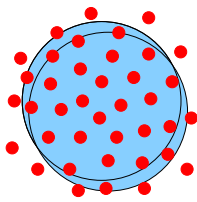
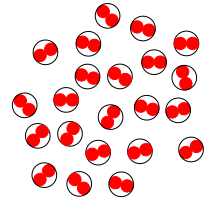
1.2.1 Relevance of Bose-Einstein condensation

Our interest in BCS–BEC crossover theory is motivated by the similarities between the pseudogap phenomena and BEC physics. Indeed, Figure 1.3(b) appears to be a very natural extension of Fig. 1.1, which incorporates BEC behavior. In a true Bose system, as the temperature becomes lower than T_{BEC} , the zero momentum state will become macroscopically occupied, as corresponds to superfluidity. This phenomenon is well known as Bose-Einstein condensation (BEC). For a system of fermions which pair to form “bosons”, in the low density, strong coupling limit, these fermions will form tightly bound pairs, which do not overlap with each other, and therefore may be treated as point-like bosons. These composite bosons will Bose condense at the condensation temperature, T_{BEC} . In a charged system, the material will become superconducting, at the BEC condensation temperature T_{BEC} , which is equivalent to the superconducting transition temperature T_c .

More generally, superconductivity at weak coupling (associated with the BCS limit) can be regarded as a special type of Bose-Einstein condensation. Here the Cooper pairs can be thought of as giant bosons. The suggestion that the superconducting transition is a Bose condensation of pairs of electrons into localized bound states (called Schafroth condensation) is one originally proposed by Schafroth, Blatt, and Butler [9, 10], before BCS theory. (Owing to mathematical difficulties associated with what they call the quasi-chemical equilibrium approach for evaluating the partition function of the system, they could not carry out calculations.) Unlike in the strong coupling limit, where the pair formation temperature, T_{pair} , is much higher than the pair condensation temperature, T_c , in the BCS case, *pair formation and pair condensation take place at the same temperature, $T_{pair} = T_c$* . In the weak coupling limit, the Cooper pairs are highly overlapping, whereas in the strong coupling limit, the pair size is small. Nevertheless, in both limits, the fermion pairs are bosons, and the condensed pairs have net momentum zero.

A schematic comparison of the weak coupling BCS and the strong coupling BEC limits is shown in Fig. 1.4. It can be seen that there are differences associated with the difference between the pair size (or, equivalently, the coherence length). Moreover, these effects lead to differences associated with the the temperature dependence of the excitation gap. In the

BCS vs Bose-Einstein Condensation

BCS	BEC
weak coupling ($g \ll g_c$)	strong coupling ($g \gg g_c$)
large pair size k-space pairing	small pair size r-space pairing
strongly overlapping Cooper pairs	ideal gas of preformed pairs
	
$T_{pair} = T_c$	$T_{pair} \gg T_c$

Energy to create fermions $\equiv \Delta$

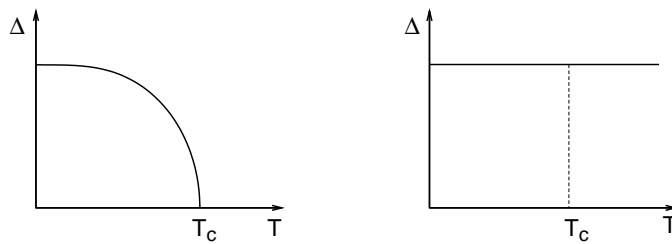


Figure 1.4: Comparison between the weak coupling BCS and strong coupling BEC limits.

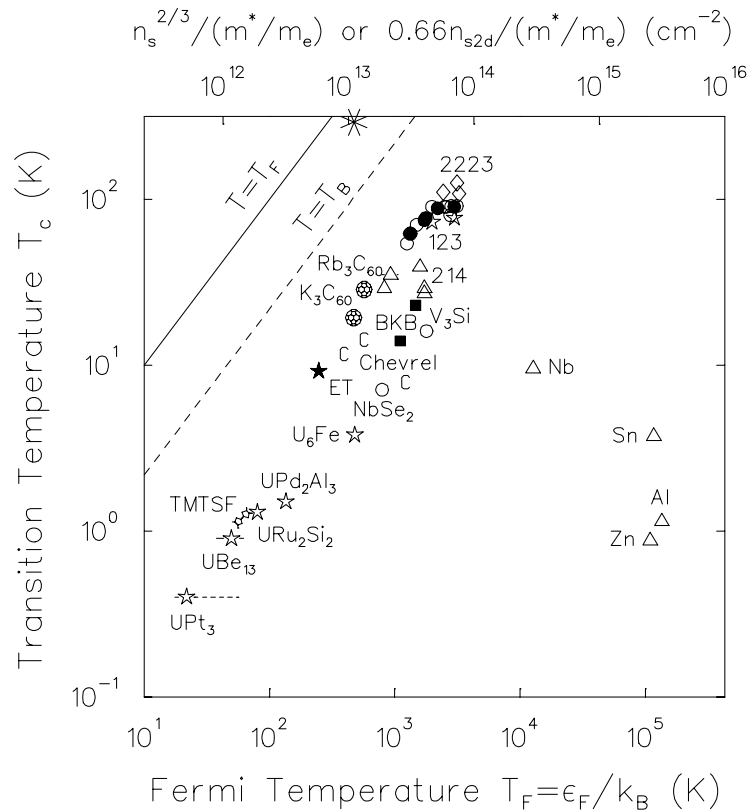


Figure 1.5: Uemura plot. Note the transition temperature scales with the Fermi energy or the superfluid density for short coherence length superconductors. In comparison, the normal metal superconductors do not follow this scaling presumably due to their large coherence length. Taken from Ref. [11].

BEC limit the fermionic excitation gap is essentially temperature independent.

If one can think of the BCS superconductivity in the weak coupling limit in terms of BEC, it should be natural to do so for an intermediate coupling strength. In general, since the pairs already form above T_c , one has to break a pair to excite a single fermion, and therefore there exists a single fermion excitation gap above T_c . This corresponds in a natural way to the pseudogap and related phenomena in the underdoped cuprates shown in Fig. 1.3. In addition, the pair size shrinks as the coupling strength increases, as is consistent with the short coherence length in the cuprates. *We may infer from pseudogap phenomena that the cuprates are intermediate between the weak coupling BCS and the strong coupling BEC limit.* Indeed, the ARPES data shown in Fig. 1.3(b) indicate that, as the doping concentration decreases, the excitation gap becomes less sensitive to the temperature, evolving

toward the BEC limit shown in Fig. 1.4.

Further suggestions for the relevance of BEC come from the famous Uemura plot [11], as shown in Fig. 1.5. As indicated in this plot, there exists a universal scaling between T_c and superfluid stiffness n_s/m (where n_s is the superfluid density) for a variety of materials, including heavy fermion systems, the cuprate superconductors and organic superconductors, etc. That T_c scales with n_s/m seems to be in line with the expectation from a Bose condensation approach. Despite the fact that these materials are very different from each other, they share one common feature, i.e., short coherence lengths.² Note the logarithmic scale in Fig. 1.5. The ordinary metal superconductors are far off the scaling behavior, as may be expected, since their extremely large coherence lengths set them apart.

In summary, given the pseudogap phenomena shown in Fig. 1.3 and the Uemura scaling between T_c and n_s/m shown in Fig. 1.5, we believe that the cuprates, as well as other short coherence length superconductors, are intermediate between the BCS and the BEC limits.

1.2.2 Overview of BCS-BEC crossover

To address the superconducting pairing for arbitrary coupling strength, one needs to add to the BCS Hamiltonian, Eq. 1.1, a term which describes an attractive interaction between pairs of nonzero net momentum:

$$H = \sum_{\mathbf{k}\sigma} \epsilon_{\mathbf{k}} c_{\mathbf{k}\sigma}^\dagger c_{\mathbf{k}\sigma} + \sum_{\mathbf{k}\mathbf{k}'\mathbf{q}} V_{\mathbf{k},\mathbf{k}'} c_{\mathbf{k}+\mathbf{q}/2}^\dagger c_{-\mathbf{k}+\mathbf{q}/2}^\dagger c_{-\mathbf{k}'+\mathbf{q}/2} c_{\mathbf{k}'+\mathbf{q}/2}. \quad (1.12)$$

Again, here the spin indices in the interaction term have been suppressed. In this way, we include pairing beyond that of the zero momentum condensate.

Studies of this Hamiltonian and of the BCS–BEC crossover problem date back to Eagles [13] early in 1969 when he studied pairing in superconducting semiconductors. However, this work was largely overlooked. In 1980, Leggett [14, 15] gave an explicit implementation of this crossover at zero temperature, in a variational wavefunction approach. This work set up a basis for all subsequent studies of the BCS–BEC crossover theory. Leggett found that as the coupling g increases, the system evolves *continuously* from BCS to BEC.

²In fact, the phase diagram of 2D organic superconductors in the κ -(BEDT-TTF)₂X family is very similar to that of the cuprates, except that the role of doping concentration is replaced by pressure [12].

A very important assumption is that the system can be described by the same BCS form of wavefunction, Ψ_0 (which we will refer to as Leggett ground state). Moreover, applying a variational approach this ground state is found to be associated with the same BCS form of gap equation [Eq. (1.11), with $f(E_{\mathbf{k}}) = 0$], provided that the chemical potential is also varied self-consistently through a fermion number constraint:

$$2 \sum_{\mathbf{k}} v_{\mathbf{k}}^2 = n. \quad (1.13)$$

Leggett pointed out that, in the strong coupling limit, the gap equation becomes a Schrödinger equation for “diatomic molecules” with a wavefunction $\psi_{\mathbf{k}} = u_{\mathbf{k}}^* v_{\mathbf{k}} = \Delta_{\mathbf{k}}/2E_{\mathbf{k}}$, and the system is essentially a condensed ideal Bose gas of these molecules. Meanwhile, the chemical potential μ becomes a large negative number, given by half the binding energy of the molecules.

In 1985, Nozières and Schmitt-Rink (NSR) [16] extended this crossover approach to a calculation for T_c , and also discussed for the first time the effects of lattice band structure. In this pioneering work, NSR introduced into the number equation the self-energy associated with the particle-particle ladder diagram (i.e., the scattering T matrix) at the lowest order. They found that T_c , as a function of the coupling strength g , first increases following the BCS calculation, then it starts to deviate and then decreases after reaching a maximum. Finally it approaches the Bose condensation temperature T_{BEC} (from above) in the strong coupling limit. This work suffers from a lack of self-consistency: (1) The self-energy is not fed back into the T -matrix (This is the so-called “ G_0G_0 scheme”), as a consequence, (2) the self-energy is not included in the gap equation. The latter is derived from a divergence of the T matrix at zero frequency following Thouless [17]. At this level of theory, there is no excitation or pseudo-gap at T_c .

Many papers have been published on the BCS–BEC crossover problem since the discovery of high T_c superconductors. Randeria, Duan, and Shieh [18, 19] recognized that crossover physics may be associated with high T_c superconductivity, and studied the crossover problem in 2D at $T = 0$ using a variational pairing *Ansatz*. Their approach was equivalent to that of NSR. Also based on this NSR scheme, Schmitt-Rink, Varma, and Ruckenstein [20] found that the 2D Fermi gas is unstable; bound fermion pairs form at

an arbitrarily weak s -wave attraction. Serene [21] pointed out that this last result is an artifact of the truncation of the particle-particle ladder series at the lowest order as in the original NSR calculations. In an attempt to improve NSR, Haussman [22, 23] calculated the crossover behavior of T_c as g increases in a 3D continuous model, using a conserving approximation for the T matrix, in which all single particle Green's functions are fully dressed by the self-energy. (This is the so-called “ GG scheme”). He found that T_{BEC} is approached from below with increasing g , as is expected physically. Within the Haussmann “ GG ” scheme, Engelbrecht and coworkers numerically studied the pseudogap state for d -wave superconductors. However, due to technical difficulties, they were restricted to a 2D lattice model, for which $T_c = 0$. Additional previous work along these lines has focused on a continuous or jellium model, at $T = 0$ or T_c , or on a lattice in strictly 2D.

Jankó, Maly and coworkers [24, 25, 26] addressed the BCS-BEC crossover problem at and above T_c in a 3D continuous model, using a third T matrix approach, the so-called “ G_0G scheme”. This scheme is the basis for the present thesis. These authors have shown that (i) as T_c is approached from above, the T matrix acquires a sharp resonance. This resonance finally becomes a divergence at T_c . The stronger the interaction and the closer to T_c , the stronger this resonance. (ii) As g increases, the resonance becomes progressively more important. This resonance causes a depletion of the fermion density of states at the Fermi energy, and thereby leads to a pseudogap.

In order to apply the crossover physics to the cuprates and to study the superconducting state, we will extend this GG_0 theoretical approach below T_c , using a realistic anisotropic 3D lattice model. Detailed derivations in Chapter 2 will provide support for this theoretical scheme.

1.3 CURRENT WORK — GENERALIZING BCS THEORY TO ARBITRARY COUPLING STRENGTH

In this thesis, we extend BCS theory to arbitrary coupling strength, by implementing BCS–BEC crossover physics below T_c . This is the regime in which (except at $T = 0$) there has been virtually no previous work. We go beyond BCS by including finite center-of-mass momentum pair excitations (which we call *pairons*) in the self-energy, and treat the single

particle and two particle propagators on an equal footing. We, then solve the resulting coupled equations self-consistently, for arbitrary temperature $T \leq T_c$. Our fundamental equations are derived by truncating the infinite series of equations of motion at the pair propagator level, following early work by Kadanoff and Martin [27]. Diagrammatically, these equations can be represented by a T matrix approximation in a G_0G scheme, where each rung of the particle-particle ladder contains one bare and one full Green's function.

The importance of the “ G_0G scheme” is that it is consistent with the Leggett ground state wavefunction for all coupling constants and, moreover it leads to a gap equation which has the BCS form, given by Eq. (1.11), for all temperatures below T_c . This equation must be supplemented by the number equation, which is also of the BCS form. One key result of the current work is that the pseudogap exists for all non-zero T , due to the existence of finite momentum pair excitations. In other words, the pseudogap is present both above and below T_c . A new equation is found, which must be solved in combination with the excitation gap equation (1.11) and the finite T generalization of the fermion number equation (1.13). This equation relates the pseudogap Δ_{pg} with the density of excited pair states:

$$a_0(\Delta^2 - \Delta_{sc}^2) = a_0\Delta_{pg}^2 = \sum_{\mathbf{q}} b(\Omega_{\mathbf{q}}) . \quad (1.14)$$

where $b(x)$ is the Bose distribution function, a_0 is a constant, and $\Omega_{\mathbf{q}}$ is the pairon dispersion. We then have three coupled equations, in place of the one of BCS theory, and of the two in the Leggett ground state variational conditions. In this way we determine T_c , as well as Δ , Δ_{sc} , and μ for $T \leq T_c$. Note now that the Δ in Eq. (1.11) is different from the order parameter Δ_{sc} .

While BCS theory contains only single fermion and zero momentum Cooper pairs, the new ingredient here is the finite momentum pair excitations. The present T matrix formalism corresponds to treating these pairs at a mean-field level, without including explicitly pair-pair interactions. In this sense, we have an improved mean field theory, at the non-interacting pair level.

In the weak coupling limit, finite momentum excitations are negligible, and we recover BCS theory. The gap closes at T_c in this case, and there is no pseudogap. As the coupling increases, finite momentum excitations become progressively more important, and

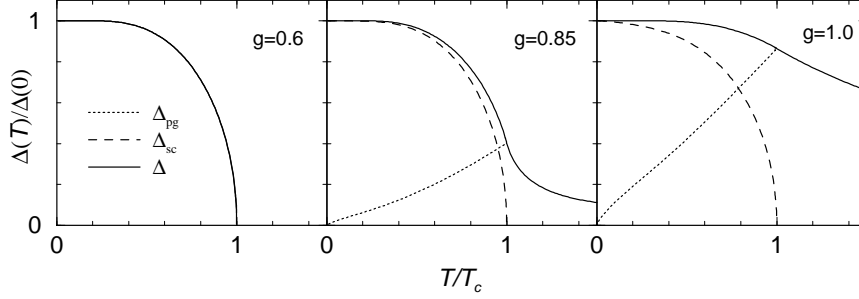


Figure 1.6: Typical evolution of the temperature dependence of the excitation gap (solid lines), the order parameter (dashed lines) and the pseudogap (dotted lines) with coupling strength. The pseudogap increases with g . The curves are calculated in 3D jellium, with the range of interaction $k_0 = 4k_F$. Here g is measured in units of g_c , the critical coupling for two fermions to form a bound state in vacuum.

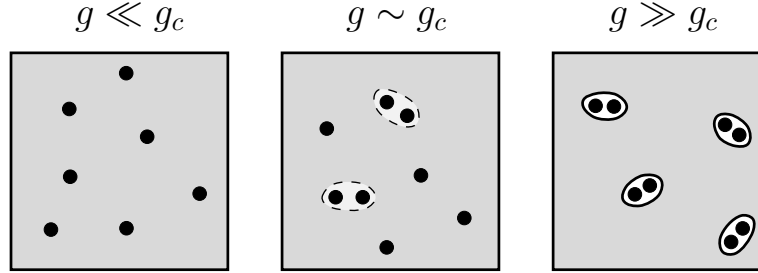


Figure 1.7: Evolution of the excitations of the system below T_c as g increases. The gray background denotes the condensate.

the pseudogap develops. In the strong coupling limit, the system behaves like an ideal Bose gas, and the new equation (1.14) becomes the boson (i.e., pair) number equation, and therefore controls the transition temperature T_c . The evolution of the gaps with coupling strength is shown in Fig. 1.6. As the temperature decreases from T_c , the order parameter develops, whereas the pseudogap decreases. At $T = 0$, the pseudogap contribution vanishes. As a consequence, we recover the Leggett ground state.

The physical picture below T_c can be schematically summarized by Fig. 1.7. In the weak coupling limit, the system is composed of the Cooper pair condensate, and fermionic quasiparticles. In the strong coupling limit, all fermions form bound pairs, and the system is composed of a Bose condensate of pairs, and finite momentum pair excitations. In the intermediate regime, fermionic quasiparticles and bosonic pair excitations will coexist, besides the condensate. This is the regime that we think is applicable to the cuprates.

Some of our key results are as follows:

- (i) At low T , pair excitations lead to new power laws in T , via the single particle self-energy. For example, they lead to a new $T^{3/2}$ term in the superfluid density; in a quasi-2D system, this new power law means a new linear T term in the specific heat.
- (ii) When applied to d -wave superconductors on a lattice (as in the cuprates), we find that the superconducting BEC regime is not accessible. The cuprates are expected to be intermediate between the BCS and the BEC limit, but well within the fermionic regime.
- (iii) We obtain a cuprate phase diagram in (semi-)quantitative agreement with experiment.
- (iv) In addition, we predict a universal behavior of the normalized superfluid density $n_s(T)/n_s(0)$ as a function of reduced temperature T/T_c , and a linear T term in the specific heat, in agreement with experiment.
- (v) Finally, we show that the onset of superconducting long range order leads to sharp features in the behavior of the specific heat at T_c , although the excitation gap is smooth across T_c .

This thesis is arranged as follows. Next, in Chapter 2, we introduce our theoretical formalism, and derive the three equations which are the basis for all numerical calculations. Then (Chapter 3) we address the superconducting instability when approached from a pseudogapped normal state, and study the effects on the behavior of T_c of low dimensionality, discrete lattice structure, and d -wave symmetry of the pairing interaction. In Chapter 4, we address the superconducting phase, including the temperature dependence of various gaps, superfluid density, specific heat, and low T power laws. In Chapter 5, we will address the gauge invariance issue and study the collective modes below T_c . In the next chapter (Chapter 6), we will apply this theory to the cuprates, and compare with experiment our predictions for the phase diagram and a variety of physical quantities. In Chapter 7, we study thermodynamic signatures of the transition in the pseudogap regime. In this context we address the doping dependence of the tunneling spectrum and the specific heat jump. Finally, in Chapter 8 we will make some concluding remarks, and discuss some issues not yet addressed.

CHAPTER 2

THEORETICAL FORMALISM

In this chapter we derive the three fundamental coupled equations which were briefly noted in Chapter 1. These equations represent a natural extension of BCS theory, and can be given a simple physical interpretation. We begin by briefly describing our physical picture. We then give a summary of the results of the formalism. Next we go into more of the details and derive a coupled set of Dyson's equations for the single and two particle propagators of the system. These coupled equations lead to a complete set of equations for the excitation gap (or transition temperature), chemical potential, and the pseudogap, which will then be deduced from these equations in the subsequent chapters.

2.1 PHYSICAL PICTURE AT ARBITRARY COUPLING STRENGTH

BCS theory describes a system of fermions with very weak pairing interactions. The electrons form pairs only at and below T_c . Therefore, in the normal state, the system is composed of electrons exclusively. Such a BCS system has a very large coherence length. However, as the coupling, or attractive interaction increases, the pair size becomes smaller, and metastable or bound pairs start to form even above T_c . There will be an intermediate temperature regime, in which the single fermions and fermion pairs coexist. As the temperature is lowered, a condensate of zero momentum (Cooper) pairs starts to develop at T_c . This T_c can be regarded as the superconducting transition temperature from the fermionic perspective; or equivalently, it can be treated as a Bose condensation temperature of the pairs. When the coupling becomes strong enough, all electrons form small, tightly bound pairs. In this case, the transition has a completely BEC nature. Nevertheless, as will be shown in Sec. 2.3.1 and Sec. 2.3.3, the superconducting instability and the BEC condition are equivalent, as they should be, so that there is a unique and well defined T_c .

This BCS-BEC crossover is schematically shown in Fig. 2.1. The short coherence length combined with the positive (fermionic) chemical potential, suggests that the high T_c

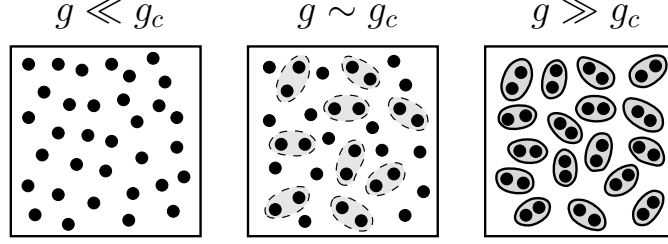


Figure 2.1: Schematic picture for BCS–BEC crossover: Evolution of the excitations in the system with coupling g above T_c . Pairs and single particles coexist in the intermediate coupling regime.

superconductors correspond to intermediate coupling strength. Here, we want to develop a theoretical formalism, to describe what happens across the transition temperature below T_c , with emphasis on the physics of intermediate coupling. Based on what we know about the cuprates, we want our theory to satisfy the following constraints:

- (i) It leads to the BCS result in the weak coupling regime;
- (ii) It leads to the ground state given by Leggett [14, 15];
- (iii) In strictly 2D, there is no superconductivity at finite T .

We will build our formalism around BCS, and obtain a natural generalization of BCS through an extended mean field theory.

Overview of the formalism

In this subsection, we review BCS theory, in terms of a somewhat unfamiliar but very useful formalism, introduced by Kadanoff and Martin [27]. This approach is then generalized to the crossover problem, following the lead of Ref. [27]. For brevity, we suppress the symmetry factor $\varphi_{\mathbf{k}}$ temporarily, and use a four vector notation: $K \equiv (\mathbf{k}, i\omega_n)$, $Q = (\mathbf{q}, i\Omega_n)$, $\sum_K = T \sum_{\mathbf{k}, \omega_n}$, etc., where ω_n and Ω_n are odd and even Matsubara frequencies, respectively.

BCS theory involves the pair susceptibility $\chi(Q) = \sum_K G(K)G_0(Q - K)$, where G is the dressed Green's function $G^{-1}(K) = G_0^{-1}(K) + \Sigma(K)$, which depends on the usual BCS self energy $\Sigma(K) = \Sigma_{sc}(K) = -\Delta_{sc}^2 G_0(-K)$. In this way the gap equation can be written as

$$1 + g\chi(0) = 0, \quad (T \leq T_c). \quad (2.0)$$

This equation is equivalent to saying that the particle-particle scattering matrix (or pair propagator) diverges in the static $Q \rightarrow 0$ limit, signaling a stable, ordered state in the pairing channel. At $Q = 0$, the summand in χ is the Gor'kov “ F ” function (up to a multiplicative factor Δ_{sc}) and *this serves to highlight the central role played in BCS theory by the more general quantity $G(K)G_0(Q - K)$* . Note that (for $Q \neq 0$), $\chi(Q)$ is *distinct from the pair susceptibility of the collective phase mode* which (as we will show in Chapter 5) enters as

$$Q_{22}(Q) = - \sum_K \{ G(K)[G(Q - K) + G(-Q - K)] + 2F(K)F(K - Q) \} .$$

Here each Gor'kov “ F ” function introduces effectively one GG_0 , so that *the collective mode propagator depends on higher order Green's functions than does the gap equation*. The observations in italics were first made in Ref. [27] where it was noted that the gap equation of BCS theory could be rederived by truncating the equations of motion so that only the one (G) and two particle (t) propagators appeared.

The coupled equations [27] for G and t can be used to recast BCS theory in this new language and, more importantly, this formalism can be readily adapted to include a generalization to the (BCS-like) ground state at moderate and strong coupling. G depends on Σ which in turn depends on t ; we write,

$$\Sigma(K) = \sum_Q t(Q)G_0(Q - K) .$$

Now, in general, t has two additive contributions (as does the associated self energy Σ): from the condensate $t_{sc}(Q) = -\Delta_{sc}^2 \delta(Q)/T$, and from the non-condensed $Q \neq 0$ pairs, with $t_{pg}(Q) = g/(1 + g\chi(Q))$. Upon expanding $t_{pg}^{-1}(Q)$, it can be easily seen that the gap equation (2.0) implies that effective pair chemical potential vanishes at $T \leq T_c$, which is the BEC condition. This provides a reinterpretation of BCS theory, along the lines of ideal Bose gas condensation. In the leading order mean field theory $\Sigma = \Sigma_{sc}$ and the BCS gap equation is obtained, as noted above.

More generally, at larger g , the above equations hold but we now include feedback from

the finite momentum pairs into Eq. (2.0), via

$$\Sigma_{pg}(K) = \sum_Q t_{pg}(Q) G_0(Q - K) \approx G_0(-K) \left(\sum_Q t_{pg}(Q) \right).$$

$\sum_Q t_{pg}(Q) \equiv -\Delta_{pg}^2$ defines a new energy scale, called the “pseudogap”. Note that under this approximation, Σ_{pg} is of the BCS form, as is the total Σ . In this way, one obtains a BCS-like gap equation (for the fermionic excitation gap), Eq. (1.11), with the order parameter Δ_{sc} replaced by the total excitation gap $\Delta = \sqrt{\Delta_{sc}^2 + \Delta_{pg}^2}$. Together with the fermion number constraint and the pseudogap definition, we have a complete set of equations. In what follows, we will give a more rigorous derivation of these equations.

2.2 GENERAL FORMALISM – DERIVATION OF THE DYSON’S EQUATIONS

In 1961, Kadanoff and Martin (KM) [27] developed a Green’s function formalism for reformulating BCS theory. This formalism is very similar to the one first used by Thouless [17] in studying the superconducting instability. In both KM and Thouless’s formalism, the self-energy which is relevant to superconductivity is assumed to arise from the particle-particle scattering T matrix. Such an approximation is usually referred to as a T matrix approximation. The KM formalism was further extended by Patton [28] to study pairing fluctuations near T_c in a dirty, low dimensional superconductor. In this context, it should be noted that the T matrix of the present theory is somewhat analogous to the “fluctuation propagator” in the early literature on fluctuation effects in low dimensional superconductors. While conventionally this propagator was evaluated at the “ $G_0 G_0$ level”, Patton introduced a “ $G_0 G$ ” level approximation, in order to avoid divergences. Here we will follow the KM approach, but extend their work slightly to feed back the effects of finite momentum pair states into the gap equations. This KM scheme is essentially the “ $G_0 G$ approximation”, referred to in the introduction.

2.2.1 Truncation of equations of motion

We adopt the same notation as KM, and start with a Hamiltonian in real space with an arbitrary singlet pairing:

$$H = \sum_{\alpha} \int d^3\mathbf{x} \psi_{\alpha}^{\dagger}(\mathbf{x}) \hat{T}(\mathbf{x}) \psi_{\alpha}(\mathbf{x}) + \frac{1}{2} \sum_{\alpha\beta} \int d^3\mathbf{x} d^3\mathbf{x}' \psi_{\alpha}^{\dagger}(\mathbf{x}) \psi_{\beta}^{\dagger}(\mathbf{x}') V(\mathbf{x}, \mathbf{x}')_{\alpha,\beta} \psi_{\beta}(\mathbf{x}') \psi_{\alpha}(\mathbf{x}), \quad (2.1)$$

where $\hat{T} = -\vec{\nabla}^2/2m$ is the kinetic energy operator. The spin indices are denoted by Greek letters, and we have restricted ourselves to interactions which do not flip the spin. A singlet pairing will impose $\alpha = -\beta$. Keeping this in mind, we will neglect the spin indices in $V(\mathbf{x}, \mathbf{x}')_{\alpha,\beta}$, for simplicity. Under this restriction, Eq. 2.1 will be equivalent to Hamiltonian Eq. 1.12 in momentum space.

For simplicity, we use notation $\equiv (\mathbf{x}, t)$, etc., and use a barred variable to denote a dummy integration variable. In addition, we define

$$V(1 - 1') \equiv V(\mathbf{x}, \mathbf{x}') \delta(t - t'),$$

$$\psi(1) = e^{iHt} \psi(\mathbf{x}) e^{-iHt},$$

and the operator

$$G_0^{-1}(1) = i \frac{\partial}{\partial t_1} - \hat{T}(1).$$

The Green's functions for our spin conserving interactions are given by the standard definition:

$$\begin{aligned} G(1 - 1') &= G^{\alpha}(1; 1') = (-i) \langle T_t \psi_{\alpha}(1) \psi_{\alpha}^{\dagger}(1') \rangle, \\ G_2^{\alpha\beta}(12; 1'2') &= (-i)^2 \langle T_t \psi_{\alpha}(1) \psi_{\beta}(2) \psi_{\beta}^{\dagger}(2') \psi_{\alpha}^{\dagger}(1') \rangle, \\ G_3^{\alpha\beta\gamma}(123; 1'2'3') &= (-i)^3 \langle T_t \psi_{\alpha}(1) \psi_{\beta}(2) \psi_{\gamma}(3) \psi_{\gamma}^{\dagger}(3') \psi_{\beta}^{\dagger}(2') \psi_{\alpha}^{\dagger}(1') \rangle, \end{aligned} \quad (2.2)$$

where T_t is the time ordering operator.

The equation of motion for ψ is given by

$$i\frac{\partial}{\partial t_1}\psi_\alpha(1) = \hat{T}(1)\psi_\alpha(1) + \sum_{\beta} V(1 - \bar{1})\psi_{\beta}^{\dagger}(\bar{1})\psi_{\beta}(\bar{1})\psi_{\alpha}(1)$$

and we have the equation of motion for the Green's function $G(1 - 1')$:

$$G_0^{-1}(1)G(1 - 1') = \delta(1 - 1') - iV(1 - \bar{1})G_2^{+-}(1\bar{1}; 1'\bar{1}^+), \quad (2.3)$$

where $1^+ = \lim_{t' \rightarrow t^+}$. Note here we have imposed singlet pairing. Stripping the uncorrelated term GG from G_2

$$G_2^{\alpha\beta}(12; 1'2') = G(1 - 1')G(2 - 2') + L^{\alpha\beta}(12; 1'2'),$$

and absorbing the Hartree term into G_0^{-1}

$$\tilde{G}_0^{-1}(1) = G_0^{-1}(1) + iV(1 - \bar{1})G(\bar{1} - \bar{1}^+), \quad (2.4)$$

we can rewrite Eq. (2.3) as

$$\tilde{G}_0^{-1}(1)G(1 - 1') = \delta(1 - 1') - iV(1 - \bar{1})L^{+-}(1\bar{1}; 1'\bar{1}^+). \quad (2.5)$$

We then have

$$G(1 - 1') = \tilde{G}_0(1 - 1') - i\tilde{G}_0(1 - \bar{1})V(\bar{1} - \bar{2})L^{+-}(\bar{1}\bar{2}; 1'\bar{2}^+). \quad (2.6)$$

Similarly, we obtain the equation of motion for G_2 :

$$\begin{aligned} G_0^{-1}(1)G_2^{\alpha\beta}(12; 1'2') &= G(2 - 2')\delta(1 - 1') - G(2 - 1')\delta(1 - 2')\delta_{\alpha\beta} \\ &\quad - i\sum_{\gamma} V(1 - \bar{1})G_3^{\alpha\beta\gamma}(12\bar{1}; 1'2'\bar{1}^+), \end{aligned} \quad (2.7)$$

where G_3 can be decomposed into terms like GGG and GG_2 , which correspond to discon-

nected diagrams, and an irreducible part L_3 , which corresponds to connected diagrams:

$$\begin{aligned}
G_3^{\alpha\beta, -\alpha}(12\bar{1}; 1'2'\bar{1}^+) &= G(2-2')G_2^{+-}(1\bar{1}; 1'\bar{1}^+) - \delta_{\alpha\beta}G(2-1')G_2^{+-}(1\bar{1}; 2'\bar{1}^+) \\
&\quad - \delta_{\alpha, -\beta}G(2-\bar{1}^+)G_2^{+-}(1\bar{1}; 1'2') + G(\bar{1}-\bar{1}^+)L^{\alpha\beta}(12; 1'2') \\
&\quad + \delta_{\alpha\beta}G(\bar{1}-\bar{1}^+)G(1-2')G(2-1') - \delta_{\alpha\beta}G(1-2')L^{+-}(2\bar{1}; 1'\bar{1}^+) \\
&\quad - \delta_{\alpha, -\beta}G(\bar{1}-2')L^{+-}(12; 1'\bar{1}^+) + G(1-1')L^{-\alpha\beta}(\bar{1}2; \bar{1}^+2') \\
&\quad + \delta_{\alpha, -\beta}G(1-1')G(2-\bar{1}^+)G(\bar{1}-2') + L_3^{\alpha\beta, -\alpha}(12\bar{1}; 1'2'\bar{1}^+) . \quad (2.8)
\end{aligned}$$

In principle, one can continue to derive an equation of motion for G_3 , and express G_3 in terms of G_4 . Unfortunately, this is technically impractical. Here following KM, we truncate the infinite series of equations of motion at the level of G_2 , and drop the connected L_3 diagrams in G_3 . In this way, we obtain

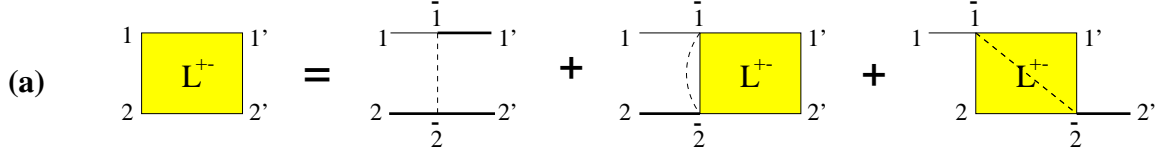
$$\begin{aligned}
G_3^{+--}(12\bar{1}; 1'2'\bar{1}^+) &\approx G(2-2')L^{+-}(1\bar{1}; 1'\bar{1}^+) + G(1-1')G(2-2')G(\bar{1}-\bar{1}^+) \\
&\quad - G(2-\bar{1}^+)G_2^{+-}(1\bar{1}; 1'2') + G(\bar{1}-\bar{1}^+)L^{+-}(12; 1'2') \\
&\quad - G(\bar{1}-2')L^{+-}(12; 1'\bar{1}^+) . \quad (2.9)
\end{aligned}$$

Note here we have used $L^{--}(12; 1'2') = -G(1-2')G(2-1')$ to get rid of L^{--} . Then we have

$$\begin{aligned}
G_0^{-1}(1)G_2^{+-}(12; 1'2') &= G(2-2')\delta(1-1') - iV(1-\bar{1})G_3^{+--}(12\bar{1}; 1'2'\bar{1}^+) \\
&= G(2-2')\delta(1-1') - iV(1-\bar{1}) [G(2-2')L^{+-}(1\bar{1}; 1'\bar{1}^+) \\
&\quad + G(1-1')G(2-2')G(\bar{1}-\bar{1}^+) - G(2-\bar{1}^+)G_2^{+-}(1\bar{1}; 1'2') \\
&\quad + G(\bar{1}-\bar{1}^+)L^{+-}(12; 1'2') - G(\bar{1}-2')L^{+-}(12; 1'\bar{1}^+)] . \quad (2.10)
\end{aligned}$$

Using definition Eq. (2.4), this can be simplified as

$$\tilde{G}_0^{-1}(1)L^{+-}(12; 1'2') = iV(1-\bar{1}) [G(2-\bar{1}^+)G_2^{+-}(1\bar{1}; 1'2') + G(\bar{1}-2')L^{+-}(12; 1'\bar{1}^+)] . \quad (2.11)$$

(a) 

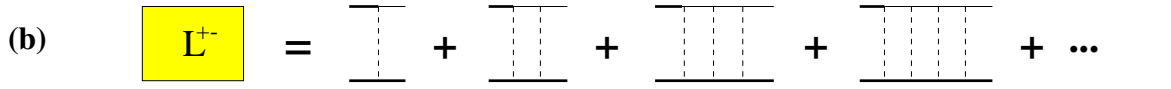
(b) 

Figure 2.2: Diagrammatic representation of (a) Eq. (2.12) and (b) Eq. (2.13). (b) is generated by reiterating the first two diagrams in (a). The thin, thick and dashed lines denote the bare Green's function \tilde{G}_0 , the full Green's function G , and the interaction V , respectively.

Then we obtain an integral equation for L^{+-} :

$$L^{+-}(12; 1'2') = i\tilde{G}_0(1-\bar{1})V(\bar{1}-\bar{2}) [G(2-\bar{2})G_2^{+-}(\bar{1}\bar{2}; 1'2') + G(\bar{2}-2')L^{+-}(\bar{1}\bar{2}; 1'2'^+)]. \quad (2.12)$$

This equation can be represented diagrammatically by Fig. 2.2(a). The first term will produce an infinite series of ladder diagrams. The second term on the right hand side stands for a non-ladder diagram, in which interaction lines cross each other. We will neglect this term, and keep only ladder diagrams. Finally, we have

$$L^{+-}(12; 1'2') = i\tilde{G}_0(1-\bar{1})V(\bar{1}-\bar{2})G(2-\bar{2})G_2^{+-}(\bar{1}\bar{2}; 1'2'). \quad (2.13)$$

Reiteration of this equation will produce the ladder diagram shown in Fig. 2.2(b).

2.2.2 Dyson's equations

In momentum space, these integral equations become algebraic equations. And one can obtain L^{+-} in terms of G immediately. We define the pair susceptibility

$$\chi = -iV\tilde{G}_0G. \quad (2.14)$$

When each rung of the ladder is not entangled with its neighbors, we obtain

$$L^{+-} = i\frac{GGV\tilde{G}_0G}{1+\chi}. \quad (2.15)$$

Note this is not always possible for a generic interaction V . The combination $V\tilde{G}_0G$ in the numerator is not written as χ because here G_0 and G are external legs. Now Eq. (2.15) and Eq. (2.6) form a closed set of equations.

The superconducting instability will be given by the divergence of L^{+-} , which signals the formation of stable pairs. Without changing the essential physics, we make one simplification, by replacing the GG pair in the numerator with \tilde{G}_0G . This non-essential approximation is equivalent to replacing one of the two full Green's functions in the leftmost rung of the particle-particle ladders in Fig. 2.2(b) with "bare" Green's function \tilde{G}_0 .

Substituting Eq. (2.15) into Eq. (2.6), we have

$$G = \tilde{G}_0 + i\tilde{G}_0 \frac{\chi V}{1 + \chi} \tilde{G}_0 G. \quad (2.16)$$

Therefore, we obtain the irreducible self-energy

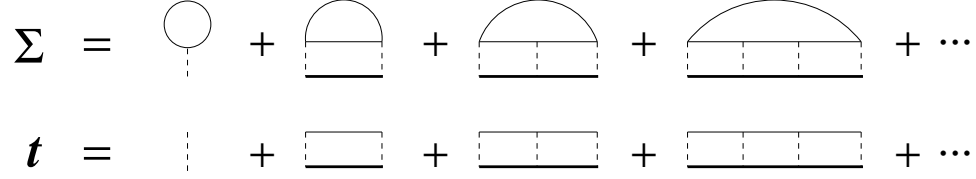
$$\Sigma = \tilde{G}_0^{-1} - G^{-1} = i \frac{\chi V}{1 + \chi} \tilde{G}_0. \quad (2.17)$$

To simplify the calculation, we make one more approximation on the Hartree self-energy. Instead of absorbing the Hartree term in the new "bare" Green's function \tilde{G}_0 , we will put it back into the self-energy, Eq. (2.17), at the lowest order, namely, $-iVG_0$. Meanwhile, we will replace \tilde{G}_0 with G_0 . In most situations, the Hartree self-energy merely causes a chemical potential shift, or at most, a slight mass renormalization. Moreover, the Hartree self-energy barely changes between the normal state and the superconducting state. Therefore, we do not expect any serious effects of this approximation. With this approximation, we have

$$\Sigma = G_0^{-1} - G^{-1} = \frac{-iVG_0}{1 + \chi} \equiv tG_0, \quad t = \frac{-iV}{1 + \chi}. \quad (2.18)$$

The diagrams for the self-energy Σ and the T matrix t are given in Fig. 2.3.

We will, from now on, switch to the finite temperature formalism and work in momentum space. Noting the difference in the Feynman rules and the definition of the Green's functions between the real time formalism and finite temperature formalism, the switch can be achieved simply by multiplying in the above equations each G with i , Σ with $-i$,

Figure 2.3: Diagrams for the self-energy and the T matrix.

G_2 , L or t matrix with -1 , and V with $-i$. Then we have

$$\Sigma = tG_0, \quad t = \frac{V}{1 + \chi}, \quad \text{with} \quad \chi = VG_0G. \quad (2.19)$$

Alternatively, we can directly write down the equations based on the diagrams in Fig. 2.3, following proper Feynman rules. For a separable potential $V_{\mathbf{k},\mathbf{k}'} = g\varphi_{\mathbf{k}}\varphi'_{\mathbf{k}'}$, we can pull g out of χ , so that

$$\chi(Q) = \sum_K G_0(Q - K)G(K)\varphi_{\mathbf{k}-\mathbf{q}/2}^2, \quad (2.20)$$

where K and $Q - K$ are the momenta of each single particle line of the ladder, and Q is the total momentum. Meanwhile, we notice $t(K, Q - K, Q) = t(Q)\varphi_{\mathbf{k}-\mathbf{q}/2}^2$, so that the dependence of the external fermion momentum K (via $\varphi_{\mathbf{k}}$) can be pulled out, and use $t(Q)$ as our new definition for T -matrix. In this way, the new T -matrix depends only on the total momentum Q .

Finally, we obtain the Dyson's equations for one and two particle propagators:

$$\Sigma(K) = G_0^{-1}(K) - G^{-1}(K) = \sum_Q t(Q)G_0(Q - K)\varphi_{\mathbf{k}-\mathbf{q}/2}^2, \quad (2.21)$$

and

$$t(Q) = \frac{g}{1 + g\chi(Q)}. \quad (2.22)$$

For an arbitrary coupling, we need to supplement with the fermion number conservation:

$$n = 2 \sum_K G(K). \quad (2.23)$$

An essential component of this thesis is to study the solution of Eqs. (2.21-2.23) for arbitrary coupling strength at $T \leq T_c$.

Some remarks are in order, before we move on to solve Dyson's equations. Note in the particle-particle ladders in Fig. 2.3, we have one single particle Green's function fully dressed while the other is bare. This is the G_0G scheme of the T matrix approximation. It is different from the fluctuation exchange (FLEX) scheme [29], in which both single particle lines are fully dressed. (This is the GG scheme.) The GG scheme can be obtained from a thermodynamical dynamical potential Ω and a functional Φ via functional derivatives (see, e.g., Ref. [21] by Serene). This can be contrasted with the approximation used by NSR [16], in which both single particle lines in the ladder are bare, and hence we refer to this as the G_0G_0 scheme. This is a perturbative approach, and thus fully dressed Green's functions do not appear in any Feynman diagram.

While the perturbative G_0G_0 scheme has no self-energy feedback in the T matrix, and thus may not be valid in strong coupling situations, the symmetric GG scheme is probably overemphasizing feedback effects. Furthermore, as KM (see Ref. [27], footnote 13) pointed out, the resulting Green's functions "can be rejected in favor of those used in BCS by means of a variational principle. They can also be rejected experimentally since they give rise to a T^2 specific heat. Finally, the formal cancellation between the terms in the perturbation series resulting from the symmetric equation ... can be indicated".

Our own work focuses on the G_0G scheme, which has a natural derivation via equations of motion. Due to the G_0^{-1} operator in the equations of motion, the mix of G_0 and G seems to an inescapable consequence. The drawback of this approach is that because of this $G_0 G$ mix, a truncation of the series of equations of motion will lead to a theory which is not Φ derivable. One cannot write down a simple thermodynamical potential Ω and a functional Φ .

2.3 SOLUTION TO DYSON'S EQUATIONS

2.3.1 Superconducting instability condition

The superconducting instability is signaled by the divergence of the T matrix at zero momentum and zero frequency. This is usually referred to as the Thouless criterion [17]. As the T matrix diverges, stable pairs of zero net momentum can exist, and thus the original

Fermi liquid become unstable. This condition can be expressed as

$$t^{-1}(Q = 0) = g^{-1} + \chi(0, T_c) = 0, \quad (2.24)$$

or

$$1 + g \sum_K G_0(-K)G(K)\varphi_{\mathbf{k}}^2 = 0. \quad (2.25)$$

In the low frequency, long wavelength limit, one can expand the inverse T matrix into powers of momentum q , and frequency Ω :

$$t^{-1}(\mathbf{q}, \Omega) = a_1\Omega^2 + a_0\Omega - \xi^2 q^2 + \tau'_0 + i\Gamma'_{\mathbf{q},\Omega}. \quad (2.26)$$

Note here the frequency is real in contrast to the discrete Matsubara frequencies. We have put all imaginary contributions inside $\Gamma'_{\mathbf{q},\Omega}$. As shown by Maly *et al.* [26], this term is very small close to T_c , and vanishes at $Q = 0$ and at T_c . Thus the Thouless condition requires $\tau'_0 = 0$. This is then equivalent to the BEC condition that the effective chemical potential μ_{pair} for the pairs vanishes. Therefore, *the Thouless criterion and the BEC condition are just two sides of the same coin.*

2.3.2 T matrix formalism of BCS theory: Relationship to the Nambu Gor'kov Green's function scheme

The Nambu-Gor'kov formulation is not suitable for extension to arbitrary coupling. (In part this is due to the fact that there are multiple energy gap parameters to be addressed). Nevertheless, in the BCS limit, where there is only one energy gap, we can re-interpret these anomalous Green's functions or “ F ” functions in terms of the present formalism. Starting from the linearized BCS Hamiltonian, Eq. (1.3), the equations of motion for the Green's function G and the anomalous Green's function F take the following form in the finite temperature formalism (see Ref. [30]):

$$G_0^{-1}(1)G(1 - 1') = \delta(1 - 1') - \Delta(1 - \bar{1})F^\dagger(\bar{1} - 1'), \quad (2.27)$$

$$\bar{G}_0^{-1}(1)F^\dagger(1 - 1') = \Delta^*(1 - \bar{1})G(\bar{1} - 1'), \quad (2.28)$$

where the anomalous Green's function is defined as

$$F(1-2) = -\langle T_\tau \psi_\uparrow(1) \psi_\downarrow(2) \rangle, \quad (2.29)$$

and the order parameter is given by

$$\Delta(1-2) = -V(1-2)F(1-2). \quad (2.30)$$

Note in Eq. (2.28) $\bar{G}_0^{-1}(1)$ denotes $G_0^{-1}(1)$ but with the sign of $\frac{\partial}{\partial \tau}$ and \vec{V} changed, satisfying $\bar{G}_0^{-1}(1)G_0(1'-1) = \delta(1-1')$, i.e., $\bar{G}_0(1-1') = G_0(1'-1)$.

From Eq. (2.28), we have

$$F^\dagger(1-1') = \Delta^*(\bar{1}-\bar{2})G_0(\bar{1}-1)G(\bar{2}-1'). \quad (2.31)$$

Substituting this equation into Eq. (2.27), we obtain

$$G_0^{-1}(1)G(1-1') = \delta(1-1') - \Delta(1-\bar{1})\Delta^*(\bar{3}-\bar{2})G_0(\bar{3}-\bar{1})G(\bar{2}-1'), \quad (2.32)$$

or

$$G(1-1') = G_0(1-1') - G_0(1-\bar{1})[\Delta(\bar{1}-\bar{4})\Delta^*(\bar{3}-\bar{2})G_0(\bar{3}-\bar{4})]G(\bar{2}-1'). \quad (2.33)$$

Now we can read off the self-energy Σ from the part inside “[...]”:

$$\Sigma(1-2) = -\Delta(1-\bar{1})G_0(\bar{2}-\bar{1})\Delta(\bar{2}-2). \quad (2.34)$$

This equation can be represented diagrammatically by Fig. 2.4(a). Note that in this diagram, we have contracted the two points 1 and 2 of $\Delta(1-2)$. The vertices $\Delta_{\mathbf{k}}$ can be easily deduced from the linearized Hamiltonian, Eq. (1.3). As the diagram indicates, the BCS self-energy arises from a process in which one particle is converted into a hole, and then is converted back into a particle, due to the presence of the condensate. Equivalently, this corresponds to the process in which two electrons form a Cooper pair, and disappear into the condensate, and then this Cooper pair breaks again.

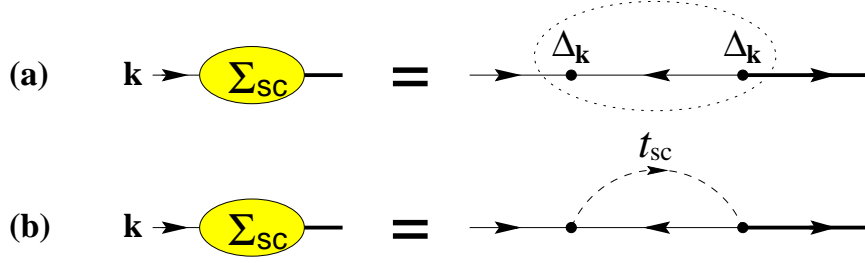


Figure 2.4: Feynman diagrams for (a) BCS self-energy and (b) its T matrix representation. The dashed line in (b) denotes the singular T matrix, t_{sc} .

In momentum space, Eq. (2.34) can be written as

$$\Sigma(K) = -\Delta_{\mathbf{k}}^2 G_0(-K) = \frac{\Delta^2 \varphi_{\mathbf{k}}^2}{i\omega + \epsilon_{-\mathbf{k}}}, \quad (2.35)$$

where $\Delta_{\mathbf{k}} = \Delta \varphi_{\mathbf{k}}$. And Eq. (2.31) becomes

$$F^\dagger(K) = \Delta \varphi_{\mathbf{k}} G_0(-K) G(K). \quad (2.36)$$

Meanwhile, the gap equation is given by the self-consistency condition Eq. (2.30):

$$\Delta_{\mathbf{k}} = - \sum_{K'} V_{\mathbf{k}, \mathbf{k}'} F(K'), \quad (2.37)$$

or

$$1 + g \sum_K G_0(-K) G(K) \varphi_{\mathbf{k}}^2 = 0, \quad (2.38)$$

which is equivalent to Eq. (1.10). It should be emphasized that this equation has exactly the same form as Eq. (2.25).

The BCS self-energy Eq. (2.35) can be expressed by Eq. (2.21) in the T matrix formalism, provided

$$t(Q) = -\frac{\Delta^2}{T} \delta(Q). \quad (2.39)$$

This amounts to splitting L^{+-} in Sec. 2.2.1 into two anomalous Green's functions:

$$L^{+-}(12; 1'2') = F(1-2) F^\dagger(1'-2'). \quad (2.40)$$

Indeed, this is what KM did with the T matrix, in order to obtain the BCS limit.

In the T matrix formalism, the BCS self-energy can be represented by the Feynman diagram shown in Fig. 2.4(b). That $t(Q)$ is singular is a consequence of the fact that the distribution of the $\mathbf{q} = 0$ Cooper pairs does not obey ordinary Bose statistics; the zero momentum pair state is macroscopically occupied. — *This is Bose-Einstein condensation!*

2.3.3 Beyond BCS: Effects of a pseudogap at finite $T \leq T_c$

At finite temperature below T_c , the self-energy comes from two contributions, one from the superconducting condensate (i.e., $\mathbf{q} = 0$ Cooper pairs), and the other from the finite \mathbf{q} pair excitations (pairons). For the former contribution, a particle decays into a virtual hole and a $\mathbf{q} = 0$ Cooper pair and then recombines; for the latter, a particle decays into a virtual hole and a $\mathbf{q} \neq 0$ incoherent pair, and then recombines. Corresponding to these two processes, it is natural to decompose the self energy into two additive contributions, one from the condensate and the other from the finite momentum pairs. In this way, we can write the T matrix as

$$t(Q) = t_{sc}(Q) + t_{pg}(Q), \quad (2.41)$$

where

$$t_{sc}(Q) = -\frac{\Delta_{sc}^2}{T} \delta(Q) \quad (2.42)$$

and

$$t_{pg}(Q) = \frac{g}{1 + g\chi(Q)}, \quad (2.43)$$

corresponding to the $\mathbf{q} = 0$ and $\mathbf{q} \neq 0$ terms, respectively. As will become clear soon, the $\mathbf{q} \neq 0$ term leads to the pseudogap. Note here we use the subscript “sc” and “pg” to distinguish the superconducting and pseudogap contributions.

Accordingly, we write the self-energy

$$\Sigma(K) = \Sigma_{sc}(K) + \Sigma_{pg}(K), \quad (2.44)$$

where

$$\Sigma_{sc}(K) = \sum_Q t_{sc}(Q) G_0(Q - K) \varphi_{\mathbf{k}-\mathbf{q}/2}^2 = -\Delta_{sc}^2 G_0(-K) \varphi_{\mathbf{k}}^2 \quad (2.45)$$

and

$$\Sigma_{pg}(K) = \sum_Q t_{pg}(Q) G_0(Q - K) \varphi_{\mathbf{k}-\mathbf{q}/2}^2 \quad (2.46)$$

are associated with the superconducting and pseudogap contributions, respectively.

The Thouless condition requires $1 + g\chi(0) = 0$ at T_c . However, this condition also applies to all temperatures below T_c , for it is simply the gap equation. This can be motivated as follows. The zero momentum pair state is macroscopically occupied. The continuity of the pair dispersion away from zero momentum is equivalent to the presumption that $\mu_{pair} = 0$. In this way a generalized Thouless condition continues to hold away from T_c . Indeed, this is the BEC condition, which requires that the effective pair chemical potential μ_{pair} vanish,

$$\mu_{pair} = 0. \quad (2.47)$$

Thus we have the gap equation (2.25) valid for all $T \leq T_c$.

Here we will make one important approximation to make the calculations and their interpretation easier. Due to the Thouless criterion, $t_{pg}(Q)$ is highly peaked at $Q = 0$, so that the main contribution to Σ_{pg} comes from the vicinity of $Q = 0$. Therefore,

$$\Sigma_{pg}(K) \approx \left[\sum_Q t_{pg}(Q) \right] G_0(-K) \varphi_{\mathbf{k}}^2 \equiv -\Delta_{pg}^2 G_0(-K) \varphi_{\mathbf{k}}^2, \quad (2.48)$$

where we have defined a pseudogap parameter Δ_{pg} via

$$\Delta_{pg}^2 \equiv - \sum_Q t_{pg}(Q). \quad (2.49)$$

The approximation made in Eq. (2.48) can be diagrammatically represented by Fig. 2.5. It is equivalent to replacing the finite momentum pairs by a ‘‘pseudo-condensate’’ such that this term gives roughly the same fermionic self energy, $\Sigma_{pg}(K)$. It is evident that, under this approximation, the pseudogap self-energy $\Sigma_{pg}(K)$ now has the BCS form. Therefore, we have the total self-energy

$$\Sigma(K) = -\Delta^2 G_0(-K) \varphi_{\mathbf{k}}^2 = \frac{\Delta^2 \varphi_{\mathbf{k}}^2}{i\omega + \epsilon_{\mathbf{k}}}, \quad (2.50)$$

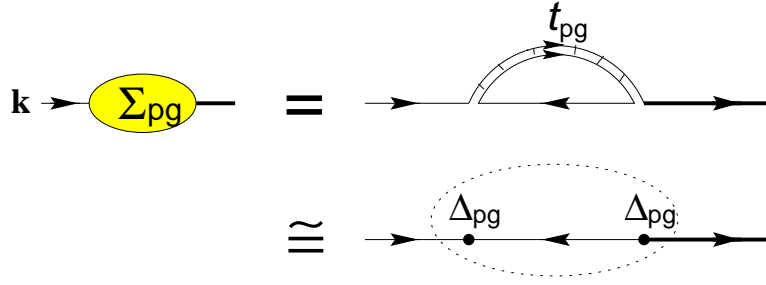


Figure 2.5: Approximation scheme for the pseudogap self-energy, $\Sigma_{pg}(K)$.

where we have used the fact $\epsilon_{\mathbf{k}} = \epsilon_{-\mathbf{k}}$. Here Δ given by

$$\Delta = \sqrt{\Delta_{sc}^2 + \Delta_{pg}^2} \quad (2.51)$$

corresponds to the total excitation gap. Now we can write down the full Green's function

$$G(K) = \frac{i\omega + \epsilon_{\mathbf{k}}}{(i\omega)^2 - E_{\mathbf{k}}^2} = \frac{u_{\mathbf{k}}^2}{i\omega - E_{\mathbf{k}}} + \frac{v_{\mathbf{k}}^2}{i\omega + E_{\mathbf{k}}}, \quad (2.52)$$

where $E_{\mathbf{k}} = \sqrt{\epsilon_{\mathbf{k}}^2 + \Delta^2 \varphi_{\mathbf{k}}^2}$ is the quasiparticle dispersion.

Now that the total gap has exactly the BCS form, and that the Thouless condition, Eq. (2.25), is formally identical to its BCS counterpart, Eq. (2.38), we can immediately write down the *gap equation*:

$$1 + g \sum_{\mathbf{k}} \frac{1 - 2f(E_{\mathbf{k}})}{2E_{\mathbf{k}}} \varphi_{\mathbf{k}}^2 = 0. \quad (2.53)$$

It should be emphasized that the gap Δ in this equation is different from the order parameter Δ_{sc} .

Substituting the full G , Eq. (2.52), into Eq. (2.23), we obtain the *fermion number equation*,

$$n = 2 \sum_{\mathbf{k}} \left[v_{\mathbf{k}}^2 + \frac{\epsilon_{\mathbf{k}}}{E_{\mathbf{k}}} f(E_{\mathbf{k}}) \right]. \quad (2.54)$$

To calculate the pseudogap parameter, we expand the inverse T matrix, as shown in Eq. (2.26). At and below T_c , we find that the Cooper pairs are essentially infinitely long lived, for the imaginary term $\Gamma'_{\mathbf{q},\Omega}$ is negligibly small at small \mathbf{q} and small Ω , and vanishes

at $\omega = \mathbf{q} = 0$. In the weak coupling limit, the ratio a_0/a_1 vanishes. Thus the pair dispersion is linear in q , as is consistent with particle-hole symmetry in the BCS limit. As g increases, a_0/a_1 increases, reflecting the presence of particle-hole asymmetry, and a_0 gradually dominates. In this regime the pair dispersion becomes quadratic in q . It should also be stressed that at small g , the residue of the T matrix is vanishingly small, and thus the contribution of finite \mathbf{q} pairs is negligible. Here, we are mostly interested in moderate and strong coupling, where the contribution from $a_1\Omega^2$ term can be neglected. These issues are discussed in more detail in Appendix A. (In principle, one can always keep this term, however, it does not lead to significant quantitative effects in our calculations.) We may rewrite the T matrix for finite \mathbf{q} as

$$t_{pg}(\mathbf{q}, \Omega) = \frac{a_0^{-1}}{\Omega - \Omega_{\mathbf{q}} + \mu_{pair} + i\Gamma_{\mathbf{q}, \Omega}}, \quad (2.55)$$

where μ_{pair} is an effective chemical potential for pair excitations. The pair dispersion $\Omega_{\mathbf{q}}$ can be written as

$$\begin{aligned} \Omega_{\mathbf{q}} &= -\frac{1}{a_0} [\chi(\mathbf{q}, 0) - \chi(\mathbf{0}, 0)] \\ &= Bq^2 \equiv \frac{q^2}{2M^*} && \text{for isotropic systems, or} \\ &= \sum_i B_i q_i^2 \equiv \sum_i \frac{q_i^2}{2M_i^*} && \text{for anisotropic systems,} \end{aligned} \quad (2.56)$$

which defines the effective pair mass. The expressions for $\Omega_{\mathbf{q}}$ and the expansion coefficients a_0 and B are given in Appendix A. Both of these quantities are essentially a constant as a function of T at low T or at all $T \leq T_c$ in strong coupling.

Finally, substituting Eq. (2.55) into the pseudogap definition, Eq. (2.49), we obtain an *equation for the pseudogap*,

$$a_0 \Delta_{pg}^2 = \sum_{\mathbf{q}} b(\Omega_{\mathbf{q}}), \quad (2.57)$$

where $b(x)$ is the Bose distribution function. From this equation, we see that Δ_{pg}^2 is proportional to the density of pair excitations. Indeed, this equation is the boson number equation. In the BEC regime, where all electrons form pairs, the right hand side must be equal to $n/2$,

the density of pairs, at T_c . In the strong coupling, low density limit with an s -wave pairing symmetry, $M^* = 2m$, and this equation alone completely determines the condensation temperature, $T_c \approx 0.218E_F$, as in an ideal Bose gas.

Equations (2.53), (2.54), and (2.57) form a complete set of self-consistent equations. Setting $\Delta_{sc} = 0$, one can solve for the transition temperature T_c , and Δ and μ at T_c . Below T_c , the first two equations form a complete subset, determining Δ and μ at a given T . The third equation indicates how to decompose Δ into the pseudogap Δ_{pg} and superconducting Δ_{sc} contributions.

Without any detailed calculations, one can immediately see from the set of equations the following limiting behavior:

- (i) There exists a pseudogap at T_c , for finite coupling strength g .
- (ii) This pseudogap persists below T_c .
- (iii) At $T = 0$, the pseudogap vanishes, i.e., $\Delta_{pg} = 0$, via Eq. (2.57), and $\Delta = \Delta_{sc}$. In this way, we recover the Leggett ground state.
- (iv) In the weak coupling limit, the pair excitations are negligible, and we recover BCS theory.
- (v) In the strong coupling limit, we have essentially an ideal Bose gas. All pairs are condensed at $T = 0$. This is different from the weakly interacting true Bose liquid.
- (vi) In 2D, the right hand side of Eq. (2.57) will diverge at any finite temperature for the quadratic pair dispersion. This means that $T_c = 0$ in 2D.
- (vii) Most importantly, $\Delta_{pg}^2 \propto T^{3/2}$ at low T . This will show up in physical quantities as new low T power laws.

It should be obvious that our theory satisfies the requirements we set forth in Sec. 2.1.

In the following chapters we will solve these coupled equations under various situations. Since the discussion of most physical quantities, e.g., the superfluid density, relies on the solution of the gaps, T_c , and μ , the physical consequences of our theory will be deferred until after we discuss the solution to the generalized gap equations.

CHAPTER 3

T_c AND THE SUPERCONDUCTING INSTABILITY OF THE NORMAL STATE

In the literature, there have been studies of T_c in the context of the BCS–BEC crossover approach, for the cases of 3D isotropic continuous (called “jellium”) or lattice system and for a strictly 2D lattice. However, a treatment of the cuprates is somewhat more complicated involving: quasi-two dimensionality, lattice periodicity, and, finally, the complexities associated with d -wave symmetry in the pairing interaction. In this Chapter, we solve the set of Eqs. (2.53), (2.54), and (2.57) for T_c , $\mu(T_c)$, and $\Delta(T_c)$ as a function of g , (by setting the order parameter $\Delta_{sc} = 0$), and in this way address the more realistic situations appropriate to the cuprates. Our goal is to study the superconducting instability of the normal state, and the effects on T_c associated with lattice structure, low dimensionality, and d -wave pairing. These studies are based on previous related work by Maly and coworkers [24, 25, 26] in a 3D jellium model. Our new results are as follows: (i) Here we find that T_c vanishes logarithmically with the mass anisotropy ratio as the strict 2D limit is approached, (ii) the chemical potential μ smoothly interpolates from E_F to large negative values in the jellium case, as the coupling varies from weak to strong. However, (iii) lattice effects yield a vanishing T_c in the strong coupling limit. This is associated with a reduction (due to the lattice) in the effective kinetic energy of the bosons or pairs. (iv) The d -wave case on a lattice is found to be different from the s -wave lattice case in one significant respect: Superconductivity disappears at relatively smaller values of g , as a result of d -wave symmetry; the pair size cannot be smaller than a lattice spacing, and, therefore, the pair mobility is strongly suppressed. Consequently, the superconducting bosonic regime is never reached for the d -wave case, except for the unphysically dilute limit.

3.1 SPECIFICATIONS FOR VARIOUS MODELS

Before we do any calculations, in this section we specify in detail the various dispersion $\epsilon_{\mathbf{k}}$ and symmetry factors $\varphi_{\mathbf{k}}$, which characterize isotropic and anisotropic jellium, s -wave and d -wave pairing, as well as discrete lattice structure. For definiteness, in our quasi-2D calculations it is assumed that the pairing interaction depends only on the in-plane momenta.

(i) *3D jellium, s -wave symmetry* – As usual, we assume a parabolic dispersion relation, $\epsilon_{\mathbf{k}} = \mathbf{k}^2/2m - \mu$, with $\varphi_{\mathbf{k}} = (1 + k^2/k_0^2)^{-1/2}$. The parameter k_0 is the inverse range of the interaction and represents a soft cutoff in momentum space for the interaction. As will be clear later, $k_0 > k_F$ is assumed in general in order to access the strong coupling limit. It is convenient to introduce a dimensionless scale g/g_c for the coupling constant. Here, following Ref. [16], we choose $g_c = -4\pi/mk_0$, which corresponds to the critical value of the coupling above which bound pairs are formed in vacuum.

(ii) *Quasi-2D jellium, s -wave symmetry*. Here we adopt an anisotropic energy dispersion

$$\epsilon_{\mathbf{k}} = \frac{\mathbf{k}_{\parallel}^2}{2m_{\parallel}} + \frac{k_{\perp}^2}{2m_{\perp}} - \mu, \quad (3.1)$$

where k_{\perp} is restricted to a finite interval ($|k_{\perp}| \leq \pi$) while \mathbf{k}_{\parallel} is unconstrained.¹ Now $\varphi_{\mathbf{k}} = (1 + k_{\parallel}^2/k_0^2)^{-1/2}$ depends only on the in-plane momentum.

By tuning the value of the anisotropy ratio m_{\perp}/m_{\parallel} from one to infinity, this model can be applied to study effects associated with continuously varying dimensionality from 3D to 2D.² For convenience, we use the parameter g_c derived for 3D jellium, as a scale factor for the coupling strength, but call it g_0 to avoid confusion.

The strict 2D limit is approached as $m_{\perp}/m_{\parallel} \rightarrow \infty$, and we find T_c vanishes logarithmically with m_{\perp}/m_{\parallel} . In this limiting case, the right hand side of Eq. (2.57) vanishes logarithmically at finite T , implying that in 2D the superconducting order is not stable against pairing fluctuations so that $T_c = 0$. This result is independent of the details of the disper-

¹We emphasize that a cut-off for k_{\perp} is crucial for the quasi two-dimensionality of the system; otherwise, by rescaling $k_{\perp} \rightarrow (m_{\perp}/m_{\parallel})^{1/2} k_{\perp}$, the system can be transformed into an isotropic 3D jellium model.

²Strictly speaking, a very large cutoff Λ for k_{\perp} or a very low particle density (i.e., $k_F \ll \Lambda$) is necessary to restore the 3D limit if $m_{\perp}/m_{\parallel} = 1$ is fixed. Alternatively, 3D can be achieved by letting $m_{\perp}/m_{\parallel} \rightarrow 0$ while fixing Λ . This complication does not occur for the lattice case, where all momenta are restricted within the first Brillouin zone.

sion or order parameter symmetry. This behavior is consistent with the Mermin-Wagner theorem.

(iii) *Quasi-2D lattice, s- and d-wave symmetry.* On a lattice we adopt a simple tight-binding model with dispersion

$$\epsilon_{\mathbf{k}} = 2 t_{\parallel}(2 - \cos k_x - \cos k_y) + 2 t_{\perp}(1 - \cos k_{\perp}) - \mu , \quad (3.2)$$

where t_{\parallel} (t_{\perp}) is the hopping integral for the in-plane (out-of-plane) motion. The isotropic 3D lattice is given by setting $t_{\parallel} = t_{\perp}$. For *s*-wave pairing, $\varphi_{\mathbf{k}} = 1$, as in the negative U Hubbard model, whereas for *d*-wave pairing,

$$\varphi_{\mathbf{k}} = \cos k_x - \cos k_y . \quad (3.3)$$

Equations (2.53), (2.54), and (2.57), together with the various models for $\varphi_{\mathbf{k}}$ and $\epsilon_{\mathbf{k}}$, were solved numerically for Δ_{pg} , μ and T_c . The numerically obtained solutions satisfy the appropriate equations with an accuracy higher than 10^{-7} . The momentum summations were calculated by numerical integration over the whole \mathbf{k} space for the jellium case, and over the entire Brillouin zone for the lattice. However, to facilitate our calculations in the case of the quasi-2D lattice with a *d*-wave pairing interaction, the momentum integral along the out-of-plane direction was generally replaced by summation on a lattice with $N_{\perp} = 16$ sites. For completeness we compared solutions obtained with and without an approximated low frequency, long wavelength expansion of the pair dispersion $\Omega_{\mathbf{q}}$ discussed above. Here we found extremely good agreement between the two different approaches. In general, we chose the ratios $m_{\perp}/m_{\parallel} = 100$ or $t_{\perp}/t_{\parallel} = 0.01$, although higher values of the anisotropy were used for illustrative purposes in some cases.

3.2 OVERVIEW: T_c AND EFFECTIVE MASS OF THE PAIRS

It was pointed out in Ref. [16] in the context of the attractive U Hubbard calculations, that the appropriate description of the strong coupling limit corresponds to *interacting* bosons on a lattice with effective hopping integral $t' \approx -2t^2/U$. It, therefore, will necessarily vanish in the strong coupling limit, as $U \rightarrow \infty$. In addition to this hopping, there is an

effective boson-boson repulsion which also varies as $V' \approx -2t^2/U$.

This description of an effective boson Hamiltonian can be related to the present calculations through Eqs. (2.55)–(2.56) which represent the boson Green’s function for such a Hamiltonian and its parameterization via *only* the pair mass M^* . It is important to stress that boson-boson interaction effects are not included at the level of the gap equations, as is consistent with the mean field character of the ground state wave function. However, there is a residue of a boson-boson interaction which enters via M^* , which we now discuss. By solving Eqs. (2.53), (2.54), and (2.57) self-consistently and identifying M^* from the effective pair propagator (or T matrix), we find that our M^* necessarily incorporates Pauli principle induced pair-pair repulsion. In addition M^* includes pairing symmetry and density related effects. Here, an indirect interaction between bosons is effectively introduced via fermionic self-energy effects which derive from the interactions between the fermions and bosons. Note, in contrast to Ref. [16], in the present work we are not restricted to the bosonic limit, nor is it essential to consider a periodic lattice. Thus, much of this language is also relevant to the moderately strong coupling (but still fermionic) regime, and can even be applied to jellium.

The goal of this section is to establish a natural framework for relating M^* to T_c . The parameters which enter into M^* via Eq. (2.56) vary according to the length scales in the various physical models. In the case of jellium, M^* depends in an important way on the ratio k_0/k_F . For the case of s -wave pairing on a lattice, M^* depends on the inverse lattice constant π/a and density n . Finally, for the case of d -wave pairing, there is an additional length scale introduced as a result of the finite spatial extent of the pair. This enters as if there were an equivalent reduction in k_0/k_F in the analogous jellium model. The following factors act to increase M^* or, alternatively, to reduce the mobility of the pairs: the presence of a periodic lattice, a spatially extended pairing symmetry (such as d -wave) or, for jellium, small values of the ratio $k_0/k_F \lesssim 0.4$ (i.e., high density).

In order to relate T_c to M^* , we observe that in an ideal Bose-Einstein system T_c is inversely proportional to the mass. Here, this dependence is maintained, in a much more complex theory, as a consequence of Eqs. (2.49) and (2.57). Eq. (2.57) is essentially an equation for the number of pairs (bosons), with renormalized mass M^* . Thus, as we increase g towards the bosonic regime, it is not surprising that T_c varies inversely with M^* .

This leads to our main observations, which apply to moderate and large g , although not necessarily in the strict bosonic regime. (i) For the general lattice case, we find that T_c vanishes, either asymptotically or abruptly, as the coupling increases, in the same way that the inverse pair mass approaches zero.³ (ii) For the case of jellium or low densities on a lattice, both T_c and M^* remain finite and are inversely proportional. These observations are consistent with, but go beyond, the physical picture in Ref. [16] that T_c is expected to be proportional to the pair hopping integral t' . It should be stressed that in the very weak coupling limit the pair size or correlation length is large. In this case, the motion of the pairs becomes highly collective, so that the effective pair mass is very small.

In the presence of a lattice, the dependence on band filling n is also important for M^* , and thereby, for T_c . We find that the bosonic regime is not accessed for large $n > n_c \approx 0.53$. There are two reasons why superconductivity abruptly disappears within the fermionic regime. This occurs primarily (in the language of Ref. [16]) as a consequence of large indirect pair-pair repulsion, relevant for high electronic densities, which leads to large M^* . In addition, there are effects associated with the particle-hole symmetry at half filling.⁴ Precisely at half filling (i.e., the “filling factor” $f = 1/2$, or $2f = n = 1$), for the band structure we consider, there is complete particle-hole symmetry and μ is pinned at E_F . Similarly, in the vicinity of $n = 1$, the chemical potential remains near E_F for very large coupling constants g .

By contrast, in the small density (lattice) limit for the s -wave case, ($n \approx 0.1$), the indirect pair-pair repulsion is relatively unimportant in M^* and there is no particle-hole symmetry. In this way the bosonic regime is readily accessed. Moreover, in this limit we see a precise scaling of T_c with $1/g$ in the same way as predicted by Ref. [16] (via the parameter $t' = -2t^2/U$). Thus in this low density limit superconductivity disappears asymptotically, rather than abruptly.

The effects of pairing symmetry should also be stressed. Because of the spatial extent of the d -wave function, the pair mobility is strongly suppressed, and, thus, M^* is relatively

³This is a high density effect at strong coupling. Lattice bandstructure effects and d -wave pairing serve to enhance this behavior. Moreover, it should be noted that the pseudogap $\Delta_{pg} \propto (T_c/(m/M^*))^{3/2}$ remains finite as both T_c and m/M^* approach zero.

⁴In a negative U Hubbard model, there also exists a competition between superconductivity and charge-density wave ordering. This may not be relevant for a d -wave pairing interaction.

larger than for the s -wave case. This lower mobility of d -wave pairs leads to the important result that superconductivity is *always abruptly* (rather than asymptotically) destroyed with sufficiently large coupling. Near half filling we find μ remains large when T_c vanishes, at large g . As the density n is reduced, away from half filling, μ decreases somewhat. It is important to note that the system remains in the fermionic regime (with positive μ) for all densities down to $n \approx 0.09$ [See Appendix B for details].

In all cases discussed thus far, T_c exhibits a non-monotonic dependence on the coupling constant. It grows exponentially at small g , following the BCS dependence, and shuts off either asymptotically or abruptly at higher g . One can view this effect as deriving from a competition between pairing energy scales and effective mass or mobility energy scales. This competition is not entirely dissimilar to that found in more conventional Eliashberg theory where the fermionic renormalized mass and the attractive interaction compete in such a way as to lead to a saturation in T_c at large coupling. However, in the present context, for intermediate and strong coupling, we are far from the Fermi liquid regime and the effective mass of the quasi-bound or bound pair is a more appropriate variable.

With this background, it should not be surprising that non-monotonic behavior will arise, even in situations as simple as in jellium models. Indeed, in this case we find that for sufficiently long range interactions or high densities (small k_0/k_F) superconductivity disappears abruptly before the bosonic regime can be reached. (As shown in Fig. B.5, T_c is reentrant for certain intermediate densities.) Even for the case of short range interactions ($k_0/k_F = 4$), there is a depression in T_c caused by an increase in the pair mass, while still in the fermionic regime.

In Fig. 3.1(a) we plot the calculated T_c for the case of an isotropic, 3D jellium model with s -wave pairing, along with the inverse pair mass m/M^* . The density of pairs, $n_{pair} = \sum_{\mathbf{q}} b(\Omega_{\mathbf{q}})$, [Eq. (2.57)], as well as the chemical potential, are plotted in Fig. 3.1(b). This figure demonstrates that as the system crosses over into the bosonic regime (i.e., μ becomes negative), essentially all electrons form pairs, $n_{pair} = n/2$, so that Eq. (2.57) becomes a real boson (pair) number equation. In this case, Eq. (2.57) alone completely determines the transition temperature at low densities. Figure 3.1 is presented primarily as a base line with which to compare subsequent plots. The parameter $k_0/k_F = 4$, is reasonably large so that the high g asymptote is found to reach the ideal Bose-Einstein limit ($T_c =$

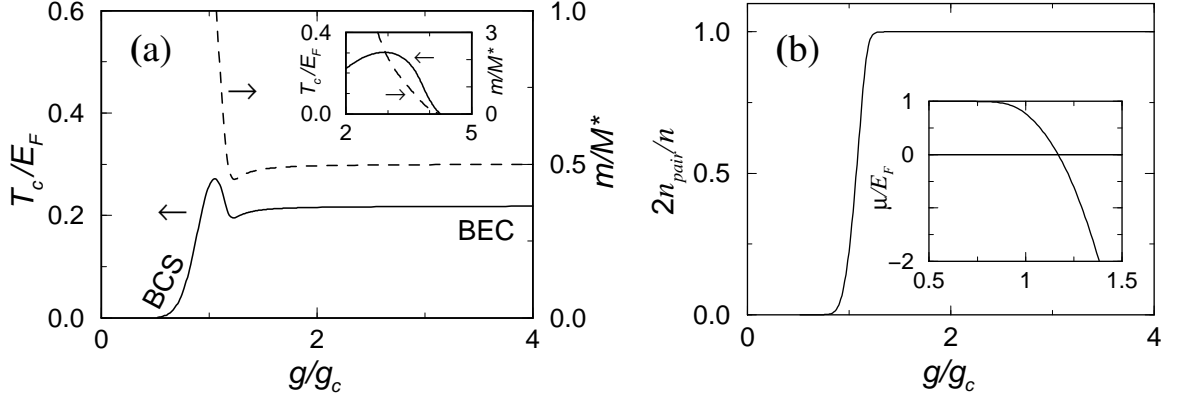


Figure 3.1: (a) T_c and m/M^* as a function of g/g_c in the 3D jellium model with $k_0/k_F = 4$ (main figure) and $k_0/k_F = 1/3$ (inset), corresponding to short range (or low density), and long range interactions (or high density), respectively. Plotted in (b) are the density of pairs (main figure) and the chemical potential (inset) as a function of g/g_c , corresponding to the main figure in (a).

$T_{BEC} = 0.218E_F$) with $M^* = 2m$. The approach to the high g asymptote is from below, as is expected [22]. This is a result of the decreasing Pauli principle repulsion associated with increasing g , and concomitant reduction in pair size. The non-monotonic behavior at intermediate $g/g_c \approx 1$ can be associated with structure in the effective pair mass, and has been discussed previously from a different perspective [26].

In the inset of Fig. 3.1(a) are plotted analogous curves for the case of long range interactions or high densities ($k_0/k_F = 1/3$). This figure illustrates how superconductivity vanishes abruptly before the bosonic regime is reached, as a consequence of a diverging pair mass.

3.3 EFFECTS OF DIMENSIONALITY

In this section we illustrate the effects of anisotropy or dimensionality on T_c (and on Δ_{pg} and μ) within the context of a jellium dispersion.⁵ A particularly important check on our theoretical interpolation scheme is to ascertain that T_c is zero in the strict 2D limit

⁵One may argue that this quasi-2D system is not physical because the kinetic energy in the perpendicular direction should have a band structure, i.e., $2t_{\perp}(1 - \cos k_{\perp})$ instead of being simply $\frac{k_{\perp}^2}{2m_{\perp}}$. As shown in Sec. A.2, in this case, $\frac{M_{\perp}^*}{M_{\parallel}^*} \propto \left(\frac{m_{\perp}}{m_{\parallel}}\right)^2$ (instead of $\frac{m_{\perp}}{m_{\parallel}}$), i.e., the pairs see a magnified anisotropy. This does not affect the conclusions here.

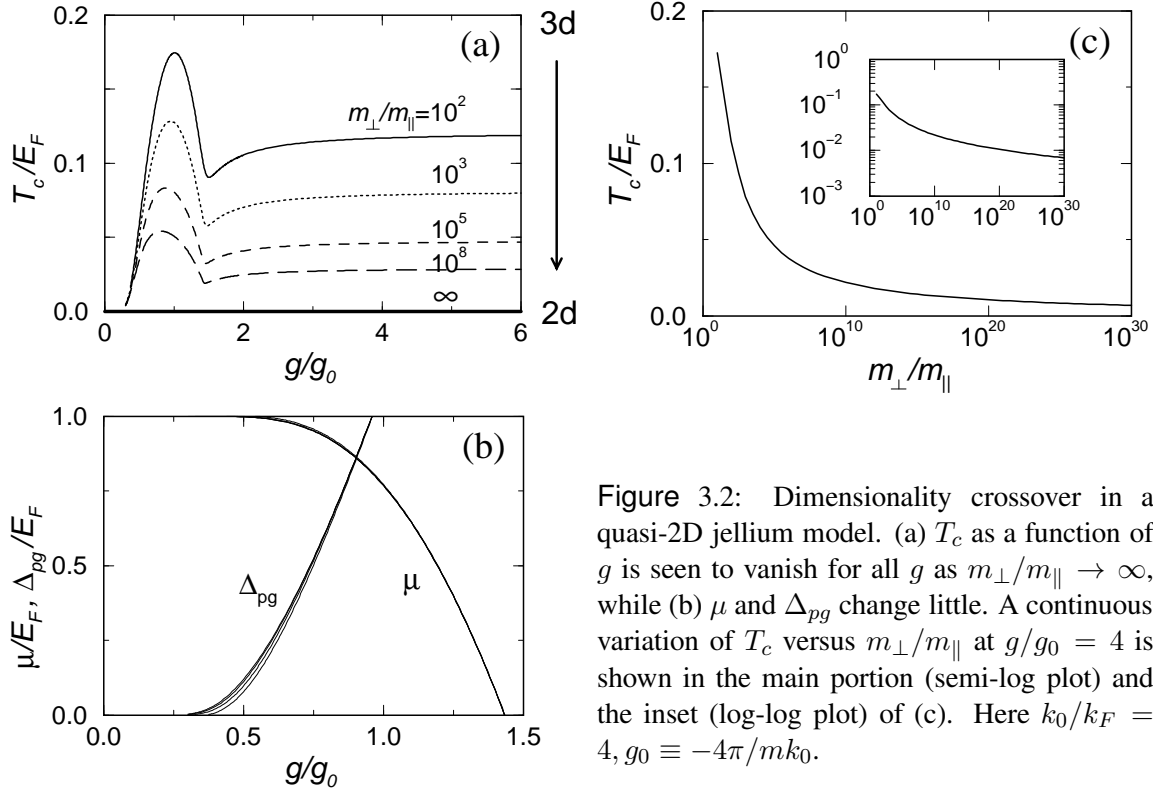


Figure 3.2: Dimensionality crossover in a quasi-2D jellium model. (a) T_c as a function of g is seen to vanish for all g as $m_\perp/m_\parallel \rightarrow \infty$, while (b) μ and Δ_{pg} change little. A continuous variation of T_c versus m_\perp/m_\parallel at $g/g_0 = 4$ is shown in the main portion (semi-log plot) and the inset (log-log plot) of (c). Here $k_0/k_F = 4$, $g_0 \equiv -4\pi/mk_0$.

and that μ varies continuously from E_F in weak coupling to the large negative values characteristic of the strong coupling bosonic limit. The present calculational scheme should be compared with that of Yamada and co-workers [31] who included “mode coupling” or feedback contributions to T_c , but only at the level of the lowest order “box” diagram discussed in Ref. [24]. These authors were unable to find a smooth interpolation between weak and strong coupling, but did successfully repair the problems [20, 21] associated with the NSR scheme, which led to negative μ even in arbitrarily weak coupling.

Figures 3.2(a) and 3.2(b) show the effect on T_c and on Δ_{pg} and μ , respectively, of introducing a layering or anisotropy into jellium with s -wave pairing. The various curves correspond to different values of the anisotropy ratio m_\perp/m_\parallel . It can be seen from these two figures that T_c approaches zero as the dimensionality approaches 2. At the same time the chemical potential μ interpolates smoothly from the Fermi energy at weak coupling towards zero at around $g/g_0 = 1.5$ to large negative values (not shown) at even larger g . The vanishing of the superconducting transition in strictly 2D was discussed in detail in Sec. 3.1.

It should be noted that quasi-two dimensionality will be an important feature as we begin to incorporate the complexity of d -wave pairing. The essential physical effect introduced by decreasing the dimensionality is the reduction in energy scales for T_c . The chemical potential and pseudogap amplitude are relatively unaffected by dimensional crossover effects.⁶ While T_c rapidly falls off when anisotropy is first introduced into a 3D system (such as is plotted in Fig. 3.1), the approach to the strict 2D limit is logarithmic and therefore slow, as can be seen explicitly in Fig. 3.2(c). Thus, in this regime, to get further significant reductions in T_c associated with a dimensionality reduction requires extremely large changes in the mass anisotropy.

3.4 EFFECTS OF A PERIODIC LATTICE

The first applications of a BCS Bose-Einstein crossover theory to a periodic lattice were presented in Ref. [16]. The present approach represents an extension of the NSR theory in two important ways: we introduce mode coupling or full self-energy effects which are parameterized by Δ_{pg} , and which enter via Eq. (2.49). Moreover, the number equation (2.54) is evaluated by including self-energy effects to all orders. This is in contrast to the approximate number equation used in Ref. [16], which includes only the first order correction. In this way we are able to capture the effects which were qualitatively treated by these authors and which are associated with the lattice.

Figure 3.3(a) plots the behavior of T_c (solid line) in an isotropic three-dimensional lattice (with s -wave pairing, $\varphi_{\mathbf{k}} = 1$) at a low density $n = 0.1$. The effects of higher electronic filling are shown in the inset. The low n behavior in the main portion of the figure can be compared with the jellium calculations of Fig. 3.1. For small n , T_c decreases asymptotically to zero at high g . For larger n , T_c vanishes abruptly before the bosonic regime ($\mu < 0$) is reached [See inset of Fig. 3.3(b)]. These various effects reflect the analogous reduction in the effective pair mobility, parameterized by the inverse pair mass m/M^* . To see the correlation with m/M^* in the low density limit, we plot this quantity in Fig. 3.3b, for the lattice as well as jellium case (where for the latter, $m/M^* \rightarrow 1/2$ at large g). Here the coupling constants are indicated in terms of g/g_c for jellium and $-g/6t$ for

⁶The onset coupling g for the pseudogap decreases when the dimensionality is reduced, and eventually vanishes in strictly 2D.

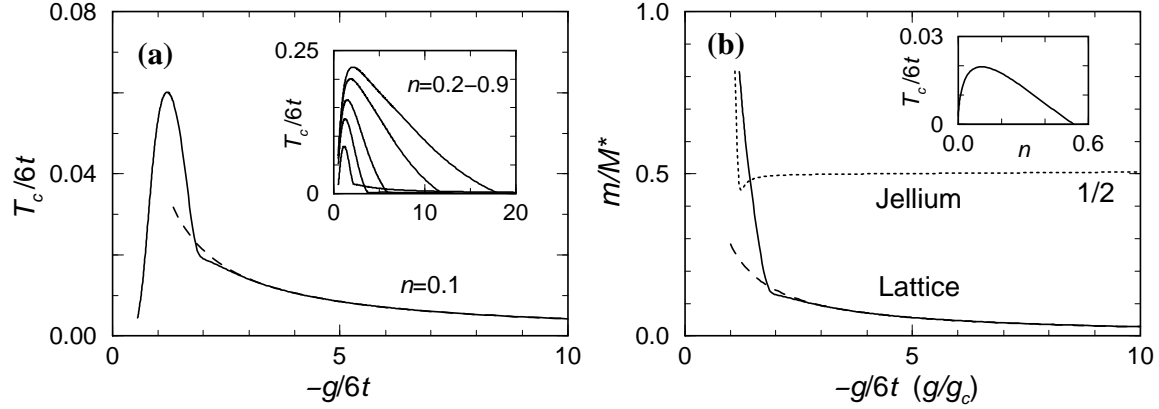


Figure 3.3: (a) T_c and (b) m/M^* (solid lines) vs g at low filling ($n = 0.1$) on a 3D lattice, and T_c at larger filling in the inset of (a). A fit to the functional form $t' = -2t^2/g$ is plotted (dashed lines) in (a) and (b) with adjusted proportionality constants. For comparison, m/M^* vs g/g_c for 3D jellium (Fig. 3.1) is replotted (dotted line) in (b). From bottom to top, the inset of (a) shows T_c for densities $n = 0.2, 0.5, 0.7, 0.85$, and 0.9 . The inset of (b) shows T_c at $\mu = 0$ as a function of n .

the lattice. The inflection points at $-g/6t \approx 2$ in both T_c and m/M^* curves correspond to $\mu = 0$, which marks the onset of the bosonic regime.

Also plotted in both Fig. 3.3(a) and 3.3(b) (dashed lines) is the effective hopping $t' = -2t^2/g$ for $n = 0.1$, rescaled such that it coincides with T_c and m/M^* , respectively, at high coupling ($-g/6t = 30$). This figure illustrates clearly the effect first noted by Nozières and Schmitt-Rink that in the entire bosonic regime, T_c varies with high precision as t' or equivalently as m/M^* .

Finally, in the inset of Fig. 3.3(b), we demonstrate the limiting value of n , above which the bosonic limit can not be accessed. What is plotted here is the value of T_c at which μ is zero as a function of density n . This figure indicates that the bosonic regime can not be reached for $n > n_c \approx 0.53$. At densities higher than this, the pair-pair repulsion increases M^* sufficiently, so that T_c vanishes abruptly, while μ is still positive.

3.5 EFFECTS OF *D*-WAVE SYMMETRY

We now introduce the effects of a *d*-wave pairing interaction. For the purposes of comparison we begin by illustrating T_c for the case of *s*-wave pairing on an anisotropic lattice,

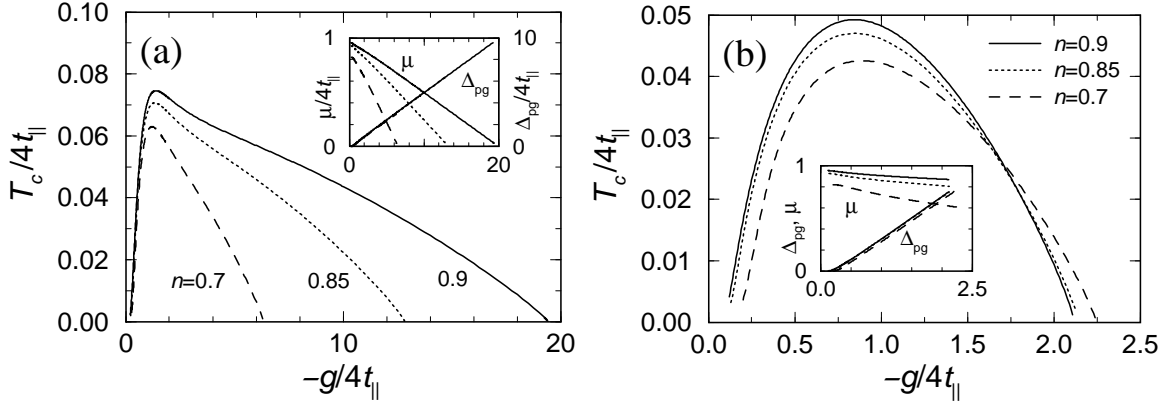


Figure 3.4: Lattice effects on T_c (main figure) and μ and Δ_{pg} (inset) as a function of g for $n=0.7$ (dashed lines), 0.85 (dotted lines), and 0.9 (solid lines) in quasi-2D for (a) s -wave and (b) d -wave pairing symmetries. Here $t_{\perp}/t_{\parallel} = 0.01$. In (b), T_c vanishes at a much smaller g than does its s -wave counterpart.

shown in Fig. 3.4(a), for three different values (0.7, 0.85, and 0.9) of the density n .⁷ The inset indicates the behavior of the pseudogap magnitude and the chemical potential. The plots of Δ_{pg} for the three different n are essentially unresolvable in the figure. Note, from the inset, that within small numerical errors T_c and μ vanish simultaneously. A comparison of the magnitude of T_c (in the main figure) with the 3D counterpart shown in the inset of Fig. 3.3(a) illustrates how T_c is suppressed by quasi-two dimensionality.⁸

In Fig. 3.4(b), similar plots are presented for the d -wave case. Here we use the same values of the filling factor as in Fig. 3.4(a), to which Fig. 3.4(b) should be compared. The essential difference between the two figures is the large g behavior. Lattice effects produce the expected cutoff for s -wave pairing. In the d -wave situation this cutoff is at even smaller g , and moreover, corresponds to $\mu \approx E_F$. Calculations similar to those shown in the inset of Fig. 3.3(b) indicate that superconductivity disappears while μ remains positive for all n above the extreme low density limit (i.e., for $n > n_c \approx 0.09$) (See Appendix B for details). This behavior is in contrast to that of the s -wave case where $n_c \approx 0.53$.

In the d -wave case, the pair size cannot be made arbitrarily small, no matter how strong the interaction. As a result of the extended size of the pairs, residual repulsive interactions

⁷We show results for these values of n in order to demonstrate the behavior of T_c in over-, optimally, and under-doped cuprates, respectively.

⁸As in the 3D (s -wave) lattice case, the bosonic regime can be accessed at $n < n_c \approx 0.53$ for sufficiently strong coupling.

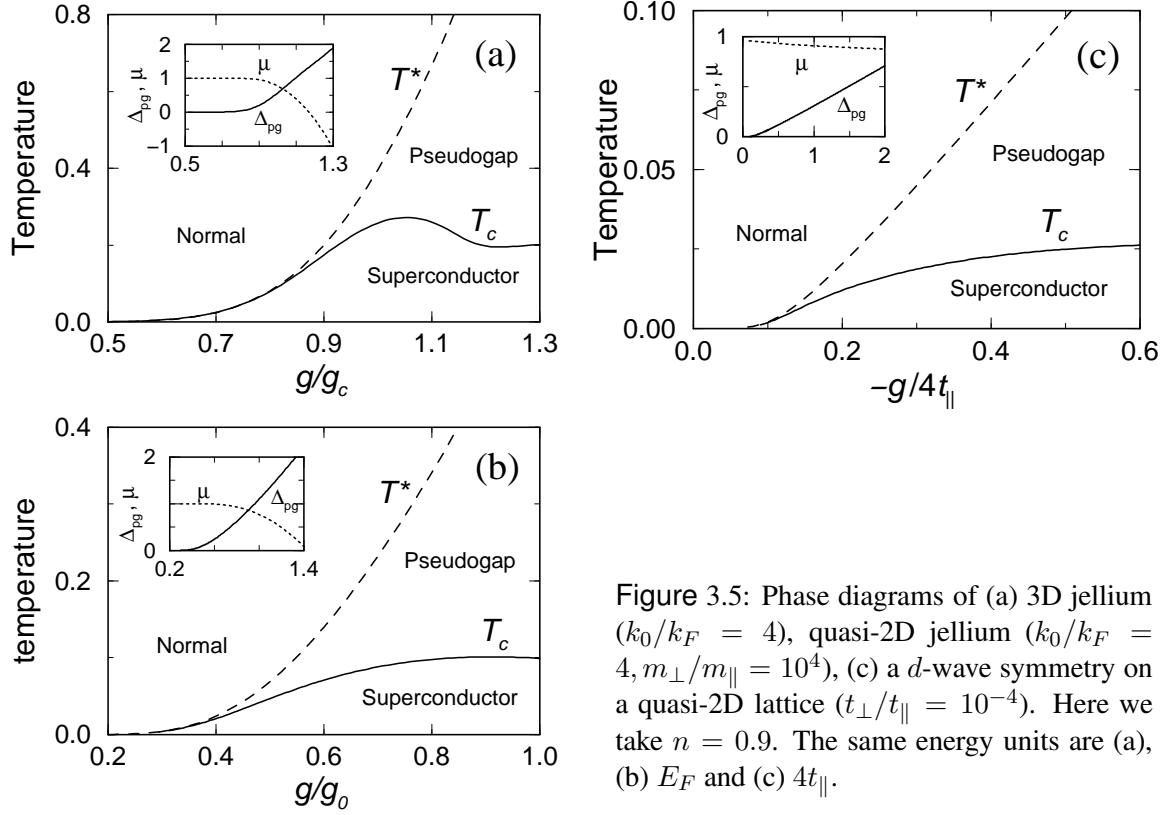


Figure 3.5: Phase diagrams of (a) 3D jellium ($k_0/k_F = 4$), quasi-2D jellium ($k_0/k_F = 4, m_{\perp}/m_{\parallel} = 10^4$), (c) a d -wave symmetry on a quasi-2D lattice ($t_{\perp}/t_{\parallel} = 10^{-4}$). Here we take $n = 0.9$. The same energy units are (a), (b) E_F and (c) $4t_{\parallel}$.

play a more important role. In this way, the pair mobility is reduced and the pair mass increased. Thus, as a consequence of the finite pair size, *in the d -wave case the system essentially never reaches the superconducting bosonic regime.*

3.6 PHASE DIAGRAMS

In this section we introduce an additional energy scale T^* , and in this way, arrive at plots of characteristic “phase diagrams” for the crossover problem. Our focus is on the pseudogap onset, so that attention is restricted to relatively small and intermediate coupling constants g ; consequently, the bosonic regime is not addressed. Here, our calculations of T^* are based on the solution of Eq. (2.53), along with Eq. (2.54), under the assumption that $\Delta_{pg} = 0$. This approximation for T^* is consistent with more detailed numerical work [26] in which this temperature is associated with the onset of a pair resonance in the T matrix.

In Figs. 3.5(a)-(c) our results are consolidated into phase diagrams for different physical situations. The case of 3D jellium, with s -wave pairing [Fig. 3.5(a)] is presented primarily

as a point of comparison. Figure 3.5(b) corresponds to quasi-2D jellium ($m_{\perp}/m_{\parallel} = 10^4$), with s -wave pairing and Fig. 3.5(c) to the case of d -wave pairing in a quasi-2D lattice case ($t_{\perp}/t_{\parallel} = 10^{-4}$).⁹ The insets indicate the behavior of μ and Δ_{pg} . Comparing T^* with T_c represents a convenient way of determining the onset of the pseudogap state. (For definiteness, we define the onset to correspond to $T^* = 1.1T_c$). It is clear from the first two figures that this occurs for 3D jellium at $g/g_c \approx 0.9$, and for the quasi-2D case at $g/g_0 \approx 0.4$. (Note here $g_0 = g_c$.) This observation reinforces the notion that pseudogap effects are easier to come by in lower-dimensional systems. Similar behavior is seen in the quasi-2D lattice situation for the d -wave case, although the energy scales on the horizontal and vertical axes reflect the parameter t_{\parallel} (rather than g_c and E_F).

In summary, in this Chapter, we have applied the theory which was developed in Chapter 2 to study the superconducting instability of the normal state, as a function of g . Our intent was to go beyond the simple 3D jellium model with s -wave pairing. In this way we have determined the effects of quasi-two dimensionality, of periodic discrete lattices, and of a d -wave pairing interaction. For the d -wave case, much of the discussion presented in this Chapter addressed densities which are relevant to the cuprate superconductors. A complete study of the d -wave crossover problem at an arbitrary density between 0 and 1, as well as a more detailed comparison with s -wave superconductors, are given in Appendix B.

⁹The phase diagram for the quasi-2D s -wave lattice case is similar to that of the quasi-2D d -wave case for the small coupling regime shown in Fig. 3.5(c).

CHAPTER 4

SUPERCONDUCTING PHASE

The existence of a pseudogap at and above T_c for the underdoped cuprates is now well established. However, whether the pseudogap or related effects persist below T_c is still under debate. From the experimental perspective the relationship (if any) between the pseudo- and superconducting gaps is unclear. ARPES [2, 32] and other measurements [33, 34] on the underdoped cuprates indicate that the normal state excitation or, equivalently, the pseudogap above T_c evolves smoothly into the excitation gap in the superconducting phase below T_c . It is unlikely that a fully developed pseudogap will abruptly disappear as the temperature falls below T_c , but precisely how it connects with the superconducting *order parameter* is not obvious. In this Chapter, we will address the evolution of the various gaps below T_c , as functions of both temperature and coupling strength. Based on the calculations of these gaps, we will further address the superfluid density and low temperature specific heat.

We find that for intermediate and strong coupling, as the temperature decreases the pseudogap Δ_{pg} persists below T_c , and vanishes eventually as $T^{3/4}$ at $T = 0$. In the meantime, the order parameter Δ_{sc} develops precisely at T_c , and is equal to the excitation gap Δ only at $T = 0$. At low T , while Δ has an exponential T dependence, as in BCS, Δ_{sc} generally has a power law T dependence. We argue that strong pairing correlations exist not only between a pair of electrons with precisely opposite momenta, but also between a pair of electrons with a finite net momentum \mathbf{q} . The latter correlation makes it possible to create low energy, incoherent pair excitations. It is the existence of these finite momentum pairs that leads to the distinction between the order parameter and the excitation gap.

The central new result of our theory is that physical measurables, in general, contain contributions from the (usual) fermionic quasiparticles (via Δ) as well as the bosonic pair states (via Δ_{pg}). In this Chapter we will demonstrate that pair excitations generally lead to new low T power laws, e.g, an extra $T^{3/2}$ term in the superfluid density n_s , and a linear in T term in the specific heat C_v in quasi-2D.

4.1 EXCITATION GAP, PSEUDOGAP, AND SUPERCONDUCTING GAP

To study the temperature evolution of the various gaps, we first solve the set of coupled equations, Eqs. (2.53), (2.54), and (2.57), for T_c . Then we determine the various gaps and chemical potential as a function of T below T_c for different situations. Without loss of generality, in this section, we will work with the simplest 3D jellium model with s -wave pairing, as specified in Sec. 3.1. The gaps for the case of d -wave pairing will be discussed when we address the cuprates in Chapter 6.

Shown in Fig. 4.1(a)–(c) are the three self-consistently determined gaps (superconducting gap Δ_{sc} , pseudogap Δ_{pg} , and the total excitation gap Δ) calculated at low density, $k_0 = 4k_F$, and $g/g_c = 0.7, 0.85$, and 1.0 in 3D jellium, for an s -wave pairing. The cases plotted correspond to weak, intermediate, and strong pseudogaps. In the weak coupling limit, the pseudogap is expected to vanish, as in BCS theory. Indeed, we find that for $g/g_c = 0.7$, Δ_{pg} is negligible, and Δ_{sc} and Δ are essentially the same. As g increases, Δ_{pg} increases, and the total gap Δ becomes independent of T in the strong coupling limit.

From Fig. 4.1(a)–(c), we see that, as the temperature decreases, the excitation gap Δ increases, from its value $\Delta = \Delta_{pg}$ at T_c . The order parameter Δ_{sc} develops at T_c , as expected. It is important to note that the pseudogap persists below T_c . As more and more pairs come into the condensate when T is lowered, the density of finite momentum pairs is reduced; energetically pairs prefer to be in the condensate. Therefore, as T decreases, Δ_{pg} decreases. Finally, Δ_{pg} vanishes at $T = 0$, as is consistent with the fact that these finite \mathbf{q} pairs are, indeed, thermal excitations.

We also show the chemical potential μ in Fig. 4.1(d) for $g/g_c = 1$, and in the inset of Fig. 4.1(a) for $g/g_c = 0.7$. These plots indicate that μ does not change much with T , as in a Fermi liquid. In fact, the relative change is the largest in the intermediate regime ($g \sim g_c$). As indicated in the inset of Fig. 4.1(a), in the weak coupling limit, T_c is small, and μ is nearly E_F for all $T \leq T_c$; In the strong coupling, low density limit (not shown here), μ becomes a large negative number, Δ is large, and T_c reaches the upper bound of $T_{BEC} = 0.218E_F$, corresponding to a free Bose gas of fermion pairs. Here, all $T \leq T_c$ corresponds essentially to the $T \rightarrow 0$ limit. In both the weak and strong coupling limit, we notice $T_c \ll |\mu|$. In contrast, at $g \sim g_c$, T_c , Δ , and μ are all comparable. This leads to a

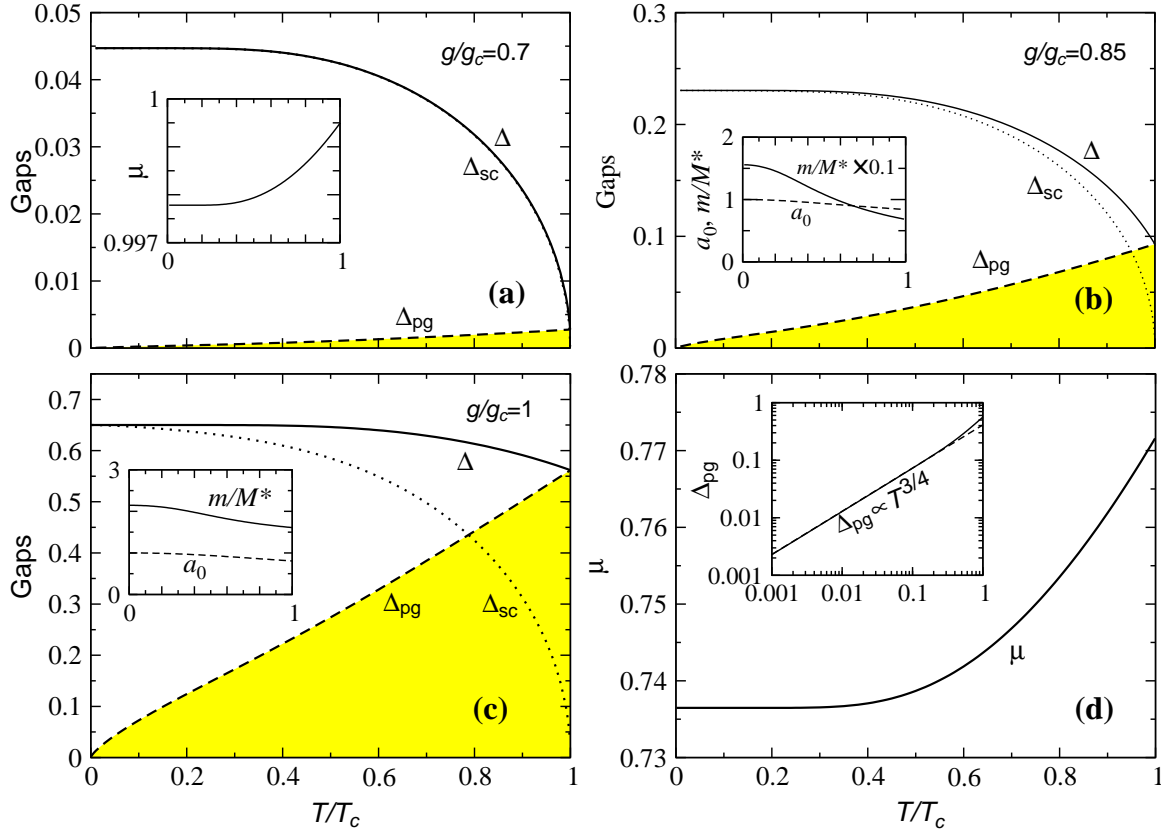


Figure 4.1: Temperature dependence of various gaps below T_c for (a) $g/g_c = 0.7$, (b) 0.85, and (c)-(d) 1.0, respectively, in a 3D s -wave jellium with $k_0 = 4k_F$. The chemical potential μ , as well as the inverse T matrix expansion coefficient a_0 (normalized at $T = 0$) and the inverse pair mass m/M^* , are shown as insets, correspondingly. A log-log plot of Δ_{pg} for $g/g_c = 1$ is shown in the inset of (d), where the dashed line is a $T^{3/4}$ fit.

relatively large change in μ in the intermediate regime, as shown in Fig. 4.1(d).

From Eq. (2.57), we expect $\Delta_{pg}^2 \propto T^{3/2}$ at low T . This analytic result relies on the presumption that the coefficient a_0 and the pair dispersion $\Omega_{\mathbf{q}}$ are roughly independent of T . To support this, in the inset of Fig. 4.1(b) and of Fig. 4.1(c), a_0 is plotted and shown to be roughly a constant for all $T \leq T_c$. The effective pair mass M^* has a stronger T dependence, but our presumption is still valid at low T .¹ The T dependence of M^* becomes weaker and weaker as g increases. Indeed, at low densities, $M^* \rightarrow 2m$ at large g [See Fig. 3.1(a)]. Shown in the inset of Fig. 4.1(d) is Δ_{pg} vs T on a log-log plot. The curve fits nearly perfectly to a $T^{3/4}$ power law (shown as the dashed line) up to $T < 0.2T_c$, i.e., $\Delta_{pg}^2 \propto T^{3/2}$.

¹The leading order corrections for both a_0 and M^* are quadratic in T in the s -wave case, as revealed by detailed numerical studies. See Fig. 6.2(e) for a d -wave example.

The bosonic nature of the pair excitations, reflected in Eq. (2.57), will lead to extra power law temperature dependences for physical quantities which are sensitive to these excitations. As will be shown in the next two sections, the superfluid density will acquire an extra $T^{3/2}$ dependence in 3D and in quasi-2D, and the specific heat will acquire a $T^{3/2}$ power law in 3D and a linear T dependence in quasi-2D.

Physically, the pseudogap below T_c can be interpreted as an extra contribution to the excitation gap, reflecting the fact that at moderate and large g , additional energy is needed to overcome the residual attraction between the fermion components of the excited fermion pairs in order to produce fermionic-like (Bogoliubov) quasi-particles. In the bosonic limit, it becomes progressively more difficult to break up these pairs and the energy Δ_{pg} increases accordingly.

In general, a fermion is attracted to all other fermions in the system, not just to the one with opposite momentum and opposite spin. This attraction makes fermions form pairs with non-zero net momentum, at the cost of a small amount of energy. In the BCS limit, because of the light pair mass M^* , the cost of energy increases immediately as the net pair momentum deviates from zero, and therefore, there is little possibility of forming finite momentum pairs; all the pairs are frozen in the condensate. As g increases, the pair dispersion becomes softer, and the opportunity to form finite momentum pairs is greater. It is these pairs that cause the pseudogap. As a consequence, there will be soft, finite momentum pair excitations at moderate coupling, in addition to the fermionic quasiparticles already existing in the weak coupling BCS limit. However, as g increases further, it becomes extremely difficult to break up a pair, so that then the probability of finding fermionic quasiparticles becomes exponentially small. In this way, in the strong coupling limit, the system below T_c will be composed of the condensate and finite momentum pairs only. This physical picture can be shown schematically in Fig. 1.7.

Note that in our scenario, Δ_{pg} is temperature dependent below T_c (as well as above T_c), and finally vanishes at $T = 0$. This is different from the “normal state gap” used phenomenologically by Loram and coworkers [35]. Upon analysis of data in underdoped cuprates, they conjectured that the measured excitation gap squared can be expressed as the sum of the squares of a pseudogap and superconducting order parameter. This purely *phenomenological* analysis leads to a similar decomposition [36] of the excitation gap, as

in Eq. (2.51). However, in contrast to the present work, these authors presumed that Δ_{pg} is temperature independent below T_c .

4.2 SUPERFLUID DENSITY

The pseudogap is an important measure of the distinction between the order parameter, Δ_{sc} , and the excitation gap, Δ . To establish the validity of the pseudogap below T_c , and to distinguish different possible theoretical models, one needs experimental tools which measure two of the three gaps below T_c , unambiguously. ARPES and tunneling probe only the total excitation gap, Δ . To measure Δ_{sc} , it is necessary to measure physical quantities which rely crucially on the superconducting order. To this end, the superfluid density is of interest; it vanishes identically at and above T_c , and can be viewed as an order parameter in the bosonic regime.

The superfluid density, n_s , can be measured via the magnetic London penetration depth λ . It takes a finite superfluid density to screen magnetic flux. In MKSA units, one has

$$\lambda_L^{-2} = \frac{\mu_0 e^2 n_s}{m}, \quad (4.1)$$

where μ_0 is the magnetic permittivity. For convenience, we will set $\mu_0 = e = 1$. Note on a lattice, n/m should be replaced by

$$\left(\frac{n}{m}\right)_{\alpha\beta} \equiv 2 \sum_{\mathbf{k}} \frac{\partial^2 \epsilon_{\mathbf{k}}}{\partial k_\alpha \partial k_\beta} n_{\mathbf{k}}, \quad (\alpha = x, y, z), \quad (4.2)$$

where $n_{\mathbf{k}}$ is the fermion density distribution in momentum space. For the quasi-2D square lattice, the in-plane mass tensor is diagonal, and $(n/m)_{xx} = (n/m)_{yy}$. (Since the out-of-plane component will be treated separately, we can treat n/m as a simple scalar.) To make our formulae general, we focus on λ_L^{-2} instead of n_s/m . Nevertheless, we may use these two quantities interchangeably.

The penetration depth is expressed in terms of the local (static) electromagnetic response kernel $K(0)$ in linear response theory [37],

$$\lambda_L^{-2} = K(0) = \left(\frac{n}{m}\right) - P_{xx}(0), \quad (4.3)$$

where $K(0)$ is defined by

$$J_\alpha(Q) = P_{\alpha\beta}A_\beta(Q) - \left(\frac{n}{m}\right)_{\alpha\beta} A_\beta(Q) = -K_{\alpha\beta}(Q)A_\beta(Q), \quad (4.4)$$

and the current-current correlation function $P_{\alpha\beta}$ is given by

$$P_{\alpha\beta}(Q) = -2 \sum_K \lambda_\alpha(K, K+Q) G(K+Q) \Lambda_\beta(K+Q, K) G(K). \quad (4.5)$$

The bare vertex is given by

$$\boldsymbol{\lambda}(K, K+Q) = \vec{\nabla}_{\mathbf{k} \in \mathbf{k}+\mathbf{q}/2} = \frac{1}{m} \left(\mathbf{k} + \frac{\mathbf{q}}{2} \right), \quad (4.6)$$

where we have used the dispersion for jellium in the last step. The full vertex $\boldsymbol{\Lambda}$ must be deduced in a manner consistent with the generalized Ward identity, applied here for the uniform static case: $Q = (\mathbf{q}, 0)$, $\mathbf{q} \rightarrow 0$ [1]. The vertex can be constructed by inserting external legs into the self-energy diagram, Fig. 2.3(a). It is convenient to write

$$\boldsymbol{\Lambda} = \boldsymbol{\lambda} + \delta\boldsymbol{\Lambda}_{pg} + \delta\boldsymbol{\Lambda}_{sc}, \quad (4.7)$$

where the pseudogap contribution $\delta\boldsymbol{\Lambda}_{pg}$ to the vertex correction follows from the Ward identity

$$\delta\boldsymbol{\Lambda}_{pg}(K, K) = \frac{\partial \Sigma_{pg}(K)}{\partial \mathbf{k}}, \quad (4.8)$$

and the superconducting vertex contribution is given by

$$\delta\boldsymbol{\Lambda}_{sc}(K+Q, K) = \Delta_{sc}^2 \varphi_{\mathbf{k}} \varphi_{\mathbf{k}+\mathbf{q}} G_o(-K-Q) G_o(-K) \boldsymbol{\lambda}(K+Q, K). \quad (4.9)$$

The latter can be obtained by proper vertex insertion to the superconducting self-energy diagram, Fig. 2.4, which will lead to the so-called Maki-Thompson term. A more detailed treatment will be given in Chapter 5, when we address gauge invariance and the collective modes.

To proceed, we rewrite Eq. (4.2) by integration by parts,

$$\begin{aligned} \left(\frac{n}{m}\right) &= \frac{2}{d} \sum_{\alpha, K} \frac{\partial^2 \epsilon_{\mathbf{k}}}{\partial k_{\alpha}^2} G(K) = -\frac{2}{d} \sum_{\alpha, K} \frac{\partial \epsilon_{\mathbf{k}}}{\partial k_{\alpha}} \frac{\partial G(K)}{\partial k_{\alpha}} \\ &= -\frac{2}{d} \sum_{\alpha, K} G^2(K) \frac{\partial \epsilon_{\mathbf{k}}}{\partial k_{\alpha}} \left(\frac{\partial \epsilon_{\mathbf{k}}}{\partial k_{\alpha}} + \frac{\partial \Sigma_{pg}}{\partial k_{\alpha}} + \frac{\partial \Sigma_{sc}}{\partial k_{\alpha}} \right). \end{aligned} \quad (4.10)$$

Note here the surface term vanishes in all cases.

Substitute Eqs. (4.5)–(4.10) and the expression for G , Eq. (2.52), into Eq. (4.3), after performing the Matsubara frequency sum, we obtain

$$\lambda_L^{-2} = \frac{2}{d} \sum_{\alpha, \mathbf{k}} \frac{\Delta_{sc}^2}{E_{\mathbf{k}}^2} \left[\frac{1 - 2f(E_{\mathbf{k}})}{2E_{\mathbf{k}}} + f'(E_{\mathbf{k}}) \right] \left[\left(\frac{\partial \epsilon_{\mathbf{k}}}{\partial k_{\alpha}} \right)^2 \varphi_{\mathbf{k}}^2 - \frac{1}{4} \frac{\partial \epsilon_{\mathbf{k}}^2}{\partial k_{\alpha}} \frac{\partial \varphi_{\mathbf{k}}^2}{\partial k_{\alpha}} \right]. \quad (4.11)$$

Inserting the appropriate $\epsilon_{\mathbf{k}}$ and $\varphi_{\mathbf{k}}$, we can obtain results for 3D s -wave jellium, as well as for a quasi-2D lattice (in-plane) with s - and d -wave pairing. For example, for 3D s -wave jellium, we have

$$n_s = m\lambda_L^{-2} = \frac{2}{3} \sum_{\mathbf{k}} \frac{\Delta_{sc}^2 \varphi_{\mathbf{k}}^2}{E_{\mathbf{k}}^2} \left[\frac{1 - 2f(E_{\mathbf{k}})}{2E_{\mathbf{k}}} + f'(E_{\mathbf{k}}) \right] [\epsilon_{\mathbf{k}}(3 - \varphi_{\mathbf{k}}^2) + 2\mu]. \quad (4.12)$$

For a quasi-2D lattice, the s -wave in-plane penetration depth, (with $\varphi_{\mathbf{k}} = 1$), becomes particularly simple,

$$\lambda_{ab}^{-2} = \sum_{\mathbf{k}} \frac{\Delta_{sc}^2}{E_{\mathbf{k}}^2} \left[\frac{1 - 2f(E_{\mathbf{k}})}{2E_{\mathbf{k}}} + f'(E_{\mathbf{k}}) \right] 4t_{\parallel}^2 (\sin^2 k_x + \sin^2 k_y). \quad (4.13)$$

Finally, for d -wave, with $\varphi_{\mathbf{k}} = \cos k_x - \cos k_y$, we find a slightly more complicated result for the in-plane penetration depth,

$$\begin{aligned} \lambda_{ab}^{-2} &= \Delta_{sc}^2 \sum_{\mathbf{k}} \frac{\varphi_{\mathbf{k}}^2}{E_{\mathbf{k}}^2} \left[\frac{1 - 2f(E_{\mathbf{k}})}{2E_{\mathbf{k}}} + f'(E_{\mathbf{k}}) \right] \\ &\quad \times [4t_{\parallel}^2 (\sin^2 k_x + \sin^2 k_y) - 2t_{\parallel} (\cos k_x + \cos k_y) \epsilon_{\mathbf{k}}]. \end{aligned} \quad (4.14)$$

Equation (4.11) is also valid for the out-of-plane penetration depth, with $d = 1$ and

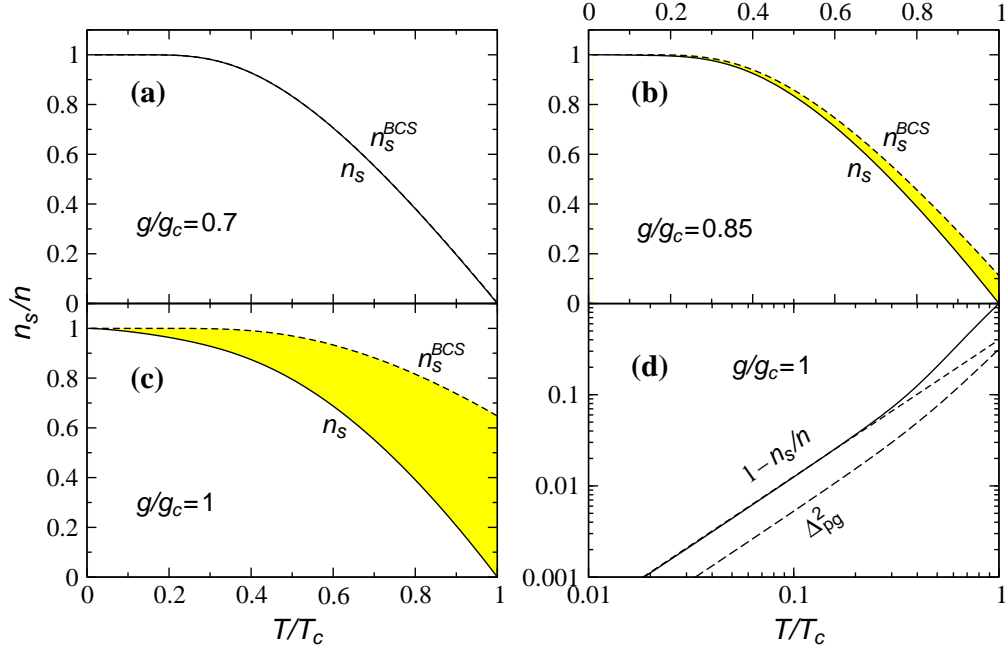


Figure 4.2: Temperature dependence of the normalized superfluid densities n_s , as well as comparison with n_s^{BCS} , for the same coupling strengths as in Fig. 4.1(a)–(d). Shown in (d) are $1 - n_s/n$ and a $T^{3/2}$ power law fit (dashed line) as well as Δ_{pg}^2 as a function of T/T_c for $g/g_c = 1$ on a log-log scale. n_s and n_s^{BCS} are calculated via Eqs. (4.11) and (4.16). The shaded regions help to clarify pseudogap effects.

$\alpha = z$. For use later, we simply write it down:

$$\lambda_c^{-2} = \Delta_{sc}^2 \sum_{\mathbf{k}} \frac{\varphi_{\mathbf{k}}^2}{E_{\mathbf{k}}^2} \left[\frac{1 - 2f(E_{\mathbf{k}})}{2E_{\mathbf{k}}} + f'(E_{\mathbf{k}}) \right] (8t_{\perp}^2 \sin^2 k_z). \quad (4.15)$$

In the absence of a pseudogap, $\Delta_{sc} = \Delta$. Then Eq. (4.11) is just the usual BCS formula, as in Ref. [1], except that we now allow for a more general $\epsilon_{\mathbf{k}}$ and $\varphi_{\mathbf{k}}$. Finally, we can define a relationship between two length scales

$$\lambda_L^{-2} = \frac{\Delta_{sc}^2}{\Delta^2} \lambda_{BCS}^{-2}, \quad (4.16)$$

where λ_{BCS}^{-2} is just λ_L^{-2} with the overall prefactor Δ_{sc}^2 replaced with Δ^2 in Eq. (4.11). Obviously, in the pseudogap phase, λ_{BCS}^{-2} does not vanish at T_c .

Shown in Fig. 4.2 is the temperature dependence of the normalized superfluid density, n_s/n , for 3D s -wave jellium, calculated from Eq. 4.12 for the same three representative

values g/g_c as in Fig. 4.1. For comparison, we also plot n_s^{BCS}/n , which is calculated via λ_{BCS}^{-2} . In agreement with Fig. 4.1, for sufficiently weak coupling ($g \leq 0.7$), n_s essentially follows the BCS calculation, the two curves are indistinguishable. As g increases, the separation between the two curves becomes evident, particularly in the vicinity of T_c . However, at zero temperature $n_s = n$, independent of the coupling. This comparison thus demonstrates how different are these “pseudogap” superconductors. Away from the weak coupling regime, one has to consider the distinction between the excitation gap Δ and the order parameter Δ_{sc} . The larger the coupling g , the larger the difference between λ_{BCS}^{-2} and λ_L^{-2} . The superfluid density reflects most directly the temperature dependence of Δ_{sc} , *not* the excitation gap. It should be noted that with our calculations of λ , *one can uniquely determine the three different gaps below T_c* : Measure Δ with ARPES or tunneling experiments, then construct λ_{BCS}^{-2} . Then measure the penetration depth λ_L , which can now be done with fairly good accuracy. Finally one obtains $\Delta_{sc}^2 = \Delta^2 \lambda_L^{-2} / \lambda_{BCS}^{-2}$ and then Δ_{pg} .

These bosonic pair excitations will lead to new low T power laws. For an isotropic s -wave superconductor, λ_{BCS}^{-2} shows an exponential behavior at low T due to the isotropic gap in the fermionic excitation spectrum [1]. With this weak T dependence, the T dependence of λ_L^{-2} will be predominantly determined by the overall prefactor, Δ_{sc}^2/Δ^2 in Eq. (4.16), which derives from the bosonic or pair contributions. As expected from Eq. (2.57), Fig. 4.1 shows that Δ_{pg}^2 follows a $T^{3/2}$ dependence. Therefore, the temperature dependence of the normal fluid density $n_n/n \equiv 1 - n_s/n$ will also follow a $T^{3/2}$ dependence in the pseudogap phase at low T . Shown in Fig. 4.2(d) are n_n/n and Δ_{pg}^2 , as well as a $T^{3/2}$ fit (dashed line) on a logarithmic scale. Obviously, these two quantities have the same $T^{3/2}$ power law.

For d -wave pairing, the fermionic quasiparticle density of states is linear in energy because of the existence of gap nodes on the Fermi surface. Thus, λ_{BCS}^{-2} has a linear T dependence. The bosonic and fermionic contributions add so that the the overall low T dependence of λ^{-2} is now given by

$$\frac{\lambda_L(0)^2}{\lambda_L(T)^2} = 1 - A \frac{T}{T_c} - B' \left(\frac{T}{T_c} \right)^{3/2}, \quad (4.17)$$

where A and B' are expansion coefficients, and explicitly calculated in Chapter 6. In the

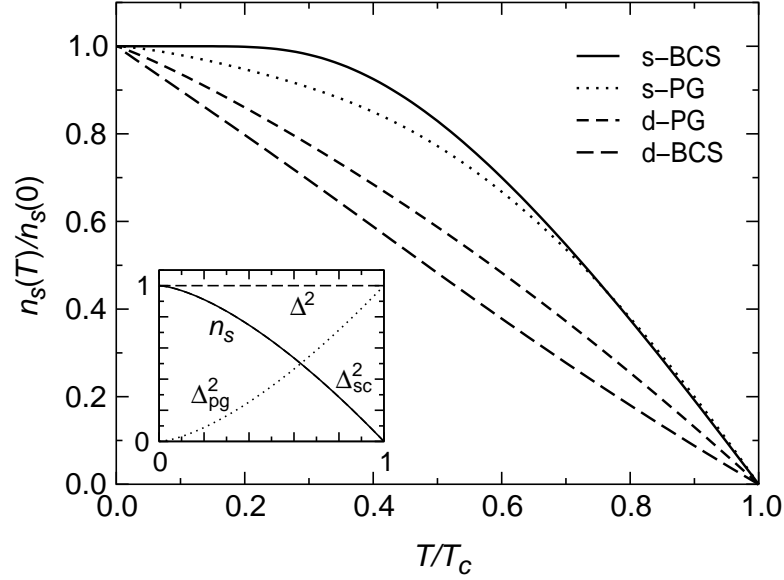


Figure 4.3: Temperature dependence of the normalized superfluid density in s - and d -wave, BCS and pseudogap cases on a quasi-2D lattice with $t_{\perp}/t_{\parallel} = 0.01$. The parameters $(n, -g/4t_{\parallel})$ are: for s -BCS: (0.5, 0.5); s -PG: (0.5, 0.7); d -BCS: (0.8, 0.225); d -PG: (0.92, 0.56). Plotted in the inset are the T dependence of the normalized n_s , Δ_{sc}^2 , Δ^2 , and Δ_{pg}^2 for $g/g_c = 1.5$ and $k_0 = 4k_F$ in 3D jellium with s -wave pairing. The first two curves overlap.

BCS limit, as expected, B' vanishes.

Plotted in Fig. 4.3 is the temperature dependence of the normalized superfluid density for s - and d -wave pairing with and without pseudogap effects. The fermionic contributions at weak coupling (labeled by “BCS”) lead to an exponentially flat s -wave curve at low T , while the weak coupling (BCS) d -wave curve is almost a straight line, going through the diagonal. In the intermediate coupling regime (labeled by “PG”), the pair excitations add a new $T^{3/2}$ power law to both, and bring them closer. Both the s - and d -wave curves now have a higher curvature at low T .

The new $T^{3/2}$ power law implies that an extremely careful data analysis is necessary when one tries to extract information about the order parameter symmetry from low T power laws. From this figure, we see that, except at very low T , $T^{3/2}$ appears very close to a linear T dependence; therefore, a pseudogapped s -wave curve might be mistaken as d -wave.

Both Fig. 4.2 and Fig. 4.3 demonstrate that as T increases, *the superfluid density is destroyed by both quasiparticles and pair excitations*. This can be most clearly seen in an

s -wave strong coupling case. Shown in the inset of Fig. 4.3 are the normalized n_s , Δ^2 , Δ_{pg}^2 , and Δ_{sc}^2 in the BEC regime ($g/g_c = 1.5$, $k_0 = 4k_F$, and $\mu/E_F \approx -3.69$) in 3D jellium with s -wave pairing. Clearly, the n_s and Δ_{sc} curves cannot be distinguished. As noted in Chapter 2, in the BEC regime, the pseudogap equation (2.57) becomes the boson number equation; $a_0\Delta^2$, $a_0\Delta_{pg}^2$, and $a_0\Delta_{sc}^2$ correspond to $n/2$, $n_n/2$, and $n_s/2$, respectively. Therefore, in the BEC regime, Eq. (4.12) can be simplified as:

$$\frac{n_s}{n} = \frac{\Delta_{sc}^2}{\Delta^2} = 1 - \left(\frac{T}{T_c}\right)^{3/2}, \quad (\text{in BEC regime}). \quad (4.18)$$

This equation is familiar from the Bose-Einstein condensation of an ideal Bose gas. [It is interesting that in the BEC regime, the superfluid density n_s and the electron density in the condensate are essentially the same. This is different from the BCS case.]

It should be emphasized that the power index $3/2$, appearing in the superfluid density, is not very sensitive to the anisotropy in the dispersion. However, as the anisotropy ratio t_\perp/t_\parallel becomes extremely small, this power eventually decreases to values somewhere between $3/2$ and 1 .

4.3 LOW TEMPERATURE SPECIFIC HEAT

Finite momentum pairs are expected to show up in thermodynamical properties. In this section, we explore the consequences of this pseudogap effect on the specific heat, C_v .

Ideally one should calculate the thermodynamical potential for our crossover problem, from which all thermodynamical properties are determined. Unfortunately, our approach is based on an equation of motion method, which in general leads to a non- ϕ derivable theory, and there is no simple expression for the thermodynamic potential. But nevertheless, we can still calculate the specific heat based on some reasonable approximations.

In the intermediate coupling regime, the system is composed of the superconducting condensate and two types of thermal excitations: quasiparticles and finite center-of-mass momentum pairs (bosons) — This leads to a simple three fluid model. Since the phase coherent condensate does not contribute to the entropy, the entropy comes from the latter two components. We will now calculate C_v via the entropy.

The approximation we made in Eq. (2.48) is equivalent to treating all the finite mo-

momentum pairs as if they were in the condensate (of course, the distribution of these pairs still obeys a Bose distribution), solely for the purpose of calculating their contribution to the single particle self-energy, Σ_{pg} . As a consequence, the full Green's function has the BCS form, which depends on the total excitation gap Δ instead of the order parameter Δ_{sc} . The contribution to the thermodynamic potential Ω from this simplified, BCS-like Green's function will lead to an entropy given purely by the fermionic quasiparticle excitations, as in BCS [1]:

$$S_{QP} = -2 \sum_{\mathbf{k}} \left\{ f(E_{\mathbf{k}}) \ln f(E_{\mathbf{k}}) + [1 - f(E_{\mathbf{k}})] \ln[1 - f(E_{\mathbf{k}})] \right\}. \quad (4.19)$$

To calculate thermodynamics, this fermionic contribution is not sufficient. One has to consider the degree of freedom introduced by the pair excitations, just as one treats the collective mode contribution to the entropy in Fermi liquid theory. In the first order contribution, we neglect the possible interactions between pairs. In this way, the pair excitations will contribute to the entropy as in an ideal Bose gas:

$$S_{pair} = - \sum_{\mathbf{q} \neq 0} \left\{ b(\Omega_{\mathbf{q}}) \ln b(\Omega_{\mathbf{q}}) - [1 + b(\Omega_{\mathbf{q}})] \ln[1 + b(\Omega_{\mathbf{q}})] \right\}. \quad (4.20)$$

This pair contribution can be derived from a T matrix ring diagram contribution to the thermodynamic potential, as shown in Fig. 4.4. This corresponds to a term in the thermodynamical potential:

$$\Omega_{pair} = \sum_Q \ln[1 + g\chi(Q)], \quad (4.21)$$

with $\chi(Q)$ given by Eq. (2.20). In calculations of the thermodynamical potential the contribution of Eq. (4.21) appears (with properly redefined χ) in both the G_0G_0 scheme (see Ref. [16]) and the GG scheme (see Ref. [21]), and we believe it also appears in the present G_0G scheme. In Appendix D, we derive Eq. (4.20) from Eq. (4.21), following the Brinkman and Engelsberg treatment of the paramagnon problem [38].

The total entropy is then given by

$$S = S_{QP} + S_{pair}. \quad (4.22)$$

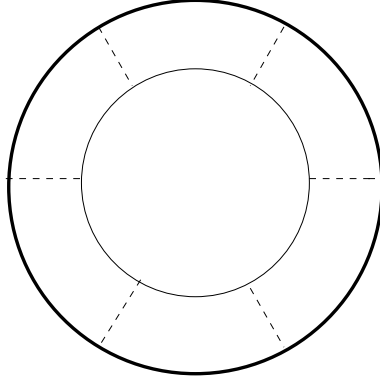


Figure 4.4: T matrix ring diagram contribution to the thermodynamic potential. The thin and thick lines are the bare and full Green's functions, respectively.

In the weak coupling limit, the quasiparticle contribution S_{QP} dominates. As g increases, the pair contribution S_{pair} becomes more important. In the strong coupling bosonic regime (which is accessible at low density with s -wave pairing), where the excitation gap becomes too large for fermionic quasiparticles to be thermally excited, the contribution comes predominantly from S_{pair} , as expected.

It follows that the specific heat is given by

$$C_v = T \frac{\partial S}{\partial T} = 2 \sum_{\mathbf{k}} E_{\mathbf{k}} \frac{\partial f(E_{\mathbf{k}})}{\partial T} + \sum_{\mathbf{q}} \Omega_{\mathbf{q}} \frac{\partial b(\Omega_{\mathbf{q}})}{\partial T}. \quad (4.23)$$

Since C_v involves the derivatives $\frac{\partial \mu}{\partial T}$, $\frac{\partial \Delta}{\partial T}$, and $\frac{\partial M^*}{\partial T}$, and these derivatives are highly non-trivial, in general, we have to calculate C_v numerically from the entropy. However, we can still obtain the qualitative behavior at low T , based on knowledge from both BCS theory and from calculations involving free bosons. For s -wave pairing, the quasiparticle contribution shows an exponential behavior at low T . For d -wave pairing, there are nodes on the Fermi surface so that the density of states $N(E) \propto E$; therefore, C_v shows a quadratic T dependence. Thus we have

$$C_{QP} \propto \begin{cases} \left(\frac{\Delta_0}{T}\right)^{1/2} e^{-\Delta_0/T}, & \text{for } s\text{-wave,} \\ T^2, & \text{for } d\text{-wave.} \end{cases} \quad (4.24)$$

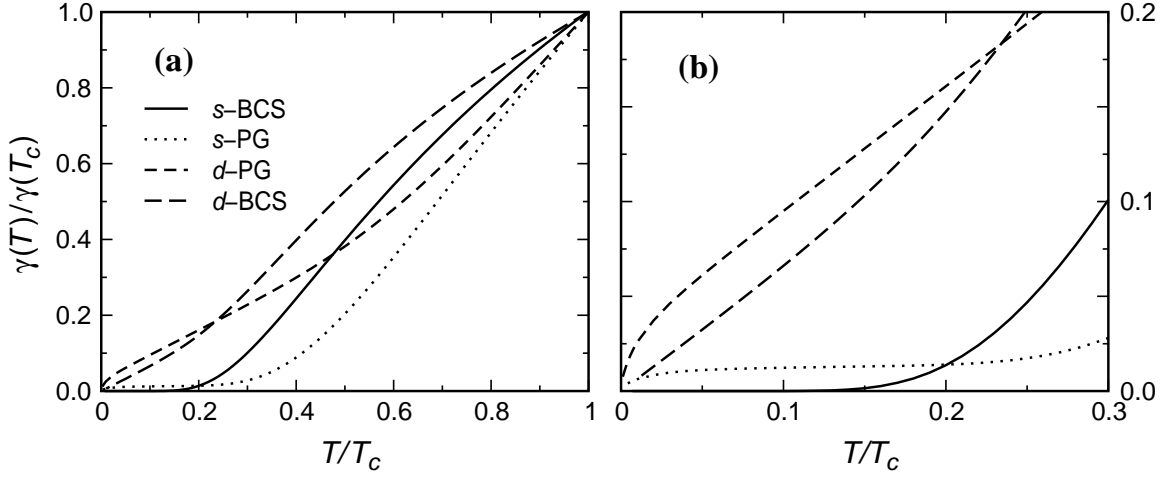


Figure 4.5: (a) Temperature dependence (normalized at T_c) of the specific coefficient γ for s - and d -wave pairing with and without pseudogap. The low T portion is magnified and shown in (b). All other parameters are the same as in Fig. 4.3. For the pseudogap cases, γ has a finite intercept γ^* if extrapolated from the data between $T/T_c = 0.05$ and 0.2.

As shown in Fig. 4.1, the effective pair mass M^* is essentially temperature independent at low T . Therefore, we may take $\Omega_{\mathbf{q}}$ as T independent. In this way, we obtain the pair contribution

$$C_{pair} \propto \begin{cases} T^{3/2}, & \text{for 3D,} \\ T, & \text{for (quasi-)2D.} \end{cases} \quad (4.25)$$

For quasi-2D, there is a crossover temperature, T_0 , below which the system is 3D, but above which the system is essentially 2D. This crossover temperature depends on the mass anisotropy t_{\perp}/t_{\parallel} , and is usually very small in a highly anisotropic system like the cuprates. For this reason, we will neglect the extremely low T (inaccessible) limit.

The low T specific ‘‘coefficient’’ $\gamma \equiv C_v/T$ is given by

$$\gamma = \begin{cases} \beta T^{1/2}, & \text{for 3D } s\text{-wave,} \\ \gamma^*, & \text{for (quasi-)2D } s\text{-wave,} \\ \gamma^* + \alpha T, & \text{for (quasi-)2D } d\text{-wave.} \end{cases} \quad (4.26)$$

In the BCS limit, β and γ^* vanish.

Shown in Fig. 4.5(a) is the temperature dependence of $\gamma(T)$, normalized at T_c , for s - and d -wave pairing in the BCS and pseudogap cases. To see the low temperature regime clearly, we magnify the plots, as shown in Fig. 4.5(b). In the weak coupling regime (la-

beled by “BCS”), the $\gamma(T)$ curves for s - and d -wave pairing show exponential and linear T dependences, respectively. However, in the intermediate coupling or pseudogap regime (labeled by “PG”), the $\gamma(T)$ curves show a finite intercept, γ^* , on the vertical axis, when extrapolated from the temperature interval between, say, $0.05T_c$ and $0.2T_c$ — in agreement with Eq. (4.26).

To understand why the specific heat is sensitive to the quasi 2D anisotropy, we note that this occurs because the (anisotropic) pair dispersion $\Omega_{\mathbf{q}}$ appears one more time in the integral for the energy, $E = \sum_{\mathbf{q}} \Omega_{\mathbf{q}} b(\Omega_{\mathbf{q}})$, whereas in calculating n_s , the relevant integral is $\Delta_{pg}^2 \propto \sum_{\mathbf{q}} b(\Omega_{\mathbf{q}})$. It turns out that the latter integral is far less sensitive to the mass anisotropy ratio used in the above calculations ($t_{\perp}/t_{\parallel} = 0.01$), than is the former.

It is worth pointing out that the (spin singlet) pair excitations do not make their presence explicitly felt in the spin susceptibility or Knight shift. There are no new low T power laws in these properties or in the nuclear spin relaxation rate.

CHAPTER 5

GAUGE INVARIANCE AND THE COLLECTIVE MODES

5.1 INTRODUCTION

In previous chapters, we demonstrated that at finite coupling strength, there exist soft, finite momentum pair excitations. These excitations are characteristic of the system in equilibrium, in the absence of the order parameter oscillations, or collective modes. It is important to stress that the pair excitations we have found are different from the collective modes. As shown in Chapter 2, they are determined by a pole of the mean field T matrix (t_{pg}), which is associated with a particular single-particle self-energy diagram (see Fig. 2.3 in our case). Moreover, the pair susceptibility χ , associated with this T matrix, is in general different from its counterpart in the linear response collective mode calculations, i.e., the generalized two-particle correlation function. This can be seen in a rather straightforward way, even in strict BCS theory. The more general two-particle correlation function corresponds to a 4×4 matrix containing multiple correlation functions, e.g., the density-density, current-current, density-current, and correlations between the phase and amplitude of the order parameter and between the order parameter and the current. The long wavelength expansion of the determinant of this general matrix determines the collective modes of the superconducting order parameter. Within this matrix, the phase modes are associated with a susceptibility which we call Q_{22} , given by Eq. (5.20), and which we demonstrate below in Sec. 5.3 is different from pair susceptibility χ . This comparison, moreover, serves to underline the fact that the collective modes introduce effectively higher order Green's functions (via $F \sim GG_0$) than does the gap equation. As a consequence, as we will see in this Chapter, the collective modes contain some degree of boson-boson interaction. *The principal effect of the incoherent pair excitations on the collective modes is via single particle self-energy and related vertex corrections which appear in each of the multiple functions of the generalized two-particle correlation function.*

In this Chapter, we will calculate the collective mode spectrum, and show explicitly that the dispersion of the (soft) phase mode is indeed different from the pair dispersion. As in BCS, to address the collective modes, one has to go beyond the level of the gap equation [27], to include gauge invariance in the problem. In this way, one sees that the collective modes introduce higher order Green's functions and thus pair-pair interactions. By contrast, as discussed in previous chapters, there are no pair-pair interactions at the level of the gap equations; these pair-pair interactions enter at the level of the collective modes. In this context the bosons are no longer free.

5.2 ELECTROMAGNETIC RESPONSE AND COLLECTIVE MODES OF A SUPERCONDUCTOR: BEYOND BCS THEORY

The purpose of this section is to study the gauge invariant (linear) response of a superconductor to an external electromagnetic (EM) field, and obtain the associated collective mode spectrum. Our discussion is generally relevant to complex situations such as those appropriate to the BCS-BEC crossover scenario. An important ingredient of this discussion is establishing the role of particle-hole asymmetry. It should be noted that there are fairly extensive discussions in the literature on the behavior of collective modes within the $T = 0$ crossover scenario [39, 40, 41, 42]. Here we review a slightly different formulation [43, 44] that introduces a matrix extension of the Kubo formalism of the normal state. We find that this approach is more directly amenable to extension to finite T , where the pair fluctuation diagrams need to be incorporated.

The definition of the collective modes of a superconductor must be made with some precision. We refer to the underlying Goldstone boson of the charged or uncharged superconductor as the “AB mode,” after Anderson [45] and Bogoliubov [46]. This AB mode appears as a pole structure in the gauge invariant formulation of the electrodynamic response functions, for example, in the density-density correlation function. Early work by Prange [47] referred to this as the “ghost mode” of the neutral system, since this term is not directly affected by the long range Coulomb interaction. By contrast, the normal modes of the charged or uncharged superconductor, which we shall call the “collective modes,” involve a coupling between the density, phase, and for the BCS-BEC case, amplitude de-

degrees of freedom. For these, one needs to incorporate a many body theoretic treatment of the particle-hole channel as well. In crossover theories this channel is not as well characterized as is the particle-particle channel.

5.2.1 Gauge invariant electromagnetic response kernel

In the presence of a weak externally applied EM field, with four-vector potential $A^\mu = (\phi, \mathbf{A})$, the four-current density $J^\mu = (\rho, \mathbf{J})$ is given by

$$J^\mu(Q) = K^{\mu\nu}(Q)A_\nu(Q) , \quad (5.1)$$

where, $Q \equiv q^\mu = (\omega, \mathbf{q})$ is a four-momentum, and $K^{\mu\nu}$ is the EM response kernel, which can be written as

$$K^{\mu\nu}(Q) = K_0^{\mu\nu}(Q) + \delta K^{\mu\nu}(Q) . \quad (5.2)$$

Here

$$K_0^{\mu\nu}(\omega, \mathbf{q}) = P^{\mu\nu}(\omega, \mathbf{q}) + \frac{ne^2}{m}g^{\mu\nu}(1 - g^{\mu 0}) \quad (5.3)$$

is the usual Kubo expression for the electromagnetic response. We define the current-current correlation function $P^{\mu\nu}(\tau, \mathbf{q}) = -i\theta(\tau)\langle [j^\mu(\tau, \mathbf{q}), j^\nu(0, -\mathbf{q})] \rangle$. In the above equation, $g^{\mu\nu}$ is the contravariant diagonal metric tensor, with diagonal elements $(1, -1, -1, -1)$, and n , e , and m are the particle density, charge and mass, respectively. In what follows, we will set $e = 1$ for simplicity, as we did in Chapter 4.

The presence of $\delta K^{\mu\nu}$ in Eq. (5.2) is due to the perturbation of the superconducting order parameter by the EM field, i.e., to the excitation of the *collective modes* of Δ_{sc} . This term is required to satisfy charge conservation $q_\mu J^\mu = 0$, which requires that

$$q_\mu K^{\mu\nu}(Q) = 0 . \quad (5.4a)$$

Moreover, gauge invariance yields

$$K^{\mu\nu}(Q)q_\nu = 0 , \quad (5.4b)$$

Note that, since $K^{\mu\nu}(-Q) = K^{\nu\mu}(Q)$, the two constraints Eqs. (5.4) are in fact equivalent.

The incorporation of gauge invariance into a general microscopic theory may be implemented in several ways. Here we do so via a general matrix linear response approach [43] in which the perturbation of the condensate is included as additional contributions $\Delta_1 + i\Delta_2$ to the applied external field. These contributions are self consistently obtained (by using the gap equation) and then eliminated from the final expression for $K^{\mu\nu}$. We now implement this procedure. Let $\eta_{1,2}$ denote the change in the expectation value of the pairing field $\hat{\eta}_{1,2}$ corresponding to $\Delta_{1,2}$. For the case of an s -wave pairing interaction $g < 0$, the self-consistency condition $\Delta_{1,2} = g\eta_{1,2}/2$ leads to the following equations:

$$J^\mu = K^{\mu\nu} A_\nu = K_0^{\mu\nu} A_\nu + R^{\mu 1} \Delta_1 + R^{\mu 2} \Delta_2, \quad (5.5a)$$

$$\eta_1 = -\frac{2\Delta_1}{|g|} = R^{1\nu} A_\nu + Q_{11}\Delta_1 + Q_{12}\Delta_2, \quad (5.5b)$$

$$\eta_2 = -\frac{2\Delta_2}{|g|} = R^{2\nu} A_\nu + Q_{21}\Delta_1 + Q_{22}\Delta_2, \quad (5.5c)$$

where $R^{\mu i}(\tau, \mathbf{q}) = -i\theta(\tau)\langle [j^\mu(\tau, \mathbf{q}), \hat{\eta}_i(0, -\mathbf{q})] \rangle$, with $\mu = 0, \dots, 3$, and $i = 1, 2$; and $Q_{ij}(\tau, \mathbf{q}) = -i\theta(\tau)\langle [\hat{\eta}_i(\tau, \mathbf{q}), \hat{\eta}_j(0, -\mathbf{q})] \rangle$, with $i, j = 1, 2$.

Thus far, the important quantities $K_0^{\mu\nu}$, $R^{\mu i}$ and Q_{ij} are unknowns that contain the details of the appropriate microscopic model. We shall return to these later in Sec. 5.3. The last two of Eqs. (5.5) can be used to express $\Delta_{1,2}$ in terms of A_ν :

$$\Delta_1 = -\frac{\tilde{Q}_{22}R^{1\nu} - Q_{12}R^{2\nu}}{\tilde{Q}_{11}\tilde{Q}_{22} - Q_{12}Q_{21}}A_\nu, \quad (5.6a)$$

$$\Delta_2 = -\frac{\tilde{Q}_{11}R^{2\nu} - Q_{21}R^{1\nu}}{\tilde{Q}_{11}\tilde{Q}_{22} - Q_{12}Q_{21}}A_\nu, \quad (5.6b)$$

where $\tilde{Q}_{ii} = 2/|g| + Q_{ii}$, with $i = 1, 2$. Finally, inserting Eqs. (5.6) into Eq. (5.5a) one obtains

$$K^{\mu\nu} = K_0^{\mu\nu} + \delta K^{\mu\nu}, \quad (5.7a)$$

with

$$\delta K^{\mu\nu} = -\frac{\tilde{Q}_{11}R^{\mu 2}R^{2\nu} + \tilde{Q}_{22}R^{\mu 1}R^{1\nu} - Q_{12}R^{\mu 1}R^{2\nu} - Q_{21}R^{\mu 2}R^{1\nu}}{\tilde{Q}_{11}\tilde{Q}_{22} - Q_{12}Q_{21}}. \quad (5.7b)$$

As can be seen from the above rather complicated equation, the electromagnetic response of a superconductor involves many different components of the generalized polarizability. Moreover, in the form of Eq. (5.7b) it is not evident that the results are gauge invariant. In order to demonstrate gauge invariance and reduce the number of component polarizabilities, we first rewrite $K^{\mu\nu}$ in a way which incorporates the effects of the amplitude contributions via a renormalization of the relevant generalized polarizabilities, i.e.,

$$K^{\mu\nu} = K_0^{\prime\mu\nu} + \delta K^{\prime\mu\nu} , \quad (5.8a)$$

where

$$K_0^{\prime\mu\nu} = K_0^{\mu\nu} - \frac{R^{\mu 1} R^{1\nu}}{\tilde{Q}_{11}} \quad (5.8b)$$

and

$$R^{\prime\mu 2} = R^{\mu 2} - \frac{Q_{12}}{\tilde{Q}_{11}} R^{\mu 2} , \quad \tilde{Q}'_{22} = \tilde{Q}_{22} - \frac{Q_{12} Q_{21}}{\tilde{Q}_{11}} . \quad (5.8c)$$

In this way we obtain a simpler expression for $\delta K^{\prime\mu\nu}$:

$$\delta K^{\prime\mu\nu} = -\frac{R^{\prime\mu 2} R^{\prime 2\nu}}{\tilde{Q}'_{22}} . \quad (5.9)$$

We now consider a particular (*a priori* unknown) gauge A'^{μ} in which the current density can be expressed as $J^{\mu} = K_0^{\prime\mu\nu} A'_{\nu}$. The gauge transformation [48] that connects the four-potential A_{μ} in an arbitrary gauge with A'_{μ} , i.e., $A'_{\mu} = A_{\mu} + i\chi q_{\mu}$, must satisfy

$$J^{\mu} = K^{\mu\nu} A_{\nu} = K_0^{\prime\mu\nu} (A_{\nu} + i\chi q_{\nu}) . \quad (5.10)$$

Now invoking charge conservation, one obtains

$$i\chi = -\frac{q_{\mu} K_0^{\prime\mu\nu} A_{\nu}}{q_{\mu'} K_0^{\prime\mu'\nu'} q_{\nu'}} , \quad (5.11)$$

and, therefore,

$$K^{\mu\nu} = K_0^{\prime\mu\nu} - \frac{\left(K_0^{\prime\mu\nu'} q_{\nu'} \right) \left(q_{\nu''} K_0^{\prime\nu''\nu} \right)}{q_{\mu'} K_0^{\prime\mu'\nu'} q_{\nu'}} . \quad (5.12)$$

The above equation satisfies two important requirements: it is manifestly gauge invariant and, moreover, it has been reduced to a form that depends principally on the four-current-current correlation functions. (The word “principally” appears because in the absence of particle-hole symmetry, there are effects associated with the order parameter amplitude contributions that enter via Eq. (5.8) and add to the complexity of the calculations). Equation (5.12) should be directly compared with Eq. (5.7b). In order for the formulations to be consistent and to explicitly keep track of the conservation laws (5.4), the following identities must be satisfied:

$$(q_\mu K_0^{\prime\mu\nu}) \tilde{Q}'_{22} = (q_\mu R^{\prime\mu 2}) R^{\prime 2\nu} , \quad (5.13a)$$

$$(K_0^{\prime\mu\nu} q_\nu) \tilde{Q}'_{22} = R^{\prime\mu 2} (R^{\prime 2\nu} q_\nu) . \quad (5.13b)$$

These identities may be viewed as “Ward identities” for the superconducting two-particle correlation functions [44]. Any theory that adds additional self-energy contributions to the BCS scheme must obey these important equations. We shall return to this issue in Sec. 5.3.

5.2.2 The Goldstone boson or AB mode

The EM response kernel [cf. Eqs. (5.8)–(5.12)] of a superconductor contains a pole structure that is related to the underlying Goldstone boson of the system. Unlike the phase mode component of the collective mode spectrum, this AB mode is independent of Coulomb effects [47]. The dispersion of this amplitude renormalized AB mode is given by

$$q_\mu K_0^{\prime\mu\nu} q_\nu = 0 . \quad (5.14)$$

For an isotropic system $K_0^{\prime\alpha\beta} = K_0^{\prime 11} \delta_{\alpha\beta}$, and Eq. (5.14) can be rewritten as

$$\omega^2 K_0^{\prime 00} + \mathbf{q}^2 K_0^{\prime 11} - 2\omega q_\alpha K_0^{\prime 0\alpha} = 0 , \quad (5.15)$$

with $\alpha = 1, 2, 3$, and in the last term on the left-hand side of Eq. (5.15) a summation over repeated Greek indices is assumed. It might seem surprising that from an analysis which incorporates a complicated matrix linear response approach, the dispersion of

the AB mode ultimately involves only the amplitude renormalized four-current correlation functions, namely the density-density, current-current, and density-current correlation functions. This result is, nevertheless, a consequence of gauge invariance.

At zero temperature $K_0^{\prime 0\alpha}$ vanishes, and the sound-like AB mode has the usual linear dispersion $\omega = \omega_{\mathbf{q}} = c|\mathbf{q}|$ with the “sound velocity” given by

$$c^2 = K_0^{\prime 11} / K_0^{\prime 00} . \quad (5.16)$$

The equations in this section represent an important starting point for our numerical analysis.

5.2.3 General collective modes

We may interpret the AB mode as a special type of collective mode which is associated with $A_\nu = 0$ in Eqs. (5.6). This mode corresponds to free oscillations of $\Delta_{1,2}$ with a dispersion $\omega = cq$ given by the solution to the equation

$$\det|Q_{ij}| = \tilde{Q}_{11}\tilde{Q}_{22} - Q_{12}Q_{21} = 0 . \quad (5.17)$$

More generally, according to Eq. (5.5a) the collective modes of the order parameter induce density and current oscillations. In the same way as the pairing field couples to the mean-field order parameter in the particle-particle channel, the density operator $\hat{\rho}(Q)$ couples to the mean field $\delta\phi(Q) = V(Q)\delta\rho(Q)$, where $V(Q)$ is an effective particle-hole interaction that may derive from the pairing channel or, in a charged superconductor, from the Coulomb interaction. Here $\delta\rho = \langle\hat{\rho}\rangle - \rho_0$ is the expectation value of the charge density operator with respect to its uniform, equilibrium value ρ_0 . Within our self-consistent linear response theory the field $\delta\phi$ must be treated on an equal footing with $\Delta_{1,2}$ and formally can be incorporated into the linear response of the system by adding an extra term $K_0^{\mu 0}\delta\phi$ to the right hand side of Eq. (5.5a). The other two Eqs. (5.5) should be treated similarly. Note that, quite generally, the effect of the “external field” $\delta\phi$ amounts to replacing the scalar potential $A^0 = \phi$ by $\bar{A}^0 = \bar{\phi} = \phi + \delta\phi$. In this way one arrives at the following set of three

linear, homogeneous equations for the unknowns $\delta\phi$, Δ_1 , and Δ_2 :

$$0 = R^{10}\delta\phi + \tilde{Q}_{11}\Delta_1 + Q_{12}\Delta_2, \quad (5.18a)$$

$$0 = R^{20}\delta\phi + Q_{21}\Delta_1 + \tilde{Q}_{22}\Delta_2, \quad (5.18b)$$

$$\delta\rho = \frac{\delta\phi}{V} = K_0^{00}\delta\phi + R^{01}\Delta_1 + R^{02}\Delta_2. \quad (5.18c)$$

The dispersion of the collective modes of the system is given by the condition that the above Eqs. (5.18) have a nontrivial solution

$$\begin{vmatrix} Q_{11} + 2/|g| & Q_{12} & R^{10} \\ Q_{21} & Q_{22} + 2/|g| & R^{20} \\ R^{01} & R^{02} & K_0^{00} - 1/V \end{vmatrix} = 0. \quad (5.19)$$

In the case of particle-hole symmetry $Q_{12} = Q_{21} = R^{10} = R^{01} = 0$ and, the amplitude mode decouples from the phase and density modes; the latter two are, however, in general coupled.

5.3 EFFECT OF PAIR FLUCTUATIONS ON THE ELECTROMAGNETIC RESPONSE: SOME EXAMPLES

Once dressed Green's functions G enter into the calculational schemes, the collective mode polarizabilities (e.g., Q_{22}) and the EM response tensor $K_0^{\mu\nu}$ must necessarily include vertex corrections dictated by the form of the self-energy Σ , which depends on the T -matrix t , which, in turn depends on the form of the pair susceptibility χ . These vertex corrections are associated with gauge invariance and with the constraints that are summarized in Eqs. (5.13). It can be seen that these constraints are even more complicated than the Ward identities of the normal state. Indeed, it is relatively straightforward to introduce collective mode effects into the electromagnetic response in a completely general fashion that is required by gauge invariance. This issue was discussed in Sec. 5.2 as well as extensively in the literature [1, 41]. The difficulty is in the implementation. In this section we begin with a discussion of the $T = 0$ behavior where the incoherent pair excitation contributions to the self-energy corrections and vertex functions vanish. In this section, we shall keep the

symmetry factor $\varphi_{\mathbf{k}}$ explicitly.

5.3.1 $T = 0$ behavior of the AB mode and pair susceptibility

It is quite useful to first address the zero temperature results since there it is relatively simple to compare the associated polarizabilities of the AB mode with that of the pair susceptibility χ . In the presence of particle-hole symmetry this collective mode polarizability can be associated with Q_{22} , which was first defined in Eq. (5.5c). In the more general case (which applies away from the BCS limit) Q_{22} must be replaced by a combination of phase and amplitude terms so that it is given by $Q'_{22} = Q_{22} - Q_{12}Q_{21}/\tilde{Q}_{11}$.

We may readily evaluate these contributions in the ground state, where $\Delta_{sc} = \Delta$. The polarizability Q_{22} is given by

$$Q_{22}(Q) = - \sum_P [G(-P)G(P-Q) + G(P)G(Q-P) + F^\dagger(P)F^\dagger(P-Q) + F(P)F(P-Q)] \varphi_{\mathbf{p}-\mathbf{q}/2}^2, \quad (5.20)$$

where $G(P)$ and $F^\dagger(P) = F(P)$ are given by Eqs. (2.52) and (2.31), respectively, with $\Delta = \Delta_{sc}$ at $T = 0$.

Using Eq. (2.31) and changing variable $P_\pm = P \pm Q/2$, one obtains

$$\begin{aligned} Q_{22}(Q) &= - \sum_P \{ G(-P_-) [G(P_+) + \Delta_{P_+} \Delta_{P_-} G(-P_+) G_0(P_-) G_0(P_+)] \\ &\quad + G(-P_+) [G(P_-) + \Delta_{P_+} \Delta_{P_-} G(-P_-) G_0(P_+) G_0(P_-)] \} \varphi_P^2 \\ &\equiv -[A(Q) + A(-Q)], \end{aligned} \quad (5.21)$$

where in the first line, we have changed the sign of $P \rightarrow -P$. Using the Dyson's equation

$$G_0^{-1}(P) = G^{-1}(P) + \Sigma(P) = G^{-1}(P) - \Delta_P^2 G_0(-P), \quad (5.22)$$

$A(Q)$ can be written as

$$A(Q) = \sum_P G(-P_-) [G(P_+) + \Delta_{P_+} \Delta_{P_-} G(-P_+) G_0(P_-) G_0(P_+)] \varphi_P^2$$

$$= \chi(Q) + \sum_P F(P_-) [F(P_+) - \Delta_{P_-} G(P_+) G_0(-P_-)] \varphi_P^2. \quad (5.23)$$

The second term vanishes if and only if $Q = 0$. At finite Q , $A(Q) \neq \chi(Q)$. In addition, Q_{22} is a symmetrized $A(Q)$. As a consequence, the phase mode dispersion determined by $\tilde{Q}_{22} = 0$ is necessarily different from the pair excitation spectrum. And this difference is apparent even at the level of BCS theory.

It is important to stress that at $Q = 0$, however, we obtain $A(0) = \chi(0)$. and, moreover, $Q_{12}(0) = Q_{21}(0) = 0$ so that $Q'_{22}(0) = Q_{22}(0) = -2\chi(0)$. Therefore, we have

$$\frac{2}{|g|} + Q'_{22}(0) = \frac{2}{|g|} [1 + g\chi(0)] = 0. \quad (5.24)$$

In this way, the AB mode propagator is soft under the same conditions which yield a soft pair excitation propagator $t_{pg}(Q)$, and these conditions correspond to the gap equation Eq. (2.53) at $T = 0$. Moreover, it can be seen that $Q'_{22}(Q) = Q'_{22}(-Q)$ so that, upon expanding around $Q = 0$, one has $\tilde{Q}_{22}(Q) = -\alpha_{22}\Omega^2 + \beta_{22}q^2$, $Q_{12}(Q) = -Q_{21}(Q) = i\Omega\alpha_{12}$, and $2/|g| + Q_{11}(Q) = 2/|g| - \alpha_{11}$, where

$$\begin{aligned} \alpha_{22} &= \sum_{\mathbf{k}} \frac{\varphi_{\mathbf{k}}^2}{4E_{\mathbf{k}}^3}, \\ \beta_{22} &= \frac{1}{d} \sum_{\mathbf{k}} \frac{1}{4E_{\mathbf{k}}^3} \left[\varphi_{\mathbf{k}}^2 (\vec{\nabla} \epsilon_{\mathbf{k}})^2 - \frac{1}{4} (\vec{\nabla} \epsilon_{\mathbf{k}}^2) \cdot (\vec{\nabla} \varphi_{\mathbf{k}}^2) \right], \\ \alpha_{12} &= \sum_{\mathbf{k}} \frac{\epsilon_{\mathbf{k}}}{2E_{\mathbf{k}}^3} \varphi_{\mathbf{k}}^2, \\ \alpha_{11} &= \sum_{\mathbf{k}} \frac{\epsilon_{\mathbf{k}}^2}{E_{\mathbf{k}}^3} \varphi_{\mathbf{k}}^2, \end{aligned} \quad (5.25)$$

where d denotes the dimensionality of the system. Thus, one obtains

$$c^2 = \frac{\beta_{22}}{\alpha_{22} + \frac{\alpha_{12}^2}{2/|g| - \alpha_{11}}}. \quad (5.26)$$

At weak coupling in three dimensions, where one has approximately particle-hole symmetry, $\alpha_{12} = 0$, the amplitude and the phase modes decouple. This leads to the well-known

result $c = v_F/\sqrt{3}$. More generally, for arbitrary coupling strength g , these equations yield results equivalent to those in the literature [39, 40, 41, 42], as well as those derived from the formalism of Sec. 5.2.2. Finally, it should be noted that since both Eqs. (5.12) and (5.9) have the same poles, the condition $\tilde{Q}'_{22}(Q) = 0$ yields the same AB mode dispersion as that determined from Eq. (5.14). This is a consequence of gauge invariance.

5.3.2 AB mode at finite temperatures

We now turn to finite temperatures where there is essentially no prior work on the collective mode behavior in the crossover scenario. At the level of BCS theory (and in the Leggett ground state) the extended “Ward identities” of Eqs. (5.13) can be explicitly shown to be satisfied. Presumably they are also obeyed in the presence of impurities, as, for example, in the scheme of Ref. [43]. However, in general, it is difficult to go beyond these simple cases in computing all components of the matrix response function. Fortunately, the calculation of the AB mode is somewhat simpler. It reduces to a solution of Eq. (5.15), which, *in the presence of particle-hole symmetry*, involves a computation of only the electromagnetic response kernel: the density-density, density-current and current-current correlation functions.

It is the goal of this section to compute these three response functions within the “pairing (or G_0G) approximation” to the T matrix. The associated [28] diagrams are shown in Fig. 5.1. Because full Green’s functions G appear in place of G_0 (as indicated by the heavy lines) these diagrams are related to but different [28] from their counterparts studied by Aslamazov and Larkin and by Maki and Thompson. This diagram scheme forms the basis for calculations published by our group [49, 50] of the penetration depth within the BCS-BEC crossover scheme.

Here we make one additional assumption. We treat the amplitude renormalizations that appear in Eqs. (5.8) only approximately, since these contributions introduce a variety of additional correlation functions, which must be calculated in a consistent fashion, so as to satisfy Eqs. (5.13). Because the amplitude mode is gapped, at least at low T , we can approximate these amplitude renormalizations by their $T = 0$ counterparts, which are much simpler to deduce.

The three electromagnetic correlation functions reduce to a calculation of $P^{\mu\nu}$, which

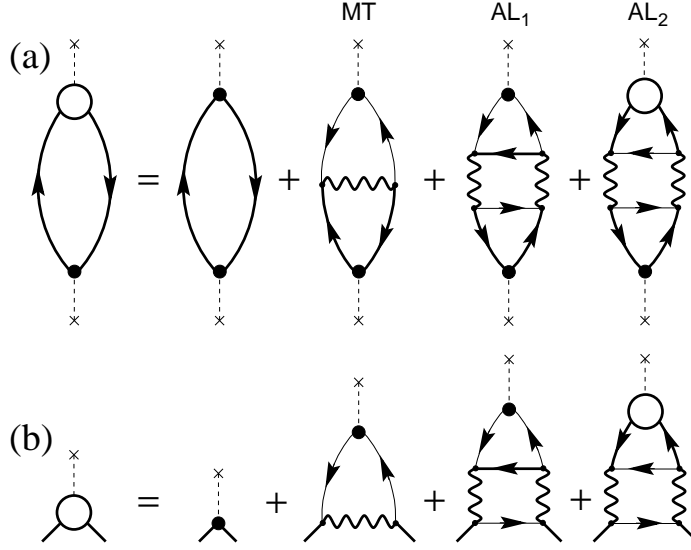


Figure 5.1: Diagrammatic representation of (a) the polarization bubble, and (b) the vertex function used to compute the electrodynamic response functions. Here the wavy lines represent the pair propagator t and it should be noted that the thin and thick lines correspond to G_0 and G respectively. The total vertex correction is given by the sum of the Maki Thompson (MT) and two Aslamazov-Larkin (AL_1 and AL_2) diagrams.

can be written as

$$P^{\mu\nu}(Q) = 2 \sum_K \lambda^\mu(K, K - Q) G(K) G(K - Q) \Lambda^\nu(K, K - Q), \quad (5.27)$$

where

$$\lambda(K, K - Q) = (1, \vec{\nabla}_{\mathbf{k} \in \mathbf{k} - \mathbf{q}/2})$$

and

$$\Lambda(K, K - Q) = \lambda(K, K - Q) + \delta\Lambda_{sc}(K, K - Q) + \delta\Lambda_{pg}(K, K - Q)$$

are the bare and full vertices, respectively. Note Eqs. (4.6) and (4.7) in Sec. 4.2 are just the spatial components of these two equations.

To evaluate the vertex function Λ^μ we decompose it into a pseudogap contribution Λ_{pg} and a superconducting contribution Λ_{sc} . (The latter can be regarded as the Gor'kov F function contribution, although we do not use that notation here). The pseudogap contribution comes from a sum of Maki-Thompson (MT) and Aslamazov-Larkin ($AL_{1,2}$) diagrams [see

Fig. 5.1(b)]. Since these vertex corrections can be obtained from a proper vertex insertion to the self-energy, it follows that there is a cancellation between these various terms that simplifies the algebra. This cancellation is shown in more detail in Appendix E. Following the analysis in Appendix E, the sum of both pg and sc contributions is given by

$$\begin{aligned} \delta\Lambda^\mu(K, K-Q) &\approx -(\Delta_{sc}^2 - \Delta_{pg}^2)\varphi_{\mathbf{k}}\varphi_{\mathbf{k}-\mathbf{q}}G_0(-K)G_0(Q-K)\lambda^\mu(Q-K, -K) \\ &\quad - \Delta_{pg}^2 G_0(-K) \frac{\partial\varphi_{\mathbf{k}-\mathbf{q}/2}^2}{\partial k_\mu}, \end{aligned} \quad (5.28)$$

where use has been made of the fact that $t_{pg}(Q)$ is highly peaked at $Q = 0$, and of the definition of Δ_{pg}^2 , Eq. (2.49).

The AB mode dispersion involves the sum of three terms that enter into Eqs. (5.14) and (5.15). We next substitute Eqs. (5.28) into Eq. (5.27). After performing the Matsubara frequency summation, and analytically continuing $i\Omega \rightarrow \Omega + i0^+$, we obtain for small Ω and \mathbf{q}

$$\begin{aligned} q_\mu K_0^{\mu\nu} q_\nu &= \mathbf{q} \cdot \left(\overset{\leftrightarrow}{\mathbf{n}} + \overset{\leftrightarrow}{\mathbf{P}} \right) \cdot \mathbf{q} - 2\Omega\mathbf{q} \cdot \mathbf{P}_0 + \Omega^2 P_{00} \\ &= \frac{2}{d} q^2 \sum_{\mathbf{k}} \frac{\Delta_{sc}^2}{E_{\mathbf{k}}^2} \left[\frac{1 - 2f(E_{\mathbf{k}})}{2E_{\mathbf{k}}} + f'(E_{\mathbf{k}}) \right] \left[\varphi_{\mathbf{k}}^2 (\vec{\nabla}\epsilon_{\mathbf{k}})^2 - \frac{1}{4} (\vec{\nabla}\epsilon_{\mathbf{k}}^2) \cdot (\vec{\nabla}\varphi_{\mathbf{k}}^2) \right] \\ &\quad - 2\Omega^2 \sum_{\mathbf{k}} \left\{ \frac{\Delta_{sc}^2 \varphi_{\mathbf{k}}^2}{E_{\mathbf{k}}^2} \left[\frac{1 - 2f(E_{\mathbf{k}})}{2E_{\mathbf{k}}} + f'(E_{\mathbf{k}}) \right] \right. \\ &\quad \left. - f'(E_{\mathbf{k}}) \frac{\Omega^2 - (\mathbf{q} \cdot \vec{\nabla}\epsilon_{\mathbf{k}})^2 - \Delta^2 (\mathbf{q} \cdot \vec{\nabla}\varphi_{\mathbf{k}})^2}{\Omega^2 - (\mathbf{q} \cdot \vec{\nabla}E_{\mathbf{k}})^2} \right] \\ &\quad \left. + \frac{\Delta_{pg}^2}{4E_{\mathbf{k}}^2} f'(E_{\mathbf{k}}) \frac{(\mathbf{q} \cdot \nabla\epsilon_{\mathbf{k}}^2)(\mathbf{q} \cdot \vec{\nabla}\varphi_{\mathbf{k}}^2) + \Delta^2 (\mathbf{q} \cdot \vec{\nabla}\varphi_{\mathbf{k}}^2)^2}{\Omega^2 - (\mathbf{q} \cdot \vec{\nabla}E_{\mathbf{k}})^2} \right\}. \end{aligned} \quad (5.29)$$

Because Eq. (5.29) is ill-behaved for long wavelengths and low frequencies, in order to calculate the AB mode velocity one needs to take the appropriate limit $\Omega = cq \rightarrow 0$. By contrast, the calculation of the London penetration depth first requires setting $\Omega = 0$ (static limit), and then $\mathbf{q} \rightarrow \mathbf{0}$. The superfluid density n_s can be calculated from the coefficient of the q^2 term in Eq. (5.29) [see, also Eq. (F.1) for $Q = 0$]. Finally, the AB mode ‘‘sound’’ velocity $c = \Omega/q$, in the absence of the amplitude renormalization, can be obtained by

solving $q_\mu K_0^{\mu\nu} q_\nu = 0$.

In the absence of the pseudogap (i.e., when $\Delta_{sc} = \Delta$) the last term inside $\{\dots\}$ in Eq. (5.29) drops out, and the resulting analytical expression reduces to the standard BCS result [51], which at $T = 0$ has the relatively simple form

$$q_\mu K_0^{\mu\nu} q_\nu = \frac{q^2}{d} \sum_{\mathbf{k}} \frac{\Delta_{sc}^2}{E_{\mathbf{k}}^3} \left[\varphi_{\mathbf{k}}^2 (\vec{\nabla} \epsilon_{\mathbf{k}})^2 - \frac{1}{4} (\vec{\nabla} \epsilon_{\mathbf{k}}^2) \cdot (\vec{\nabla} \varphi_{\mathbf{k}}^2) \right] - \Omega^2 \sum_{\mathbf{k}} \frac{\Delta_{sc}^2 \varphi_{\mathbf{k}}^2}{E_{\mathbf{k}}^3}. \quad (5.30)$$

At finite T , the AB mode becomes damped, and the real and imaginary parts of the sound velocity have to be calculated numerically. Although, the algebra is somewhat complicated, it can be shown that the AB mode satisfies $c \rightarrow 0$ as $T \rightarrow T_c$, as expected.

To include the amplitude renormalization, using Eq. (5.8b), we can write

$$\begin{aligned} q_\mu K_0^{\prime\mu\nu} q_\nu &= q_\mu K_0^{\mu\nu} q_\nu - \frac{q_\mu R^{\mu 1} R^{1\nu} q_\nu}{\tilde{Q}_{11}} \\ &\approx q_\mu K_0^{\mu\nu} q_\nu - \Omega^2 \frac{R^{01} R^{10}}{\tilde{Q}_{11}}, \end{aligned} \quad (5.31)$$

where in the second line, we have used the $T = 0$ approximation for the second term, so that $R^{i1}(0) = 0 = R^{1i}(0)$ for $i = 1, 2, 3$, $\tilde{Q}_{11}(0) = 2/|g| - \alpha_{11}$, and

$$R^{10}(0) = R^{01}(0) = -\Delta_{sc} \sum_{\mathbf{k}} \frac{\epsilon_{\mathbf{k}}}{E_{\mathbf{k}}^3} \varphi_{\mathbf{k}}^2. \quad (5.32)$$

This greatly simplifies the numerical calculations.

It should be noted that the temperature dependence of the amplitude contribution is always suppressed by the Fermi function $f(E_{\mathbf{k}})$. This amplitude renormalization is negligible at weak coupling strengths, where the T dependence may be strong near T_c due to the small size of the gap. On the other hand, when the coupling strength increases, and thus amplitude effects become more important, the excitation gap becomes large for all $T \leq T_c$. This follows as a result of pseudogap effects. Hence, the amplitude contribution is rather insensitive to T . Therefore, it is reasonable, in both the strong and weak coupling cases, to neglect the T dependence of the amplitude contribution in the numerical analysis.

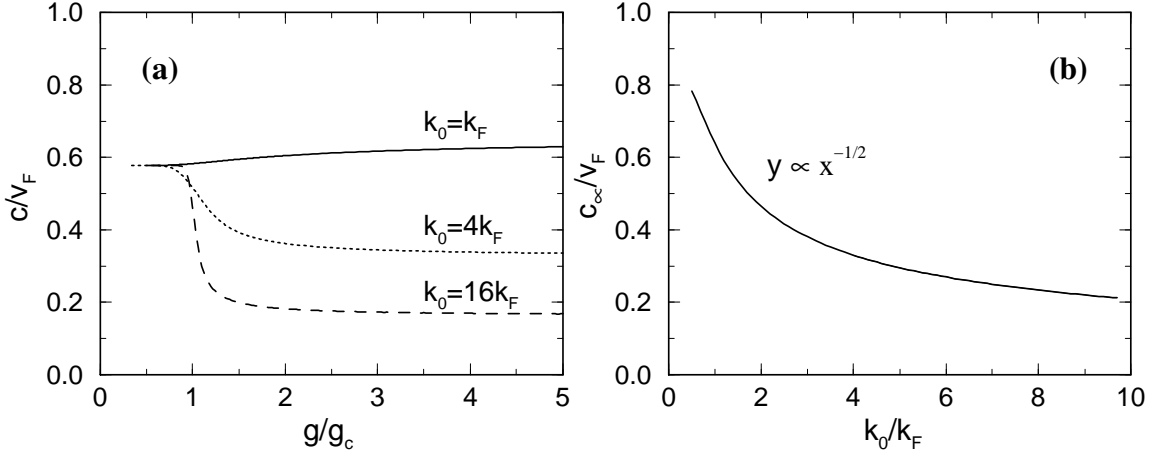


Figure 5.2: (a) AB mode velocity c/v_F as a function of the coupling strength for various densities characterized by k_0/k_F in 3D jellium, as well as (b) the large g asymptote c_∞/v_F , versus k_0/k_F , which varies as $(k_F/k_0)^{1/2}$, as expected.

5.4 NUMERICAL RESULTS: ZERO AND FINITE TEMPERATURES

In this section we summarize numerical results obtained for the AB mode velocity c associated with the electromagnetic response kernel, as obtained by solving Eqs. (5.14) and (5.15). We also briefly discuss the behavior for the $T = 0$ phase mode velocity v_ϕ that results from the coupling to density fluctuations, as well [see Eq. (5.19)]. The former, which has physical implications for the behavior of the dielectric constant [47, 44], is the more straightforward to compute, because it does not require any new approximations associated with the effective interactions V in the particle-hole channel. The analysis of this section provides information about the nature of the strong coupling limit, which from the perspective of the gap equations appears as a “quasi-ideal” Bose gas. Here we study this limit via plots of the infinite g asymptote of the AB mode, called c_∞ and show that in the collective modes there are pair-pair interactions present (which result from the fact that the collective modes introduce higher order Green’s functions than does the T matrix of the gap equations). This analysis also helps to clarify how pair fluctuations contribute, at finite temperatures, to the collective mode dispersion. Our $T = 0$ calculations are based on the Leggett ground state which corresponds to that of the pairing approximation as well. At finite T , we numerically evaluate the AB sound dispersion from Eq. (5.29), obtained within the framework of the pairing approximation.

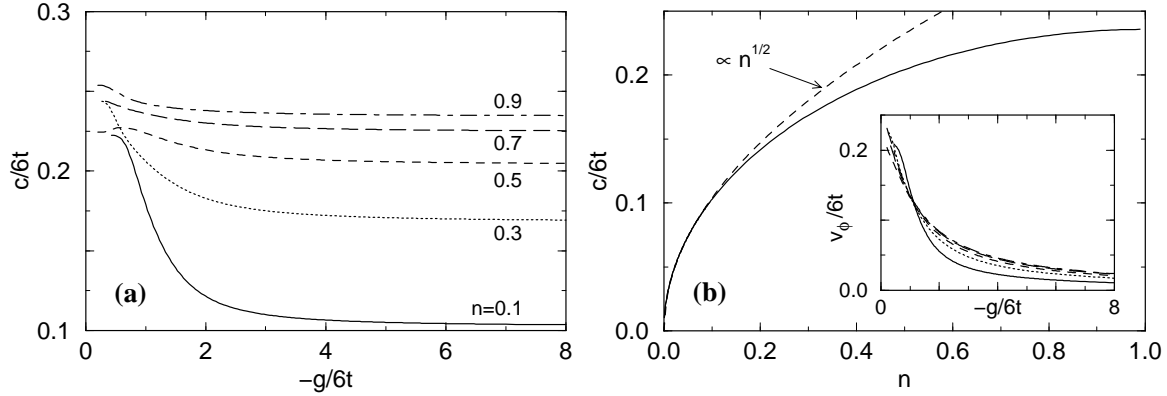


Figure 5.3: (a) Normalized AB mode velocity, $c/6ta$, on a 3D lattice with an s -wave pairing interaction for various densities as a function of g , and (b) the large g limit for $c/6ta$ as a function of density n for fixed $-g/6t = 20$. (Here $6t$ is the half bandwidth). The dashed line in (b) shows a fit to the expected low density dependence $n^{1/2}$. Plotted in the inset is the velocity of the phase and density coupled collective mode $v_{\phi}/6ta$ with the particle-hole channel treated at the RPA level, for the same n as in (a).

In Fig. 5.2(a) we plot the zero-temperature value of c as a function of the coupling strength g/g_c in a 3D jellium model with s -wave pairing at three different electron densities, which are parameterized via k_0/k_F . The most interesting feature of these and related curves is shown in Fig. 5.2(b) where we plot the asymptotic limit as a function of density or, equivalently, k_0 . This numerically obtained asymptote reflects the *effective* residual boson-boson interactions in the strong coupling limit of the collective modes. This asymptote is close to the value calculated in Ref. [42] whose functional dependence is given by $c_{\infty}/v_F \propto \sqrt{k_F/k_0}$ or, equivalently, $c_{\infty} \propto \sqrt{n/k_0}$. Interpreting the physics as if the system were a true interacting Bose system, one would obtain the effective interaction $U(0) \approx 3\pi^2/mk_0$, *independent of g in the strong coupling limit*. As expected, these inter-boson interactions come exclusively from the underlying fermion character of the system, and can be associated with the repulsion between the fermions due to the Pauli principle. All of this is seen most directly [23, 52, 53] by noting that the behavior displayed in the inset can be interpreted in terms of the effective scattering length of the bosons a_B , which is found to be twice that of the fermions a_F in the strong coupling limit. Effects associated with the coupling constant g are, thus, entirely incorporated into making bosons out of a fermion pair, and are otherwise invisible.

The same calculations are repeated in Fig. 5.3 for a 3D tight binding lattice band struc-

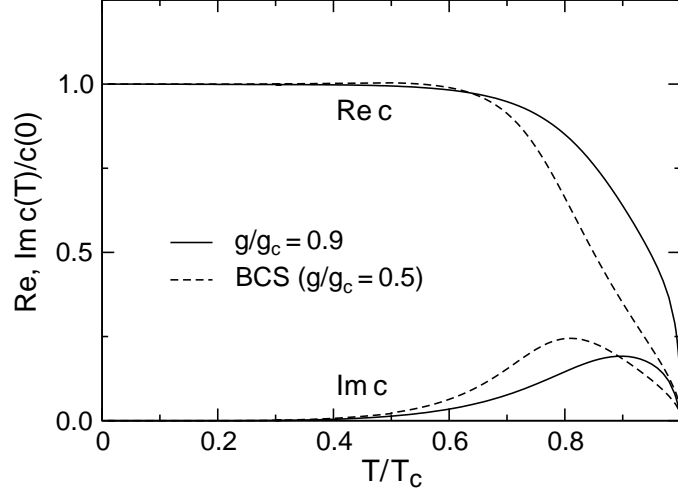


Figure 5.4: Temperature dependence of the real ($\text{Re } c$) and imaginary ($\text{Im } c$) parts of the AB mode velocity for moderate coupling (solid lines) and weak coupling BCS (dashed lines) in 3D jellium with $k_0 = 4k_F$. The mode is highly damped as T_c is approached.

ture with $\varphi_{\mathbf{k}} = 1$ at $T = 0$. Figure 5.3(a) plots the sound velocity for different densities n , as a function of the coupling constant; the behavior of the large g limit is shown in Fig. 5.3(b) as a function of density for a fixed g . Near half filling, where there is particle-hole symmetry, the amplitude contributions are irrelevant and the large g limit for c , from Eq. (5.30), is $c = \sqrt{2}t$, where t is the hopping integral. At low n the AB velocity varies as \sqrt{n} , which is consistent with the results shown above for jellium. In both cases the behavior again reflects the underlying fermionic character, since it is to be associated with a Pauli principle induced repulsion between bosons. Unlike in the jellium case, where c approaches a finite asymptote as g increases, here c vanishes asymptotically due to the increase of the pair mass associated with lattice effects [16, 50]. For completeness, we also show, as an inset in Fig. 5.3(b), the behavior of v_ϕ , where we have used the RPA approximation to characterize the parameter V in the particle-hole channel. This approximation is in the spirit of previous work by Belkhir and Randeria [39], although it cannot be readily motivated at sufficiently large g .

Finally, in Fig. 5.4 we plot the temperature dependence of the AB mode velocity (both real and imaginary parts), for moderately strong coupling (solid lines) and the BCS limit (dashed lines). This figure suggests that the AB mode velocity reflects the same transition temperature T_c as is computed via the excited pair propagator or T -matrix. This represents

an important self-consistency check on the present formalism.

5.5 SOME ADDITIONAL REMARKS

5.5.1 Pair excitations vs phase fluctuations

As a result of the distinction between *incoherent* pair excitations and the *coherent* phase mode of the order parameter, our theory is different from the phase fluctuation scenario proposed by Emery and Kivelson [8]. In our theory, we deal with a homogeneous system, in which the order parameter vanishes identically above T_c , and there is no macroscopic occupation of the zero momentum pair states. In contrast, in the phase fluctuation scenario, the system is inhomogeneous, consisting of microscopic “superconducting” regions, e.g., stripes or superconducting grains. In each of these regions, there is a local (fluctuating) order parameter, and the zero momentum pair state is macroscopically occupied. Above T_c , there is no phase coherence between these locally condensed regions so that the spatial, as well as temporal, average of the local order parameter (which defines the order parameter at a macroscopic level) vanishes.

The pseudogap in both scenarios is associated with the difference between the excitation gap and the superconducting order parameter. In the present scenario it is a consequence of incoherent pair excitations. In the scenario of Emery and Kivelson, this difference is caused by phase fluctuations. One can also arrive at a picture (for the T -dependence of the excitation gap and of the order parameter) that is similar to Fig. 4.1 within the phase fluctuation scenario [8]. What is different here is the “tuning parameter,” which corresponds to the coupling strength g in the crossover picture, and the phase stiffness parameter n_s/m in the phase fluctuation picture.

5.5.2 Strong coupling limit: Composite vs true bosons

In the strong coupling limit at low density with s -wave pairing, our interpretation of the gap equations leads to the observation that the system forms essentially an ideal Bose system of tightly bound, non-overlapping pairs. This quasi-ideal Bose gas behavior is a consequence of the mean field nature of the ground state wavefunction. Nevertheless, from the perspective of the collective modes (which involve effectively higher order Green’s functions), the

pairs still have some residual interactions between each other, owing to the Pauli exclusion between the constituent fermions. The bosons are composite objects, which are different from true point-like bosons; for example, they can exchange their constituents through a scattering process. Our understanding of composite bosons is still incomplete although many people have tried to think of this system as a true Bose liquid. However, *some important distinctions between this composite boson system and a true Bose liquid have to be noted.*

A first important distinction can be found, between the composite bosons of the present theory and “true” bosons, at the level of the Leggett ground state. From previous work on the BCS-BEC crossover at $T = 0$ in the strong coupling limit, it can be seen that this ground state contains a mix of quasi-ideal and interacting Bose gas character. The gap equation is associated [14] with “noninteracting diatomic molecules,” whereas, the collective mode spectrum [39, 40, 41] reflects an effective boson-boson interaction deriving from the Pauli statistics of the constituent fermions. This is seen most clearly in jellium models where the Anderson-Bogoliubov sound velocity remains finite at infinite g , with an asymptote associated with these residual interactions [23, 22].

A second important difference between true and the composite bosons discussed here arises from the fact that this superconducting ground state corresponds to one in which there is *full condensation* so that, as in the BCS phase, the condensate fraction $n_0 = n$. By contrast, in a Bose superfluid there is always a depletion of the condensate at $T = 0$, caused by the existence of an inter-boson repulsion.

As a final important difference, we note that the behavior of the pair propagator $t(Q)$, which must necessarily be consistent with the $T = 0$ gap and number equations [14], is highly circumscribed and rather different from what one might deduce based on the standard model for a Bose liquid [30]. The fermionic degrees of freedom can never be fully “integrated out”. The fermionic excitation gap Δ and the pair chemical potential $\mu_{pair} = 0$ are, moreover, closely inter-related via, e.g., the gap equation (2.53). These effects have no natural counterpart in the Bose liquid (where the fermionic excitation gap is of no consequence).

It should finally be noted that we did not consider the Coulomb interaction in the treat-

ment of the gap-equation-associated T matrix. Coulomb interactions do, however, affect the collective modes. Indeed, within the BCS formalism (as well as in the Leggett ground state) long range Coulomb interactions do not enter in an important way to change the gap equation structure. If things were otherwise, this would compromise the self-consistent conditions on Δ and μ in the ground state. Coulomb effects are presumed to be already included in the pairing interaction. Indeed, at large g , we have seen that essentially all signs of the two-body (g dependent) fermion-fermion interaction are absent in the effective boson-boson interaction, which is deduced from the sound mode velocity. One might anticipate how Coulomb effects will enter the physics. For real superconductors, the electron pairs overlap with each other, and feel the Coulomb interaction predominantly as two nearly independent constituent fermions, rather than as a rigid point boson. In this way, the Coulomb interaction is expected to affect the pair dispersion only indirectly and rather weakly through the single fermion dispersion.

CHAPTER 6

APPLICATION TO THE CUPRATES

In previous chapters, we have addressed, quite generally, the superconducting instability of the normal state as well as pseudogap phenomena for $T \leq T_c$. In this process, we studied the effects of low dimensionality, lattice band structure, and pairing symmetry. In addition, we computed measurable properties below T_c such as the superfluid density and specific heat. In this context, we have deduced that there are important incoherent, finite momentum pair excitations and have seen that they lead to new low temperature powers in n_s and C_v . These power laws are in addition to the usual contributions arising from the fermionic quasiparticles. This series of studies shows how to extend BCS theory (using the crossover ground state wave function Ψ_0) from weak coupling (where only fermionic quasiparticles are relevant) to moderate coupling (where both fermionic and bosonic excitations coexist), and finally, to strong coupling (where the excitations are purely bosonic). Our work represents the first contribution along these lines to address non-zero temperatures below T_c .

In this Chapter, we will apply these results to the cuprates, and compare our theoretical predictions with experimental measurements. We begin by computing a cuprate phase diagram. Next we study the superfluid density and make predictions for the quasi-universal behavior of n_s and the c -axis Josephson critical current, as a function of temperature. We follow with a study of the low temperature specific heat, and discuss the experimental evidence for new low T power laws which we predict, in both n_s and C_v .

6.1 CUPRATE PHASE DIAGRAM

There is a general consensus [54] that the cuprate superconductors are quasi-2D systems with short coherence lengths ξ , having a $d_{x^2-y^2}$ order parameter symmetry. While the overdoped materials appear to exhibit Fermi liquid properties, the cuprates become Mott insulators at half filling, owing to the strong on-site Coulomb repulsion. Both the Mott

insulating state and the generally smooth crossover to Fermi liquid behavior have to be accommodated in any complete theory of the cuprate phase diagram.

To address the cuprates, we assume a tight-binding, anisotropic band structure given by Eq. (3.2), and use the same $\varphi_{\mathbf{k}}$ given by Eq. (3.3) in all our calculations.¹ In what follows it should be noted that the coupling strength g enters in dimensionless form via g/t_{\parallel} , so that one might expect the characteristic dimensionless coupling strength to increase as the Mott insulator is approached, since the latter is associated with a decrease in electronic energy scales, such as t_{\parallel} . In order to generate physically realistic values for the various energy scales, we make two assumptions: (1) We take g as doping-independent (which is not unreasonable in the absence of any more detailed information about the pairing mechanism) and (2) incorporate the effect of the Mott transition at half filling, by introducing a doping concentration (x) dependence into the in-plane hopping matrix elements t_{\parallel} , as would be expected in the limit of strong on-site Coulomb interactions in a Hubbard model [4]. Thus the hopping matrix element is renormalized as $t_{\parallel}(x) \approx t_0(1 - n) = t_0x$, where t_0 is the matrix element in the absence of Coulomb effects. This x dependent energy scale is consistent with the requirement that the plasma frequency vanish at $x = 0$.

These assumptions now leave us with essentially one free parameter $-g/4t_0$. We choose this parameter based on studies in Appendix B, where we located the cuprates on an $n - g$ phase diagram, and showed in Fig. B.3 that $0.1 < -g/4t_{\parallel}(x) < 2$. Therefore, there is not much freedom in adjusting this parameter. We take $-g/4t_0 = 0.047$ to optimize the overall fit of the phase diagram to experiment. We take $t_{\perp}/t_{\parallel} \approx 0.003$,² and $t_0 \approx 0.6$ eV, which is reasonably consistent with experimentally based estimates [55]. It is worth pointing out that the pseudogap crossover temperature T^* and the zero temperature excitation gap $\Delta(0)$ are independent of the choice of t_{\perp}/t_{\parallel} , as long as $t_{\perp}/t_{\parallel} \ll 1$. T_c depends on t_{\perp}/t_{\parallel} only logarithmically.

Now we solve the set of equations (2.53), (2.54), and (2.57) for T_c and $\Delta_{pg}(T_c)$ as a function of doping x . We also determine the $T = 0$ values for $\Delta(0)$ as a function

¹It should be noted that experimentalists tend to normalize $\varphi_{\mathbf{k}}$ at the $(\pi, 0)$ points in the Brillouin zone, i.e., $\varphi_{\mathbf{k}} = \frac{1}{2}(\cos k_x - \cos k_y)$. so that when (and only when) the gap values are *involved explicitly in comparison with experiment* in a given plot, we will multiply the gaps by a factor of 2. Particularly, we will use Δ_0 to denote the gap magnitude at $(\pi, 0)$.

²We did not fine-tune the ratio t_{\perp}/t_{\parallel} since only T_c depends slightly on its value (see Sec. 3.3), which is presumably also doping dependent.

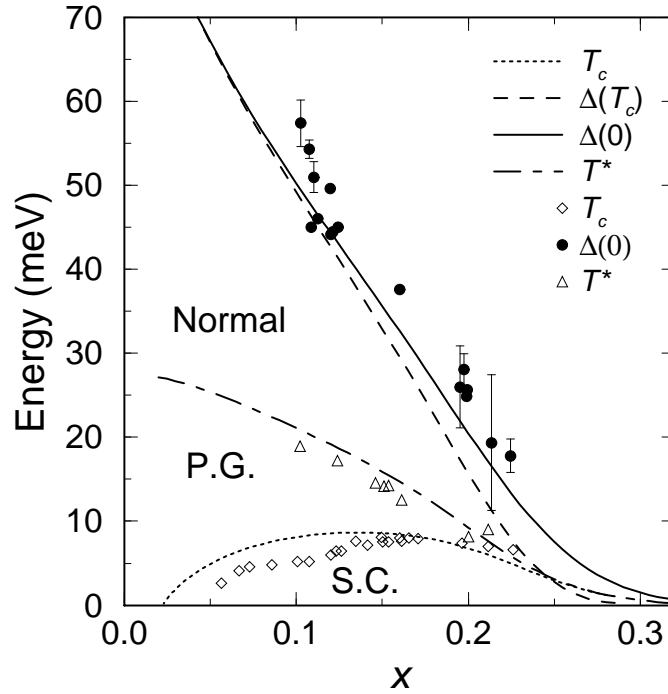


Figure 6.1: Cuprate phase diagram showing $\Delta(0)$, T_c , $\Delta_{pg}(T_c)$, and T^* , calculated for $-g/4t_0 = 0.047$, and $t_{\perp}/t_{\parallel} = 0.003$. Shown as symbols are experimental data, taken from: (●) Miyakawa *et al.* [56]; (◇) Rossat-Mignod *et al.* [57]; (△) Oda *et al.* [58]. The normal, pseudogap, and superconducting phases are labeled with “Normal”, “P.G.”, and “S.C.”, respectively.

of x (which derive from the first two equations only). It should be stressed that there is essentially an inverse relationship between the x -dependence of T_c and that of $\Delta(0)$ in the underdoped regime. This can be seen already in the studies of Chapter 3, where at strong coupling, but still in the fermionic regime, T_c was suppressed as a result of the growth of the pseudogap. This comes, in turn, from the fact that, crudely speaking, there are fewer fermions available to form Cooper pairs, as the pseudogap grows in strength.

As a zeroth order approximation, T^* is roughly given by the mean-field solution for T_c . The results for these quantities are plotted in Fig. 6.1. The relative size of $\Delta_{pg}(T_c)$, compared to $\Delta(0)$, increases with decreasing x . In the highly overdoped limit this ratio approaches zero, and the BCS limit is recovered. While $T^* = T_c$ in the BCS regime, it becomes much larger than T_c in the underdoped regime. A pseudogap phase exists between T_c and T^* , as observed experimentally. Evidently, the calculated curves are in good agreement with experimental data taken from the literature, shown as symbols. This phase diagram sets the energy scales for use in subsequent calculations as a function of doping

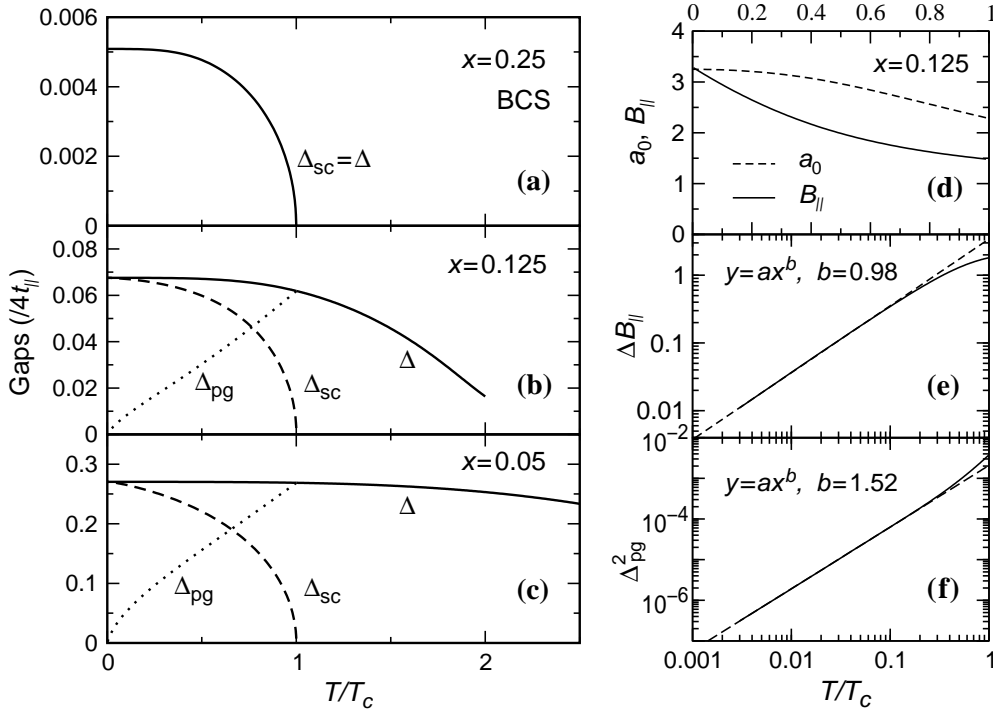


Figure 6.2: Temperature dependence of various gaps for (a) highly overdoped, (b) underdoped, and (c) highly underdoped samples. The coupling and bandwidth are taken from the theoretical phase diagram, Fig. 6.1. The gap above T_c is calculated via an extrapolation scheme given in Appendix C. Also plotted are the temperature dependence of (d) the T matrix expansion coefficients a_0 and $B_{\parallel} = 1/8t_{\parallel}M_{\parallel}^*$, (e) leading order correction of B_{\parallel} , and (f) Δ_{pg}^2 on a log-log scale, for $x = 0.125$.

concentration.

Note that, in principle, the anisotropy ratio t_{\perp}/t_{\parallel} should be x dependent; experiment reveals that it is much smaller in the underdoped regime than in the overdoped regime. If this is taken into account, T_c will be further suppressed in the underdoped regime, giving better agreement for T_c between theory and experiment. However, we choose a doping independent t_{\perp}/t_{\parallel} , to keep the physics simpler.

Next we use the different doping concentration dependent energy scales from this phase diagram, to plot the temperature dependence of the pseudogap Δ_{pg} , the order parameter Δ_{sc} , and the total excitation gap Δ below T_c . Shown in Fig. 6.2 are the gaps for (a) $x = 0.25$, (b) $x = 0.125$, and (c) $x = 0.05$, corresponding to highly overdoped (BCS), underdoped, and highly underdoped samples, respectively. We also show the gap *above* T_c , which is calculated based on an extrapolation scheme given in Appendix C. In agreement with experiment, as x decreases, the pseudogap develops, and, thus, Δ_{sc} and Δ separate.

In this way, the system evolves from a BCS-like to a strong pseudogap phase. Meanwhile, the ratio $\Delta(T_c)/\Delta(0)$ varies from 0 to 1. The gap Δ in (c) is essentially T independent up to a very high temperature. This can also be seen from Fig. 6.1. It should be noted that this behavior is expected as one approaches the BEC regime. See Fig. 1.4, where this was anticipated. In comparison with Fig. 4.1, we see here the decreasing doping level plays the role of an increased coupling strength g , via a shrinking band width. We also show for $x = 0.125$ the T matrix expansion coefficients a_0 and B_{\parallel} in Fig. 6.2(d). Both are roughly a constant at low T . In comparison with the s -wave case, the mass M_{\parallel}^* has a stronger T dependence. The leading order corrections are quadratic for a_0 (as in s -wave) and linear in T for B_{\parallel} . The correction ΔB_{\parallel} is plotted in Fig. 6.2(e). Despite the quasi-two dimensionality and this slightly stronger T dependence of the pair mass, Δ_{pg}^2 follows a $T^{3/2}$ law, as shown in Fig. 6.2(f). Just as in the s -wave case shown in Fig. 4.1, Δ_{pg} vanishes at $T = 0$, owing to the pseudogap equation (2.57).³

6.2 IN-PLANE PENETRATION DEPTH AND c -AXIS JOSEPHSON CRITICAL CURRENT

6.2.1 Quasi-universal behavior of normalized superfluid density vs T/T_c

Once we have obtained the phase diagram, it is straightforward to calculate the temperature dependence of the penetration depth as a function of doping concentration. As discussed in Sec. 4.2, the pseudogap contribution to the superfluid density introduces a new $T^{3/2}$ power law which may appear as quasi-linear. We now rewrite Eq. (4.17) in a slightly different form:

$$\frac{\lambda_L^2(0)}{\lambda_L^2(T)} = 1 - [A + B(T)] \frac{T}{T_c}, \quad (6.1)$$

where $B(T) = B' \sqrt{T/T_c}$ depends on T very weakly.

The normalized in-plane superfluid density, calculated from Eq. (4.14), is plotted in Fig. 6.3(a) as a function of T/T_c for several representative values of x , ranging from the

³It should, however, be noted that this result is applicable only to situations where T_c is finite. It does not apply for $x < x_c \approx 0.025$, where there is no superconducting phase transition at any finite T . In this low x regime, the system is always in the normal state, and Eq. (2.53) cannot be satisfied; nevertheless, Eq. (2.57), which parameterizes the normal state self-energy [24, 25], implies that there are pairing fluctuation effects associated with finite Δ_{pg} down to $T = 0^+$.

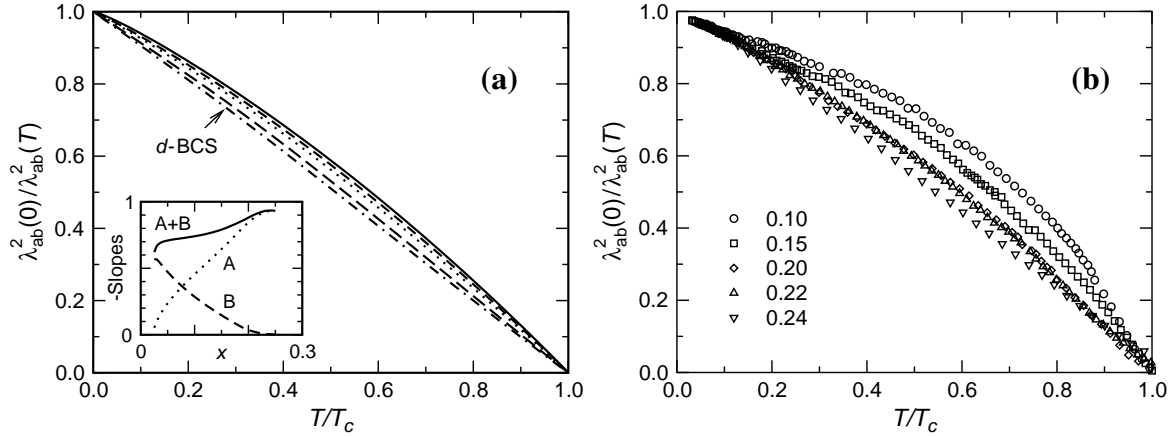


Figure 6.3: (a) Theoretical prediction and (b) experimental measurement of the temperature dependence of the ab-plane inverse squared penetration depth. In (a), from bottom to top are plotted for $x = 0.25$ (BCS limit, dot-dashed line), 0.2 (long-dashed), 0.155 (dotted), 0.125 (dashed) and 0.05 (solid line). Shown in the inset are (A) the slope given by the low temperature expansion assuming a constant $\Delta_{sc}(T) = \Delta(0)$, (B) the ratio $\frac{\Delta_{pg}^2(T)}{\Delta^2(0)} \frac{T}{T_c}$ at $T/T_c = 0.2$, and (A+B) the sum of two contributions. Experimental data on LSCO shown in (b) are taken from Ref. [59].

highly over- to highly underdoped regimes. These plots clearly indicate a “quasi-universal” behavior with respect to x : $\lambda_L^2(0)/\lambda_L^2(T)$ vs. T/T_c depends only slightly on x . Moreover, the shape of these curves follows closely that of the weak-coupling BCS theory. The, albeit, small variation with x is systematic, with the lowest value of x corresponding to the top curve.

This quasi-universal behavior has been confirmed experimentally, as have the systematic deviations with x . Early in 1996, Hardy and coworkers [60] reported this universality of the normalized a -axis inverse square of the in-plane penetration depth,⁴ $\lambda_a^2(0)/\lambda_a^2(T)$, as a function of T/T_c from underdoped ($T_c = 59$ K) to slightly overdoped ($T_c = 89$ K) samples in $\text{YBa}_2\text{Cu}_3\text{O}_{7-\delta}$ (YBCO) single crystals.⁵ Recently, Panagopoulos *et al* [59] observed this quasi-universal behavior of the in-plane penetration depth in $\text{La}_{2-x}\text{Sr}_x\text{CuO}_4$ (LSCO) polycrystalline samples with a small, but systematic x dependence of the slope. Their result, as shown in Fig. 6.3(b), are in good agreement with our predictions.⁶

⁴For the a -axis penetration depth, there are no chain effects, in YBCO

⁵Further evidence comes from the measurements of the ab-plane penetration depth on YBCO by the Cambridge group [61]. These authors did not distinguish the a - and b axes.

⁶While Hardy *et al.* had the most accurate measurement of $\Delta\lambda$ on the best quality YBCO single crystals, they had to take the values for $\lambda(0)$ from the literature to calculate the superfluid density. It is believed [62] that the values they used in Ref. [60] may be too large for their high purity samples. In addition,

This universal behavior appears surprising at first sight [6, 63] because of the strong x dependence in the ratio $T_c/\Delta(0)$. To understand the origin of this effect, we plot the fermionic quasiparticle (A) and bosonic pair excitation (B) contributions to the slope, as well as the total slope ($A + B$), in the inset of Fig. 6.3(a). Here A is given by expansion at the gap nodes:

$$\begin{aligned} A &= \frac{2 \ln 2}{\pi} \frac{v_F}{v_2} \frac{T_c}{(n/m)} = \frac{2 \ln 2}{\pi} \frac{T_c}{\Delta_0} \frac{4t_{\parallel}}{(n/m)}, \\ &= \frac{8 \ln 2}{\pi} \frac{\mu_0 e^2}{d\hbar^2} t_{\parallel} \lambda_{ab}^2(0) \frac{k_B T_c}{\Delta_0}, \end{aligned} \quad (6.2)$$

where we have included e , μ_0 , k_B , and the mean inter-plane distance d explicitly in the second line for later use. Here Δ_0 is the gap magnitude at the $(\pi, 0)$ points in the momentum space, i.e., twice $\Delta(0)$ in our convention. v_F is the Fermi velocity at the nodes, v_2 is the velocity along the tangential direction, $v_2 = \frac{\partial \Delta_{\mathbf{k}}}{\partial k_2}$, where $k_2 = \frac{\delta k_x - \delta k_y}{\sqrt{2}}$. We use a tight binding band structure and for the d -wave $\varphi_{\mathbf{k}}$ we take, $\frac{v_F}{v_2} = \frac{4t_{\parallel}}{\Delta_0}$. As shown in the figure, A decreases with decreasing x , since T_c/Δ_0 decreases. $B(T)$ is calculated at $T = 0.2T_c$, since it vanishes strictly at $T = 0$. The figure shows that B increases as A decreases; the pair excitation contributions become progressively more important towards the underdoped regime. This increase of B compensates the decrease of A , so that the total slope $A + B$ is relatively doping independent. This compensation effect explains the quasi-universality. The destruction of the superconducting state comes dominantly from pair excitations at small x , and quasiparticles at large x . Without the bosonic pair excitations, one would expect that the slope becomes smaller and smaller with underdoping.

Lee and Wen [6] proposed an alternative explanation for a strictly universal behavior of the superfluid density in the *underdoped* regime, based on a spin-charge separation picture, in which the charge carrier density is given by x , instead of $n = 1 - x$. Their explanation relies on the assumption that Δ_0 is doping independent (which does not appear to be confirmed experimentally, as can be seen from the phase diagram plots of Fig. 6.1). In this way

since $\lambda(0)$ was unknown in a fully oxygenated (slightly overdoped) YBCO sample, they used the value for an optimally doped sample instead. As a consequence, the curvature of the superfluid density curves were higher than expected. In contrast, Panagopoulos and coworkers measured $\lambda(0)$ directly for different doping concentrations. Therefore, the slope of the various curves, as well as doping dependence, in Fig. 6.3(b) may be more reliable.

they derive the Uemura scaling [11] result $T_c \propto x$. According to their explanation, $\lambda_{ab}^{-2}(T)$ as a function of T should have the same universality as $\lambda_{ab}^2(0)/\lambda_{ab}^2(T)$ does as function of T/T_c , since both $\lambda_{ab}^{-2}(0)$ and T_c are proportional to x . Their result does not seem to be appropriate, in particular, it does not apply in the overdoped regime. As will be seen in Sec. 6.2.4, $\lambda_{ab}^{-2}(T)$ as a function of T appears to have a much stronger doping dependence than they presume.

6.2.2 Quasi-universal behavior of c -axis Josephson critical current

Similar quasi-universal behavior can also be found in the c -axis Josephson critical current, which also depends explicitly on the order parameter as an overall multiplicative factor. Following Mahan [64], we obtain the general expression for the Josephson critical current

$$I_c = 2e \sum_{\mathbf{k}\mathbf{p}} |T_{\mathbf{k}\mathbf{p}}|^2 \frac{\Delta_{sc,\mathbf{k}}\Delta_{sc,\mathbf{p}}}{E_{\mathbf{k}}E_{\mathbf{p}}} \left[\frac{1 - f(E_{\mathbf{k}}) - f(E_{\mathbf{p}})}{E_{\mathbf{k}} + E_{\mathbf{p}}} + \frac{f(E_{\mathbf{k}}) - f(E_{\mathbf{p}})}{E_{\mathbf{k}} - E_{\mathbf{p}}} \right]. \quad (6.3)$$

For c -axis Josephson tunneling, the tunneling matrix can presumably be written as

$$|T_{\mathbf{k}\mathbf{p}}|^2 = |T_0|^2 \delta_{\mathbf{k}_{\parallel}\mathbf{p}_{\parallel}} + |T_1|^2, \quad (6.4)$$

where only the first (coherent) term, which conserves the in-plane momentum, contributes for a d -wave superconductor. As a consequence, we finally obtain for the cuprates

$$\begin{aligned} I_c &= 2e |T_0|^2 \Delta_{sc}^2 \sum_{\mathbf{k}\mathbf{p}} \delta_{\mathbf{k}_{\parallel}\mathbf{p}_{\parallel}} \frac{\varphi_{\mathbf{k}}\varphi_{\mathbf{p}}}{E_{\mathbf{k}}E_{\mathbf{p}}} \left[\frac{1 - f(E_{\mathbf{k}}) - f(E_{\mathbf{p}})}{E_{\mathbf{k}} + E_{\mathbf{p}}} + \frac{f(E_{\mathbf{k}}) - f(E_{\mathbf{p}})}{E_{\mathbf{k}} - E_{\mathbf{p}}} \right] \\ &\approx 2e |T_0|^2 \Delta_{sc}^2 \sum_{\mathbf{k}} \frac{\varphi_{\mathbf{k}}^2}{E_{\mathbf{k}}^2} \left[\frac{1 - 2f(E_{\mathbf{k}})}{2E_{\mathbf{k}}} + f'(E_{\mathbf{k}}) \right], \end{aligned} \quad (6.5)$$

where in the second line, use has been made of the fact $t_{\perp} \ll t_{\parallel}$. Here we have assumed that the two superconductors are identical so that Δ_{sc} is the same for both. This situation is relevant to both break junction experiments [56] and to intrinsic Josephson tunneling [65] as well. Equation (6.5), like Eq. (4.14), differs from the usual BCS form (as well as that assumed by Lee and Wen [6, 63]) in that the prefactor Δ_{sc}^2 is no longer the total excitation gap Δ^2 . Comparing this equation with Eq. (4.15), one immediately sees, under the current

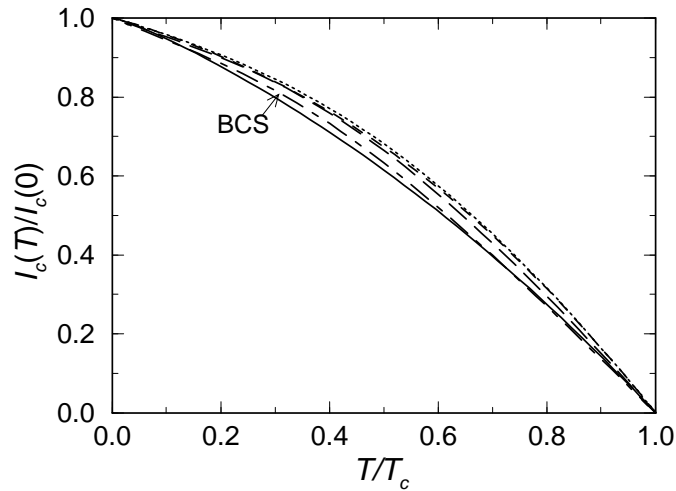


Figure 6.4: Temperature dependence of normalized c -axis Josephson critical current with doping given by the legends in Fig. 6.3(a).

assumption of the c -axis bandstructure, that $I_c \propto \lambda_c^{-2}$. Plotted in Fig. 6.4 is the temperature dependence of normalized c -axis Josephson critical current with the same doping concentrations as in Fig. 6.3(a). Similar to the superfluid density, T_c exhibits a quasi-universal behavior, except that now the small variation of the slope with x is not systematic. This behavior is in contrast to the strongly x dependent quasiparticle tunneling characteristics which can be inferred from the temperature dependent excitation gap plotted in Fig. 6.2. The origin of this universality is essentially the same as that for n_s , deriving from two mutually compensating contributions. At this time, there do not appear to be detailed studies of $I_c(T)$ as a function of x , although future measurements will, ultimately, be able to determine this quantity. In these future experiments the quasiparticle tunneling characteristics should be simultaneously measured, along with $I_c(T)$, so that direct comparison can be made to the excitation gap; in this way, the predictions indicated in Fig. 6.4 can be tested. Indications, thus far [56, 66], are that this tunneling excitation gap coincides rather well with values obtained from photoemission data (see Fig. 6.1).

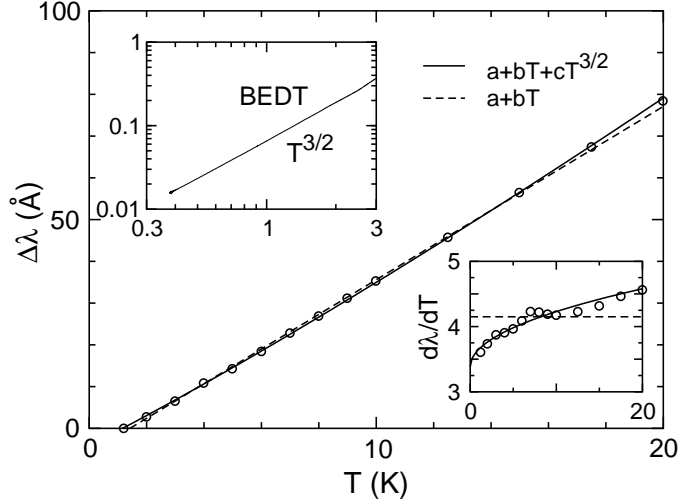


Figure 6.5: Comparison of penetration depth data [67], $\Delta\lambda$, along a -axis, in nominally pure $\text{YBCO}_{6.95}$ single crystal, with different theoretical fits corresponding to BCS d -wave (dashed curve) and to BCS-BEC (solid curve) predictions. The corresponding derivatives are plotted in the lower inset. In the upper inset are experimental data ($\Delta\lambda$ vs T) for the organic superconductor BEDT from Ref. [68].

6.2.3 Search for bosonic pair excitation contributions in penetration depth

At low temperature, the change in the penetration depth, $\Delta\lambda \equiv \lambda(T) - \lambda(0)$, will acquire the same power law T dependence as the superfluid density, via a Taylor expansion

$$\frac{\Delta\lambda}{\lambda_0} = \left(\frac{\lambda_0^2}{\lambda^2}\right)^{-1/2} - 1 \approx \frac{1}{2} \left[A + B(T) \right] \frac{T}{T_c}, \quad (6.6)$$

where $\lambda_0 \equiv \lambda(0)$. Since the temperature dependence of B is very weak, the experimentally obtained $\Delta\lambda$ will always appear to be quasi-linear. When there is a large quasiparticle contribution A , it will be hard to separate the fermionic and bosonic contributions to the T dependence of $\Delta\lambda$. To make the distinction between A and B more prominent, we take the temperature derivative,

$$\frac{d\lambda}{dT} \approx \frac{1}{2} \frac{\lambda_0}{T_c} \left[A + \frac{3}{2} B(T) \right]. \quad (6.7)$$

In this way, the d -wave quasiparticle contribution is a constant, whereas the pair excitation contribution still has a T dependence, with a negative curvature.

We take the experimentally measured a -axis penetration depth, $\Delta\lambda_a$, in optimally doped,

high quality, pure YBCO_{6.95} single crystals from Hardy and coworkers [67]. Their original data, along with different theoretical fits corresponding to BCS *d*-wave (dashed curve) and to BCS-BEC (solid curve) predictions are plotted in Fig. 6.5. These two fits are essentially indistinguishable, for the reasons mentioned above. In the lower inset we plot the slopes $d\lambda/dT$ where the difference between the two sets of curves is more apparent. Here it is shown that the low temperature downturn of the derivative, seen to a greater or lesser extent in all $\Delta\lambda(T)$ measurements, fits our predicted $T^{1/2} + \text{const.}$ dependence rather well. This downturn has been frequently associated with impurity effects, which yield a linear in T slope for $\Delta\lambda$ at very low T , and in this case, provide a poorer fit. While these cuprate experiments were performed on a nearly optimal sample, the same analysis of an underdoped material yielded similarly good agreement, but with a $T^{3/2}$ coefficient about a factor of two larger. Future more precise and systematic low T experiments on additional underdoped samples are needed.

Evidence for the pair excitation contributions also comes from other short coherence length superconductors. Plotted in the upper inset of Fig. 6.5 are data [68] on the organic superconductor κ -(ET)₂Cu[N(CN)₂]Br (BEDT, $T_c \approx 11$ K) which fit a pure $T^{3/2}$ power law over a wide temperature regime; in contrast to the cuprates, there is no leading order linear term. These authors have found this low temperature pure $T^{3/2}$ power law for $\Delta\lambda$ on a variety of different samples. At present, there seems to be no other explanation, besides the bosonic pair excitation mechanism presented here, for this unusual power law at the lowest temperatures. However, this explanation also implies that these organic superconductors have an order parameter with *s*-wave symmetry, for which other evidence is somewhat controversial.

6.2.4 Slope of in-plane inverse squared penetration depth: Quantitative analysis

In this subsection, we shall calculate *quantitatively* the doping dependence of λ_0 and $\frac{d\lambda^{-2}}{dT}$ for a variety of different cuprates, using the experimentally determined lattice constants.

For λ_0 , we have

$$\lambda_0^{-2} = \frac{e^2\mu_0}{a^2d} \left(\frac{n}{m}\right) \propto x, \quad (6.8)$$

where a and b are the in-plane lattice constants, and d is the mean inter-plane distance. The

lattice parameters are:

- For YBCO: $a \approx b = 3.9 \text{ \AA}$, $c = 11.8 \text{ \AA}$, $d = 5.9 \text{ \AA}$;
- For Bi2212: $a = 5.4 \text{ \AA}$, $c = 30.8 \text{ \AA}$, $d = 7.7 \text{ \AA}$;
- For LSCO: $a = 3.79 \text{ \AA}$, $c = 13.2 \text{ \AA}$, $d = 6.6 \text{ \AA}$.

Here the density n is given by the number of electrons per in-plane unit cell, and $1/m$ implicitly contains a factor a^2/\hbar^2 . The factor $n/m \propto x$ in our case is a consequence of the Coulomb-associated reduction in the bandwidth, whereas the charge carrier density $n = 1 - x$ changes only slightly. This is different from alternate scenarios, such as that of Lee and Wen [6], in which the charge carrier density is x , with a doping independent mass m .

The temperature derivative is given by

$$\left| \frac{d\lambda^{-2}}{dT} \right| = \frac{\lambda_0^{-2}}{T_c} \left[A + \frac{3}{2} B(T) \right]. \quad (6.9)$$

The first term is associated with the fermionic quasiparticle contribution, and has a simple, explicit expression

$$\left| \frac{d\lambda^{-2}}{dT} \right|_{QP} = \frac{8 \ln 2}{\hbar c} \frac{\alpha k_B v_F}{d v_2} = \frac{17.65 v_F}{d v_2}, \quad (6.10)$$

where $\alpha = 1/137$ is the fine structure constant. Each quantity in the last equation must be in MKSA units, except for the dimensionless ratio v_F/v_2 . Here we write down the full expression for v_F and v_2 at the nodes for a simple tight-binding model with d -wave pairing:

$$v_F = 2\sqrt{2} \frac{t_{\parallel} a}{\hbar} \sin \frac{k_F a}{\sqrt{2}}, \quad v_2 = \frac{a \Delta_0}{\hbar \sqrt{2}} \sin \frac{k_F a}{\sqrt{2}}, \quad \frac{v_F}{v_2} = \frac{4t_{\parallel}}{\Delta_0}. \quad (6.11)$$

As x increases toward the extreme overdoped limit, v_F increases proportionally, but v_2 (which follows the excitation gap Δ) must decrease toward zero. The second term in Eq. (6.9) is associated with bosonic pair excitations. we calculate this term numerically at $T = 0.2T_c$, as we did for the inset of Fig. 6.3.

The results for λ_0 and $d\lambda^{-2}/dT$ for various cuprates are plotted in Fig. 6.6. The doping dependence of v_F and v_2 are also shown, in the insets of Fig. 6.6(a) and Fig. 6.6(b), respectively. Despite the large scatter of the data, our theoretical predictions are consistent with

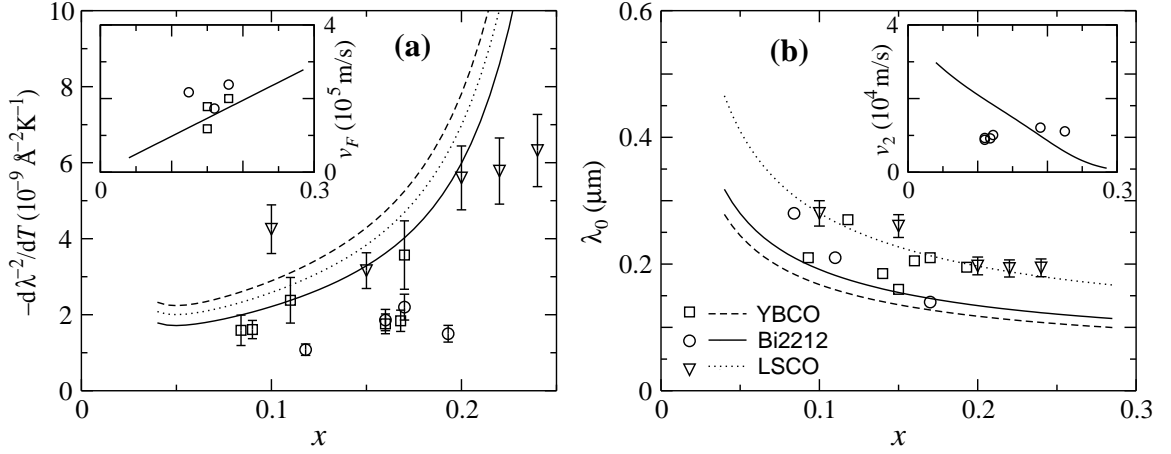


Figure 6.6: Doping dependence of (a) the slope $|d\lambda^{-2}/dT|$ and (b) zero temperature penetration depth λ_0 for various cuprates. Theoretical predictions are represented by lines, and experimental data by symbols. Shown in the insets of (a) and (b) are the doping dependence of v_F and v_2 , respectively. The experimental data on v_F are taken from (\circ) Refs. [70, 71, 69, 72] (\square) [6, 73], v_2 from Ref. [74], others (\circ , Bi2212) Refs. [69, 72]; (\square , YBCO) [60, 61]; (∇ , LSCO) [59].

experiment, for both λ_0 and $d\lambda^{-2}/dT$. This agreement is best for LSCO, for which λ_0 and $\Delta\lambda(T)$ are measured more consistently within the same group of experiments.⁷ Unfortunately, it is hard to measure λ_0 accurately; this quantity may also be sensitive to the sample quality.⁸

As expected from Eqs. (6.11), the insets of Fig. 6.6 show that the quasiparticle contribution, $\left|\frac{d\lambda^{-2}}{dT}\right|_{QP}$ roughly varies as $\frac{v_F}{v_2} \sim x^2$. Without the contribution from pair excitations, the slope $\left|\frac{d\lambda^{-2}}{dT}\right|$ would be much smaller in the underdoped regime, and, therefore, inconsistent with experiment. Bosonic pair excitations become more and more important with underdoping. Figure 6.6 also reveals that the slope $d\lambda^{-2}/dT$ has a fairly strong doping dependence, particularly in the overdoped regime. This is in contrast to the quasi-universal behavior of the normalized λ^{-2} vs T/T_c .

⁷The discrepancy in $\Delta\lambda(T)$ for YBCO and Bi2212 may be associated with errors in λ_0 , since $\left|\frac{d\lambda^{-2}}{dT}\right| = \frac{2}{\lambda^3} \frac{d\lambda}{dT}$, so that a 10% error in λ_0 would cause a 30% error in $d\lambda^{-2}/dT$.

⁸For this reason, the Bi2212 data for $d\lambda^{-2}/dT$ from Waldman *et al.* [69] are not as reliable since they had difficulty observing the linear T dependence of $\Delta\lambda$ associated with the nodal quasiparticles.

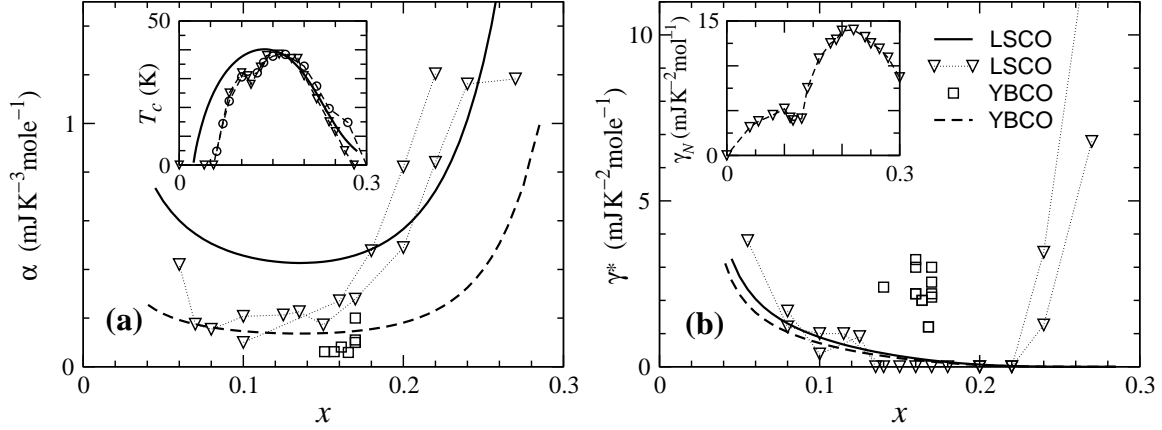


Figure 6.7: (a) Quadratic and (b) linear T contributions to C_v in various cuprates. T_c is shown in the inset of (a). Data are from (∇) Refs. [75, 76] and (\square) Refs. [77, 78, 79, 80]. The inset in (b) shows normal state result from Ref. [76]. The symbols (experiment) and lines (theory) (per mole of formula units) can be compared.

6.3 SPECIFIC HEAT AT LOW T

In this section, we apply our three fluid model in the context of specific heat calculations (based on the discussion in Sec. 4.3) to the cuprates. In this way we calculate the coefficients α and γ^* in Eq. (4.26) as a function of doping.

For d -wave superconductors, the fermionic quasiparticle contributes a quadratic T dependence, αT^2 , to the specific heat, where α is given by

$$\alpha = \frac{18\zeta(3)}{\pi} \frac{k_B^3}{\hbar^2} \frac{1}{d} \frac{1}{v_F v_2}. \quad (6.12)$$

The pair excitation contribution, γ^* , will be calculated directly from Eq. (4.20). Here we use our results for the various gaps and chemical potential below T_c as a function of both doping and temperature.

The results for α and γ^* are plotted in Fig. 6.7(a) and (b), respectively, for LSCO and YBCO. As can be seen, the theory is consistent with the experimental data, especially for LSCO. For YBCO, it has been difficult to see the αT^2 term in C_v . Indeed, as shown in Fig. 6.7, there is a large discrepancy between the measurements of different groups, so that the YBCO results may be less reliable.

There are several important observations from this figure and Eq. (6.12) regarding the

behavior of C_v . (i) As the doping x decreases, pair excitations become more significant, and, as a consequence, γ^* increases with decreasing x . (ii) On the *overdoped* side, α increases rapidly with x . This can be expected from Eq. (6.12), since $1/v_2 \propto 1/\Delta_0 \propto \gamma_N/T_c$ increases rapidly with overdoping. [Here γ_N is the normal state γ , which is plotted in the inset of Fig. 6.7(b).] This increase coincides with the rapid drop of T_c , as shown in the inset of Fig. 6.7(a). On simple physical grounds, a small T_c in the overdoped regime implies that $\gamma \approx \alpha T$ must increase from 0 to the normal state value γ_N within a narrow temperature range, and α has to increase to accommodate this rapid change. (iii) In the *underdoped* regime, as x further decreases, T_c drops rapidly, so that $\alpha \propto \gamma_N/T_c$ also increases gradually, (although γ_N also decreases, but it does not decrease as fast as T_c does). (iv) Experimentally, as T_c approaches zero on either side, γ should approach γ_N . The fact that γ^* increases again in the extremely overdoped limit can be associated with the fact that the low T behavior may be obscured by the low T upturn in $\gamma(T)$ curve deriving, presumably, from extrinsic paramagnetic scattering centers, etc.

Our pair excitation mechanism for the widely observed γ^* term, offers a more natural and systematic explanation, than previous claims which associate this term with extrinsic effects. The agreement between theory and experiment [Fig. 6.7(b)] seems to be favorable.

CHAPTER 7

THERMODYNAMIC SIGNATURES OF THE SUPERCONDUCTING TRANSITION

Both ARPES and tunneling measurements have shown that in a pseudogapped superconductor, the excitation gap evolves smoothly across the superconducting phase transition temperature, T_c , as plotted in Fig. 6.2. It, therefore, follows that the superconducting order parameter and the excitation gap are distinct. Moreover, this distinction is essential to the more general mean field theory which we have proposed in this Thesis. These observations, along with the measured behavior of the excitation gap, leads to an important question: Will there be any sign of the phase transition in thermodynamical properties such as the specific heat and the tunneling spectra (or, equivalently, electronic density of states) in a pseudogapped superconductor? We know that the answer must be yes on general physical grounds, since the superconducting and normal states are distinct phases; thus, we expect thermodynamical signatures at T_c . Moreover, experimentally, it has been established from specific heat measurements in the cuprates that there is a step discontinuity or a maxima at T_c , depending on the doping level [75, 81]. It should be recalled that in BCS theory, the specific heat jump at T_c results from the opening of the excitation gap. Clearly, there must be something more subtle going on in the cuprates — to give rise to a thermodynamical signature at T_c . This is one of the main issues to be addressed in this Chapter.

In addition, in this Chapter we address the thermodynamic characteristics of the extrapolated (below T_c) “normal state”. This represents a very important concept. The free energy of this extrapolated normal state is needed in writing down a Landau-Ginzburg expansion for traditional superconductors. Here the situation is far more complex and we ask how this extrapolation should be done when the normal state is not a Fermi liquid? We pose this question in the context of the condensation energy — which has been deduced from specific heat measurements [81]. So far, the magnetic field dependent measurements of the normal phase inside a vortex core [82] or at a field above H_{c2} [83] suggest that for

a pseudogapped superconductor the fermionic excitation gap persists when the superconductivity is destroyed below T_c . These experiments are consistent with the present physical picture.

The results obtained within the present theoretical scheme show that upon entering the superconducting phase, the onset of the coherent condensate leads to dramatic sharpening of the peaks in the electronic spectral function, which is observable in both tunneling spectra and ARPES measurements. This sharpening, in conjunction with the temperature dependence of the excitation gap, will cause a specific heat jump. This general picture is applied to the cuprates where we show that in the overdoped regime, this jump (in C_v) is mainly attributable to the temperature dependence of the excitation gap (as in the traditional BCS case), whereas in the underdoped regime, it is mainly a consequence of the onset of off-diagonal long range order. This jump becomes smaller towards underdoping, and behaves more like a λ transition in Bose-Einstein condensation. We also discuss the subtlety of extracting the condensation energy from specific heat data, and we show that a proper treatment of the pseudogap in the extrapolated “normal state” is important.

In previous chapters, we have used the approximation, Eq. (2.48), in order to simplify the calculations. Thereby, we defined the pseudogap parameter, Δ_{pg} . Under this approximation, the pseudogap self-energy Σ_{pg} has a BCS-like form, so that the spectral function is given by two δ -functions at $\pm E_{\mathbf{k}}$. These approximations were justified in the context of the applications we considered, thus far. However, in order to study the thermodynamic behavior at T_c and above T_c , in this Chapter, we will relax this simplifying approximation and allow for lifetime effects in Σ_{pg} . This more realistic form incorporates a finite broadening due to the incoherent nature of the finite center-of-mass momentum pair excitations. To avoid extremely heavy and difficult numerical computations, we will not solve for the broadening and chemical potential, etc. self-consistently, but rather take the broadening as a phenomenological, tunable input parameter such that it gives a realistic density of states, etc. We will use the gaps, T_c , and the chemical potential μ obtained in chapters 4 and 6 in our calculations.

7.1 SPECTRAL FUNCTIONS AND THE DENSITY OF STATES

We begin with the building block of this chapter, the spectral function $A(\mathbf{k}, \omega)$. Both theoretical studies [26] and ARPES data [84] show that above T_c , the spectral function can be roughly approximated by a broadened BCS-like form. Therefore, we can write down Σ_{pg} in a general form,

$$\Sigma_{pg}(\mathbf{k}, \omega) = \frac{\Delta_{\mathbf{k},pg}^2}{\omega + \epsilon_{\mathbf{k}} + \lambda + i\gamma} + \nu - i\Sigma_0, \quad (7.1)$$

where for given \mathbf{k} , λ and γ are constants, ν and Σ_0 may be a function of ω , and ν is the real part contribution introduced by Σ_0 via the Kramers-Krönig relations. Since the pseudogap self-energy results from the incoherent finite momentum pair excitations both above and below T_c , this expression will also be valid in the superconducting state. On the other hand, since the superconducting self-energy, Σ_{sc} , results from the phase-coherent zero-momentum condensate, *there should be no broadening in Σ_{sc}* . In this way, we obtain the inverse Green's function

$$G^{-1}(\mathbf{k}, \omega) = \omega - \epsilon_{\mathbf{k}} - \nu - \frac{\Delta_{\mathbf{k},sc}^2}{\omega + \epsilon_{\mathbf{k}}} - \frac{\Delta_{\mathbf{k},pg}^2}{\omega + \epsilon_{\mathbf{k}} + \lambda + i\gamma} + i\Sigma_0. \quad (7.2)$$

Thus, the spectral function is given by¹

$$\begin{aligned} A(\mathbf{k}, \omega) &= -2 \operatorname{Im} G(\mathbf{k}, \omega + i0) \\ &= 2 \frac{(\omega + \epsilon_{\mathbf{k}}) [(\omega + \epsilon_{\mathbf{k}} + \lambda)C - \gamma D]}{C^2 + D^2}, \end{aligned} \quad (7.3a)$$

where

$$\begin{aligned} C &= \gamma [\omega^2 - \epsilon_{\mathbf{k}}^2 - \Delta_{\mathbf{k},sc}^2 - \nu(\omega + \epsilon_{\mathbf{k}})] + (\omega + \epsilon_{\mathbf{k}})(\omega + \epsilon_{\mathbf{k}} + \lambda)\Sigma_0, \\ D &= (\omega + \epsilon_{\mathbf{k}}) [\omega^2 - E_{\mathbf{k}}^2 - \nu(\omega + \epsilon_{\mathbf{k}}) - \Sigma_0\gamma] + \lambda [\omega^2 - \epsilon_{\mathbf{k}}^2 - \Delta_{\mathbf{k},sc}^2 - \nu(\omega + \epsilon_{\mathbf{k}})]. \end{aligned}$$

¹Note here the spectral function satisfies the normalization $\int_{-\infty}^{\infty} \frac{d\omega}{2\pi} A(\mathbf{k}, \omega) = 1$, which follows the convention used in some standard textbooks (see, e.g., Refs. [30] and [64]), but is different from that used by some authors in the literature [84].

Above T_c , where $\Delta_{sc} = 0$, the spectral function can be simplified as

$$A(\mathbf{k}, \omega) = 2 \frac{(\omega + \epsilon_{\mathbf{k}} + \lambda)C' - \gamma D'}{C'^2 + D'^2}, \quad (7.3b)$$

where

$$\begin{aligned} C' &= \gamma(\omega - \epsilon_{\mathbf{k}} - \nu) + \Sigma_0(\omega + \epsilon_{\mathbf{k}} + \lambda) \\ D' &= \omega^2 - E_{\mathbf{k}}^2 - \nu(\omega + \epsilon_{\mathbf{k}}) + \lambda(\omega - \epsilon_{\mathbf{k}} - \nu) - \gamma \Sigma_0. \end{aligned}$$

ARPES data [84] show that Σ_0 is very small for small ω . However, it can be as large as 300 meV for large ω , and this is associated with a huge incoherent background, whose origin is still under debate. (A proper choice for Σ_0 can give the peak/dip/hump features observed in ARPES measurements and in some tunneling data). Here we are not particularly interested in the high energy features and will take $\nu = \Sigma_0 = 0$ to simplify the calculations, without loss of generality.² In addition, we have no particular reason to support the choice of nonzero λ , and hence will also set it to zero. Finally, we obtain a greatly simplified expression for $A(\mathbf{k}, \omega)$:

$$A(\mathbf{k}, \omega) = \begin{cases} \frac{2\Delta_{\mathbf{k},pg}^2 \gamma (\omega + \epsilon_{\mathbf{k}})^2}{(\omega + \epsilon_{\mathbf{k}})^2 (\omega^2 - E_{\mathbf{k}}^2)^2 + \gamma^2 (\omega^2 - \epsilon_{\mathbf{k}}^2 - \Delta_{\mathbf{k},sc}^2)^2}, & (T < T_c), \\ \frac{2\Delta_{\mathbf{k}}^2 \gamma}{(\omega^2 - E_{\mathbf{k}}^2)^2 + \gamma^2 (\omega - \epsilon_{\mathbf{k}})^2}, & (T > T_c). \end{cases} \quad (7.4)$$

From Eqs. (7.3) and (7.4), we see that the spectral function contains a zero at $\omega = -\epsilon_{\mathbf{k}}$ below T_c , whereas it has no zero above T_c . This difference is at the heart of the different thermodynamical behavior of the system above and below T_c .

In Fig. 7.1, we plot the spectral function for $\epsilon_{\mathbf{k}} = 0$ (on the Fermi surface) at different temperatures from slightly above T_c [Fig. 7.1(a)] to temperatures within the superconducting phase [Fig. 7.1(f)]. Note that in these plots we do not need to specify the pairing symmetry, but only the magnitude of the gap along the direction specified by the given

²We find that Σ_0 must decrease with ω as $\omega \rightarrow \pm\infty$, in order to conserve the system energy. Otherwise, the energy of the system will diverge.

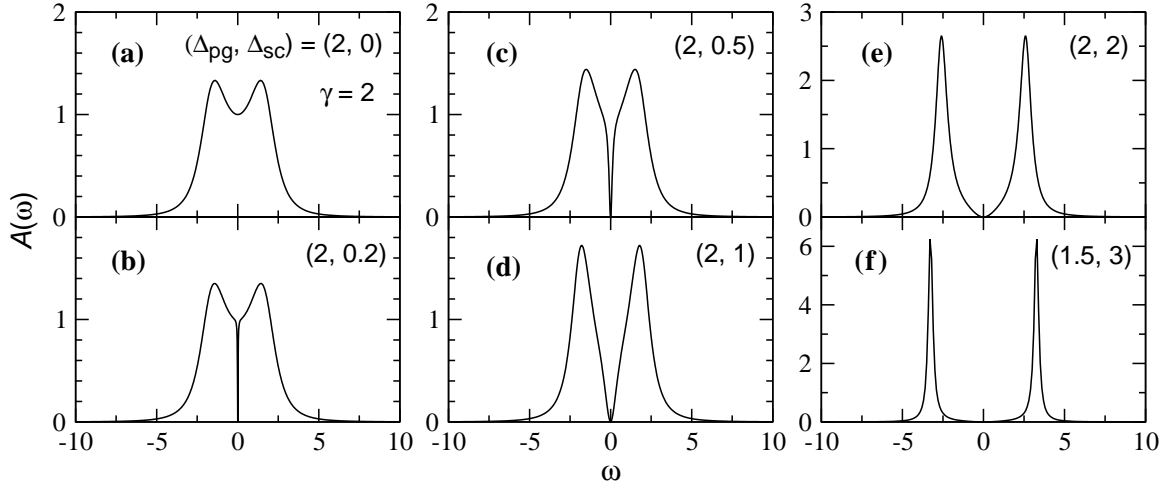


Figure 7.1: Effects of the superconducting long range order on behavior of the spectral function at the Fermi level $\epsilon_{\mathbf{k}} = 0$ as a function of temperature in a pseudogapped superconductor, in arbitrary units. Here we take $\gamma = 2$ for all the figures. The parameters $(\Delta_{pg}, \Delta_{sc})$ are labeled in pairs. Figures (a)-(f) correspond to various temperatures decreasing from $T = T_c$. A true gap opens up below T_c as a consequence of the onset of the condensate.

wave vector. Since we have seen (in Fig. 1.6, for example) that varying temperature corresponds to varying the relative size of Δ_{pg} and Δ_{sc} , we chose to vary these energy scale parameters, rather than T directly. For illustrative purposes, we take $\gamma(T) = \Delta_{pg}(T_c)$. In this way we ignore any T dependence in γ and, thus, single out the long range order effects associated with Δ_{sc} . Figure 7.1(a) is appropriate for the spectral function at and slightly above T_c . Slightly below T_c , a very small condensate contribution leads to the depletion of the spectral weight at the Fermi level, as shown in Fig. 7.1(b). As the temperature continues to decrease, and the superconducting gap increases, the two peaks in the spectral function become increasingly well separated, as plotted in Figs. 7.1(c)-(f). This last panel, Fig. 7.1(f), is computed with a slightly smaller Δ_{pg} and slightly larger Δ_{sc} , as is consistent with the behavior for $T/T_c \sim 0.7$, seen in, e.g., Fig. 6.2. Even at these relatively high temperatures the spectral peaks are quite sharp — only slightly broadened relative to their BCS counterparts (where the spectral function is composed of two δ functions). It should be noted that these narrow peaks derive from long range order, via Δ_{sc} , and that lifetime effects via γ do not lead to significant peak broadening. To understand this last point, one needs to note two facts: (i) A non-zero Δ_{sc} forces the spectral function to vanish at the Fermi level $\omega = 0$ (for $\epsilon_{\mathbf{k}} = 0$) so that the two peaks are necessarily separated; (ii) The

imaginary part of the pseudogap self-energy at the peak location $E_{\mathbf{k}}$ is given by

$$\gamma' = \gamma \frac{\Delta_{\mathbf{k},pg}^2}{(E_{\mathbf{k}} + |\epsilon_{\mathbf{k}}|)^2 + \gamma^2} = \gamma \frac{\Delta_{\mathbf{k},pg}^2}{\Delta_{\mathbf{k}}^2 + \gamma^2}, \quad (7.5)$$

so that the effective peak width, determined by γ' , decreases rapidly as T decreases. [Here in the second equation above, we have used $\epsilon_{\mathbf{k}} = 0$ which is relevant to Fig. 7.1]. It should be emphasized that below T_c , the spectral functions in Eqs. (7.3) and (7.4), are very different from those obtained using a broadened BCS form; there is no true gap for the latter, in contrast to the present case.

The density of states, which is given by

$$N(\omega) = \sum_{\mathbf{k}} A(\mathbf{k}, \omega), \quad (7.6)$$

can be easily obtained from the spectral function. It should be stressed that the peak sharpening effects discussed above, associated with superconducting long range order, will also be reflected in the density of states. For illustrative purposes, in this section, we present our results for the case of s -wave pairing. In Fig. 7.2(a)-(f), we plot the density of states for a quasi-2D s -wave superconductor. As in Fig. 7.1, we emphasize here the effects associated with long range order, via Δ_{sc} , taking the same energy scales as used in Fig. 7.1. Due to the contributions of the states with $\epsilon_{\mathbf{k}} \neq 0$, the narrow dips in Fig. 7.1(b)-(c) do not show up here. However, as is evident, the density of states within the gap region decreases quickly, as the superconducting condensate develops. In comparison with the much weaker temperature dependence of the density of states above T_c , it can be inferred from the figure that there will be something like a step discontinuity in the derivative of the density of states with respect to T , $dN(\omega)/dT$.

7.2 SPECIFIC HEAT

The rapid decrease of the density of states with decreasing T , in the vicinity of T_c , will be reflected in the behavior of the specific heat, C_v . These effects will, thereby, lead to a thermodynamical signature of the phase transition. To calculate C_v in terms of the more general spectral function (which now contains lifetime effects) requires an approach dif-

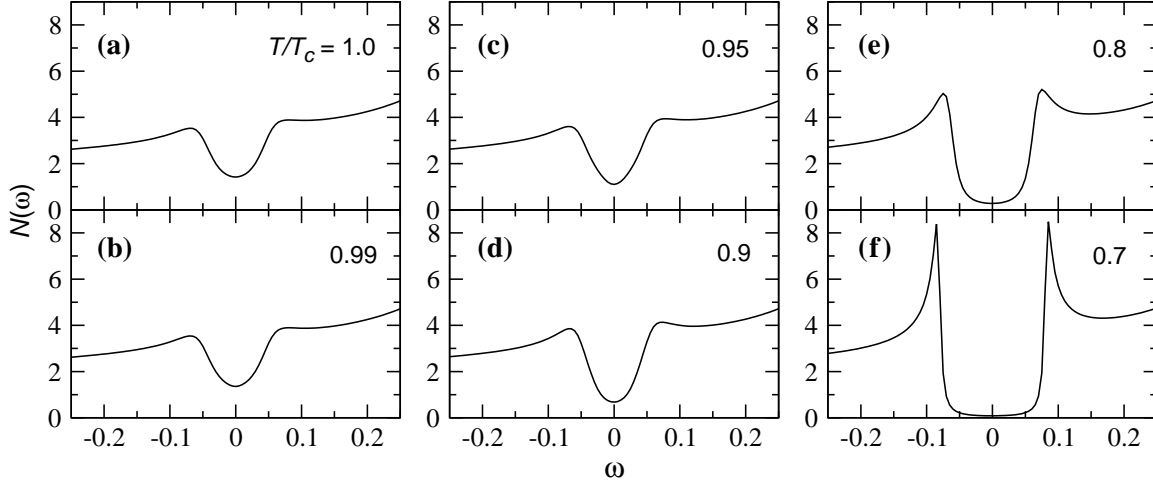


Figure 7.2: Effects of superconducting long range order on the behavior of the density of states as a function of temperature in a pseudogapped s -wave superconductor with $n = 0.5$. Here we take the parameters Δ_{pg} , Δ_{sc} , and γ same as those used in Fig. 7.1, but measured in terms of the unit $4t_{\parallel}$, the half band width. Figures (a)-(f) correspond to various temperatures decreasing from $T = T_c$, as labeled in the figure. At $T/T_c \sim 0.7$, as shown in (f), the density of states is close to that of strict BCS theory.

ferent from that used to obtain Eq. (4.19). Here, we derive C_v directly from the energy of the system via $C_v = dE/dT$, where the energy E is calculated using a direct spectral integration of the energy distribution, as given in Ref. [30]:

$$\begin{aligned}
 E &= 2T \sum_{\mathbf{k}, n} \frac{1}{2} (i\omega_n + \epsilon_{\mathbf{k}}^0 + \mu) G(\mathbf{k}, i\omega_n) \\
 &= \sum_{\mathbf{k}} \int_{-\infty}^{\infty} \frac{d\omega}{2\pi} (\omega + \epsilon_{\mathbf{k}} + 2\mu) A(\mathbf{k}, \omega) f(\omega), \quad (7.7)
 \end{aligned}$$

where $\epsilon_{\mathbf{k}}^0 = \epsilon_{\mathbf{k}} + \mu$ is the dispersion measured with respect to the bottom of the band, which is, therefore, temperature independent. It is not difficult to show that for the BCS spectral function, $A(\mathbf{k}, \omega) = 2\pi[u_{\mathbf{k}}^2\delta(\omega - E_{\mathbf{k}}) + v_{\mathbf{k}}^2\delta(\omega + E_{\mathbf{k}})]$, this equation reduces to Eq. (1.9). To determine the various contributions to the specific heat, we rewrite Eq. (7.7) as

$$E = \int_{-\infty}^{\infty} \frac{d\omega}{2\pi} [(\omega + \mu)N(\omega) + K(\omega)]f(\omega), \quad (7.8)$$

where we have defined $K(\omega) \equiv \sum_{\mathbf{k}} \epsilon_{\mathbf{k}}^0 A(\mathbf{k}, \omega)$, which can be regarded as the contribution associated with the kinetic energy of the system. In this way, we obtain

$$C_v = \int_{-\infty}^{\infty} \frac{d\omega}{2\pi} \left\{ \frac{\partial \mu}{\partial T} N(\omega) f(\omega) - [(\omega + \mu)N(\omega) + K(\omega)] \frac{\omega}{T} f'(\omega) + \left[(\omega + \mu) \frac{\partial N(\omega)}{\partial T} + \frac{\partial K(\omega)}{\partial T} \right] f(\omega) \right\}. \quad (7.9)$$

The two terms on the right hand side, appearing in the first line of the equation, are present in the general Fermi liquid case, whereas the term on the second line derives from the temperature dependence of the density of states.³ In a Fermi liquid at low T , where $f'(\omega) \sim -\delta(\omega)$ and $N(\omega) \approx N(0)$, the first two terms lead to a contribution to C_v/T which is proportional to $N(\omega)$. However, when $N(\omega)$ is a function of T , the second term will be significant and sometimes dominant. *In this case, C_v/T no longer reflects the density of states.* Indeed, it is this term that gives rise to the specific heat discontinuity at T_c in BCS theory. Similarly, for the case of a pseudogap superconductor, this non-Fermi liquid term also leads to a step discontinuity.

In Fig. 7.3 we plot the temperature dependence of C_v in both (a) the weak coupling BCS case and (b) the moderate coupling pseudogap case with s -wave pairing. We choose the broadening $\gamma(T) = T$ for the second of these calculations, although our results are not particularly sensitive to the form of this parameter, provided it is non-zero. We also indicate in the insets, the respective temperature dependent excitation gaps, which have been assumed in producing the figure. It can be seen here that for the pseudogap case, we have presumed there is some small feature in the excitation gap at T_c , which was not evident in our more naive calculations (see Appendix C) which ignored lifetime effects of the finite momentum pairs.

In the BCS case as shown in Fig. 7.3(a), the specific heat jump arises exclusively from the discontinuity of the derivative of this excitation gap, via

$$\Delta C_v = -N(0) \frac{d\Delta^2}{dT}. \quad (7.10)$$

³Strictly speaking, in a Fermi liquid, the density of states is also T -dependent, via the chemical potential in $A(\mathbf{k}, \omega)$. However, this T -dependence is usually negligible.

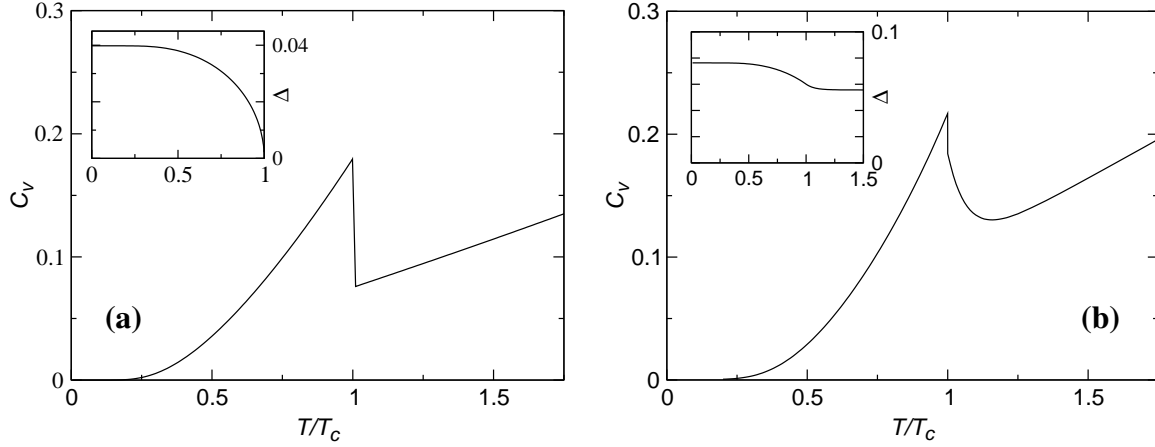


Figure 7.3: Comparison of the temperature dependence of the specific heat in (a) the weak coupling BCS case and (b) moderate coupling pseudogap case. Shown here are quasi-2D s -wave results, at $n = 0.5$, $-g/4t_{\parallel} = 0.5$ and 0.6 , respectively. The T dependence of the gap is shown as insets. The C_v jump at T_c can be accounted for by the discontinuity of $dN(\omega)/dT$ in both cases.

In contrast, in the pseudogap case, the gap Δ and its derivative $d\Delta/dT$ are presumed to be continuous across T_c as shown in Fig. 7.3(b). In this case, this jump arises from the discontinuity of $dN(\omega)/dT$ which results from the onset of the superconducting order. Above T_c , $dN(\omega)/dT$ decreases and in this way C_v also decreases. It should be emphasized that the temperature dependence of C_v at $T \gtrsim T_c$ is dominated by $dN(\omega)/dT$, instead of $N(\omega)$ itself. In fact the contributions of these two functions are in opposite directions as a function of temperature. This observation implies that one cannot extract the size of the excitation gap from the specific heat without taking proper account of the T dependence of the density of states. At higher T away from T_c , however, $dN(\omega)/dT$ decreases gradually to zero, and in this way, C_v is controlled by $N(\omega)$. The shape of the anomaly in Fig. 7.3(b) is more representative of a λ -like behavior, although there is a precise step function discontinuity just at T_c . The curvature above, but in the vicinity of T_c , can be associated with the subtle feature at T_c which appears in the excitation gap.⁴

In summary, we have seen above that Eq. (7.10) is only valid in the weak coupling BCS

⁴One may ask what happens to the pairon $T^{3/2}$ contribution to the specific heat in the present model. To answer this question, we note that C_v calculated through the derivative of the energy of the system, Eq. (7.7), in principle, contains all possible contributions. However, here we model the pseudogap self-energy by a parameter γ and have suppressed the pair dispersion. This is not sufficient to capture the pairon contributions properly. In fact, this finite γ modeling is only meant for high T , whereas at low T when both the quasiparticles and the pair excitations are very long lived, the formalism we developed in Sec. 4.3 should be used, instead.

limit; it necessarily breaks down in the pseudogap phase. *We conclude that $dN(\omega)/dT$ is a more appropriate quantity for describing the specific heat jump at T_c than is $-d\Delta^2/dT$.* This result is implicitly used to derive the simpler form of Eq. (7.10). The important temperature dependence in the temperature derivative of the density of states comes, in turn, from the onset of long range order via Δ_{sc} . Comparing Fig. 7.3(a) and (b), one can see that the gradual decrease of $dN(\omega)/dT$ in the pseudogap case leads to a more gradual decrease in C_v above the transition, so that C_v looks more like what would be expected in a λ transition, as distinct from a BCS step discontinuity.

7.3 APPLICATION TO THE CUPRATES

The results obtained in Sec. 7.1 and Sec. 7.2 are generally valid for both s - and d -wave cases, and can be readily applied to the d -wave cuprates. In this subsection we test the physical picture and the results obtained above, by studying the tunneling spectra and the specific heat behavior in the cuprates, as a function of doping and of temperature.

7.3.1 Tunneling spectra

We first turn to calculations of tunneling spectra for which there is substantial experimental data. These experiments were among the first to provide information about the excitation gap — which measurements seem to be consistent with ARPES data.

Here we treat the hole concentration dependence of the electronic energy scales as in Chapter 6. However, in order to compare with tunneling spectra, in this subsection, we use a slightly more realistic band structure which includes a next-nearest neighbor hopping term, characterized by t' , in the band dispersion, $\epsilon_{\mathbf{k}}$. This is discussed in more detail in Appendix A. ARPES measurements indicate that both the under- and optimally doped cuprates have a hole-like Fermi surface [85], which can be roughly modeled by choosing $t'/t \approx 0.4$. For this choice of t' , the van Hove singularities appear inside the filled lower half band. Because these effects were not particularly relevant in our previous studies, this complication was ignored until this Chapter.

For a given density of states $N(\omega)$, the quasiparticle tunneling current across a super-

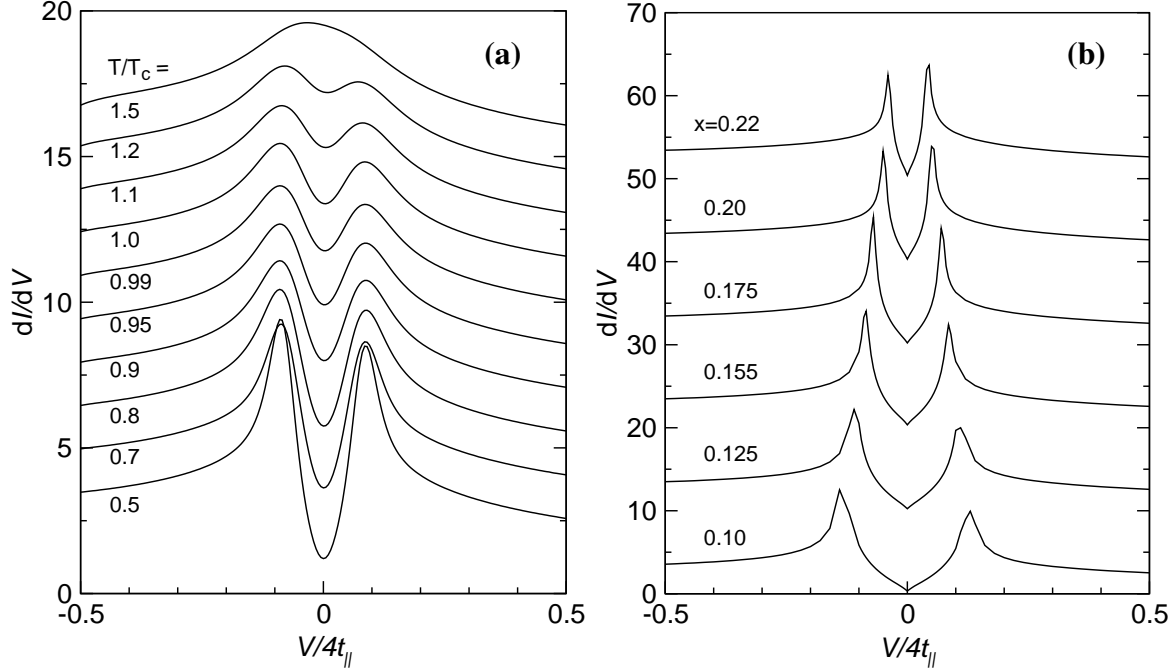


Figure 7.4: (a) Temperature and (b) doping dependence of tunneling spectra across an SIN junction. Shown in (a) are the dI/dV characteristics calculated for optimal doping at various temperatures from above to below T_c . Shown in (b) are tunneling spectra at low T (around $0.2T_c$) for various doping x . The units for dI/dV are $e^2 N_0 T_0^2 / 4t_{||}$. For clarity, the curves in (a) and (b) are vertically offset by 1.5 and 10, respectively.

conducting-insulator-normal (SIN) junction can be readily calculated [64],

$$I_{SIN} = 2eN_0T_0^2 \int_{-\infty}^{\infty} \frac{d\omega}{2\pi} N(\omega) [f(\omega - eV) - f(\omega)] , \quad (7.11)$$

where we have assumed a constant density of states, N_0 , for the normal metal, and taken T_0 as the isotropic tunneling matrix element. At low T , one obtains

$$\left(\frac{dI}{dV} \right)_{SIN} \approx \frac{e^2 N_0 T_0^2}{\pi} N(eV) . \quad (7.12)$$

It can be seen that at low T , the tunneling spectra and the density of states are equivalent, up to a multiplicative constant coefficient. However, at high T comparable to T_c , the tunneling spectra reflect a thermally broadened density of states.

In Fig. 7.4(a), we plot the SIN tunneling spectra, calculated for optimal doping at temperatures varying from above to below T_c . The van Hove singularity introduces a broad

maximum in the spectra at high temperatures, as seen for the top curve in Fig. 7.4(a). [It should be noted that the density of states contains (pseudo)gap like features which lead to two peaks even at this relatively high temperature]. The figure shows that even for this optimal sample, as is consistent with the phase diagram of Fig. 7.1, [although not so evident in the first generation experiments summarized in Fig. 1.3(b)], there is a pseudogap at T_c . Because the optimal sample is reasonably well within the pseudogap regime, it is reasonable to presume, as in our calculations, that the excitation gap increases only slightly with decreasing temperature.⁵ In Fig. 7.4(b), we show the calculated tunneling spectra at low T for variable doping concentration.⁶ As expected from the phase diagram (Fig. 6.1), which consolidates both tunneling and ARPES data, the excitation gap seen in Fig. 7.4(b) increases with underdoping. Indeed, the behavior of the tunneling spectra shown in both plots is similar to what is observed experimentally by Renner and coworkers [66] and by Miyakawa *et al* [56]. It should be noted that there is no direct feature in the tunneling curves associated with Δ_{sc} . There are, however, indirect effects arising from the onset of long range order, which lead to the sharpening of the density of states peaks. Note that we have ignored (as previously) other self-energy contributions (e.g., arising from the particle-hole channel) which would enter into the parameter Σ_0 in Eq. (7.1). Finally, we point out that the asymmetry of the high energy background in tunneling data is a natural consequence of a non-zero t' .

7.3.2 Specific heat

We, next, discuss the behavior of the specific heat in the cuprates as a function of temperature and hole concentration. Here, too, there is a substantial amount of experimental data, although primarily from one experimental group [81]. In the present calculations there are two important parameters which we treat phenomenologically, rather than by iteratively solving our set of three coupled integral equations. They are the total gap Δ and the pair lifetime γ . In the analyses of previous chapters the latter played no important role, so that Δ could be reasonably accurately calculated by ignoring lifetime effects. For C_v this is no

⁵Thermal broadening of the spectral peaks tends to push the peaks apart and may lead to a seemingly increasing gap with T above T_c in some cases.

⁶These doping dependent measurements are usually taken at 4.2 K

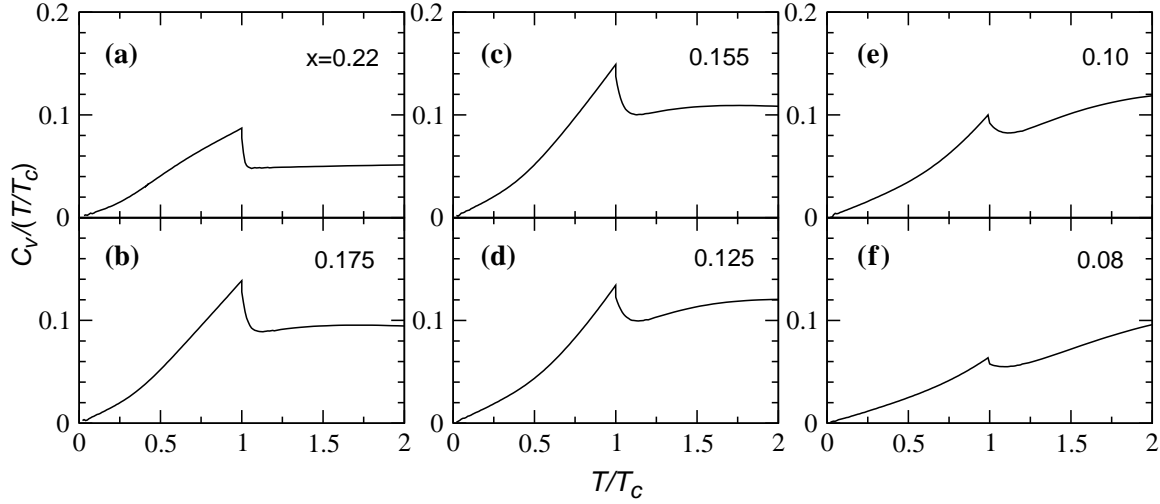


Figure 7.5: Temperature dependence of the specific heat for various doping concentrations, calculated with $a = 1/4$ in Eq. 7.13.

longer the case and γ , particularly, must be chosen with some care. As is consistent with lifetime estimates in the literature, we take $\gamma \propto T^3$ below T_c and linear in T above T_c .⁷ For the doping dependence, we assume that γ varies inversely with Δ since when the gap is large, the available quasiparticle scattering decreases. With this reasonable assumption, along with the continuity of γ at T_c , we obtain a simple form:

$$\gamma = \begin{cases} aT^3/T_c\Delta, & (T < T_c), \\ aTT_c/\Delta, & (T > T_c). \end{cases} \quad (7.13)$$

Here, the coefficient a is of the order of, or less than, unity. Our choice for the excitation gaps is shown in Fig. 7.6. Here, at this higher level of approximation we expect some, albeit weak, structure to be introduced at T_c (since γ varies around T_c). This provides a small correction to the first order solutions shown in Fig. 6.2, and discussed in Appendix C.

The results for C_v/T are plotted in Fig. 7.5(a)-(f), from over- to underdoped systems. As shown in these plots, the behavior of C_v is BCS-like in the overdoped regime. As the system passes from optimal doping towards underdoping, the behavior is more representa-

⁷Recalling that $\Delta_{pg}^2 \propto T^{3/2}$ at low T and is roughly linear in T , this choice of γ will give rise to a temperature dependence of the effective quasiparticle peak width $\gamma' \propto T^{4-4.5}$ for $T \leq T_c$, via Eq. (7.5). This is consistent with the experimentally observed $T^4 - T^5$ dependence of the quasiparticle scattering rate [86]. Above T_c , the T -dependence of Δ_{pg} is weak, so that $\gamma' \propto T$, in agreement with ARPES data [70].

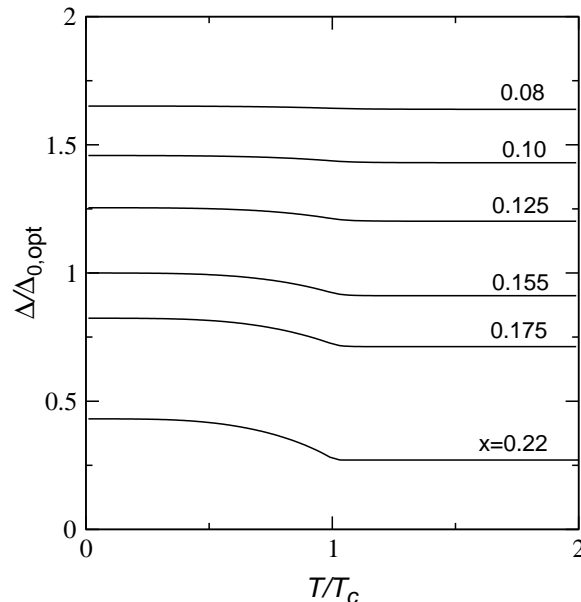


Figure 7.6: Temperature dependence of the excitation gaps for various doping concentrations used for calculations in Fig. 7.5. The units for the gaps are the zero T gap at optimal doping.

tive of a λ -like anomaly. This latter shaped curve is similar to what was seen in the s -wave case discussed in Sec. 7.2 and can be traced to the very weak feature in the temperature dependence of Δ at T_c . All these trends seem to be qualitatively consistent with experimental data [75, 81]. As can be seen from the figures, in the underdoped regime at high T , there is a maximum in C_v/T , around T^* . Note the difference at low T between the d -wave results here and the s -wave behavior of Fig. 7.3. Here, the d -wave nodes lead to a larger quasiparticle specific heat at low T .

The experimentally observed λ -like anomaly of C_v at T_c has been interpreted previously as evidence for a Bose condensation description. Here, in contrast, we see that within our generalized mean field theory, this anomaly naturally arises from the temperature dependence of the fermionic excitation gap which has some structure at, but persists above T_c . (Thus, this is a property of superconductors which have a well established pseudogap!) That the experimental data, (which, except at extremely reduced hole concentrations), show a reasonably sharp (λ -like) structure at T_c — seems to reinforce the general theme of this Chapter and Thesis — that corrections to BCS theory may be reasonably accounted for by an improved mean field theory, rather than by, say, including fluctuation effects.

7.4 LOW T EXTRAPOLATION OF THE PSEUDOGAPPED NORMAL STATE

One important consequence of specific heat measurements is that they, in principle, may provide information about the condensation energy, which is the energy gained upon transforming from the normal to the superconducting states. What is required, however, is to make an extrapolation of the normal state down to low $T < T_c$. This low T extrapolated (“normal”) state has played an important role in traditional superconductors, where the condensation energy can be precisely determined by integrating the difference between the entropy of the superconducting state and that of the extrapolated normal state with respect to T . In this final section, we discuss the thermodynamical variables associated with the extrapolated normal state in pseudogap superconductors.

As in any phase transition, one has to compare the free energies of the disordered and ordered phases in order to establish their relative thermodynamical stability. This extrapolated normal state is at the basis of the free energy functional of Landau-Ginzburg theory. Moreover, considerable attention has been paid recently to the related condensation energy in the context of determining the pairing “mechanism” in the high temperature superconductors [87, 88]. However, in order to address the mechanism at a microscopic level, one needs to extract the condensation energy accurately along with determining the behavior of the various extrapolated polarizabilities (e.g., magnetic and electric) below T_c . In this way, one has to address the nature of the extrapolated normal state and, more specifically, the question of whether this normal state is a Fermi liquid — at temperatures below T_c , as in BCS theory. The answer we provide is unequivocally no, on all but the overdoped side of the cuprate phase diagram. There are several simple ways to support this answer using experimental thermodynamical data, which compare quite favorably with the calculations of this Chapter. We discuss here two ways, based on the specific heat — or entropy, and on the tunneling density of states.

In Fig. 7.7 we plot the calculated C_v/T and entropy S for (a)-(b) the BCS case, and compare it with the counterparts obtained for the pseudogap superconductor in (c) and (d). The dotted lines represent the Fermi liquid extrapolation. Figures 7.7(a) and (b) show that the Fermi liquid extrapolation is sensible for the BCS case — C_v/T is a constant, and S is a straight line going through the origin, yielding the consistent result: $S = 0$ at $T = 0$.

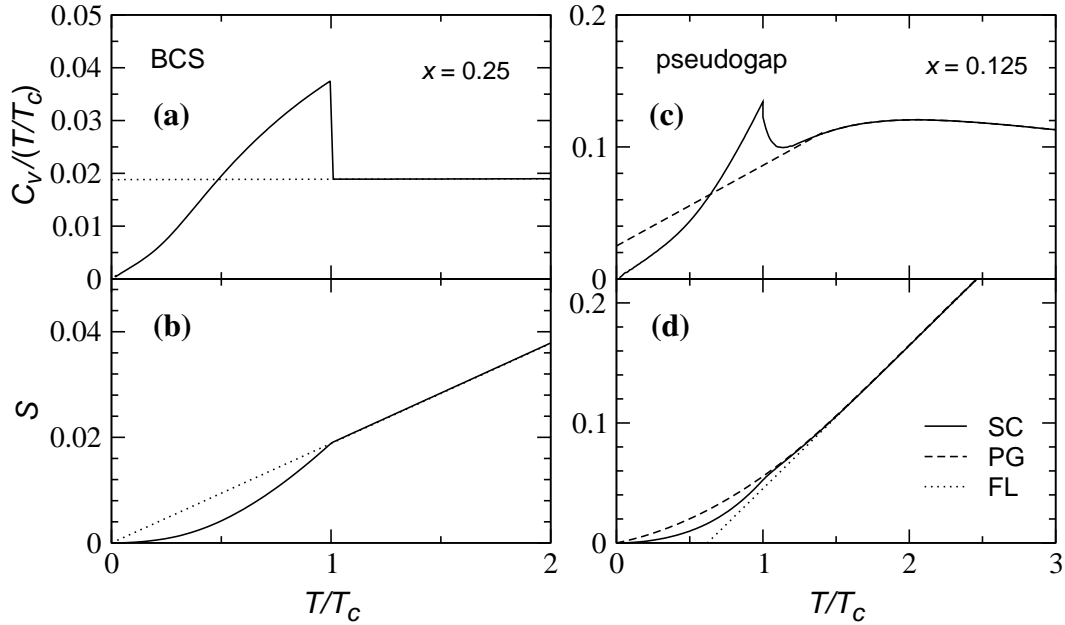


Figure 7.7: Comparison of the extrapolated normal state below T_c in (a)-(b) BCS and (c)-(d) pseudogap superconductors. Shown are the extrapolations for C_v/T and the entropy S in the upper and lower panels, respectively.

In contrast, for the pseudogap case, the Fermi liquid extrapolation is unphysical, approaching a negative entropy at low T . Finally, the dashed lines in Fig. 7.7(c)-(d) show a fairly sensible extrapolated normal state. The extrapolated C_v/T in Fig. 7.7(c) is consistent with conservation of entropy, $S = \int_0^T C_v/T dT$, i.e., the area under the C_v/T curves. The “normal” state entropy is obtained via integrating the extrapolated C_v/T , leading to a vanishing entropy at $T = 0$. Indeed, this is in fact the empirical procedure followed experimentally [81], and Figs. 7.7(c)-(d) are similar to what is observed experimentally [81] in underdoped cuprates. The “normal” state C_v/T and S turn out to be linear and quadratic in T , respectively. A rough estimate of the condensation energy can be obtained from the integral area between the solid line (for the superconducting state) and the dashed line (for the extrapolated normal state) in Fig. 7.7(d). It can be noted that, while a more precise measure of the condensation energy may be obtained by computing the field dependent Gibbs free energy, this is more complicated to implement both theoretically and experimentally.

Finally, it should be stressed that the behavior of the extrapolated C_v/T indicates that *there exists a pseudogap below T_c* . This is the same conclusion as reached in previous empirical studies of the specific heat [81].

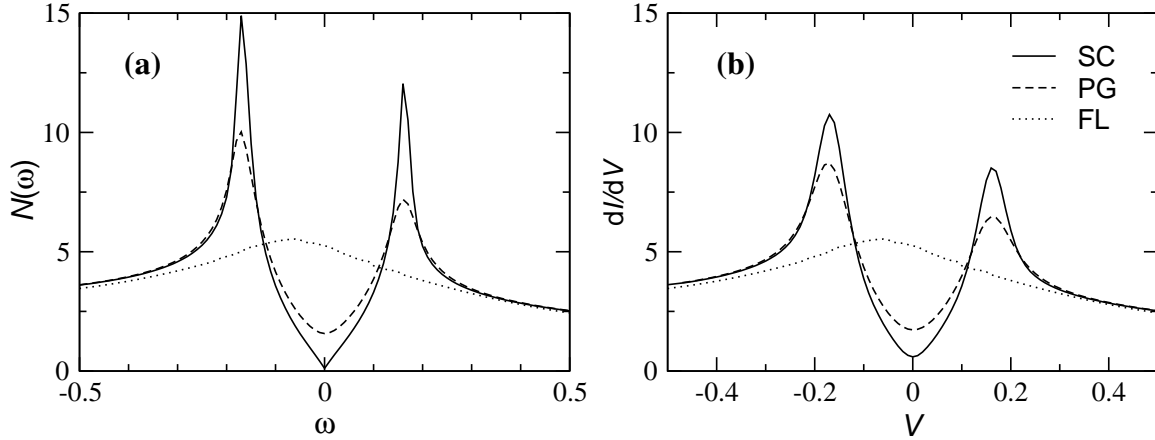


Figure 7.8: (a) Density of states and (b) SIN tunneling dI/dV characteristics of an extrapolated pseudogap “normal state” below T_c . For comparison, also plotted are Fermi liquid extrapolations.

The pseudogap also appears in the extrapolated normal state density of states below T_c . In Fig. 7.8, we show the three analogous curves for the density of states as well as the tunneling spectra, calculated at $T = 0.5T_c$. The solid curves correspond to the superconducting phase, the dotted curves to the Fermi liquid extrapolation and the dashed curves to the calculated normal state of the pseudogap phase. For the latter we assume that the full excitation gap exists without superconducting long range order. There is some experimental support for our extrapolated normal state (or PG) curves which can be obtained from vortex core spectroscopy STM measurements [82]. Thus, *we deduce from tunneling measurements that some manifestation of a pseudogap exists below T_c .*

These two studies provide reasonably strong support for the present theoretical picture.

In concluding this Chapter, we note that the onset of the superconducting long range order at T_c leads to a rapid sharpening of the quasiparticle spectral peaks, and to a discontinuity of the derivative of the density of states across T_c . As a consequence, the superconducting phase transition manifests itself as a step discontinuity or a λ -like anomaly in C_v at T_c , depending on the doping concentration. We have further shown that the pseudogap exists in extrapolated thermodynamical properties below T_c , and must be properly accounted for in a proper analysis of the condensation energy and the “pairing mechanism” or related calculated polarizabilities below T_c .

CHAPTER 8

CONCLUDING REMARKS

The work outlined in this thesis is viewed as having an impact which goes beyond understanding high T_c superconductors. Even in the days before BCS, there was a longstanding interest in Bose-Einstein condensation and its relation to superconductivity. These ideas led to the picture of Schafroth condensation, which did not receive much attention following the BCS proposal. Today, with the resurgence of interest in BEC in the alkali gases, it is even more important to understand the relationship between a BCS and BEC description of superfluidity or superconductivity. Moreover, with the discovery of more and more “exotic” superconductors, which have short coherence lengths, interest has again focused on the connections between BCS and BEC. Indeed, BEC-like or pseudogap behavior has been found (for example, in the Knight shift) in 2D organic (short ξ) superconductors. In this context, the Uemura plot of Fig. 1.5 is particularly important (not only because it suggests a BEC-like scaling between T_c and the superfluid density but) because it suggests that the cuprates are not particularly special when compared with other short ξ superconductors, including organic, heavy fermion superconductors, etc. This leads naturally to the conclusion that the most likely reason for the failure of BCS theory in these materials is the small size of ξ . A radical departure from BCS theory may not be warranted. At the very least, whatever complicated physics needs to be additionally introduced, as a *baseline*, it seems essential to address the fundamental non-BCS-mean-field effects associated with short ξ .

Beyond these general observations one may ask what is the strongest support for applying our theoretical BCS-BEC based scheme to the cuprates. After all, there are alternatives in the literature and these seem to fall into two main categories. (i) The excitations of the superconducting state are purely fermionic, and more or less describable by d -wave BCS theory, except for the introduction of Fermi liquid renormalizations. This school of thought is called “Fermi liquid based superconductivity”. (ii) The excitations of the superconducting state are essentially bosonic. This leads to the “phase fluctuation” approaches, which

are based in large part on the small values of the phase stiffness n_s/m in the very underdoped regime. Ours is a third alternative in which both fermionic and bosonic excitations coexist (although the bosonic excitations here are *not* phase fluctuations).

In establishing support for the present viewpoint, it is important to note that there are many other features of the cuprates which suggest BCS theory is not strictly applicable. Impurity effects are found to be highly local (unlike the behavior predicted by the Abrikosov-Gor'kov generalization of BCS). This locality is presumed to arise from short ξ . Moreover, there are unexpectedly localized states in the vortex cores, which are also presumed to be associated with short ξ . Even more interesting, perhaps, is that the normal state *below* T_c in a vortex core is found to have a pseudogap, much as we would expect; it is not a Fermi liquid normal state, as in BCS theory. In addition there are unusual anomalies in the thermal conductivity and an unexpectedly small non-linear Meissner effect.

8.1 SUMMARY

In this thesis, we have extended BCS theory in a natural way to short coherence length superconductors, based on a simple physical picture in which incoherent, finite momentum pairs become increasingly important as the pairing interaction becomes stronger. We went beyond the BCS mean field treatment of the single particles and the superconducting condensate, by including these finite momentum pairs at a mean field level, and we, thereby, treated the pairs and the single particles on an equal footing. Within our picture, the superconducting transition from the fermionic perspective and Bose-Einstein condensation from the bosonic perspective are just two sides of the same coin.

In this context, we have found a third equation which we call the pseudogap equation. This equation must be solved in conjunction with the excitation gap equation and the fermion number equation. The single particle number equation characterizes the single particles, the pseudogap equation, which is essentially a pair number equation, characterizes the pairs. The single particles and the pairs are interrelated via the gap equation. On one hand, this gap equation ensures the softness of the pair dispersion; on the other hand, it controls the gapping of the fermionic or single particle dispersion. In contrast to BCS, the gap equation now contains new ingredients associated with the finite momentum pairs, in

addition to the zero momentum Cooper pair condensate. The incoherent pairs lead to the pseudogap above T_c and to the very important distinction between the excitation gap and the superconducting order parameter below T_c , at intermediate and strong coupling.

In contrast to most other theoretical approaches, our theory is capable of making quantitative predictions, which can be tested. This theory was applied to the cuprates to obtain a phase diagram. (We believe this may be the first time that the cuprate phase diagram has been calculated quantitatively within any single theory). In addition, because this fitted (with one free parameter) phase diagram represented experiment quite well, it was possible to quantitatively address derived quantities, such as the hole concentration and temperature dependences of the in-plane penetration depth and specific heat. The mutually compensating contributions from fermionic quasiparticles and bosonic pair excitations have provided a natural explanation for the unusual quasi-universal behavior of the normalized in-plane superfluid density as a function of reduced temperature. Our bosonic pair excitations also demonstrate an intrinsic origin for the long mysterious linear T term in the specific heat. We found new qualitative effects as well, associated with predicted low T power laws, which arise from incoherent pair contributions. These power laws seem to be consistent with existing experiments, although more systematic experimental studies are needed. Finally, we showed that the onset of superconducting long range order leads to sharp features in specific heat at T_c , in both over- and underdoped regime. In addition, we demonstrated that the pseudogap exists in the extrapolated normal state below T_c , and must be properly accounted for in extracting the condensation energy from specific heat data.

8.2 REMARKS

The BCS form of the gap equation found in our theory is crucially related to the Leggett ground state and the G_0G scheme within the T matrix approximation. Unlike a diagrammatic GG scheme, the present G_0G scheme derives from a truncation of the equations of motion at the pair level. Our approach should be viewed as a generalized mean field theory. This is the essence of the T matrix approximation. Incoherent pairs are treated at the mean field level, no explicit pair-pair interactions are involved. To include inter-pair interactions, one presumably needs to truncate the equations of motion at a higher order. In line with this

picture, at the T matrix level, the pair dispersion is always quadratic, (except in the weak coupling limit when exact particle-hole symmetry is assumed). This dispersion is clearly different from the order parameter collective modes, which effectively include inter-pair interactions through higher order diagrams. The pairs should be thought of as “single” objects, rather than collective excitations.

One natural consequence of the T matrix approximation is the quasi-ideal Bose gas nature of the system in the strong coupling limit. The pairs (bosons) are essentially free. There is a full condensation at $T = 0$, consistent with the Leggett ground state. This is different from a “true” interacting Bose system. This is required by the BCS form of the gap equation. Had the Cooper pairs been interacting with each other, one would presumably not get the BCS gap equation. Requiring the strong coupling limit to be a true Bose liquid would be equivalent to abandoning the Leggett ground state equations, at least in the large g limit.

8.3 SPECULATIONS

Would one find a true Bose liquid in the strong coupling limit if one included higher order Green’s functions? We have tried to go beyond the T matrix approximation by truncating the equations of motion at G_4 , in the hope of retaining explicitly pair-pair interaction diagrams. Unfortunately, as pointed out by Kadanoff and Martin, it is technically extremely difficult to implement this procedure. We did find terms corresponding to pair-pair interactions but the set of coupled equations is much more complicated than would be the case for a true Bose system. In this procedure the one particle i.e, fermionic Green’s functions also enter since the starting Hamiltonian involves only inter-fermion interactions. We are, thus, not sure whether one would get a true boson like dispersion for the incoherent pairs in the strong coupling limit if one could carry out these complex calculations.

An alternative physically intuitive approach to the strong coupling limit would be to treat the pairs as fundamental objects, which might virtually decay into two fermions. (This is analogous to the π meson problem, in which each meson is composed of a quark-anti-quark pair.) In this case, one would tend to dress the two electrons within a pair in the same way. The bosons would interact only via virtual processes. It might be possible to find a

true Bose liquid behavior of the system. It should be stressed that this procedure would amount to a modification of the Leggett ground state. In addition, the two constraining equations of the Leggett formalism — the fermionic chemical potential and excitation gap — would presumably no longer be meaningful. We believe these issues are interesting on general theoretical grounds, but that this limit is not appropriate when the system is still in the fermionic regime, as seems to be the case for all known superconductors.

8.4 FUTURE DIRECTIONS

It is clear that in our formalism, the ratio T_c/Δ is not given by the BCS universal constant. Rather T_c is controlled by the pseudogap in the intermediate coupling regime. This may explain the absence of clear isotope effects. Because the pseudogap is enhanced by lower dimensionality, a higher mass anisotropy will suppress T_c . This may also be relevant to pressure effects on T_c . T_c has been found to increase with pressure in most cuprate superconductors. As the pressure increases, the interlayer distance decreases, and, thus, the interlayer hopping matrix element may increase substantially; in this way T_c is enhanced.

There are obvious extensions of the present work to include inhomogeneity and magnetic field effects. A simple speculation regarding the latter would be that a magnetic field is effective in destroying phase coherence, but does *not* affect pair formation, so that T^* and Δ are less strongly field dependent. If a pseudogapped superconductor is driven normal by a large field, it may still exhibit an excitation gap, so that it is not in a metallic phase. Said, alternatively, without phase coherence, pairs can still contribute to the excitation gap, but not to the superconductivity. Experiments which involve inhomogeneity are localized impurity effects, vortex core states, Andreev reflection, etc. An extension along these lines will be very important.

There are many other experiments we need to address. For example, the unexpectedly weak non-linear Meissner effect, the unexpectedly strong field dependence of C_v around T_c , the electrical (ac and dc) conductivity, above T_c , and the unusual anomalies in the thermal conductivity recently reported by Ong *et al* [89]. To address some of these experiments, it will be necessary to extend the current formalism above T_c to make it more practical and less computational, as was achieved here below T_c .

APPENDIX A

EXPRESSION FOR PAIR DISPERSION, $\Omega_{\mathbf{q}}$

In the long wavelength, low frequency limit, one can expand the inverse T matrix as:¹

$$t_{pg}^{-1}(\mathbf{q}, \Omega) = a_1 \Omega^2 + a_0 \Omega - \xi^2 q^2 + \tau'_0 + i\Gamma'_{\mathbf{q}, \Omega} . \quad (\text{A.1})$$

Here the imaginary terms, which are included in $\Gamma'_{\mathbf{q}, \Omega}$, are negligible below T_c . The linear contribution (\mathbf{q}) is absent due to the inversion symmetry ($\mathbf{q} \leftrightarrow -\mathbf{q}$) of the system.

In the weak coupling limit, the ratio a_0/a_1 is vanishingly small; when the system has exact particle-hole symmetry (e.g., a 2D tight binding band at half filling with a nearest neighbor hopping), a_0 vanishes. In this case the dispersion determined via

$$t_{pg}^{-1}(\mathbf{q}, \Omega) = 0 \quad (\text{A.2})$$

is linear in q , $\Omega_{\mathbf{q}} \sim cq$. In the absence of particle-hole symmetry, as g increases, a_0/a_1 increases, thus $a_0 \Omega$ gradually dominates and we find the important result: $\Omega_{\mathbf{q}} \sim Bq^2$. For any finite g and arbitrarily small q , the dispersion is always quadratic, at the lowest energies.

We are interested in the moderate and strong coupling cases, where we can drop the $a_1 \Omega^2$ term in Eq. (A.1), and hence we have

$$t_{pg}(\mathbf{q}, \Omega) = \frac{a_0^{-1}}{\Omega - \Omega_{\mathbf{q}} + \mu_{pair} + i\Gamma_{\mathbf{q}, \Omega}} , \quad (\text{A.3})$$

where

$$\Omega_{\mathbf{q}} = Bq^2 = \frac{\xi^2}{a_0} q^2 \equiv \frac{q^2}{2M^*} \quad (\text{A.4})$$

is quadratic. This defines the effective pair mass, M^* . Below T_c , we have $\mu_{pair} = 0$, as a consequence of the gap equation, $t^{-1}(Q = 0) = 0$, as is consistent with ideal Bose gas condensation.

¹Note here that the ξ which appears in the q^2 term, following the conventional notation for a Ginzburg-Landau expansion, is different from the coherence length we talk about in this Thesis.

For an anisotropic 3D or a quasi-2D case, this becomes

$$\Omega_{\mathbf{q}} = B_{\parallel} q_{\parallel}^2 + B_{\perp} q_{\perp}^2 \equiv \frac{q_{\parallel}^2}{2M_{\parallel}^*} + \frac{q_{\perp}^2}{2M_{\perp}^*} \quad (\text{A.5})$$

The inverse T matrix can be written explicitly:

$$t_{\mathbf{q}, i\Omega_n}^{-1} = g^{-1} + \sum_{\mathbf{k}} \left[\frac{1 - f(E_{\mathbf{k}}) - f(\epsilon_{\mathbf{k}-\mathbf{q}})}{E_{\mathbf{k}} + \epsilon_{\mathbf{k}-\mathbf{q}} - i\Omega_n} u_{\mathbf{k}}^2 - \frac{f(E_{\mathbf{k}}) - f(\epsilon_{\mathbf{k}-\mathbf{q}})}{E_{\mathbf{k}} - \epsilon_{\mathbf{k}-\mathbf{q}} + i\Omega_n} v_{\mathbf{k}}^2 \right] \varphi_{\mathbf{k}-\mathbf{q}/2}^2, \quad (\text{A.6})$$

where $\Omega_n = 2n\pi T$ is Matsubara frequency for a boson field. After analytical continuation, $i\Omega_n \rightarrow \Omega + i0^+$, one obtains

$$t_{\mathbf{q}, \Omega+i0^+}^{-1} = g^{-1} + \sum_{\mathbf{k}} \left[\frac{1 - f(E_{\mathbf{k}}) - f(\epsilon_{\mathbf{k}-\mathbf{q}})}{E_{\mathbf{k}} + \epsilon_{\mathbf{k}-\mathbf{q}} - \Omega - i0^+} u_{\mathbf{k}}^2 - \frac{f(E_{\mathbf{k}}) - f(\epsilon_{\mathbf{k}-\mathbf{q}})}{E_{\mathbf{k}} - \epsilon_{\mathbf{k}-\mathbf{q}} + \Omega + i0^+} v_{\mathbf{k}}^2 \right] \varphi_{\mathbf{k}-\mathbf{q}/2}^2. \quad (\text{A.7})$$

From Eq. (A.3), we have

$$\begin{aligned} a_0 &= \left. \frac{\partial}{\partial \Omega} t_{\mathbf{q}, \Omega}^{-1} \right|_{q=0, \Omega=0} \\ &= \sum_{\mathbf{k}} \left[\frac{1 - f(E_{\mathbf{k}}) - f(\epsilon_{\mathbf{k}-\mathbf{q}})}{(E_{\mathbf{k}} + \epsilon_{\mathbf{k}-\mathbf{q}})^2} u_{\mathbf{k}}^2 + \frac{f(E_{\mathbf{k}}) - f(\epsilon_{\mathbf{k}-\mathbf{q}})}{(E_{\mathbf{k}} - \epsilon_{\mathbf{k}-\mathbf{q}})^2} v_{\mathbf{k}}^2 \right] \varphi_{\mathbf{k}}^2 \\ &= \frac{1}{2\Delta^2} \sum_{\mathbf{k}} \left[[1 - 2f(\epsilon_{\mathbf{k}})] - \frac{\epsilon_{\mathbf{k}}}{E_{\mathbf{k}}} [1 - 2f(E_{\mathbf{k}})] \right] \\ &= \frac{1}{2\Delta^2} \left[n - 2 \sum_{\mathbf{k}} f(\epsilon_{\mathbf{k}}) \right], \end{aligned} \quad (\text{A.8})$$

where use has been made of the number equation (2.54) in the last step in Eq. (A.8). The imaginary part of the pair dispersion is given by

$$\begin{aligned} \Gamma_{\mathbf{q}, \Omega} &= \frac{\pi}{a_0} \sum_{\mathbf{k}} \left\{ [1 - f(E_{\mathbf{k}}) - f(\epsilon_{\mathbf{k}-\mathbf{q}})] u_{\mathbf{k}}^2 \delta(E_{\mathbf{k}} + \epsilon_{\mathbf{k}-\mathbf{q}} - \Omega) \right. \\ &\quad \left. + [f(E_{\mathbf{k}}) - f(\epsilon_{\mathbf{k}-\mathbf{q}})] v_{\mathbf{k}}^2 \delta(E_{\mathbf{k}} - \epsilon_{\mathbf{k}-\mathbf{q}} + \Omega) \right\} \varphi_{\mathbf{k}-\mathbf{q}/2}^2. \end{aligned} \quad (\text{A.9})$$

While it clearly depends on Ω in general, however, $\Gamma_{\mathbf{q}, \Omega}$ is relevant only at $\Omega = \Omega_{\mathbf{q}}$. For s -wave pairing, $\Gamma_{\mathbf{q}, \Omega_{\mathbf{q}}}$ vanishes identically when $-(E_{\mathbf{k}} - \epsilon_{\mathbf{k}-\mathbf{q}})_{\min} < \Omega_{\mathbf{q}} < (E_{\mathbf{k}} + \epsilon_{\mathbf{k}-\mathbf{q}})_{\min}$.

For d -wave pairing, detailed numerical calculations show that $\Gamma_{\mathbf{q},\Omega_{\mathbf{q}}}$ is always much smaller than $\Omega_{\mathbf{q}}$ for small \mathbf{q} , $T \leq T_c$. In both cases, the pair dispersion is well defined for small (\mathbf{q}, Ω) at $T \leq T_c$, and is given by

$$\begin{aligned}
\Omega_{\mathbf{q}} &= -\frac{1}{a_0} t_{\mathbf{q},\Omega=0}^{-1} \\
&= -\frac{1}{a_0} \left\{ g^{-1} + \sum_{\mathbf{k}} \left[\frac{1 - f(E_{\mathbf{k}}) - f(\epsilon_{\mathbf{k}-\mathbf{q}})}{E_{\mathbf{k}} + \epsilon_{\mathbf{k}-\mathbf{q}}} u_{\mathbf{k}}^2 - \frac{f(E_{\mathbf{k}}) - f(\epsilon_{\mathbf{k}-\mathbf{q}})}{E_{\mathbf{k}} - \epsilon_{\mathbf{k}-\mathbf{q}}} v_{\mathbf{k}}^2 \right] \varphi_{\mathbf{k}-\mathbf{q}/2}^2 \right\} \\
&= -\frac{1}{a_0} \left\{ \sum_{\mathbf{k}} \left[\frac{1 - f(E_{\mathbf{k}}) - f(\epsilon_{\mathbf{k}-\mathbf{q}})}{E_{\mathbf{k}} + \epsilon_{\mathbf{k}-\mathbf{q}}} u_{\mathbf{k}}^2 - \frac{f(E_{\mathbf{k}}) - f(\epsilon_{\mathbf{k}-\mathbf{q}})}{E_{\mathbf{k}} - \epsilon_{\mathbf{k}-\mathbf{q}}} v_{\mathbf{k}}^2 \right] \varphi_{\mathbf{k}-\mathbf{q}/2}^2 \right. \\
&\quad \left. - \frac{1 - 2f(E_{\mathbf{k}})}{2E_{\mathbf{k}}} \varphi_{\mathbf{k}}^2 \right\} \\
&= \sum_i B_i q_i^2 + \dots, \quad (i = 1, 2, 3). \tag{A.10}
\end{aligned}$$

Here we have used the gap equation (2.53) in the 4th line. We have verified numerically that this leading order expansion of $\Omega_{\mathbf{q}}$ is sufficient, so that higher order terms in the expansion can be dropped.

$$\begin{aligned}
-a_0 \frac{\partial \Omega_{\mathbf{q}}}{\partial \mathbf{q}} &= \sum_{\mathbf{k}} \left[-\frac{u_{\mathbf{k}}^2}{E_{\mathbf{k}} + \epsilon_{\mathbf{k}-\mathbf{q}}} + \frac{v_{\mathbf{k}}^2}{E_{\mathbf{k}} - \epsilon_{\mathbf{k}-\mathbf{q}}} \right] f'(\epsilon_{\mathbf{k}-\mathbf{q}}) \varphi_{\mathbf{k}-\mathbf{q}/2}^2 \vec{\nabla}_{\mathbf{q}} \epsilon_{\mathbf{k}-\mathbf{q}} \\
&\quad - \left[\frac{1 - f(E_{\mathbf{k}}) - f(\epsilon_{\mathbf{k}-\mathbf{q}})}{(E_{\mathbf{k}} + \epsilon_{\mathbf{k}-\mathbf{q}})^2} u_{\mathbf{k}}^2 + \frac{f(E_{\mathbf{k}}) - f(\epsilon_{\mathbf{k}-\mathbf{q}})}{(E_{\mathbf{k}} - \epsilon_{\mathbf{k}-\mathbf{q}})^2} v_{\mathbf{k}}^2 \right] \varphi_{\mathbf{k}-\mathbf{q}/2}^2 \vec{\nabla}_{\mathbf{q}} \epsilon_{\mathbf{k}-\mathbf{q}} \\
&\quad + \left[\frac{1 - f(E_{\mathbf{k}}) - f(\epsilon_{\mathbf{k}-\mathbf{q}})}{E_{\mathbf{k}} + \epsilon_{\mathbf{k}-\mathbf{q}}} u_{\mathbf{k}}^2 - \frac{f(E_{\mathbf{k}}) - f(\epsilon_{\mathbf{k}-\mathbf{q}})}{E_{\mathbf{k}} - \epsilon_{\mathbf{k}-\mathbf{q}}} v_{\mathbf{k}}^2 \right] \vec{\nabla}_{\mathbf{q}} \varphi_{\mathbf{k}-\mathbf{q}/2}^2 \\
&\equiv (1) + (2) + (3), \tag{A.11}
\end{aligned}$$

where $f'(x) = -f(x)[1 - f(x)]/T$. Thus,

$$-a_0 \frac{\partial^2 \Omega_{\mathbf{q}}}{\partial \mathbf{q}^2} \Big|_{\mathbf{q}=0} = (\text{I}) + (\text{II}) + (\text{III}), \tag{A.12}$$

where

$$(\text{I}) = -a_0 \frac{\partial^2 \Omega_{\mathbf{q}}}{\partial \mathbf{q}^2} \Big|_{\mathbf{q}=0} : \text{1st term}$$

$$\begin{aligned}
&= \sum_{\mathbf{k}} \left[\frac{u_{\mathbf{k}}^2}{(E_{\mathbf{k}} + \epsilon_{\mathbf{k}-\mathbf{q}})^2} + \frac{v_{\mathbf{k}}^2}{(E_{\mathbf{k}} - \epsilon_{\mathbf{k}-\mathbf{q}})^2} \right] f'(\epsilon_{\mathbf{k}-\mathbf{q}}) \varphi_{\mathbf{k}-\mathbf{q}/2}^2 (\vec{\nabla}_{\mathbf{q}} \epsilon_{\mathbf{k}-\mathbf{q}})^2 \Big|_{\mathbf{q}=\mathbf{0}} \\
&= \sum_{\mathbf{k}} \left[\frac{u_{\mathbf{k}}^2}{(E_{\mathbf{k}} + \epsilon_{\mathbf{k}})^2} + \frac{v_{\mathbf{k}}^2}{(E_{\mathbf{k}} - \epsilon_{\mathbf{k}})^2} \right] f'(\epsilon_{\mathbf{k}}) \varphi_{\mathbf{k}}^2 (\vec{\nabla}_{\mathbf{k}} \epsilon_{\mathbf{k}})^2 \\
&= \frac{1}{\Delta^2} \sum_{\mathbf{k}} f'(\epsilon_{\mathbf{k}}) (\vec{\nabla}_{\mathbf{k}} \epsilon_{\mathbf{k}})^2, \tag{A.13a}
\end{aligned}$$

$$\begin{aligned}
\text{(II)} &= -a_0 \frac{\partial^2 \Omega_{\mathbf{q}}}{\partial \mathbf{q}^2} \Big|_{\mathbf{q}=\mathbf{0}} : \text{2nd term} \\
&= \sum_{\mathbf{k}} \left\{ \left[\frac{u_{\mathbf{k}}^2}{(E_{\mathbf{k}} + \epsilon_{\mathbf{k}-\mathbf{q}})^2} + \frac{v_{\mathbf{k}}^2}{(E_{\mathbf{k}} - \epsilon_{\mathbf{k}-\mathbf{q}})^2} \right] f'(\epsilon_{\mathbf{k}-\mathbf{q}}) \varphi_{\mathbf{k}-\mathbf{q}/2}^2 (\vec{\nabla}_{\mathbf{q}} \epsilon_{\mathbf{k}-\mathbf{q}})^2 \right. \\
&\quad + 2 \left[\frac{1 - f(E_{\mathbf{k}}) - f(\epsilon_{\mathbf{k}-\mathbf{q}})}{(E_{\mathbf{k}} + \epsilon_{\mathbf{k}-\mathbf{q}})^3} u_{\mathbf{k}}^2 - \frac{f(E_{\mathbf{k}}) - f(\epsilon_{\mathbf{k}-\mathbf{q}})}{(E_{\mathbf{k}} - \epsilon_{\mathbf{k}-\mathbf{q}})^3} v_{\mathbf{k}}^2 \right] \varphi_{\mathbf{k}-\mathbf{q}/2}^2 (\vec{\nabla}_{\mathbf{q}} \epsilon_{\mathbf{k}-\mathbf{q}})^2 \\
&\quad - \left[\frac{1 - f(E_{\mathbf{k}}) - f(\epsilon_{\mathbf{k}-\mathbf{q}})}{(E_{\mathbf{k}} + \epsilon_{\mathbf{k}-\mathbf{q}})^2} u_{\mathbf{k}}^2 + \frac{f(E_{\mathbf{k}}) - f(\epsilon_{\mathbf{k}-\mathbf{q}})}{(E_{\mathbf{k}} - \epsilon_{\mathbf{k}-\mathbf{q}})^2} v_{\mathbf{k}}^2 \right] \\
&\quad \times \left[\varphi_{\mathbf{k}-\mathbf{q}/2}^2 \vec{\nabla}_{\mathbf{q}}^2 \epsilon_{\mathbf{k}-\mathbf{q}} + (\vec{\nabla}_{\mathbf{q}} \epsilon_{\mathbf{k}-\mathbf{q}}) \cdot (\vec{\nabla}_{\mathbf{q}} \varphi_{\mathbf{k}-\mathbf{q}/2}^2) \right] \left. \right\} \\
&= \frac{1}{\Delta^2} \sum_{\mathbf{k}} f'(\epsilon_{\mathbf{k}}) (\vec{\nabla}_{\mathbf{k}} \epsilon_{\mathbf{k}})^2 \\
&\quad + \frac{1}{\Delta^4} \sum_{\mathbf{k}} E_{\mathbf{k}} \left[\left(1 + \frac{\epsilon_{\mathbf{k}}^2}{E_{\mathbf{k}}^2} \right) [1 - 2f(E_{\mathbf{k}})] - 2 \frac{\epsilon_{\mathbf{k}}}{E_{\mathbf{k}}} [1 - 2f(\epsilon_{\mathbf{k}})] \right] \varphi_{\mathbf{k}}^{-2} (\vec{\nabla}_{\mathbf{k}} \epsilon_{\mathbf{k}})^2 \\
&\quad - \frac{1}{2\Delta^2} \sum_{\mathbf{k}} \left[[1 - 2f(\epsilon_{\mathbf{k}})] - \frac{\epsilon_{\mathbf{k}}}{E_{\mathbf{k}}} [1 - 2f(E_{\mathbf{k}})] \right] \varphi_{\mathbf{k}}^{-2} \\
&\quad \times \left[\varphi_{\mathbf{k}}^2 \vec{\nabla}_{\mathbf{k}}^2 \epsilon_{\mathbf{k}} + \frac{1}{2} (\vec{\nabla}_{\mathbf{k}} \epsilon_{\mathbf{k}}) \cdot (\vec{\nabla}_{\mathbf{k}} \varphi_{\mathbf{k}}^2) \right], \tag{A.13b}
\end{aligned}$$

$$\begin{aligned}
\text{(III)} &= -a_0 \frac{\partial^2 \Omega_{\mathbf{q}}}{\partial \mathbf{q}^2} \Big|_{\mathbf{q}=\mathbf{0}} : \text{3rd term} \\
&= \sum_{\mathbf{k}} \left\{ \left[-\frac{1 - f(E_{\mathbf{k}}) - f(\epsilon_{\mathbf{k}-\mathbf{q}})}{(E_{\mathbf{k}} + \epsilon_{\mathbf{k}-\mathbf{q}})^2} u_{\mathbf{k}}^2 - \frac{f(E_{\mathbf{k}}) - f(\epsilon_{\mathbf{k}-\mathbf{q}})}{(E_{\mathbf{k}} - \epsilon_{\mathbf{k}-\mathbf{q}})^2} v_{\mathbf{k}}^2 \right] \right. \\
&\quad \times (\vec{\nabla}_{\mathbf{q}} \epsilon_{\mathbf{k}-\mathbf{q}}) \cdot (\vec{\nabla}_{\mathbf{q}} \varphi_{\mathbf{k}-\mathbf{q}/2}^2) \\
&\quad + \left[\frac{1 - f(E_{\mathbf{k}}) - f(\epsilon_{\mathbf{k}-\mathbf{q}})}{E_{\mathbf{k}} + \epsilon_{\mathbf{k}-\mathbf{q}}} u_{\mathbf{k}}^2 - \frac{f(E_{\mathbf{k}}) - f(\epsilon_{\mathbf{k}-\mathbf{q}})}{E_{\mathbf{k}} - \epsilon_{\mathbf{k}-\mathbf{q}}} v_{\mathbf{k}}^2 \right] \vec{\nabla}_{\mathbf{q}}^2 \varphi_{\mathbf{k}-\mathbf{q}/2}^2 \left. \right\} \\
&= -\frac{1}{4\Delta^2} \sum_{\mathbf{k}} \left[[1 - 2f(\epsilon_{\mathbf{k}})] - \frac{\epsilon_{\mathbf{k}}}{E_{\mathbf{k}}} [1 - 2f(E_{\mathbf{k}})] \right] \varphi_{\mathbf{k}}^{-2} (\vec{\nabla}_{\mathbf{k}} \epsilon_{\mathbf{k}}) \cdot (\vec{\nabla}_{\mathbf{k}} \varphi_{\mathbf{k}}^2)
\end{aligned}$$

$$+ \frac{1}{4} \sum_{\mathbf{k}} \frac{1 - 2f(E_{\mathbf{k}})}{2E_{\mathbf{k}}} \vec{\nabla}_{\mathbf{k}}^2 \varphi_{\mathbf{k}}^2. \quad (\text{A.13c})$$

Finally, one has

$$\begin{aligned} \left. \frac{\partial^2 \Omega_{\mathbf{q}}}{\partial \mathbf{q}^2} \right|_{\mathbf{q}=0} &= -\frac{1}{a_0 \Delta^2} \sum_{\mathbf{k}} \left\{ \left[2f'(\epsilon_{\mathbf{k}}) + \frac{E_{\mathbf{k}}}{\Delta^2 \varphi_{\mathbf{k}}^2} \right. \right. \\ &\quad \times \left. \left[\left(1 + \frac{\epsilon_{\mathbf{k}}^2}{E_{\mathbf{k}}^2} \right) [1 - 2f(E_{\mathbf{k}})] - 2 \frac{\epsilon_{\mathbf{k}}}{E_{\mathbf{k}}} [1 - 2f(\epsilon_{\mathbf{k}})] \right] \right] (\vec{\nabla}_{\mathbf{k}} \epsilon_{\mathbf{k}})^2 \\ &\quad - \frac{1}{2} \left[[1 - 2f(\epsilon_{\mathbf{k}})] - \frac{\epsilon_{\mathbf{k}}}{E_{\mathbf{k}}} [1 - 2f(E_{\mathbf{k}})] \right] \left[\vec{\nabla}_{\mathbf{k}}^2 \epsilon_{\mathbf{k}} + \varphi_{\mathbf{k}}^{-2} (\vec{\nabla}_{\mathbf{k}} \epsilon_{\mathbf{k}}) \cdot (\vec{\nabla}_{\mathbf{k}} \varphi_{\mathbf{k}}^2) \right] \\ &\quad \left. + \frac{\Delta^2}{4} \frac{1 - 2f(E_{\mathbf{k}})}{2E_{\mathbf{k}}} \vec{\nabla}_{\mathbf{k}}^2 \varphi_{\mathbf{k}}^2 \right\}, \quad (\text{A.14}) \end{aligned}$$

and

$$\begin{aligned} B &= \frac{1}{6} \left. \frac{\partial^2 \Omega_{\mathbf{q}}}{\partial \mathbf{q}^2} \right|_{\mathbf{q}=0} && \text{for isotropic 3D, or} \\ B_{\parallel} &= \frac{1}{4} \left. \frac{\partial^2 \Omega_{\mathbf{q}}}{\partial \mathbf{q}_{\parallel}^2} \right|_{\mathbf{q}=0}, \quad B_{\perp} = \frac{1}{2} \left. \frac{\partial^2 \Omega_{\mathbf{q}}}{\partial \mathbf{q}_{\perp}^2} \right|_{\mathbf{q}=0}, && \text{for quasi-2D.} \quad (\text{A.15}) \end{aligned}$$

We will list below the results for different physical situations.

A.1 3D S-WAVE JELLIUM

The fermion dispersion and the symmetry factor are given by

$$\epsilon_{\mathbf{k}} = \frac{k^2}{2m} - \mu, \quad \varphi_{\mathbf{k}}^2 = \frac{1}{1 + \left(\frac{k}{k_0}\right)^2}. \quad (\text{A.16a})$$

$$\begin{aligned} (\vec{\nabla}_{\mathbf{k}} \epsilon_{\mathbf{k}})^2 &= \frac{k^2}{m^2} = \frac{2}{m} (\epsilon_{\mathbf{k}} + \mu), \quad \vec{\nabla}_{\mathbf{k}}^2 \epsilon_{\mathbf{k}} = \frac{3}{m}, \\ \vec{\nabla}_{\mathbf{k}}^2 \varphi_{\mathbf{k}}^2 &= \frac{2}{k_0^2} \varphi_{\mathbf{k}}^4 (1 - 4\varphi_{\mathbf{k}}^2), \quad (\vec{\nabla}_{\mathbf{k}} \epsilon_{\mathbf{k}}) \cdot (\vec{\nabla}_{\mathbf{k}} \varphi_{\mathbf{k}}^2) = -\frac{2}{m} \varphi_{\mathbf{k}}^2 (1 - \varphi_{\mathbf{k}}^2) \quad (\text{A.16b}) \end{aligned}$$

Substituting Eqs. (A.16b) into Eqs. (A.14), one obtains

$$\begin{aligned}
B = & -\frac{1}{6a_0\Delta^2} \sum_{\mathbf{k}} \left\{ \frac{4}{m} (\epsilon_{\mathbf{k}} + \mu) f'(\epsilon_{\mathbf{k}}) \right. \\
& + \frac{2}{m} \frac{E_{\mathbf{k}} (\epsilon_{\mathbf{k}} + \mu)}{\Delta^2 \varphi_{\mathbf{k}}^2} \left[\left(1 + \frac{\epsilon_{\mathbf{k}}^2}{E_{\mathbf{k}}^2} \right) [1 - 2f(E_{\mathbf{k}})] - 2 \frac{\epsilon_{\mathbf{k}}}{E_{\mathbf{k}}} [1 - 2f(\epsilon_{\mathbf{k}})] \right] \\
& - \frac{1}{2m} \left[[1 - 2f(\epsilon_{\mathbf{k}})] - \frac{\epsilon_{\mathbf{k}}}{E_{\mathbf{k}}} [1 - 2f(E_{\mathbf{k}})] \right] (1 + 2\varphi_{\mathbf{k}}^2) \\
& \left. + \frac{\Delta^2}{2k_0^2} \frac{1 - 2f(E_{\mathbf{k}})}{2E_{\mathbf{k}}} \varphi_{\mathbf{k}}^4 (1 - 4\varphi_{\mathbf{k}}^2) \right\}, \tag{A.17}
\end{aligned}$$

where a_0 is given by Eq. (A.8)

A.2 QUASI-2D S-WAVE JELLIUM

As in 3D jellium, the fermion dispersion and symmetry factor are given by

$$\epsilon_{\mathbf{k}} = \frac{k_{\parallel}^2}{2m_{\parallel}} + \frac{k_{\perp}^2}{2m_{\perp}} - \mu, \quad \varphi_{\mathbf{k}}^2 = \frac{1}{1 + \left(\frac{k_{\parallel}}{k_0}\right)^2} \quad m_{\perp} \gg m_{\parallel} \quad -\pi < k_{\perp} \leq \pi. \tag{A.18a}$$

$$(\vec{\nabla}_{\mathbf{k}} \epsilon_{\mathbf{k}})^2 = \frac{k_{\parallel}^2}{m_{\parallel}^2} \oplus \frac{k_{\perp}^2}{m_{\perp}^2} = \frac{2}{m_{\parallel}} \epsilon_F \left(\frac{k_{\parallel}^2}{k_F^2} \oplus \frac{m_{\parallel}^2 k_{\perp}^2}{m_{\perp}^2 k_F^2} \right), \quad \vec{\nabla}_{\mathbf{k}}^2 \epsilon_{\mathbf{k}} = \frac{2}{m_{\parallel}} \oplus \frac{1}{m_{\perp}},$$

$$\vec{\nabla}_{\mathbf{k}}^2 \varphi_{\mathbf{k}}^2 = \frac{4}{k_0^2} \varphi_{\mathbf{k}}^4 (1 - 2\varphi_{\mathbf{k}}^2) \oplus 0, \quad (\vec{\nabla}_{\mathbf{k}} \epsilon_{\mathbf{k}}) \cdot (\vec{\nabla}_{\mathbf{k}} \varphi_{\mathbf{k}}^2) = -\frac{2}{m_{\parallel}} \varphi_{\mathbf{k}}^2 (1 - \varphi_{\mathbf{k}}^2) \oplus 0. \tag{A.18b}$$

The ‘‘Fermi energy’’ $\epsilon_F = k_F^2/2m_{\parallel}$ is defined in a strictly 2D case, i.e., $n = \int_0^{k_F} 2d^2k/(2\pi)^2$.

Note here I have used direct sum ‘‘ \oplus ’’ to indicate that the terms will enter B_{\parallel} and B_{\perp} separately. Substituting Eqs. (A.16b) into Eqs. (A.14), one obtains

$$\begin{aligned}
B_{\parallel} = & -\frac{1}{4a_0\Delta^2} \sum_{\mathbf{k}} \left\{ \frac{4}{m_{\parallel}} \epsilon_F f'(\epsilon_{\mathbf{k}}) \frac{k_{\parallel}^2}{k_F^2} \right. \\
& + \frac{2}{m_{\parallel}} \frac{E_{\mathbf{k}} \epsilon_F}{\Delta^2 \varphi_{\mathbf{k}}^2} \left[\left(1 + \frac{\epsilon_{\mathbf{k}}^2}{E_{\mathbf{k}}^2} \right) [1 - 2f(E_{\mathbf{k}})] - 2 \frac{\epsilon_{\mathbf{k}}}{E_{\mathbf{k}}} [1 - 2f(\epsilon_{\mathbf{k}})] \right] \frac{k_{\parallel}^2}{k_F^2} \\
& \left. - \frac{1}{m_{\parallel}} \left[[1 - 2f(\epsilon_{\mathbf{k}})] - \frac{\epsilon_{\mathbf{k}}}{E_{\mathbf{k}}} [1 - 2f(E_{\mathbf{k}})] \right] \varphi_{\mathbf{k}}^2 \right\}
\end{aligned}$$

$$+ \frac{\Delta^2}{k_0^2} \frac{1 - 2f(E_{\mathbf{k}})}{2E_{\mathbf{k}}} \varphi_{\mathbf{k}}^4 (1 - 2\varphi_{\mathbf{k}}^2) \left. \vphantom{\frac{\Delta^2}{k_0^2}} \right\}, \quad (\text{A.19a})$$

$$\begin{aligned} B_{\perp} &= -\frac{1}{2a_0\Delta^2 m_{\parallel}} \sum_{\mathbf{k}} \left\{ 4\epsilon_F f'(\epsilon_{\mathbf{k}}) \frac{k_{\perp}^2}{k_F^2} \frac{m_{\parallel}^2}{m_{\perp}^2} \right. \\ &\quad + 2 \frac{E_{\mathbf{k}} \epsilon_F}{\Delta^2 \varphi_{\mathbf{k}}^2} \left[\left(1 + \frac{\epsilon_{\mathbf{k}}^2}{E_{\mathbf{k}}^2} \right) [1 - 2f(E_{\mathbf{k}})] - 2 \frac{\epsilon_{\mathbf{k}}}{E_{\mathbf{k}}} [1 - 2f(\epsilon_{\mathbf{k}})] \right] \frac{k_{\perp}^2}{k_F^2} \frac{m_{\parallel}^2}{m_{\perp}^2} \\ &\quad \left. - \frac{1}{2} \left[[1 - 2f(\epsilon_{\mathbf{k}})] - \frac{\epsilon_{\mathbf{k}}}{E_{\mathbf{k}}} [1 - 2f(E_{\mathbf{k}})] \right] \frac{m_{\parallel}}{m_{\perp}} \right\} \\ &\sim \frac{1}{2a_0\Delta^2 m_{\parallel}} \sum_{\mathbf{k}} \left[[1 - 2f(\epsilon_{\mathbf{k}})] - \frac{\epsilon_{\mathbf{k}}}{E_{\mathbf{k}}} [1 - 2f(E_{\mathbf{k}})] \right] \frac{m_{\parallel}}{m_{\perp}} \\ &= \frac{1}{2m_{\perp}} \quad \text{as} \quad \frac{m_{\parallel}}{m_{\perp}} \rightarrow 0. \end{aligned} \quad (\text{A.19b})$$

Here, use has been made of Eq. (A.8) in the last line.

If we assume that the 3rd (out-of-plane) dimension corresponds to a periodic lattice so that

$$\epsilon_{\mathbf{k}} = \frac{k_{\parallel}^2}{2m_{\parallel}} + \frac{1}{m_{\perp}} (1 - \cos k_{\perp}) - \mu, \quad (\text{A.20a})$$

and thus

$$(\vec{\nabla}_{\mathbf{k}} \epsilon_{\mathbf{k}})^2 = \frac{k_{\parallel}^2}{m_{\parallel}^2} \oplus \frac{\sin^2 k_{\perp}}{m_{\perp}^2} \quad \vec{\nabla}_{\mathbf{k}}^2 \epsilon_{\mathbf{k}} = \frac{2}{m_{\parallel}} \oplus \frac{1}{m_{\perp}} \cos k_{\perp}, \quad (\text{A.20b})$$

then

$$\begin{aligned} B_{\parallel} &= -\frac{1}{4a_0\Delta^2} \sum_{\mathbf{k}} \left\{ 2f'(\epsilon_{\mathbf{k}}) \frac{k_{\parallel}^2}{m_{\parallel}^2} \right. \\ &\quad + \frac{E_{\mathbf{k}}}{\Delta^2 \varphi_{\mathbf{k}}^2} \left[\left(1 + \frac{\epsilon_{\mathbf{k}}^2}{E_{\mathbf{k}}^2} \right) [1 - 2f(E_{\mathbf{k}})] - 2 \frac{\epsilon_{\mathbf{k}}}{E_{\mathbf{k}}} [1 - 2f(\epsilon_{\mathbf{k}})] \right] \frac{k_{\parallel}^2}{m_{\parallel}^2} \\ &\quad - \frac{1}{m_{\parallel}} \left[[1 - 2f(\epsilon_{\mathbf{k}})] - \frac{\epsilon_{\mathbf{k}}}{E_{\mathbf{k}}} [1 - 2f(E_{\mathbf{k}})] \right] \varphi_{\mathbf{k}}^2 \\ &\quad \left. + \frac{\Delta^2}{k_0^2} \frac{1 - 2f(E_{\mathbf{k}})}{2E_{\mathbf{k}}} \varphi_{\mathbf{k}}^4 (1 - 2\varphi_{\mathbf{k}}^2) \right\}, \end{aligned} \quad (\text{A.21a})$$

$$\begin{aligned}
B_{\perp} &= -\frac{1}{2a_0\Delta^2 m_{\parallel}} \sum_{\mathbf{k}} \left\{ \frac{2}{m_{\parallel}} f'(\epsilon_{\mathbf{k}}) \frac{m_{\parallel}^2}{m_{\perp}^2} \sin^2 k_{\perp} \right. \\
&\quad + \frac{1}{m_{\parallel}} \frac{E_{\mathbf{k}}}{\Delta^2 \varphi_{\mathbf{k}}^2} \left[\left(1 + \frac{\epsilon_{\mathbf{k}}^2}{E_{\mathbf{k}}^2} \right) [1 - 2f(E_{\mathbf{k}})] - 2 \frac{\epsilon_{\mathbf{k}}}{E_{\mathbf{k}}} [1 - 2f(\epsilon_{\mathbf{k}})] \right] \frac{m_{\parallel}^2}{m_{\perp}^2} \sin^2 k_{\perp} \\
&\quad \left. - \frac{1}{2} \left[[1 - 2f(\epsilon_{\mathbf{k}})] - \frac{\epsilon_{\mathbf{k}}}{E_{\mathbf{k}}} [1 - 2f(E_{\mathbf{k}})] \right] \frac{m_{\parallel}}{m_{\perp}} \cos k_{\perp} \right\} \\
&\sim \frac{1}{m_{\parallel}} \left(\frac{m_{\parallel}}{m_{\perp}} \right)^2 \quad \text{as} \quad \frac{m_{\parallel}}{m_{\perp}} \longrightarrow 0 .
\end{aligned} \tag{A.21b}$$

Eq. (A.21b) indicates that the anisotropy mass ratio m_{\parallel}/m_{\perp} of the single particle dispersion is magnified in the pair dispersion.

A.3 QUASI-2D LATTICE: S- AND D-WAVE

We assume a tight binding model for the electron dispersion and include next nearest neighbor hopping terms:

$$\epsilon_{\mathbf{k}} = 2t(2 - \cos k_x - \cos k_y) - 2t'(1 - \cos k_x \cos k_y) - 2t_z(1 - \cos k_z) - \mu \tag{A.22a}$$

$$\vec{\nabla}_{\mathbf{k}}^2 \epsilon_{\mathbf{k}} = 2t(\cos k_x + \cos k_y) - 4t' \cos k_x \cos k_y \oplus 2t_z \cos k_z$$

$$\begin{aligned}
(\vec{\nabla}_{\mathbf{k}} \epsilon_{\mathbf{k}})^2 &= 4t^2(\sin^2 k_x + \sin^2 k_y) + 4t'^2(\cos k_x - \cos k_y)^2 \\
&\quad + 4t'[-2t(\cos k_x + \cos k_y) + 2t' \cos k_x \cos k_y](1 - \cos k_x \cos k_y) \\
&\quad \oplus 4t_z^2 \sin^2 k_z
\end{aligned} \tag{A.22b}$$

A.3.1 Quasi-2D lattice: s-wave

$$\varphi_{\mathbf{k}} = 1, \quad \vec{\nabla}_{\mathbf{k}}^2 \varphi_{\mathbf{k}}^2 = (\vec{\nabla}_{\mathbf{k}} \epsilon_{\mathbf{k}}) \cdot (\vec{\nabla}_{\mathbf{k}} \varphi_{\mathbf{k}}^2) = 0 . \tag{A.23}$$

$$\begin{aligned}
B_{\parallel} = & -\frac{1}{4a_0\Delta^2} \sum_{\mathbf{k}} \left\{ \left[2f'(\epsilon_{\mathbf{k}}) + \frac{E_{\mathbf{k}}}{\Delta^2} \left[\left(1 + \frac{\epsilon_{\mathbf{k}}^2}{E_{\mathbf{k}}^2} \right) [1 - 2f(E_{\mathbf{k}})] - 2\frac{\epsilon_{\mathbf{k}}}{E_{\mathbf{k}}} [1 - 2f(\epsilon_{\mathbf{k}})] \right] \right] \right. \\
& \times \left[4t^2(\sin^2 k_x + \sin^2 k_y) + 4t'^2(\cos k_x - \cos k_y)^2 \right. \\
& + 4t'[-2t(\cos k_x + \cos k_y) + 2t' \cos k_x \cos k_y](1 - \cos k_x \cos k_y)] \\
& \left. - \frac{1}{2} \left[[1 - 2f(\epsilon_{\mathbf{k}})] - \frac{\epsilon_{\mathbf{k}}}{E_{\mathbf{k}}} [1 - 2f(E_{\mathbf{k}})] \right] [2t(\cos k_x + \cos k_y) - 4t' \cos k_x \cos k_y] \right\} \quad (\text{A.24a})
\end{aligned}$$

$$\begin{aligned}
B_{\perp} = & -\frac{1}{2a_0\Delta^2} \sum_{\mathbf{k}} \left\{ \left[2f'(\epsilon_{\mathbf{k}}) + \frac{E_{\mathbf{k}}}{\Delta^2} \left[\left(1 + \frac{\epsilon_{\mathbf{k}}^2}{E_{\mathbf{k}}^2} \right) [1 - 2f(E_{\mathbf{k}})] - 2\frac{\epsilon_{\mathbf{k}}}{E_{\mathbf{k}}} [1 - 2f(\epsilon_{\mathbf{k}})] \right] \right] \right. \\
& \left. \times 4t_z^2 \sin^2 k_z - \frac{1}{2} \left[[1 - 2f(\epsilon_{\mathbf{k}})] - \frac{\epsilon_{\mathbf{k}}}{E_{\mathbf{k}}} [1 - 2f(E_{\mathbf{k}})] \right] 2t_z \cos k_z \right\} \quad (\text{A.24b})
\end{aligned}$$

When $t' = 0$, B_{\parallel} becomes much simpler:

$$\begin{aligned}
B_{\parallel} = & -\frac{1}{4a_0\Delta^2} \sum_{\mathbf{k}} \left\{ \left[2f'(\epsilon_{\mathbf{k}}) + \frac{E_{\mathbf{k}}}{\Delta^2} \left[\left(1 + \frac{\epsilon_{\mathbf{k}}^2}{E_{\mathbf{k}}^2} \right) [1 - 2f(E_{\mathbf{k}})] - 2\frac{\epsilon_{\mathbf{k}}}{E_{\mathbf{k}}} [1 - 2f(\epsilon_{\mathbf{k}})] \right] \right] \right. \\
& \times [4t^2(\sin^2 k_x + \sin^2 k_y)] \\
& \left. - \frac{1}{2} \left[[1 - 2f(\epsilon_{\mathbf{k}})] - \frac{\epsilon_{\mathbf{k}}}{E_{\mathbf{k}}} [1 - 2f(E_{\mathbf{k}})] \right] [2t(\cos k_x + \cos k_y)] \right\} \quad (\text{A.25})
\end{aligned}$$

Setting $t_z = t$ and $t' = 0$, one obtains $B = B_{\parallel} = B_{\perp}$ for a 3D isotropic lattice with s -wave pairing $\varphi_{\mathbf{k}} = 1$ within the nearest neighbor approximation.

A.3.2 Quasi-2D lattice: d -wave

$$\varphi_{\mathbf{k}} = \cos k_x - \cos k_y, \quad \vec{\nabla}_{\mathbf{k}}^2 \varphi_{\mathbf{k}}^2 = -2(\cos 2k_x + \cos 2k_y) + 4 \cos k_x \cos k_y \quad (\text{A.26a})$$

$$(\vec{\nabla}_{\mathbf{k}} \epsilon_{\mathbf{k}}) \cdot (\vec{\nabla}_{\mathbf{k}} \varphi_{\mathbf{k}}^2) = [4t(\cos k_x + \cos k_y) - 4t'(1 + \cos k_x \cos k_y)] \varphi_{\mathbf{k}}^2. \quad (\text{A.26b})$$

$$B_{\parallel} = -\frac{1}{4a_0\Delta^2} \sum_{\mathbf{k}} \left\{ \left[2f'(\epsilon_{\mathbf{k}}) + \frac{E_{\mathbf{k}}}{\Delta^2 \varphi_{\mathbf{k}}^2} \left[\left(1 + \frac{\epsilon_{\mathbf{k}}^2}{E_{\mathbf{k}}^2} \right) [1 - 2f(E_{\mathbf{k}})] - 2\frac{\epsilon_{\mathbf{k}}}{E_{\mathbf{k}}} [1 - 2f(\epsilon_{\mathbf{k}})] \right] \right] \right\}$$

$$\begin{aligned}
& \times \left[4t^2(\sin^2 k_x + \sin^2 k_y) + 4t'^2 \varphi_{\mathbf{k}}^2 \right. \\
& + 4t' [-2t(\cos k_x + \cos k_y) + 2t' \cos k_x \cos k_y] (1 - \cos k_x \cos k_y) \\
& - \frac{1}{2} \left[[1 - 2f(\epsilon_{\mathbf{k}})] - \frac{\epsilon_{\mathbf{k}}}{E_{\mathbf{k}}} [1 - 2f(E_{\mathbf{k}})] \right] \\
& \times [6t(\cos k_x + \cos k_y) - 4t'(1 + 2 \cos k_x \cos k_y)] \\
& \left. + \Delta^2 \frac{1 - 2f(E_{\mathbf{k}})}{2E_{\mathbf{k}}} \left[-\frac{1}{2}(\cos 2k_x + \cos 2k_y) + \cos k_x \cos k_y \right] \right\}, \quad (\text{A.27a})
\end{aligned}$$

$$\begin{aligned}
B_{\perp} &= -\frac{1}{2a_0 \Delta^2} \sum_{\mathbf{k}} \left\{ \left[2f'(\epsilon_{\mathbf{k}}) + \frac{E_{\mathbf{k}}}{\Delta^2 \varphi_{\mathbf{k}}^2} \left[\left(1 + \frac{\epsilon_{\mathbf{k}}^2}{E_{\mathbf{k}}^2} \right) [1 - 2f(E_{\mathbf{k}})] - 2 \frac{\epsilon_{\mathbf{k}}}{E_{\mathbf{k}}} [1 - 2f(\epsilon_{\mathbf{k}})] \right] \right] \right. \\
& \left. \times 4t_z^2 \sin^2 k_z - \frac{1}{2} \left[[1 - 2f(\epsilon_{\mathbf{k}})] - \frac{\epsilon_{\mathbf{k}}}{E_{\mathbf{k}}} [1 - 2f(E_{\mathbf{k}})] \right] 2t_z \cos k_z \right\} \quad (\text{A.27b})
\end{aligned}$$

When $t' = 0$, Eq. (A.27a) becomes

$$\begin{aligned}
B_{\parallel} &= -\frac{1}{4a_0 \Delta^2} \sum_{\mathbf{k}} \left\{ \left[2f'(\epsilon_{\mathbf{k}}) + \frac{E_{\mathbf{k}}}{\Delta^2} \left[\left(1 + \frac{\epsilon_{\mathbf{k}}^2}{E_{\mathbf{k}}^2} \right) [1 - 2f(E_{\mathbf{k}})] - 2 \frac{\epsilon_{\mathbf{k}}}{E_{\mathbf{k}}} [1 - 2f(\epsilon_{\mathbf{k}})] \right] \right] \right. \\
& \times [4t^2(\sin^2 k_x + \sin^2 k_y)] \\
& - \frac{1}{2} \left[[1 - 2f(\epsilon_{\mathbf{k}})] - \frac{\epsilon_{\mathbf{k}}}{E_{\mathbf{k}}} [1 - 2f(E_{\mathbf{k}})] \right] [6t(\cos k_x + \cos k_y)] \\
& \left. + \Delta^2 \frac{1 - 2f(E_{\mathbf{k}})}{2E_{\mathbf{k}}} \left[-\frac{1}{2}(\cos 2k_x + \cos 2k_y) + \cos k_x \cos k_y \right] \right\} \quad (\text{A.28})
\end{aligned}$$

A.4 WEAK COUPLING LIMIT

In this section, we explore in more detail the significance of pair excitations in the weak coupling limit. We expand Eq. (A.7) to Ω^2 , so that

$$\begin{aligned}
a_1 &= \frac{1}{2} \frac{\partial^2}{\partial \Omega^2} t_{\mathbf{q}, \Omega}^{-1} \Big|_{q=0, \Omega=0} \\
&= \left[\frac{1 - f(E_{\mathbf{k}}) - f(\epsilon_{\mathbf{k}})}{(E_{\mathbf{k}} + \epsilon_{\mathbf{k}})^3} u_{\mathbf{k}}^2 - \frac{f(E_{\mathbf{k}}) - f(\epsilon_{\mathbf{k}})}{(E_{\mathbf{k}} - \epsilon_{\mathbf{k}})^3} v_{\mathbf{k}}^2 \right] \varphi_{\mathbf{k}}^2 \\
&= \frac{1}{2\Delta^4} \sum_{\mathbf{k}} E_{\mathbf{k}} \left[\left(1 + \frac{\epsilon_{\mathbf{k}}^2}{E_{\mathbf{k}}^2} \right) [1 - 2f(E_{\mathbf{k}})] - 2 \frac{\epsilon_{\mathbf{k}}}{E_{\mathbf{k}}} [1 - 2f(\epsilon_{\mathbf{k}})] \right] \varphi_{\mathbf{k}}^{-2} \quad (\text{A.29})
\end{aligned}$$

The main contribution to this integral comes from the neighborhood of $\epsilon_{\mathbf{k}} = 0$. To illustrate this, take for example a simple 3D isotropic s -wave case at $T = 0$. When $|\epsilon_{\mathbf{k}}| \gg \Delta$, one

has

$$a_1 = \frac{1}{2\Delta^4} \sum_{\mathbf{k}} \frac{(E_{\mathbf{k}} - |\epsilon_{\mathbf{k}}|)^2}{E_{\mathbf{k}} \varphi_{\mathbf{k}}^2} \approx \sum_{\mathbf{k}} \frac{\varphi_{\mathbf{k}}^2}{8E_{\mathbf{k}}^3} = \frac{N(0)}{4\Delta^2}, \quad (\text{A.30})$$

where $N(0)$ is the density of states for one spin orientation. Meanwhile, under the same approximation, one has

$$a_0 \approx \sum_{\mathbf{k}} \frac{\varphi_{\mathbf{k}}^2}{4E_{\mathbf{k}}^2} \text{sgn}(\epsilon_{\mathbf{k}}) \propto \Delta^{-1}. \quad (\text{A.31})$$

Therefore, $a_0/a_1 \propto \Delta$, and is vanishingly small as g approaches zero. In the presence of particle-hole symmetry, a_0 vanishes identically. Similarly, one can obtain approximations for $\xi^2 = a_0 B$ from Eq. (A.14). Now take $\varphi_{\mathbf{k}} = 1$, and approximate $(\vec{\nabla} \epsilon_{\mathbf{k}})^2$ by v_F^2 , one obtains

$$\xi^2 = \frac{1}{6} \left[\frac{3}{2\Delta^2} N(0) v_F^2 + a_0 \frac{3}{m} \right] \approx \frac{N(0)}{4\Delta^2} v_F^2 = a_1 v_F^2. \quad (\text{A.32})$$

Finally,

$$c = \sqrt{\xi^2/a_1} = v_F, \quad (\text{for isotropic 3D}). \quad (\text{A.33})$$

For quasi-2D, this velocity will become $c = \sqrt{\frac{3}{2}} v_F$.

It should be stressed that the residue of the pair propagator vanishes as $1/\sqrt{a_1 \xi^2} \propto \Delta^2$, and therefore does not lead to a significant contribution to the pseudogap at small g , so that one recovers BCS theory in the weak coupling limit.

An additional important observation should be made. Note here the velocity for the pair dispersion is different from that for the collective phase mode of the superconducting order parameter, given by $v_F/\sqrt{3}$ (in 3D).

A.5 EFFECTS OF THE Ω^2 TERM OF THE INVERSE T MATRIX

The two roots of the inverse T matrix are

$$\Omega_{\mathbf{q}} = \frac{-a_0 \pm \sqrt{a_0^2 + 4a_1 \xi^2 q^2}}{2a_1}. \quad (\text{A.34})$$

The contribution to pseudogap comes from the positive root:

$$\Omega_{\mathbf{q}} = \frac{1}{2} \left[\sqrt{\left(\frac{a_0}{a_1}\right)^2 + 4 \left(\frac{a_0}{a_1}\right) \Omega_{\mathbf{q}}^0} - \frac{a_0}{a_1} \right], \quad (\text{A.35})$$

where $\Omega_{\mathbf{q}}^0 = Bq^2$ is the dispersion in the absence of a_1 . In the limit $a_1/a_0 \rightarrow 0$, $\Omega_{\mathbf{q}} \rightarrow \Omega_{\mathbf{q}}^0$.

The residue of the T matrix at this pole is given by

$$\frac{1}{\sqrt{a_0^2 + 4a_1\xi^2q^2}} = \frac{1}{a_0} \frac{1}{\sqrt{1 + 4 \left(\frac{a_1}{a_0}\right) \Omega_{\mathbf{q}}^0}}. \quad (\text{A.36})$$

Note $\Omega_{\mathbf{q}}$ is quadratic in q in the long wavelength limit. Now the pseudogap equation is modified slightly:

$$a_0 \Delta_{pg}^2 = \sum_{\mathbf{q}} \left[1 + 4 \left(\frac{a_1}{a_0}\right) \Omega_{\mathbf{q}}^0 \right]^{-1/2} b(\Omega_{\mathbf{q}}). \quad (\text{A.37})$$

The ratio a_0/a_1 can be easily obtained from Eq. (A.8) and Eq. (A.29).

Since a_1 is considerable only at weak coupling, where the pseudogap is weak, we do not anticipate a strong effect of a_1 in calculations. Indeed, numerical studies show that T_c is almost unaffected, whereas Δ_{pg} is modified (enhanced) only at very weak couplings.

Among various situations, the effect of the $a_1\Omega^2$ term is most prominent in 3D jellium. Shown in Fig. A.1(a) is a comparison between the solutions for T_c , $\mu(T_c)$, and $\Delta(T_c)$ calculated with and without $a_1\Omega^2$ as a function of g in a 3D jellium model with s -wave pairing. Even in this case, the difference is very small. The values of T_c and Δ are only slightly suppressed when calculated with a_1 . Similar plots for quasi-2D with d -wave pairing shows that the curves calculated in both ways coincide.

Most importantly, the $a_1\Omega^2$ term does not modify the low T power laws in any appreciable way. In Fig. A.1(b), we plot the gap values as a function of T below T_c for the overdoped cuprates, $x = 0.175$. Evidently, the two sets of curves almost completely overlap except for the tiny (about 1%) difference in T_c . Both the main figure and the inset show that the $T^{3/4}$ dependence of Δ_{pg} is unaffected. As the pseudogap develops with underdoping (or equivalently, with increasing $-g/4t_{\parallel}$), the ratio a_1/a_0 becomes smaller, [see,

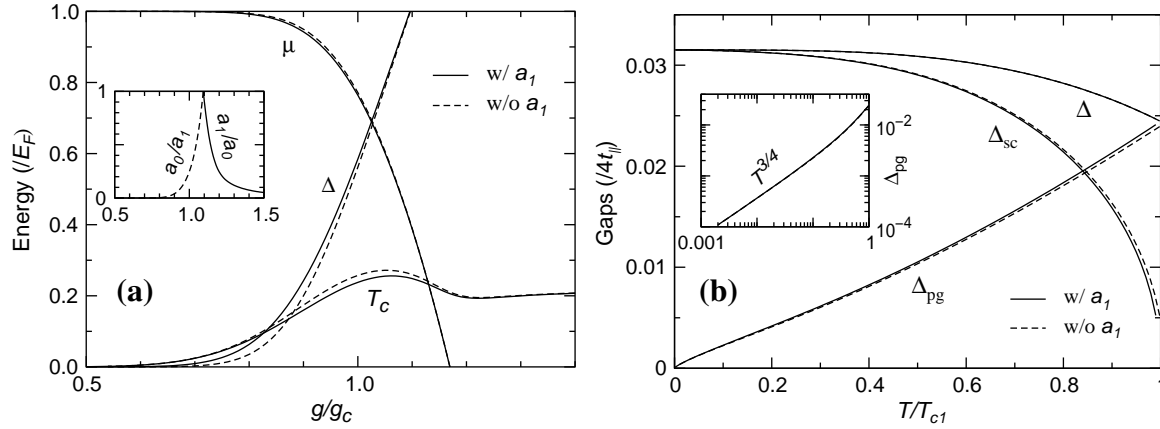


Figure A.1: Effects of the $a_1\Omega^2$ term in the T matrix expansion on the solutions for various gaps as well as T_c as a function of g and T . The solid line is calculated with the $a_1\Omega^2$ term, whereas the dashed ones without this term. Plotted in (a) are the solutions for T_c , $\Delta(T_c)$, and $\mu(T_c)$ vs g for $k_0 = 4k_F$ in 3D jellium with s -wave pairing. The ratio a_0/a_1 is shown in the inset. Plotted in (b) are the three gaps below T_c for the overdoped cuprates with doping $x = 0.175$, coupling $-g/4t_{||} = 0.26$, and anisotropy $t_{\perp}/t_{||} = 0.01$. Here $T_{c1}/4t_{||} = 0.0210$ and $T_{c2}/4t_{||} = 0.0212$ correspond to the solutions obtained with and without the $a_1\Omega^2$ term, respectively. The inset shows that the low T power law of $\Delta_{pg} \propto T^{3/4}$ is unaffected.

e.g., the inset of Fig. A.1(a)], and, therefore, the effect of $a_1\Omega^2$ becomes even weaker. We conclude that the $a_1\Omega^2$ term in the inverse T matrix expansion can be safely dropped in all calculations.

APPENDIX B

BCS–BEC CROSSOVER FOR A QUASI-2D *D*-WAVE SUPERCONDUCTOR AT ARBITRARY DENSITY

In Chapter 3, we studied the effects of low dimensionality, lattice band structure and pairing symmetry. For the *d*-wave case, we only presented the situation where the electron density was near half filling, as is relevant to the cuprates. In this Appendix, we extend this study to the whole density-coupling phase diagram, and will locate from a more general perspective the region appropriate to high T_c superconductors. In this context, we also study the difference between *d* and the *s*-wave pairing symmetries.

B.1 BOSONIC *D*-WAVE SUPERCONDUCTORS: EXTREME LOW DENSITY LIMIT

In contrast to the case of *s*-wave pairing, for a quasi-2D lattice with *d*-wave pairing, there exists a rather large threshold coupling, g_{th} , below which T_c is essentially zero. This threshold increases with decreasing electron density. This can be shown in Fig. B.1, for various densities from high to low. From the inset of Fig. 3.3(a), one can see that the threshold for the *s*-wave case is very small, since the curve follows the BCS exponential dependence; moreover, it is roughly the same for various n . By contrast, for *d*-wave pairing, Fig. B.1 shows that this threshold is very large, and is strongly density dependent. In addition, Fig. B.1 also shows that T_c survives for only a small range of g , in agreement with Fig. 3.4(b). Quite generally, T_c vanishes before μ becomes negative.

An important consequence of these observations is that the bosonic superconducting regime on a *d*-wave lattice is accessible only at extremely low and unphysical density. In this limit, the inter-particle distance is much larger than the pair size at sufficiently strong coupling, and therefore, the internal structure of the pair wavefunction becomes less important. Shown in Fig. B.2 are the behavior of T_c , Δ_{pg} , and $\mu(T_c)$ with increasing g . The threshold coupling is even larger than that shown in Fig. B.1 because of lower density.

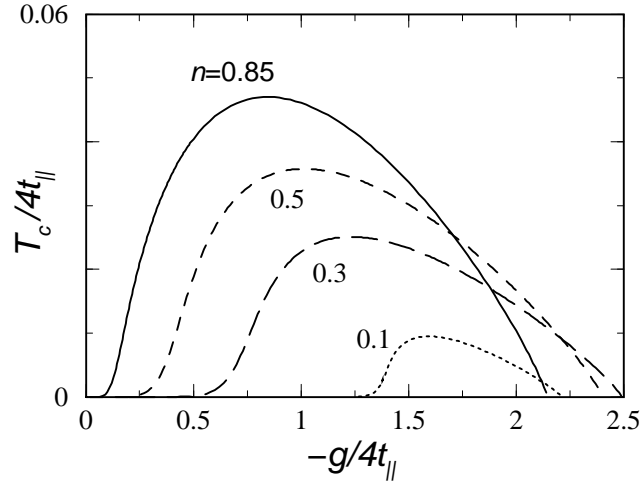


Figure B.1: T_c as a function of g for various density n on a quasi-2D lattice with d -wave pairing. Unlike in s -wave case, there exists an threshold coupling, below which T_c essentially vanishes. T_c survives only a small range of g .

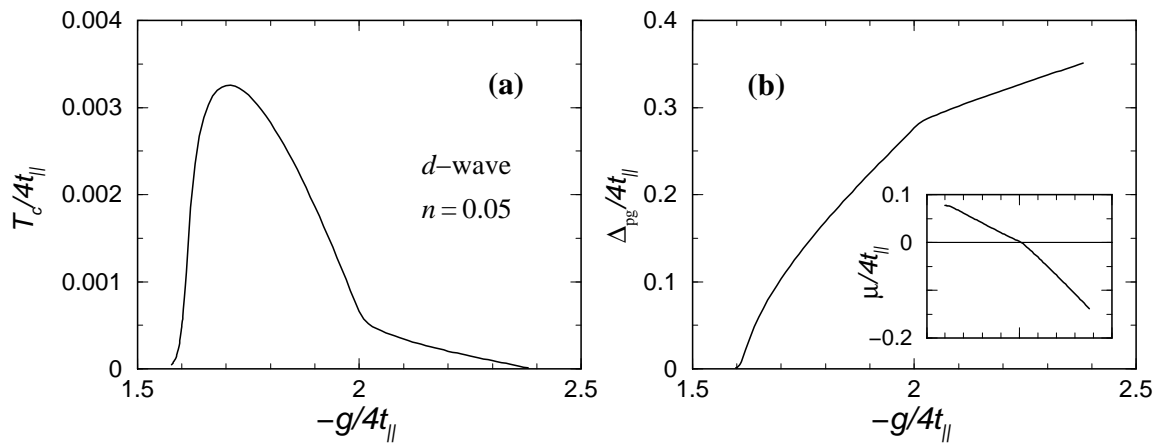


Figure B.2: (a) T_c , (b) $\Delta_{pg}(T_c)$, and $\mu(T_c)$ (inset) behavior as a function of g at very low density, $n = 0.05$. Bosonic superconducting regime is accessible for this low n . There is a kink in all three curves. $t_{\perp}/t_{\parallel} = 0.01$.

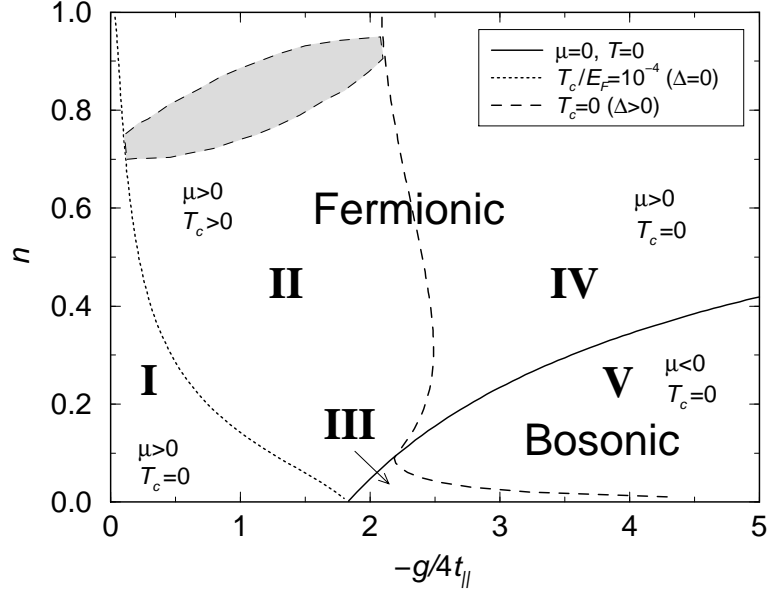


Figure B.3: $n - g$ phase diagram for a quasi-2D d -wave superconductor. There are five physically distinct regions. Bosonic superconducting regime exists only in region III, the unphysically low density limit.

The bosonic superconductor regime is accessible for roughly $-g/4t_{||} > 2$; thereafter, T_c continues to gradually decline. In contrast to s -wave pairing, it is interesting to notice that there is a kink in all three curves, as the chemical potential μ changes sign. As will be shown below, a similar kink would also appear at high densities if the bosonic superconducting regime could be accessed.

B.2 n - g PHASE DIAGRAM

Although the bosonic superconducting regime does not exist for moderate and high densities for d -wave pairing, one can still use BCS mean-field theory to solve for the chemical potential at $T = 0$, as a function of g and n , treating the system as if it were superconducting. In this way, we can find where the chemical potential changes sign and associate the sign change with the bosonic regime. We now obtain a phase diagram on a n - g plot for a quasi-2D superconductor, as shown in Fig. B.3. This phase diagram is composed of five physically distinct regions. The boundaries which separate different regions are given by the threshold coupling $g_{th}(n)$ [dotted line], $g_{max}(n)$ where T_c vanishes in the pseudogap regime [dashed line], and where the chemical potential changes sign, $\mu(n, g) = 0$

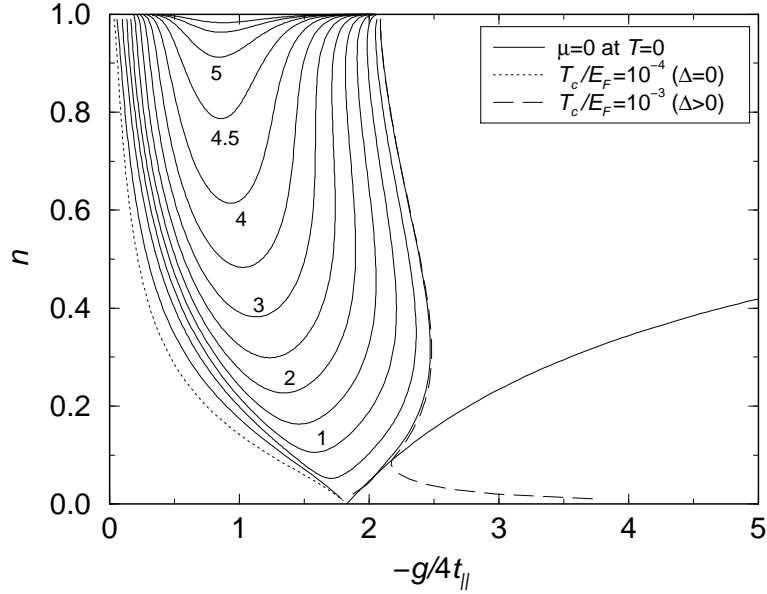


Figure B.4: Contour plot of T_c as a function of n and g for a quasi-2D d -wave superconductor, shown in Fig. B.3. The T_c value is labeled in unit of $10^{-2}E_F$, calculated for $t_{\perp}/t_{\parallel} = 0.01$.

[Solid line]. While the former two separate the superconducting regions from the non-superconducting ones, the latter separate the bosonic from fermionic regions. In region I, the coupling strength g is below the threshold g_{th} , (or, alternatively, n is too low), so that T_c is essentially zero. This is a fermionic, non-superconducting region. Region II is a fermionic, superconducting region; Region III a bosonic, superconducting region; Region IV and V are non-superconducting, fermionic and bosonic, respectively. Note here, roughly speaking, this phase diagram is independent of the anisotropy ratio t_{\perp}/t_{\parallel} except when it is extremely small.

The evolution of T_c with n and g can be plotted in a contour plot, as shown in Fig. B.4 for $t_{\perp}/t_{\parallel} = 10^{-2}$. As can be seen, as a function of g for given n , there is a maximum T_c , as also shown in Fig. B.1. On the other hand, for a given g , roughly speaking, a higher n corresponds to a higher T_c .

Now we are ready to find out where the cuprates fit into this phase diagram. For the cuprates, T_c is nonzero only when the doping concentration $x = 1 - n$ falls between about 0.05 and 0.3. In addition, there is an optimal T_c around $x = 0.15$, i.e., $n = 0.85$. Therefore, we conclude that the cuprate superconductors correspond to the shaded area in Fig. B.3.

Determining the parameter range for high T_c superconductors is very important. In

the literature (see, e.g. ref. [42]), the coupling constant is often taken to be very large. As we see here, this larger value corresponds to the non-superconducting region IV, and, therefore, is not an appropriate choice. In addition, we conclude that the cuprates are far from the bosonic regime. As shown in the inset of Fig. 3.4(b), the chemical potential is only slightly lower relative to E_F . Therefore, *the pairs in a d -wave superconductor above T_c are not bound pairs, they are sharp resonant states.* Thus, we are not in what is frequently referred to as the pre-formed pair limit.

B.3 COMPARISON WITH S -WAVE SUPERCONDUCTORS

To make the distinction between d - and s -wave clearer, we plot the $n - g$ phase diagram for a s -wave superconductor on a quasi-2D lattice, as shown in Fig. B.5(a). For a 3D jellium, the density can be roughly quantified by $(k_F/k_0)^3$. Our results are shown as a k_F/k_0 (and k_0/k_F) vs g plot, in Fig. B.5(b) (inset). Figure B.5 demonstrates that, for an s -wave superconductor, the bosonic regime can be readily accessed for intermediate and low densities. Meanwhile, there is a narrow range of n (or k_0/k_F), for which T_c disappears. It then reappears at larger g .

The threshold coupling for the s -wave lattice case is very small, in comparison with the d -wave case. This can be attributed to the d -wave pairing symmetry factor $\varphi_{\mathbf{k}} = \cos k_x - \cos k_y$ which is very small near the Fermi surface at low density. Therefore, the net coupling strength, $|g\varphi_{\mathbf{k}}^2|$, is very weak. This depressed coupling does not occur for an s -wave lattice. The situation with 3D, s -wave jellium is slightly more complicated, since g_c is related to k_0 via $g_c = -4\pi/mk_0$. For small k_F/k_0 and fixed k_F , g_c decreases with decreasing k_F/k_0 , therefore, it takes a larger g_{th}/g_c . On the other hand, for large k_F/k_0 , the net coupling at Fermi energy, $g\varphi_{\mathbf{k}}^2 \approx g(k_0/k_F)^2$, becomes small as k_0 decreases. This effect dominates the increase of g_c , and, therefore, g_{th} increases gradually with k_F/k_0 , as shown in Fig. B.5(b) and the inset.

For both s -wave cases, the high density part of the $T_c = 0$ curve closely follows the $\mu = 0$ curve. For the lattice s -wave case, these two essentially merge, as shown in Fig. B.5(a), so T_c vanishes as the system begins to enter the bosonic regime. This is very different from the d -wave case shown in Fig. B.3.

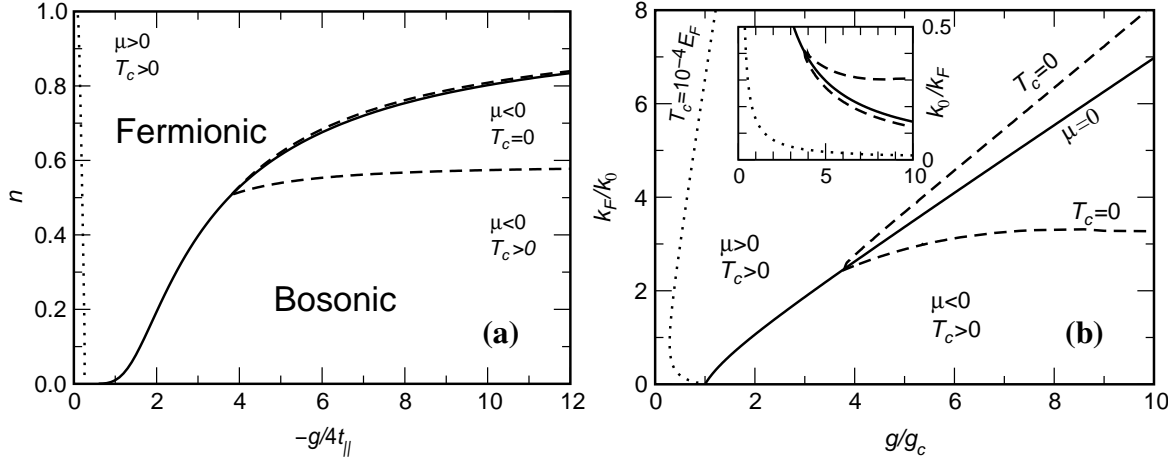


Figure B.5: (a) $n - g$ phase diagram for an s -wave superconductor on a quasi-2D lattice, and (b) $k_F/k_0 - g$ phase diagram in an isotropic 3D jellium model with s -wave pairing. The bosonic superconducting regime can be readily accessed at intermediate and low densities. A $k_0/k_F - g$ version is shown in the inset. The legends are the same as in Fig. B.3.

B.4 EFFECTIVE PAIR MASS

The $T_c = 0$ curves in the pseudogap regime in the above $n - g$ phase diagrams are calculated via the divergence of the effective pair mass, M^* , at $T = 0$. Additional differences between s - and d -wave cases come from the g dependence of M^* . M^* can be calculated at $T = 0$ via the expansion of the inverse T matrix, Eq. (2.56), assuming BCS is valid at $T = 0$. In this way, we will obtain a negative pair mass in the non-superconducting region IV and V in Fig. B.3.

Plotted in Fig. B.6(a) and (b) are the in-plane M^* vs g for quasi-2D s - and d -wave pairing, respectively. They are calculated for densities close to the critical value at which the bosonic superconducting regime exists. In both Fig. B.6(a) and Fig. B.6(b), the curve with the smallest n remains positive into the bosonic regime (i.e., $\mu < 0$), whereas the one with the highest n already becomes negative before entering the bosonic regime. For the s -wave $n = 0.55$ case, M^* becomes positive again later, signaling a re-entrant T_c .

It is interesting to note that in both cases, there is always a kink in the m/M^* curve. This kink corresponds to $\mu = 0$, that is, the boundary between fermionic and bosonic regimes. However, there is one obvious difference between the s - and d -wave cases. For the former, m/M^* increases slightly upon entering the bosonic regime, whereas for the latter, m/M^* continues to decrease. Usually, a high density will severely limit the mobility of the pairs,

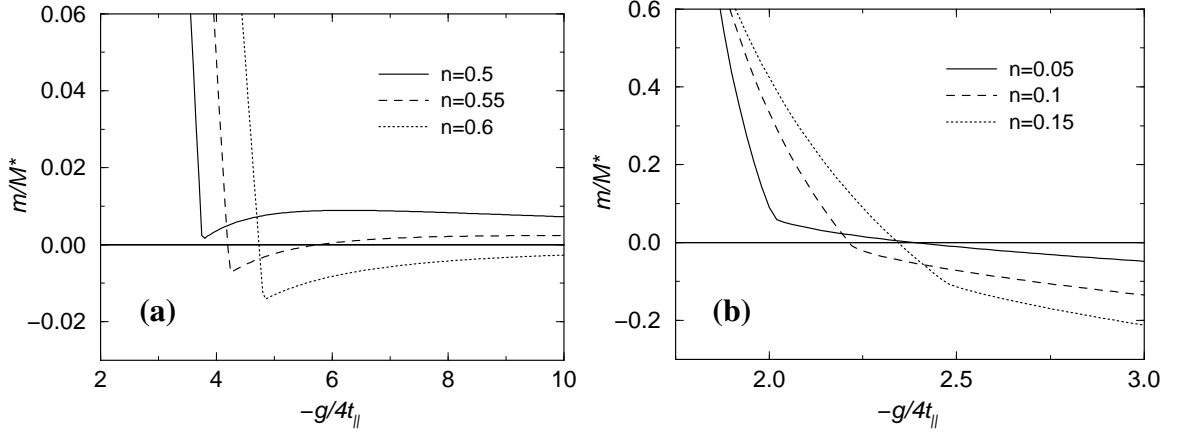


Figure B.6: In-plane effective pair mass M^* as a function of g in quasi-2D with (a) s -wave and (b) d -wave pairing, calculated at densities close to the critical value for a bosonic superconductor to exist. The parameter t_{\perp}/t_{\parallel} takes 10^{-2} and 10^{-3} , respectively.

and thus make the pairs heavy. This is due to the Pauli exclusion between the component fermions of the pairs. For the d -wave case, the interaction will become repulsive if the two electrons within a pair come too close. Therefore, a d -wave superconductor is effectively always in the large density limit. Consequently, m/M^* always monotonically decreases with g .

What happens when M^* diverges? When M^* diverges, the leading order term in the pair dispersion becomes $\Omega_{\mathbf{q}} \propto q^4$, and the critical dimension becomes 4. Therefore, T_c vanishes in 3D. The calculations beyond this point may not be meaningful. A negative pair mass means that the pair chemical potential is not zero, and thus the BCS gap equation should not be satisfied. We speculate that the Leggett ground state (BCS mean field theory + self-consistently varying μ) may not be applicable to the negative pair mass regime.

B.5 PAIR SIZE OR CORRELATION LENGTH

In this subsection, we study the pair size as a function of g , for the two pairing symmetries. This is presumed to correspond to the correlation length ξ .

Following Leggett [14, 90], the pair size at $T = 0$ can be calculated in momentum space by

$$\xi_0^2 = \frac{\langle \psi_{\mathbf{k}} | -\vec{\nabla}_{\mathbf{k}}^2 | \psi_{\mathbf{k}} \rangle}{\langle \psi_{\mathbf{k}} | \psi_{\mathbf{k}} \rangle}, \quad (\text{B.1})$$

where

$$\psi_{\mathbf{k}} = u_{\mathbf{k}}^* v_{\mathbf{k}} = \frac{\Delta \varphi_{\mathbf{k}}}{2E_{\mathbf{k}}} \quad (\text{B.2})$$

is the pair wavefunction in momentum space. Since $\langle \psi_{\mathbf{k}} | -\vec{\nabla}_{\mathbf{k}}^2 | \psi_{\mathbf{k}} \rangle = \langle \vec{\nabla}_{\mathbf{k}} \psi_{\mathbf{k}} | \vec{\nabla}_{\mathbf{k}} \psi_{\mathbf{k}} \rangle$ and

$$\vec{\nabla}_{\mathbf{k}} \psi_{\mathbf{k}} = \frac{\Delta \epsilon_{\mathbf{k}}}{2E_{\mathbf{k}}^3} \left(\epsilon_{\mathbf{k}} \vec{\nabla}_{\mathbf{k}} \varphi_{\mathbf{k}} - \varphi_{\mathbf{k}} \vec{\nabla}_{\mathbf{k}} \epsilon_{\mathbf{k}} \right), \quad (\text{B.3})$$

we integrate by parts, and obtain

$$\xi_0^2 = \frac{\sum_{\mathbf{k}} \frac{\epsilon_{\mathbf{k}}^2}{E_{\mathbf{k}}^6} \left[\epsilon_{\mathbf{k}}^2 (\vec{\nabla}_{\mathbf{k}} \varphi_{\mathbf{k}})^2 + \varphi_{\mathbf{k}}^2 (\vec{\nabla}_{\mathbf{k}} \epsilon_{\mathbf{k}})^2 - 2\epsilon_{\mathbf{k}} \varphi_{\mathbf{k}} (\vec{\nabla}_{\mathbf{k}} \epsilon_{\mathbf{k}}) \cdot (\vec{\nabla}_{\mathbf{k}} \varphi_{\mathbf{k}}) \right]}{\sum_{\mathbf{k}} \frac{\varphi_{\mathbf{k}}^2}{E_{\mathbf{k}}^2}}. \quad (\text{B.4})$$

Shown in Fig. B.7(a) is the pair size ξ_0 as a function of g for a quasi-2D lattice with s -wave pairing. Also plotted here is the chemical potential, μ . As expected, for s -wave pairing, as g increases, the pair size ξ_0 shrinks, and μ decreases.

In contrast, for the d -wave case, the situation is very different. In the fermionic regime ($\mu > 0$), the integrand of the numerator in Eq. (B.4) contains four *essential* singularities (one in each quadrant) where the Brillouin zone diagonals cross the Fermi surface (so that $E_{\mathbf{k}} = 0$). In contrast to a simple pole, these singularities have a different limiting behavior when approached from different directions. When approached along the Fermi surface, the integrand vanishes identically, whereas when approached along the diagonals, as well as any other direction, the integrand diverges as $1/\delta k^2$, where δk is the deviation of the momentum away from these singularities. These singularities lead to a logarithmic divergence of the integral ($\propto \ln \delta k$). This reflects the non-local effect that the correlation length in the nodal directions diverges (as $1/\Delta_{\mathbf{k}}$). The logarithmic divergence may be regularized by a small scattering rate between quasiparticles so that $E_{\mathbf{k}}$ never vanishes identically. Equivalently, one may add a tiny lower bound to $\varphi_{\mathbf{k}}^2$. However, in the bosonic regime, the d -wave gap nodes disappear, and the minimum excitation gap is given by $|\mu|$ at the original nodal points. Plotted in Fig. B.7(b) is the pair size ξ_0 for the d -wave case. As g increases, ξ_0 first decreases rapidly, and then increases slightly before $\mu = 0$ is reached. As is evident from the figure, there is a jump when μ changes sign. This jump is associated with the full

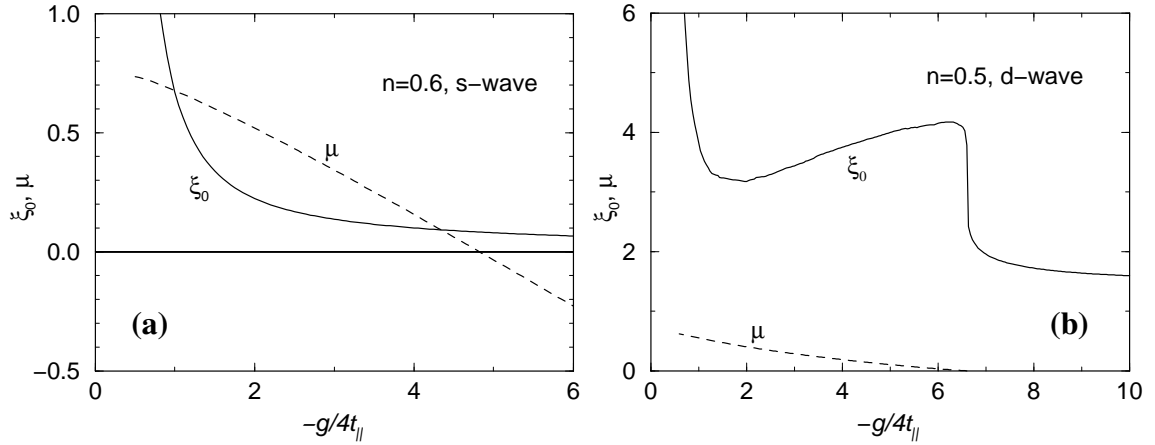


Figure B.7: Pair size ξ_0 as a function of g with (a) s - and (b) d -wave pairing on a quasi-2D lattice. Also plotted is μ . There is a jump in ξ_0 with d -wave pairing across the fermionic-bosonic boundary. We set a lower bound 10^{-12} for $\varphi_{\mathbf{k}}^2$ in (b). The unit for ξ_0 is a , the lattice constant.

gapping of the excitation spectrum. In the bosonic regime, the pair size shrinks gradually as g further increases. In this respect, the system behaves like an anisotropic s -wave superconductor. On the other hand, the pairing interaction still has a d -wave symmetry, and therefore, the pair size cannot be smaller than the lattice spacing a . As can be seen from the figure, ξ_0 is much larger in the d -wave case than in the s -wave case. The former is always larger than a , whereas the latter is much smaller than a .

In summary, in this Appendix, we studied in detail the difference between s - and d -wave superconductors as a function of g and n . We constructed a phase diagram for a generic quasi-2D superconductor as an $n - g$ plot, and compared with that for an s -wave superconductor, associated with either a quasi-2D lattice or 3D jellium. We found that d -wave symmetry leads to a very different behavior. The cuprate superconductors are far from the bosonic regime in the $n - g$ phase diagram. Finally, we showed that d -wave symmetry also leads to different behavior of the effective pair mass and pair size, as a function of g . Due to the large pair size, the inverse pair mass m/M^* monotonically decreases with g in the d -wave case, whereas in the s -wave case it starts to increase again at intermediate and low densities upon entering the bosonic regime. For the very dilute limit, we find that, unlike the s -wave case, there are kinks in the T_c , μ , and Δ curves as the coupling g crosses the fermionic-bosonic boundary (where $\mu = 0$). Associated with these kinks, there is a jump in the pair size across this boundary.

APPENDIX C

EXTRAPOLATION FOR THE COUPLED EQUATIONS ABOVE T_c

Above T_c , the effective chemical potential, μ_{pair} is no longer zero, so that the gap equation no longer holds. Close to T_c , we can still use the T matrix expansion, Eq. (2.55), which implies

$$t_{pg}^{-1}(\mathbf{0}, 0) = a_0 \mu_{pair} . \quad (\text{C.1})$$

Since now $t_{pg}(Q)$ no longer diverges at $Q = 0$, in principle, Eq. (2.48) may no longer be a good approximation. However, for a *crude* estimate, it may still be reasonably good when T is close to T_c , where μ_{pair} is small.

Associated with this non-vanishing μ_{pair} , the pair dispersion $\Omega_{\mathbf{q}}$ must be replaced by $\Omega_{\mathbf{q}} - \mu_{pair}$. Neglecting the effects of a finite life time for both the fermions and the pairs, the number equation remains unchanged. Finally, we arrive at (with $\Delta = \Delta_{pg}$)

$$a_0 g \mu_{pair} = 1 + g \sum_{\mathbf{k}} \frac{1 - 2f(E_{\mathbf{k}})}{2E_{\mathbf{k}}} \varphi_{\mathbf{k}}^2 , \quad (\text{C.2a})$$

$$n = 2 \sum_{\mathbf{k}} \left[v_{\mathbf{k}}^2 + \frac{\epsilon_{\mathbf{k}}}{E_{\mathbf{k}}} f(E_{\mathbf{k}}) \right] , \quad (\text{C.2b})$$

$$a_0 \Delta^2 = \sum_{\mathbf{q}} b(\Omega_{\mathbf{q}} - \mu_{pair}) . \quad (\text{C.2c})$$

This set of equations should be supplemented by

$$a_0 \Delta^2 = \frac{1}{2} \left[n - 2 \sum_{\mathbf{k}} f(\epsilon_{\mathbf{k}}) \right] . \quad (\text{C.2d})$$

Equations (C.2) can be used to obtain an *approximate* solution for $(\Delta, \mu, \mu_{pair})$, as well as a_0 , for given g and $T \geq T_c$.

APPENDIX D

DERIVATION FOR THE PAIRON CONTRIBUTION TO THE SPECIFIC HEAT

In this appendix, we derive Eq. (4.20) for the pair excitation contribution to the entropy, starting from Eq. (4.21). We will use the analytically continued real frequency representation for the T matrix and the pair susceptibility χ . Since $t_{pg}(Q) = t(Q)$ for $Q \neq 0$, we will drop the subscript “pg” of the T matrix for brevity.

Equation (4.21) can be rewritten as

$$\Omega_{pair} = \sum_{\mathbf{q} \neq 0} \int_C \frac{d\Omega}{2\pi i} b(\Omega) \ln [1 + g\chi(\mathbf{q}, \Omega)] , \quad (\text{D.1})$$

where the contour c encircles the real axis clockwise but excludes the origin. The entropy is given by

$$\begin{aligned} S_{pair} &= -\frac{\partial \Omega}{\partial T} \\ &= -\sum_{\mathbf{q}} \int_C \frac{d\Omega}{2\pi i} \left[\frac{\partial b(\Omega)}{\partial T} \ln [1 + g\chi(\mathbf{q}, \Omega)] - b(\Omega)t(\mathbf{q}, \Omega) \frac{\partial \chi(\mathbf{q}, \Omega)}{\partial T} \right] \\ &\equiv (\text{I}) + (\text{II}) . \end{aligned} \quad (\text{D.2})$$

The first term is associated with the scattering phase shift:

$$\begin{aligned} (\text{I}) &= \sum_{\mathbf{q}} \int_{-\infty}^{\infty} \frac{d\Omega}{\pi} \frac{\partial b(\Omega)}{\partial T} \text{Arg} \frac{t(\mathbf{q}, \Omega + i0)}{g} \\ &= \sum_{\mathbf{q}} \int_{-\infty}^{\infty} \frac{d\Omega}{\pi} \frac{\partial b(\Omega)}{\partial T} \theta(\Omega - \Omega_{\mathbf{q}}) \left[\pi - \tan^{-1} \frac{\Gamma_{\mathbf{q}}}{\Omega - \Omega_{\mathbf{q}}} \right] , \end{aligned} \quad (\text{D.3})$$

where in the second step, we have used the T matrix expansion, Eq. (2.55) (with $\mu_{pair} = 0$), and the fact that $g < 0$ as well as $a_0 > 0$. Here $\theta(x)$ is the usual step function. We have replaced $\Gamma_{\mathbf{q}, \Omega}$ by $\Gamma_{\mathbf{q}, \Omega_{\mathbf{q}}} \equiv \Gamma_{\mathbf{q}}$. As can be seen from Eq. (A.9), $\Gamma_{\mathbf{q}} = 0$ when

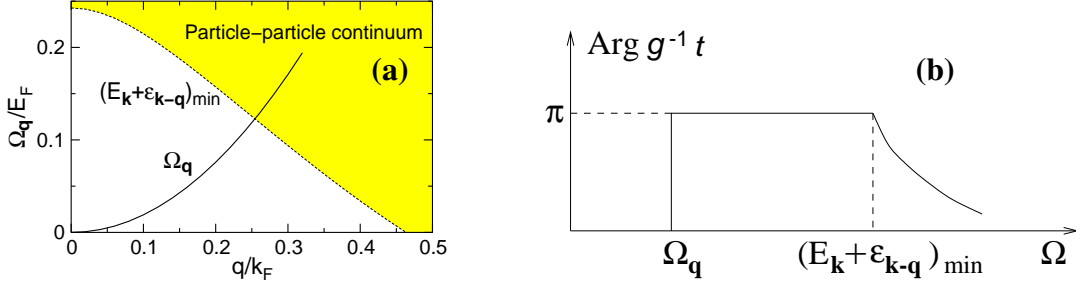


Figure D.1: Typical behavior of (a) the pair dispersion $\Omega_{\mathbf{q}}$ and of (b) the scattering phase shift in the T matrix with s -wave pairing. $\Omega_{\mathbf{q}}$ in (a) is calculated at $T = 0.5T_c$, $g = g_c$, and $k = 4k_F$ in 3D jellium.

$-(E_{\mathbf{k}} - \epsilon_{\mathbf{k}-\mathbf{q}})_{\min} < \Omega_{\mathbf{q}} < (E_{\mathbf{k}} + \epsilon_{\mathbf{k}-\mathbf{q}})_{\min}$. When $\Omega_{\mathbf{q}} > (E_{\mathbf{k}} + \epsilon_{\mathbf{k}-\mathbf{q}})_{\min}$, the pair dispersion intersects the particle-particle continuum, and therefore becomes damped, with $\Gamma_{\mathbf{q}} > 0$. Shown in Fig. D.1(a) is an example, calculated at intermediate coupling in 3D jellium with s -wave pairing. In this context, the typical behavior of the phase shift is $\delta = \text{Arg } g^{-1}t(\mathbf{q}, \Omega)$ for s -wave pairing is plotted in Fig. D.1(b). $\delta = \pi$ before $\Omega_{\mathbf{q}}$ intersects the particle-particle continuum. For d -wave pairing, $\min(E_{\mathbf{k}} + \epsilon_{\mathbf{k}-\mathbf{q}}) = 0$, nevertheless, $\Gamma_{\mathbf{q}}$ is small and $\delta \approx \pi$ for small \mathbf{q} , since the phase space for low energy (nodal) quasiparticle excitations is small. Furthermore, the main contribution in Eq. (D.3) comes from the small \mathbf{q} region, therefore we may neglect the contribution of $\Gamma_{\mathbf{q}}$ so that

$$(I) \approx \sum_{\mathbf{q}} \int_{\Omega_{\mathbf{q}}}^{\infty} d\Omega \frac{\partial b(\Omega)}{\partial T}. \quad (\text{D.4})$$

This approximation amounts to treating the pair excitations as free bosons.

The second term in Eq. (D.2) can be further split into two terms:

$$\begin{aligned} (\text{II}) &= - \sum_{\mathbf{q}} \int_{-\infty}^{\infty} \frac{d\Omega}{\pi} b(\Omega) \left[\text{Im } t(\mathbf{q}, \Omega + i0) \text{Re} \frac{\partial \chi(\mathbf{q}, \Omega)}{\partial T} + \text{Re } t(\mathbf{q}, \Omega + i0) \text{Im} \frac{\partial \chi(\mathbf{q}, \Omega)}{\partial T} \right] \\ &\equiv (\text{II}a) + (\text{II}b), \end{aligned} \quad (\text{D.5})$$

where

$$\text{Im } t(\mathbf{q}, \Omega + i0) = -\frac{1}{a_0} \frac{\Gamma_{\mathbf{q}}}{(\Omega - \Omega_{\mathbf{q}})^2 + \Gamma_{\mathbf{q}}^2} \approx -\frac{\pi}{a_0} \delta(\Omega - \Omega_{\mathbf{q}}), \quad (\text{D.6})$$

$$\text{Re} \frac{\partial \chi(\mathbf{q}, \Omega)}{\partial T} = \frac{\partial}{\partial T} [a_0(\Omega - \Omega_{\mathbf{q}})] \approx -a_0 \frac{\partial \Omega_{\mathbf{q}}}{\partial T}, \quad (\text{D.7})$$

and

$$\text{Im} \frac{\partial \chi(\mathbf{q}, \Omega)}{\partial T} = \frac{\partial}{\partial T} (a_0 \Gamma_{\mathbf{q}}) \approx 0. \quad (\text{D.8})$$

Here use has been made of the fact that a_0 is essentially temperature independent. (See, e.g., Figs. 4.1 and 6.2). In this way, we have

$$(\text{II}a) \approx - \sum_{\mathbf{q}} b(\Omega_{\mathbf{q}}) \frac{\partial \Omega_{\mathbf{q}}}{\partial T}, \quad \text{and} \quad (\text{II}b) \approx 0. \quad (\text{D.9})$$

Substituting Eqs. (D.3), (D.5), and (D.9) into Eq. (D.2), we finally obtain

$$S_{pair} = \sum_{\mathbf{q}} \int_{\Omega_{\mathbf{q}}}^{\infty} d\Omega \frac{\partial b(\Omega)}{\partial T} - \sum_{\mathbf{q}} b(\Omega_{\mathbf{q}}) \frac{\partial \Omega_{\mathbf{q}}}{\partial T}. \quad (\text{D.10})$$

The first term corresponds to a free boson contribution, and the second term reflects the effect of the T dependence of the pair dispersion. In general, $\Omega_{\mathbf{q}}$ does not change much with temperature, especially in the low T regime, and may thereby be neglected. In this way, we obtain the free boson-like expression, Eq. (4.20), for the pairon contribution to the entropy. The frequency integration in Eq. (D.10) can be easily carried out. We then obtain a simple expression for Ω_{pair} :

$$\Omega_{pair} = - \sum_{\mathbf{q}} \int_{\Omega_{\mathbf{q}}}^{\infty} b(\Omega) d\Omega. \quad (\text{D.11})$$

This describes free bosons with dispersion $\Omega_{\mathbf{q}}$.

To see the equivalence between the first term of Eq. (D.10) and Eq. (4.20), it suffices to note that

$$\frac{\partial b(\Omega)}{\partial T} = - \frac{\partial b(\Omega)}{\partial \Omega} \frac{\Omega}{T}, \quad \text{and} \quad \frac{b(\Omega)}{T} = - \frac{\partial \ln[1 + b(\Omega)]}{\partial \Omega}, \quad (\text{D.12})$$

so that

$$\begin{aligned} \int_{\Omega_{\mathbf{q}}}^{\infty} d\Omega \frac{\partial b(\Omega)}{\partial T} &= - \int_{\Omega_{\mathbf{q}}}^{\infty} d\Omega \frac{\Omega}{T} \frac{\partial b(\Omega)}{\partial \Omega} \\ &= b(\Omega_{\mathbf{q}}) \frac{\Omega_{\mathbf{q}}}{T} - \int_{\Omega_{\mathbf{q}}}^{\infty} d\Omega \frac{\partial \ln[1 + b(\Omega_{\mathbf{q}})]}{\partial \Omega} \\ &= [1 + b(\Omega_{\mathbf{q}})] \ln[1 + b(\Omega_{\mathbf{q}})] - b(\Omega_{\mathbf{q}}) \ln b(\Omega_{\mathbf{q}}). \end{aligned} \quad (\text{D.13})$$

APPENDIX E

EVALUATION OF THE VERTEX CORRECTIONS

In this appendix we demonstrate an explicit cancellation between the Maki-Thompson (MT) and Aslamazov-Larkin (AL) diagrams of Fig. 3. In this way we prove that the contribution to the vertex correction $\delta\Lambda$ from the superconducting order parameter is given by the Maki-Thompson diagram, and the pseudogap contribution $\delta\Lambda_{pg}$ comes from MT and AL diagrams. It is easy to demonstrate a cancellation between the MT diagram and the AL diagrams, which will greatly simplify the calculations. In general, we have

$$\delta\Lambda_{pg}^\mu(K, K - Q)q_\mu = -(MT)_{pg} + \sum_P t_{pg}(P)G_0(P - K)\frac{\partial\varphi_{\mathbf{k}-\mathbf{p}/2-\mathbf{q}/2}^2}{\partial\mathbf{k}} \cdot \mathbf{q}, \quad (\text{E.1})$$

where $(MT)_{pg}$ refers to the MT diagram contribution, and $t_{pg}(Q \neq 0)$ is the T matrix or pair propagator.

To prove this cancellation, we notice that the vertex corrections in the (four-)current-current correlation functions can be obtained from proper vertex insertions in the single particle Green's functions in the self-energy diagram. In the pairing approximation (G_0G scheme) we have

$$\Sigma_{pg}(K) = \sum_L t_{pg}(K + L)G_0(L)\varphi_{(K-L)/2}^2, \quad (\text{E.2})$$

where L is the four-momentum of the fermion loop, this procedure leads to one Maki-Thompson diagram and two Aslamazov-Larkin diagrams.

Obviously, L in the Eq. (E.2) is a dummy variable so that its variation does not change $\Sigma(K)$, namely,

$$\begin{aligned} 0 &= \sum_L [t_{pg}(K + L + \Delta L)G_0(L + \Delta L)\varphi_{(K-L-\Delta L)/2}^2 - t_{pg}(K + L)G_0(L)\varphi_{(K-L)/2}^2] \\ &= \sum_L \left\{ [t_{pg}(K + L + \Delta L) - t_{pg}(K + L)] G_0(L + \Delta L)\varphi_{(K-L-\Delta L)/2}^2 \right. \end{aligned}$$

$$\begin{aligned}
& + t_{pg}(K+L)[G_0(L+\Delta L) - G_0(L)]\varphi_{(K-L-\Delta L)/2}^2 \\
& + t_{pg}(K+L)G_0(L)[\varphi_{(K-L-\Delta L)/2}^2 - \varphi_{(K-L)/2}^2] \} \quad (E.3)
\end{aligned}$$

Using $G(K)G^{-1}(K) = 1$, we obtain

$$\begin{aligned}
G(K+\Delta K) - G(K) &= -G(K)[G^{-1}(K+\Delta K) - G^{-1}(K)]G(K+\Delta K) \\
&= -G(K)\Lambda_\mu(K+\Delta K, K)G(K)\Delta K^\mu, \quad (E.4a)
\end{aligned}$$

where $G^{-1}(K+\Delta K) - G^{-1}(K) \approx \Lambda_\mu(K+\Delta K, K)\Delta K^\mu$ is the full vertex. Similarly, we have

$$\begin{aligned}
G_0(K+\Delta K) - G_0(K) &= -G_0(K)[G_0^{-1}(K+\Delta K) - G_0^{-1}(K)]G_0(K+\Delta K) \\
&= -G_0(K)\lambda_\mu(K+\Delta K, K)G_0(K)\Delta K^\mu, \quad (E.4b)
\end{aligned}$$

where $G_0^{-1}(K+\Delta K) - G_0^{-1}(K) \approx \lambda_\mu(K+\Delta K, K)\Delta K^\mu$ is the bare vertex, and $\lambda^\mu(K+\Delta K, K) = (1, \vec{\nabla}_{\mathbf{k}}\epsilon_{\mathbf{k}+\Delta\mathbf{k}/2})$. Equations (E.4a) correspond to the vertex insertions diagrammatically along the full and bare Green's functions, respectively.

Using $t_{pg}(K+L) = \frac{g}{1+g\chi(K+L)}$, we obtain

$$t_{pg}(K+L+\Delta L) - t_{pg}(K+L) = -t_{pg}(K+L+\Delta L)[\chi(K+L+\Delta L) - \chi(K+L)]t_{pg}(K+L) \quad (E.5)$$

Writing $\chi(K+L) = \sum_{L'} G(L')G_0(K+L-L')\varphi_{L'-(K+L)/2}^2$, we have

$$\begin{aligned}
& \chi(K+L+\Delta L) - \chi(K+L) \\
&= \sum_{L'} G(L') \left\{ [G_0(K+L-L'+\Delta L) - G_0(K+L-L')] \varphi_{L'-(K+L+\Delta L)/2}^2 \right. \\
& \quad \left. + G_0(K+L-L')[\varphi_{L'-(K+L+\Delta L)/2}^2 - \varphi_{L'-(K+L)/2}^2] \right\}. \quad (E.6)
\end{aligned}$$

On the other hand, writing $\chi(K+L) = \sum_{L'} G(K+L-L')G_0(L')\varphi_{(K+L)/2-L'}^2$, we get

$$\chi(K+L+\Delta L) - \chi(K+L)$$

$$\begin{aligned}
&= \sum_{L'} \left\{ [G(K+L-L'+\Delta L) - G(K+L-L')] G_0(L') \varphi_{(K+L+\Delta L)/2-L'}^2 \right. \\
&\quad \left. + G(L') G_0(K+L-L') [\varphi_{L'-(K+L-\Delta L)/2}^2 - \varphi_{L'-(K+L)/2}^2] \right\}. \quad (\text{E.7})
\end{aligned}$$

Combining Eq. (E.6) and Eq. (E.7), we obtain to the first order of ΔL

$$\begin{aligned}
&\chi(K+L+\Delta L) - \chi(K+L) \\
&= \frac{1}{2} \sum_{L'} \left\{ G(L') [G_0(K+L-L'+\Delta L) - G_0(K+L-L')] \varphi_{L'-(K+L+\Delta L)/2}^2 \right. \\
&\quad \left. + [G(K+L-L'+\Delta L) - G(K+L-L')] G_0(L') \varphi_{L'-(K+L+\Delta L)/2}^2 \right\}, \quad (\text{E.8})
\end{aligned}$$

where we have assumed in general $\varphi_K^2 = \varphi_{-K}^2$. Substituting Eq. (E.8) and Eq. (E.5) into Eq. (E.3), we obtain

$$\begin{aligned}
0 &= -\frac{1}{2} \sum_{LL'} t_{pg}(K+L+\Delta L) t_{pg}(K+L) \left\{ G(L') [G_0(K+L-L'+\Delta L) \right. \\
&\quad \left. - G_0(K+L-L')] \varphi_{L'-(K+L+\Delta L)/2}^2 \right. \\
&\quad \left. + [G(K+L-L'+\Delta L) - G(K+L-L')] \right. \\
&\quad \left. \times G_0(L') \varphi_{L'-(K+L+\Delta L)/2}^2 \right\} G_0(L+\Delta L) \varphi_{(K-L-\Delta L)/2}^2 \\
&\quad + \sum_L t_{pg}(K+L) [G_0(L+\Delta L) - G_0(L)] \varphi_{(K-L-\Delta L)/2}^2 \\
&\quad + \sum_L t_{pg}(K+L) G_0(L) [\varphi_{(K-L-\Delta L)/2}^2 - \varphi_{(K-L)/2}^2] \quad (\text{E.9})
\end{aligned}$$

Comparing this with the analytical expressions corresponding to the diagrams in Fig. 3, it is easy to identify the first two terms as the two AL diagrams (which we denote by AL_1 and AL_2) and the third one with the MT diagram for the pseudogap vertex corrections. Therefore,

$$\frac{1}{2} [(AL_1) + (AL_2)] + (MT)_{pg} + \sum_L t_{pg}(K+L) G_0(L) [\varphi_{(K-L-\Delta L)/2}^2 - \varphi_{(K-L)/2}^2] = 0. \quad (\text{E.10})$$

Finally, we have

$$\begin{aligned} \delta\Lambda_{pg}^\mu(K, K - \Delta L)\Delta L_\mu &= (AL_1) + (AL_2) + (MT)_{pg} & (E.11) \\ &= -(MT)_{pg} - 2 \sum_L t_{pg}(K + L)G_0(L) \frac{\partial \varphi_{(K-L-\Delta L)/2}^2}{\partial L} \cdot \Delta L . \end{aligned}$$

Changing variables $K + L \rightarrow P$, $\Delta L \rightarrow Q$ leads to Eq. (E.1).

The two contributions which enter Eq. (5.28) result from adding the superconducting gap and pseudogap terms which are given, respectively, by

$$\delta\Lambda_{sc}(K, K - Q) = -\Delta_{sc}^2 \varphi_{\mathbf{k}} \varphi_{\mathbf{k}-\mathbf{q}} G_0(-K) G_0(Q - K) \lambda(Q - K, -K) \quad (E.12a)$$

and

$$\begin{aligned} \delta\Lambda_{pg}^\mu(K, K - Q) &= - \sum_P t_{pg}(P) \varphi_{\mathbf{k}-\mathbf{p}/2} \varphi_{\mathbf{k}-\mathbf{q}-\mathbf{p}/2} G_0(P - K) G_0(P + Q - K) \lambda^\mu(P + Q - K, P - K) \\ &\quad + \sum_P t_{pg}(P) G_0(P - K) \frac{\partial \varphi_{\mathbf{k}-\mathbf{p}/2-\mathbf{q}/2}^2}{\partial k_\mu} , \end{aligned} \quad (E.12b)$$

APPENDIX F

FULL EXPRESSIONS FOR THE CORRELATION FUNCTIONS $\overset{\leftrightarrow}{\mathbf{P}}$, \mathbf{P}_0 , AND P_{00}

It is useful here to write down the component contributions to the different correlation functions in the electromagnetic response. After adding the superconducting and pseudo-gap contributions one finds for the current-current correlation function

$$\begin{aligned} \frac{\overset{\leftrightarrow}{\mathbf{n}}}{\mathbf{m}} + \overset{\leftrightarrow}{\mathbf{P}} &= 2 \sum_{\mathbf{k}} \frac{\Delta_{sc}^2}{E_{\mathbf{k}}^2} \left[\frac{1 - 2f(E_{\mathbf{k}})}{2E_{\mathbf{k}}} + f'(E_{\mathbf{k}}) \right] \left[\varphi_{\mathbf{k}}^2(\vec{\nabla}\epsilon_{\mathbf{k}})(\vec{\nabla}\epsilon_{\mathbf{k}}) - \frac{1}{4}(\vec{\nabla}\epsilon_{\mathbf{k}}^2)(\vec{\nabla}\varphi_{\mathbf{k}}^2) \right] \\ &\quad - 2 \sum_{\mathbf{k}} f'(E_{\mathbf{k}}) \frac{\Omega^2}{\Omega^2 - (\mathbf{q} \cdot \vec{\nabla}E_{\mathbf{k}})^2} (\vec{\nabla}\epsilon_{\mathbf{k}})(\vec{\nabla}\epsilon_{\mathbf{k}}) \\ &\quad + \sum_{\mathbf{k}} \frac{\Delta_{pg}^2}{E_{\mathbf{k}}^2} f'(E_{\mathbf{k}}) \frac{\Omega^2}{\Omega^2 - (\mathbf{q} \cdot \vec{\nabla}E_{\mathbf{k}})^2} \left[\varphi_{\mathbf{k}}^2(\vec{\nabla}\epsilon_{\mathbf{k}})(\vec{\nabla}\epsilon_{\mathbf{k}}) - \frac{1}{4}(\vec{\nabla}\epsilon_{\mathbf{k}}^2)(\vec{\nabla}\varphi_{\mathbf{k}}^2) \right], \end{aligned} \quad (\text{F.1})$$

and for the current-density correlation function

$$\mathbf{P}_0 = -2\Omega \sum_{\mathbf{k}} \frac{\epsilon_{\mathbf{k}}}{E_{\mathbf{k}}} f'(E_{\mathbf{k}}) \frac{\mathbf{q} \cdot \vec{\nabla}E_{\mathbf{k}}}{\Omega^2 - (\mathbf{q} \cdot \vec{\nabla}E_{\mathbf{k}})^2} \vec{\nabla}\epsilon_{\mathbf{k}}, \quad (\text{F.2})$$

and finally for the density-density correlation function

$$P_{00} = -2 \sum_{\mathbf{k}} \frac{\Delta_{sc}^2 \varphi_{\mathbf{k}}^2}{E_{\mathbf{k}}^2} \left[\frac{1 - 2f(E_{\mathbf{k}})}{2E_{\mathbf{k}}} + f'(E_{\mathbf{k}}) \right] + 2 \sum_{\mathbf{k}} f'(E_{\mathbf{k}}) \frac{\Omega^2 \Delta_{sc}^2 \varphi_{\mathbf{k}}^2 - E_{\mathbf{k}}^2 (\mathbf{q} \cdot \vec{\nabla}E_{\mathbf{k}})^2}{E_{\mathbf{k}}^2 [\Omega^2 - (\mathbf{q} \cdot \vec{\nabla}E_{\mathbf{k}})^2]}. \quad (\text{F.3})$$

In deriving the first of these we have integrated by parts to evaluate

$$\begin{aligned} \frac{\overset{\leftrightarrow}{\mathbf{n}}}{\mathbf{m}} &= 2 \sum_{\mathbf{k}} \frac{\partial^2 \epsilon_{\mathbf{k}}}{\partial \mathbf{k} \partial \mathbf{k}} G(K) = -2 \sum_{\mathbf{k}} G^2(K) (\vec{\nabla}\epsilon_{\mathbf{k}}) \left[\vec{\nabla}\epsilon_{\mathbf{k}} + \vec{\nabla}\Sigma(K) \right] \\ &= 2 \sum_{\mathbf{k}} \frac{\Delta^2}{E_{\mathbf{k}}^2} \left[\frac{1 - 2f(E_{\mathbf{k}})}{2E_{\mathbf{k}}} + f'(E_{\mathbf{k}}) \right] \left[\varphi_{\mathbf{k}}^2(\vec{\nabla}\epsilon_{\mathbf{k}})(\vec{\nabla}\epsilon_{\mathbf{k}}) - \frac{1}{4}(\vec{\nabla}\epsilon_{\mathbf{k}}^2)(\vec{\nabla}\varphi_{\mathbf{k}}^2) \right] \end{aligned}$$

$$-2 \sum_{\mathbf{k}} f'(E_{\mathbf{k}}) (\vec{\nabla}_{\epsilon_{\mathbf{k}}}) (\vec{\nabla}_{\epsilon_{\mathbf{k}}}). \quad (\text{F.4})$$

These expressions are then used to evaluate Eq. (5.29) in the text.

BIBLIOGRAPHY

- [1] J. R. Schrieffer, *Theory of Superconductivity*, 3rd ed. (Perseus Books, Reading, MA, 1983).
- [2] H. Ding *et al.*, *Nature* **382**, 51 (1996).
- [3] P. W. Anderson, *Science* **235**, 1196 (1987).
- [4] G. Baskaran, Z. Zou, and P. W. Anderson, *Solid State Commun.* **63**, 973 (1987).
- [5] For a review of spin-charge separation, see P. A. Lee, *Physica C* **317-318**, 194 (1999).
- [6] P. A. Lee and X.-G. Wen, *Phys. Rev. Lett.* **78**, 4111 (1997).
- [7] S.-C. Zhang, *Science* **275**, 1089 (1997).
- [8] V. J. Emery and S. A. Kivelson, *Nature* **374**, 434 (1995).
- [9] M. R. Schafroth, J. M. Blatt, and S. T. Butler, *Helv. Phys. Acta* **30**, 93 (1957); M. R. Schafroth, *Phys. Rev.* **111**, 72 (1958).
- [10] J. M. Blatt, *Theory of Superconductivity* (Academic Press, New York, 1964).
- [11] Y. J. Uemura, *Physica C* **282-287**, 194 (1997).
- [12] R. H. McKenzie, *Science* **278**, 820 (1997).
- [13] D. M. Eagles, *Phys. Rev.* **186**, 456 (1969).
- [14] A. J. Leggett, in *Modern Trends in the Theory of Condensed Matter*, edited by A. Pekalski and J. Przystawa (Springer-Verlag, Berlin, 1980), pp. 13–27.
- [15] A. J. Leggett, *J. Phys. (Paris)* **41**, C7/19 (1980).
- [16] P. Nozières and S. Schmitt-Rink, *J. Low Temp. Phys.* **59**, 195 (1985).

- [17] D. J. Thouless, *Ann. Phys. (NY)* **10**, 553 (1960).
- [18] M. Randeria, J.-M. Duan, and L.-Y. Shieh, *Phys. Rev. Lett.* **62**, 981 (1989).
- [19] M. Randeria, J.-M. Duan, and L.-Y. Shieh, *Phys. Rev. B* **41**, 327 (1990).
- [20] S. Schmitt-Rink, C. M. Varma, and A. E. Ruckenstein, *Phys. Rev. Lett.* **63**, 445 (1989).
- [21] J. W. Serene, *Phys. Rev. B* **40**, 10 873 (1989).
- [22] R. Haussmann, *Phys. Rev. B* **49**, 12 975 (1994).
- [23] R. Haussmann, *Z. Phys. B* **91**, 291 (1993).
- [24] B. Janko, J. Maly, and K. Levin, *Phys. Rev. B* **56**, R11 407 (1997).
- [25] J. Maly, B. Jankó, and K. Levin, *Phys. Rev. B* **59**, 1354 (1999).
- [26] J. Maly, B. Jankó, and K. Levin, *Physica C* **321**, 113 (1999).
- [27] L. P. Kadanoff and P. C. Martin, *Phys. Rev.* **124**, 670 (1961).
- [28] B. R. Patton, Ph.D Thesis, Cornell University, 1971 (unpublished); *Phys. Rev. Lett.* **27**, 1273 (1971).
- [29] N. E. Bickers, D. J. Scalapino, and S. R. White, *Phys. Rev. Lett.* **62**, 961 (1989); N. E. Bickers and D. J. Scalapino, *Ann. Phys.* **193**, 206 (1989).
- [30] A. L. Fetter and J. D. Walecka, *Quantum Theory of Many-Particle Systems* (McGraw-Hill, San Francisco, 1971).
- [31] A. Tokumitsu, K. Miyake, and K. Yamada, *Physica B* **165-166**, 1039 (1990); *Prog. Theor. Phys. Suppl. No.* **106**, 63 (1991); *Phys. Rev. B* **47**, 11 988, (1993).
- [32] A. G. Loeser *et al.*, *Science* **273**, 325 (1996).
- [33] J. W. Loram *et al*, *Phys. Rev. Lett.* **71**, 1740 (1993); *Physica C* **235-240**, 134 (1994).
- [34] W. W. Warren *et al.*, *Phys. Rev. Lett.* **62**, 1193 (1989).

- [35] J. W. Loram *et al.*, J. Supercond. **7**, 243 (1994).
- [36] J. W. Loram, K. A. Mirza, J. R. Cooper, and J. L. Tallon, Physica C **282-287**, 1405 (1997).
- [37] A. A. Abrikosov, L. P. Gor'kov, and I. E. Dzyaloshinski, *Methods of quantum field theory in statistical physics* (Prentice-Hall, Englewood Cliffs, N.J., 1963). We use the London gauge in our calculations of n_s .
- [38] W. F. Brinkman and S. Engelsberg, Phys. Rev. **169**, 417 (1968). In the present case, the pair susceptibility which appears as a contribution to the thermodynamical potential is given by GG_0 rather than G_0G_0 .
- [39] L. Belkhir and M. Randeria, Phys. Rev. B **45**, 5087 (1992).
- [40] T. Kostyrko and R. Micnas, Phys. Rev. B **46**, 11 205 (1992).
- [41] R. Cote and A. Griffin, Phys. Rev. B **48**, 10 404 (1993).
- [42] J. R. Engelbrecht, M. Randeria, and C. A. R. Sá de Melo, Phys. Rev. B **55**, 15 153 (1997).
- [43] I. O. Kulik, O. Entin-Wohlman, and R. Orbach, J. Low Temp. Phys. **43**, 591 (1981).
- [44] Y. Y. Zha, K. Levin, and D. Z. Liu, Phys. Rev. B **51**, 6602 (1995).
- [45] P. W. Anderson, Phys. Rev. **112**, 1900 (1958).
- [46] N. N. Bogoliubov, Nuovo Cimento **7**, 794 (1958).
- [47] R. E. Prange, Phys. Rev. **129**, 2495 (1963).
- [48] R. A. Klemm, K. Scharnberg, D. Walker, and C. T. Rieck, Z. Phys. B **72**, 139 (1988).
- [49] I. Kosztin, Q. J. Chen, B. Jankó, and K. Levin, Phys. Rev. B **58**, R5936 (1998).
- [50] Q. J. Chen, I. Kosztin, B. Jankó, and K. Levin, Phys. Rev. B **59**, 7083 (1999).
- [51] A. G. Aronov and V. L. Gurevich, Zh. Éksp. Teor. Fiz. **70**, 955 (1976) [Sov. Phys. JETP **43**, 498 (1976)].

- [52] C. A. R. Sá de Melo, M. Randeria, and J. R. Engelbrecht, *Phys. Rev. Lett.* **71**, 3202 (1993).
- [53] M. Drechsler and W. Zwerger, *Ann. Physik* **1**, 15 (1992).
- [54] J. F. Annett, N. D. Goldenfeld, and A. J. Leggett, preprint cond-mat/9601060 (unpublished).
- [55] Our choice for t_0 leads to $E_F \approx 300$ meV for $x = 0.15$, in agreement with photoemission data. See, e.g., Z.-X. Shen *et al.*, *Science* **267**, 343 (1995); M. C. Schabel *et al.*, *Phys. Rev. B* **57**, 6090 (1998).
- [56] N. Miyakawa, P. Guptasarma, J. F. Zasadzinski, D. G. Hinks, and K. E. Gray, *Phys. Rev. Lett.* **80**, 157 (1998); N. Miyakawa *et al.*, *Phys. Rev. Lett.* **83**, 1018 (1999).
- [57] J. Rossat-Mignod *et al.*, *Physica B* **169**, 58 (1991).
- [58] M. Oda *et al.*, *Physica C* **281**, 135(1997).
- [59] C. Panagopoulos *et al.*, *Phys. Rev. B* **60**, 14 617 (1999).
- [60] D. A. Bonn, S. Kamal, A. Bonakdarpour, R. X. Liang, W. N. Hardy, C. C. Homes, D. N. Basov, and T. Timusk, *Czech J. Phys.* **46**, suppl. 6, 3195 (1996).
- [61] C. Panagopoulos, J. R. Cooper, and T. Xiang, *Phys. Rev. B* **57**, 13 422 (1998).
- [62] T. Xiang and C. Panagopoulos, private communications.
- [63] A. J. Millis, S. M. Girvin, L. B. Ioffe, and A. I. Larkin, *J. Phys. Chem. Solids* **59**, 1742 (1998).
- [64] G. D. Mahan, *Many-Particle Physics*, 2nd ed. (Plenum Press, New York, 1990).
- [65] See, e.g., M. Rapp, A. Murk, R. Semerad, and W. Prusseit, *Phys. Rev. Lett.* **77**, 928 (1996).
- [66] Ch. Renner, B. Revaz, J.-Y. Genoud, K. Kadowaki, and Ø. Fischer, *Phys. Rev. Lett.* **80**, 149 (1998).

- [67] A. Hosseini *et al.*, Phys. Rev. Lett. **81**, 1298 (1998).
- [68] A. Carrington *et al.*, Phys. Rev. Lett. **83**, 4172 (1999). Here the authors show that a dirty d -wave fit works over a broad T regime, but not at the lowest T (where $T^{3/2}$ is observed).
- [69] O. Waldmann *et al.*, Phys. Rev. B **53**, 11 825 (1996).
- [70] T. Valla *et al.*, Science **285**, 2110 (1999).
- [71] X. J. Zhou, private communications (data on v_F).
- [72] S.-F. Lee *et al.*, Phys. Rev. Lett. **77**, 735 (1996).
- [73] K. Krishana, J. M. Harris, and N. P. Ong, Phys. Rev. Lett. **75**, 3529 (1995).
- [74] J. Mesot *et al.*, Phys. Rev. Lett. **83**, 840 (1999).
- [75] J. W. Loram *et al.*, in *Proc. 10th Ann HTS workshop*, edited by B. Batlogg *et al.* (World Scientific, Singapore, 1996), pp. 341–344.
- [76] N. Momono *et al.*, Physica C **233**, 395 (1994).
- [77] K. A. Moler *et al.*, Phys. Rev. B **55**, 3954 (1997).
- [78] A. Junod *et al.*, Proceedings of LT22 (Helsinki, August 1999).
- [79] D. A. Wright *et al.*, Phys. Rev. Lett. **82**, 1550 (1999), see also J. P. Emerson *et al.*, Phys. Rev. Lett. **82**, 1546 (1999).
- [80] R. A. Fisher *et al.*, Physica C **252**, 237 (1995).
- [81] J. W. Loram, K. A. Mirza, J. R. Cooper, and J. L. Tallon, J. Phys. Chem. Solids **59**, 2091 (1998).
- [82] C. Renner *et al.*, Phys. Rev. Lett. **80**, 3606 (1998).
- [83] G. S. Boebinger *et al.*, Phys. Rev. Lett. **77**, 5417 (1996).
- [84] M. R. Norman *et al.*, Phys. Rev. B **60**, 7585 (1999).

- [85] H. Ding *et al.*, Phys. Rev. Lett. **78**, 2628 (1997).
- [86] A. Hosseini *et al.*, Phys. Rev. B **60**, 1349 (1999).
- [87] E. Demler and S.-C. Zhang, Nature **396**, 733 (1998).
- [88] M. R. Norman, M. Randeria, B. Jankó, and J. C. Campuzano, Phys. Rev. B **61**, 14 742 (2000).
- [89] N. P. Ong, talk presented at the M²S-HTSC-VI centennial conference, (Houston, TX, Feb. 2000), and at the American Physical Society March Meeting, (Minneapolis, MN, Mar., 2000).
- [90] A. J. Leggett, *Quantum Liquids*, J. Ruvalds and T. Regge (eds), (Elsevier/North Holland, Amsterdam, 1978).